Single strontium atoms in optical tweezers

ACADEMISCH PROEFSCHRIFT

ter verkrijging van de graad van doctor
aan de Universiteit van Amsterdam
op gezag van de Rector Magnificus
prof. dr. ir. P.P.C.C. Verbeek
ten overstaan van een door het College voor Promoties ingestelde commissie,
in het openbaar te verdedigen in de Agnietenkapel
op dinsdag 25 april 2023, te 12.00 uur

door Alexander Albert Urech

geboren te Michigan

Promotiecommissie

Promotor	prof. dr. F. E. Schreck	Universiteit van Amsterdam
Co-promotor	dr. R. J. C. Spreeuw	Universiteit van Amsterdam
Overige leden	prof. dr. T. Pfau	University of Stuttgart
	prof. dr. S. J. J. M. F. Kokkelmans	Technische Universiteit Eindhoven
	prof. dr. C. J. M. Schoutens	Universiteit van Amsterdam
	dr. A. Safavi Naini	Universiteit van Amsterdam
	dr. R. Gerritsma	Universiteit van Amsterdam

Faculteit der Natuurwetenschappen, Wiskunde en Informatica (FNWI)

The research reported in this thesis was carried out at the Van der Waals-Zeeman Institute, Institute of Physics, University of Amsterdam. The work was financially supported by the Dutch Research Council (NWO/OCW), as part of the Quantum Software Consortium programme (project number 024.003.037) and under grant No. FOM-153. This work was also supported by the Dutch National Growth Fund (NGF), as part of the Quantum Delta NL programme.

Contents

Chapter 1

Introduction

Single atoms trapped in tightly focused optical dipole traps, known as optical tweezers, have emerged as a promising tool for quantum applications such as quantum simulation, computation, and metrology. In this thesis we will discuss the development of an experimental setup for trapping single strontium atoms in preparation for quantum simulation and computation experiments.

This chapter is ordered as follows. First we will present a short historical background on the origins of optical tweezers, laser cooling of atoms, and quantum simulation and computing. Second we will discuss some more specific details of strontium. Third we will mention some state of the art results in the field of single atoms trapped in optical tweezers, and fourth we conclude with an outline of this thesis.

1.1 Historical Background

We will give a brief overview of the origins of the experimental tools and theoretical ideas used in this thesis. This review is by no means exhaustive, but we cite detailed review articles for each topic to point interested readers to more information on each of the subjects.

The story of optical tweezers begins with the ideas of Nobel laureate Arthur Ashkin [1]. In the early 1970s, Ashkin began studying the idea of using the radiative pressure of light to optically trap neutral particles. This lead to the first simple optical tweezer experiment in which the Gaussian focus of a laser beam was used to trap latex spheres suspended in a water solution [2]. Ashkin, along with many others, began to consider the possibilities of using this radiative force to trap individual atoms and molecules and the ideas of laser cooling began to emerge and be experimentally realized in the late 70s and 80s [1, 3, 4, 5]. This led to the first optical tweezer for neutral atoms, also

known as an optical dipole trap [6]. On the way to this result, Ashkin also pursued other possible applications for optical tweezers, such as trapping proteins, viruses, and even organelles inside living cells [7, 8, 9]. This led to huge developments in the microscopy of biological samples.

The field of laser cooling of neutral atoms also continued to evolve [4, 10]. These new laser cooling techniques aided in the preparation of colder and denser atomic gases and eventually in the production of the first Bose-Einstein condensate [11]. Now many different atomic samples have been cooled to quantum degeneracy opening many new interesting areas of study for atomic physics experiments [10, 12, 13, 14].

Also in the 1980s, the ideas of quantum simulation and computing began to emerge. Richard Feynman first proposed the idea of simulating one quantum system with another more controlled quantum system in 1982 giving rise to the concept of quantum simulation [15]. In 1985, David Deutsch expanded on these ideas describing for the first time a "universal quantum computer" on which "every finitely realizible physical system can be perfectly simulated by a universal model computing machine operating by finite means" [16]. In 2002, the generalization from a 2 level quantum bit of information (qubit) to any number of internal states, d, known as a qudit was made in [17]. A number of different possible platforms for a quantum computer have been proposed and realized such as trapped atoms, superconductors, photons, and quantum dots, see [18, 19].

The fields quantum simulation and computation continued to expand with many different ideas. Some ideas for quantum simulation included using the newly created field of quantum gases as the simulation platform leading to many proposals and experiments [12, 13, 14]. Around the same time, the first proposals of using strong interactions of Rydberg gases (highly excited atoms) for quantum computing began to appear [20, 21], closely followed by the first single atoms trapped in optical tweezers, which would make a great platform for such computations [22]. The field of single atom optical tweezer experiments continued to evolve over the next decade leading to the first observation of the Rydberg blockade effect for two tweezers [23, 24] and the first entanglement operations between two neighboring tweezer sites [25]. The research area of single atoms in optical tweezers for quantum computing began to expand more [26], and has been growing at a staggering rate in recent years with new experiments popping up around the world [27, 28].

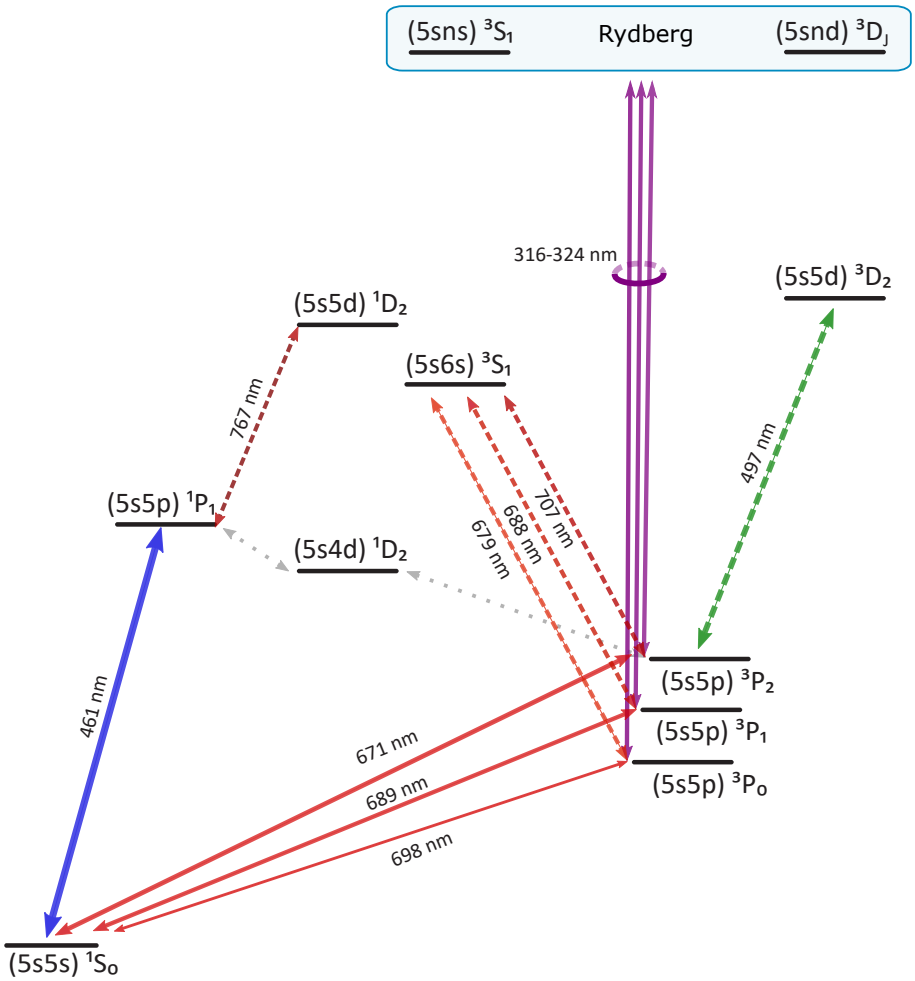

FIGURE 1.1: Level diagram for bosonic strontium. All transitions mentioned in this thesis have been included.

1.2 Strontium

The atom used throughout this thesis is strontium. Strontium has four different isotopes, three bosonic (^{84}Sr, ^{86}Sr, and ^{88}Sr) and one fermionic (^{87}Sr with nuclear spin $I = 9/2$). Strontium is a group-two element also known as an alkaline earth metal. Alkaline earth(-like) metals have a helium like atomic structure with two valence electrons in an s-orbital, giving a ground state configuration of $^1S_0$. The two valence electrons make two types of electron excitation possible since the spins of the two valence electrons can remain anti-parallel or become parallel, giving rise to singlet and triplet excited states respectively [29], see Fig. 1.1 for a level diagram of strontium with all levels relevant to this thesis.

The triplet states of the alkaline earth-like metals are one of their unique properties. More specifically, the lowest lying ^3P_J states are metastable states allowing for new experimental applications in comparison to the more commonly used alkali metals. The $^3P_1$ state can be used for a second stage narrow-linewidth magneto-optical trap (MOT) operating on the $^1S_0$ - $^3P_1$ transition, which allows for colder temperatures to be achieved along with opening the door to other valuable cooling methods and continuous Bose-Einstein condensation [29, 30, 31, 32, 33]. The $^3P_0$ state is a metastable state with long lifetime, leading to an ultranarrow $^1S_0$ - $^3P_0$ transition, which has no spin orbit coupling and is insensitive to magnetic fields to first order, making it a great transition for optical atomic clocks [29, 34, 35, 36, 37, 38]. The $^3P_2$ state is also a long lived metastable state with an electronic magnetic moment. The additional ultranarrow $^1S_0$ - $^3P_2$ transition opens additional possibilities for quantum simulation and quantum computing [39, 40, 41]. For an extensive review and more details on strontium and other alkaline earth(-like) metals see [29, 42].

Out of the alkaline earth-like atoms, strontium and ytterbium have become popular choices for optical tweezer experiments over the last four years [30, 43, 44, 45, 46, 47, 48]. For both atoms two different isotopes have been used, the most abundant bosonic isotope, ^{174}Yb [43] and ^{88}Sr [30, 44, 45], and a fermionic isotope, ^{171}Yb [47, 48] and ^{87}Sr [46]. These experiments have already begun to show very impressive results, some of which we will outline in the next section.

1.3 State of the art

The initial single atom optical tweezer experiments focused primarily on rubidium atoms [23, 24]. Similar experiments with rubidium have been developed to a stage where they can perform large scale quantum simulations [49, 50] and explore other interesting topics such as increasing the number and lifetime of single atoms in tweezer arrays [51, 52] and entanglement transportation [53]. Cesium atoms in optical tweezers are now also used as a good candidate for quantum computing [54].

Although significantly less time has passed since the first alkaline earth-like single atoms in tweezers [30, 43, 44], there have already been many impressive results. Groups have demonstrated two types of imaging methods, one that uses the broad $^1S_0$ - $^1P_1$ transition [30, 43, 44, 48] and another that uses the narrow $^1S_0$ - $^3P_1$ transition [43, 47, 55], along with exploring different tweezer wavelengths in strontium [32, 34, 45] and

ytterbium [47]. Multiple types of high fidelity qubits have been demonstrated as well including direct addressing of the clock transition as a qubit [56], metastable state to Rydberg state qubits [56, 57, 58], and hyperfine ground state qubits in the fermionic isotopes [46, 47, 48]. With strontium, groups have demonstrated optical clocks using tweezer arrays [34, 35, 36], and demonstrated loading single atoms from tweezer traps into a 2D optical lattice opening other new opportunities [56, 59]. The fact that alkaline earth atoms have two valence electrons has also been exploited for Rydberg atom trapping [60] since the remaining ground state electron allows for the atom to remain trapped [60, 61].

1.4 Thesis outline

The remainder of this thesis is outlined as follows:

- In Chapter 2, we present the main experimental results of this thesis that have been published as "Narrow-line imaging of single strontium atoms in shallow optical tweezers" [55]. Here we present our results on the first demonstration of high-fidelity imaging of single Sr atoms using its narrow (7.4 kHz-wide) $^1S_0$-$^3P_1$ transition, where we trap the atoms in *non*-magic wavelength tweezers. After an introduction, this article starts with an overview of our experimental procedure (Section 2.3) and continues with the details and characterization of our red imaging method (Section 2.4). This section includes a description of the attractive Sisyphus cooling process, optimized parameters, detection fidelity, and survival probabilities. We proceed with our results on selectively imaging (hiding) a specific tweezer trap of the array (Section 2.5). The ability to selectively image a single site is a specific advantage of narrow-line imaging in non-magic wavelength tweezers and could prove useful for quantum error correction or state specific detection in ^{87}Sr. After the conclusion (Section 2.6), additional details of the experimental setup are presented in the appendices (Section 2.7 and Section 2.8).

- In Chapter 3, we present some theoretical calculations. In Section 3.1, we discuss how light and magnetic fields affect the internal states of the atom and outline how to calculate the polarizability (light shift) and Zeeman shift for different internal states of strontium including the ones of fermionic ^{87}Sr. Calculating these

shifts accurately is important for characterizing trap depths, and to find magic-wavelengths between different internal states. In Section 3.2, we briefly outline the method for composing an n-level coupling Hamiltonian and evolving this Hamiltonian with dissipation by using the Lindblad master equation. This evolution is required for the calculations of the following two sections. In Section 3.3, we cover in detail our simulation of the attractive Sisyphus cooling process mentioned in Section 2.4 including additional results and limits of the cooling parameters. The simulation outlined in this section works for other types of laser cooling in an optical tweezer, including sideband cooling and *repulsive*-Sisyphus cooling. In Section 3.4, we present the main theoretical result of this thesis with the author's main contribution to the publication "Solving correlation clustering with QAOA and a Rydberg qudit system: a full-stack approach" [41]. In this section, we propose a single qudit coupling scheme in ^{87}Sr. We calculate the required transition dipole moments for varying magnetic field strength in order to determine coupling strengths, analyse the dominant error sources and summarize the limits or required parameters, and present a possible method for experimental implementation.

- In Chapter 4, we present some additional experimental details and results. This section's primary focus is to give additional details that were excluded from Chapter 2 and try to highlight methods that we found useful in initially acquiring single atom results. In Section 4.1 we begin with a brief overview of the experimental setup, focusing on the changes to the experiment after the theses of O. Onishchenko [62] and S. Piatchenkov [63]. In Section 4.2, we outline the optical setup of the tweezer system including the alignment and characterization procedure along with the alignment to the vacuum chamber. In Section 4.3, we present our initial results with NIR-tweezers including the wavelengths of 785 nm and 813 nm. We focus on our preliminary results and first signs of single atoms in order to help future experiments work through this initial period as fast as possible. We also include our first red imaging results and alignment of the spatial light modulator tweezer array after our first single atom results. In Section 4.4, we continue with some of the critical parameters that we have found to help significantly improve the performance of our experimental setup and allow for us

to achieve the results presented in Chapter 2. In Section 4.5 we finish with presenting some additional information on our site-selective imaging technique and our results on using an additional movable tweezer to sort the atoms of the array into a defect-free array. This process is required for using Rydberg excitation of the atoms for engineering interactions between atoms in different tweezer sites.

- In Conclusion and outlook, we briefly mention some of the ongoing work in the lab along with future plans for the experiment and conclude the thesis.

Chapter 2

Narrow-line imaging of single strontium atoms in shallow optical tweezers

This chapter has been published as [55].

2.1 Abstract

Single strontium atoms held in optical tweezers have so far only been imaged using the broad $^1S_0$ - $^1P_1$ transition. For Yb, use of the narrow (183 kHz-wide) $^1S_0$ - $^3P_1$ transition for simultaneous imaging and cooling has been demonstrated in tweezers with a magic wavelength for the imaging transition. We demonstrate high-fidelity imaging of single Sr atoms using its even narrower (7.4 kHz-wide) $^1S_0$ - $^3P_1$ transition. The atoms are trapped in *non*-magic-wavelength tweezers. We detect the photons scattered during Sisyphus cooling, thus keeping the atoms near the motional ground state of the tweezer throughout imaging. The fidelity of detection is 0.9991(4) with a survival probability of 0.97(2). An atom in a tweezer can be held under imaging conditions for 79(3) seconds allowing for hundreds of images to be taken, limited mainly by background gas collisions. The use of a fully closed (cycling) transition for imaging will provide a useful tool for state specific detection. We detect atoms in an array of 36 tweezers with 813.4-nm light and trap depths of 135(20) μK. This trap depth is three times shallower than typically used for imaging on the broad $^1S_0$ - $^1P_1$ transition. Narrow-line imaging opens the possibility to even further reduce this trap depth, as long as all trap frequencies are kept larger than the imaging transition linewidth. Imaging using a narrow-linewidth

transition in a non-magic-wavelength tweezer also allows for selective imaging of a given tweezer. As a demonstration, we selectively image (hide) a single tweezer from the array. This provides a useful tool for quantum error correction protocols.

2.2 Introduction

Optical tweezers have emerged as a powerful tool for quantum applications. They enable state of the art quantum simulation and computation [49, 50, 56, 58], high fidelity and long coherence time qubits [46, 47, 48, 57, 64], quantum metrology [34, 35, 36], quantum chemistry [65, 66], among numerous other applications. Optical tweezers with alkaline-earth(-like) atoms, in particular with strontium and ytterbium, have been recently realized, offering new possibilities in expanding these applications [30, 43, 44].

In all strontium tweezer experiments demonstrated so far, the fluorescence of single atoms on the broad (30 MHz) $^1S_0$ - $^1P_1$ transition at 461 nm was recorded, while simultaneously cooling the atoms on the narrow (7.4 kHz) $^1S_0$ - $^3P_1$ transition at 689 nm [30, 32, 34, 35, 36, 44, 45, 46, 56, 57]. This 'blue imaging' method allows for high-fidelity detection of single atoms in tweezers with high survival probability [30, 32, 44]. However, blue imaging requires repumpers to close the 5s4d $^1D_2$ decay channel, which can only be done at tweezer wavelengths where also the $^1D_2$ state is trapped [32, 34, 46, 57]. Furthermore, the slightly higher scattering rate obtained in the blue imaging process ($\sim$75 kHz) can only be used as long as the tweezers are sufficiently deep. Any excess heating from the imaging process can then be cooled away after the image. As the trap depth of the tweezer is reduced, the advantage of fast imaging is lost because the scattering rate must also be reduced to balance heating from imaging and cooling. Reducing the tweezer trap depth has the advantages of decreased laser power requirement per tweezer (allowing for more tweezers using a given laser source) and increasing metastable state lifetimes (reduced off-resonant scattering of tweezer light).

A simpler method for imaging alkaline-earth(-like) atoms in tweezers is to use the narrow $^1S_0$ - $^3P_1$ transition for both cooling and imaging. Single atom detection by fluorescence imaging on a (less) narrow transition has previously been demonstrated in ytterbium for two different isotopes. In both cases tweezers with a magic-wavelength for the imaging transition were used [43, 47].

Here we detect single ^{88}Sr atoms using only the $^1S_0$ - $^3P_1$ transition for simultaneous'red imaging' and cooling. We use optical tweezers that are *non*-magic for the imaging transition, but magic for the Sr clock transition ($^1S_0$ - $^3P_0$). We detect the photons scattered during an *attractive* Sisyphus cooling process [32], thus keeping the atoms near the motional ground state of the tweezer throughout imaging.

Attractive Sisyphus cooling is possible at tweezer wavelengths where the excited state experiences a deeper trap depth than the ground state. More specifically, at our tweezer wavelength of 813.4 nm, the excited state ($|e\rangle \equiv {}^3P_1\,|m_j| = 1$) confinement is 1.24 times greater than the ground state ($|g\rangle \equiv {}^1S_0$), see Fig. 2.1(a). This cooling process can be very efficient with a proper choice of parameters, leading to a large reduction in energy per scattered photon, and a small number of scattered photons needed to cool the atom [67]. In addition, the non-magic trapping causes the harmonic oscillator states of $|e\rangle$ and $|g\rangle$ to be non-orthogonal, for both the radial and axial directions. A single cooling beam can thus remove energy from all directions [32, 67].

With balanced heating and cooling from the imaging process, the trap depth can be significantly decreased, reducing the power required per tweezer. Additionally, red imaging can be performed without repumpers, since optical pumping to metastable states is much reduced. The only remaining pumping is due to off-resonant scattering of 813-nm tweezer light when the atom is in $|e\rangle$, which has a low rate that is even further decreased by using shallow tweezers. Specifically, the calculated off-resonant scattering rate of tweezer photons from an atom in the $^3P_1$ state is 1.3 Hz under imaging conditions, where the finite fraction of time spent in the excited state is taken into account.

Imaging in shallow tweezers does limit the scattering rate that can be achieved without unacceptable atom loss, for both red and blue imaging. Shallow tweezer imaging therefore requires a longer exposure time for high-fidelity single atom detection compared to imaging in deeper tweezers. We show for red imaging that the maximum scattering rate ($\Gamma/2 \approx 23$ kHz for the $^1S_0$ - $^3P_1$ transition, where $\Gamma = 2\pi\times 7.4$ kHz is the transition linewidth) can be closely approached with proper modulation of the frequency and intensity of the cooling beam, while maintaining a lower temperature than when using blue imaging. This allows for a reduction of the trap depth by a factor of ~ 3, while only marginally increasing the imaging duration and maintaining a near unity detection fidelity and survival probability.

We proceed by presenting an overview of the experimental setup and the procedure

for preparing single atoms in Sec. 2.3. In Sec. 2.4, we present our imaging method along with a description of the attractive Sisyphus cooling process, optimized parameters, detection fidelity, and survival probabilities. In Section 2.5 we demonstrate the ability to selectively image (dark out) a specific tweezer from the array and we conclude in Sec. 2.6.

2.3 Overview of experimental setup and procedure

Similar to previously demonstrated strontium tweezer experiments, we load the optical tweezers with a small and random number of atoms from a magneto-optical trap (MOT) operating on the narrow $^1S_0$ - $^3P_1$ transition [30, 32, 34, 35, 36, 44, 46, 56, 57]. Our procedure for creating the MOT is similar to the one of [68], but uses a reduced number of MOT beams to make space for a microscope objective and dynamically moves the MOT from a loading position into the objective focus, see Appendix A.

We create two dimensional arrays of optical tweezers using a phase-only spatial light modulator (SLM) to imprint a phase onto an 813.4-nm laser beam creating an array of foci [49, 50]. This array is then imaged onto the narrow linewidth MOT through an NA=0.5 microscope objective. An additional dynamically movable tweezer is created using the same microscope objective and a pair of crossed acousto-optic deflectors (AODs), see Appendix B.

The tweezer trap depth used throughout this paper is 135(20) μK unless otherwise specified. For our $1/e^2$ tweezer waist of $\sim 0.84\,\mu$m, the ground state radial (axial) trap frequencies are $\omega_{\text{radial}} = 43(3)$ kHz ($\omega_{\text{axial}} = 6.6(5)$ kHz), respectively. This trap depth is chosen such that the excited state axial trap frequency (7.3(6) kHz) is comparable to the linewidth of the $^1S_0$ - $^3P_1$ transition. We characterize the trap depth and waist of our tweezers spectroscopically on both the m_j=0 and $|m_j|$=1 $^1S_0$ - $^3P_1$ transitions, see Appendix B. The trap frequencies are calculated from the estimated values of the waist and the measured AC Stark shifts.

Once the tweezers have been loaded and the MOT is switched off, a single (non-retro-reflected) 689-nm beam is used to address the tweezer array during all further experimental stages that need 689-nm light (light-assisted collisions, imaging, cooling, spectroscopy), see Fig. 2.1(b). This beam, here simply called imaging beam, is linearly polarized perpendicular to the tweezer propagation axis to maximize the fluorescence into the microscope. Additionally, we tune the linear polarization of the tweezer light

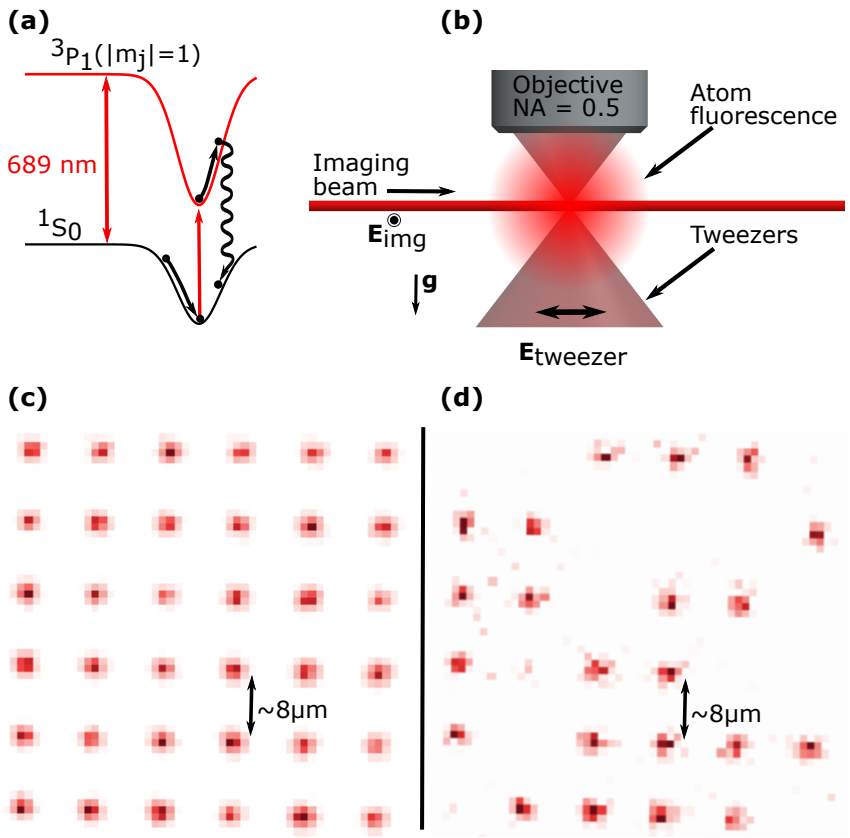

FIGURE 2.1: **(a)** A sketch of the Sisyphus cooling process at the root of our imaging technique. The tweezer potential is deeper for the excited state ($^3P_1$) than for the ground state ($^1S_0$). The order of events for a cooling cycle is shown from left to right. The atom initially rolls down the ground state potential where it is preferentially excited near the bottom of the potential. The atom then rolls up the steeper excited state potential before decaying back to the ground state at a lower energy. This leads to a reduction in energy per scattered photon related to the trap depth mismatch [32, 67]. **(b)** A simplified schematic of the experimental setup. A high numerical aperture objective (NA = 0.5) creates the optical tweezers and collects the atomic fluorescence. A single beam (imaging beam) is used for light-assisted collisions, cooling, and imaging in the tweezer array. The polarization of both this imaging beam ($\mathbf{E}_{\text{img}}$) and the SLM tweezer pattern ($\mathbf{E}_{\text{tweezer}}$) are shown. The direction of gravity with respect to the objective is also shown (**g**). **(c)** Averaged fluorescence of strontium atoms in the 6×6 array of tweezers used throughout the majority of this work. We collect photons scattered from the $^1S_0$ - $^3P_1$ ($|m_j| = 1$) transition during the cooling process in order to image the atoms in the array. The image is the average of 100 experimental realizations using 500 ms of exposure each. **(d)** Image obtained by one such experimental run. Approximately half of the tweezer traps are filled on average.

to match the propagation axis of the imaging beam. This maximises the $\sigma^{\pm}$ component of the imaging beam because we operate the tweezers at a 0 G magnetic field making the tweezer polarization the dominant quantization axis.

To prepare tweezers containing either a single or no atom, we use light-assisted collisions to induce pairwise loss, leaving either zero or one atom remaining in each tweezer [69]. The imaging light used in this process is tuned to a frequency between the Stark shifted resonance of the $^1S_0$ - $^3P_1$ $(|m_j| = 1)$ transition and an electronically excited molecular state that is further red detuned and that asymptotically corresponds to the $^3P_1$ state [30, 70].

We perform imaging by collecting the scattered photons from the Sisyphus cooling process as presented in Sec. 2.4. The fluorescence is collected via the same microscope objective used to generate the tweezers, and then separated using a long pass dichroic mirror with 750-nm cutoff. The collected fluorescence light is sent onto an EMCCD camera [71, 72]. The number of photons in 5×5 pixel regions of interest (ROIs) around each tweezer center is summed. We collect photons for 100 ms in order to separate the single atom signal from the background noise of the camera. This procedure leads to a histogram with two peaks, corresponding to zero and one atom in a tweezer, as shown in Fig. 2.4(a). An atom is assumed to be in a tweezer if the photon number lies above a threshold located between the two peaks, see Sec. 2.4(D).

In the previously demonstrated blue imaging technique, the metastable $^3P_0$ and $^3P_2$ states must be repumped to the ground state during imaging because of decay of $^1P_1$ to those metastable states [32, 34]. During red imaging, these repumpers are only used to compensate optical pumping into $^3P_{0,2}$ by the tweezer light that can happen when the atom is in the $^3P_1$ $(|m_j| = 1)$ state. However, we find that this is unnecessary for the shallow traps used in this work. Nonetheless, we have the ability to repump the metastable states via the $^3S_1$ state using two lasers at 679 nm and 707 nm for the $^3P_0$ and $^3P_2$ states respectively.

For all the results presented in this paper, we begin an experimental run by preparing single atoms using the above method followed by an initial image to determine which tweezers are filled. After this,we perform measurements as required by the experiment under consideration. The average initial image of 100 preparations for a 6×6 array and an image of a single run is shown in Fig. 2.1(c) and (d) respectively.

All plots presented are for 100 repetitions of each experiment unless stated otherwise and the data is the average of all 36 tweezer sites. Taking into account the typical tweezer loading efficiency of 50%, each data point consists of approximately 1800 realizations. The error bars for the entire paper show the standard deviation over the array and are dominated by variation originating from tweezer depth inhomogeneities across the array. The raw data and the analysis tools used in this research can be found in Ref. [73].

2.4 Imaging via Sisyphus cooling

Our imaging and cooling relies on the attractive Sisyphus cooling technique first proposed in [67, 74] and more recently observed experimentally in tweezer arrays [32, 34, 46] as well as in a continuous beam decelerator [31]. We can keep the scattering rate near maximum with near zero trap loss or heating in tweezers as shallow as 135(20) μK by intentionally keeping the imaged atoms slightly hotter than the coldest possible temperature, and by proper choice of imaging/cooling parameters.

2.4.1 Sisyphus cooling criteria

Attractive Sisyphus cooling relies on a trap depth mismatch between the excited and ground state potentials as shown in Fig. 2.1(a). In addition, three conditions must be fulfilled for the cooling to work. First, the excited state of the atom must experience stronger confinement than the ground state. Second, one must have the ability to excite the atom selectively from the bottom of the potential, and third the excited atom must have sufficient time to move away from the center of the potential before decaying [67]. The first condition is fulfilled in our setup by properly choosing the trapping wavelength, while the second and third conditions can be fulfilled by using the narrow linewidth $^1S_0$ - $^3P_1$ transition in strontium.

The first condition is needed for the atoms to lose kinetic energy by rolling up the steeper potential of the excited state before decaying. This allows for a reduction in potential energy on the order of the differential trap depth per scattering event. The narrow linewidth of the transition allows for the atoms to be selectively excited from the bottom of the trap if the differential trap depth is larger than the linewidth. The

lifetime of the narrow transition is long enough to satisfy the third condition if the trap frequencies are larger than the linewidth. The atom will then more likely decay near the motional turning point, away from the center of the trap.

2.4.2 Optimal cooling

To investigate the performance of our cooling/imaging technique and find optimal cooling parameters, we measure the temperature by the release and recapture method [75]. We switch the tweezers off, wait a time t_{release} before turning them back on again, and then image the atoms to determine their survival fraction. Atoms are lost quicker when they are hotter. The temperature is determined by comparing the survival fraction for several values of t_{release} with Monte-Carlo atom trajectory simulations [32, 75].

To characterize cooling performance, we start by preparing a sample and detecting which tweezers contain an atom (see Sec. 2.3). We then cool for a time t_{cool} and perform release and recapture. Next, we cool the array again before taking a final image to see which atoms survived and calculate the survival fraction.

The results of such measurements under optimal cooling conditions for three t_{cool} are shown as examples in Fig. 2.2(a). The first measurement is taken directly after the first image ($t_{\text{cool}} = 0$ ms, red circles). The second briefly cools the atoms ($t_{\text{cool}} = 2$ ms, green squares). The third approaches the asymptotically coldest achievable temperature by using a long cooling time ($t_{\text{cool}} = 20$ ms, blue triangles).

Comparing this data with release and recapture simulations yields a temperature of approximately 1.8 μK (dashed line in same figure) for an optimally cooled atom ($t_{\text{cool}} = 20$ ms), which is consistent with a temperature near the radial motional ground state energy of roughly $T = \frac{\hbar\omega}{2k_b} \sim 1.1\,\mu$K for our trap depth [75]. The release and recapture simulations are based on classical trajectories and could lead to an overestimation in the temperature as the atom approaches the motional ground state of the trap. Therefore we take this temperature estimate as an upper bound.

To optimize cooling, we vary cooling light frequency or intensity while keeping $t_{\text{release}} = 60\,\mu$s and $t_{\text{cool}} = 20$ ms fixed. Figure 2.2(b) shows an example of such a measurement for which the detuning is varied. As explained in Sec. 2.4(C), the imaging process is also interlaced with brief cooling phases. Here we vary the cooling frequency both during the period t_{cool} and during the brief cooling stages interlacing the imaging process. We find the highest recapture fraction, and therefore optimal cooling,

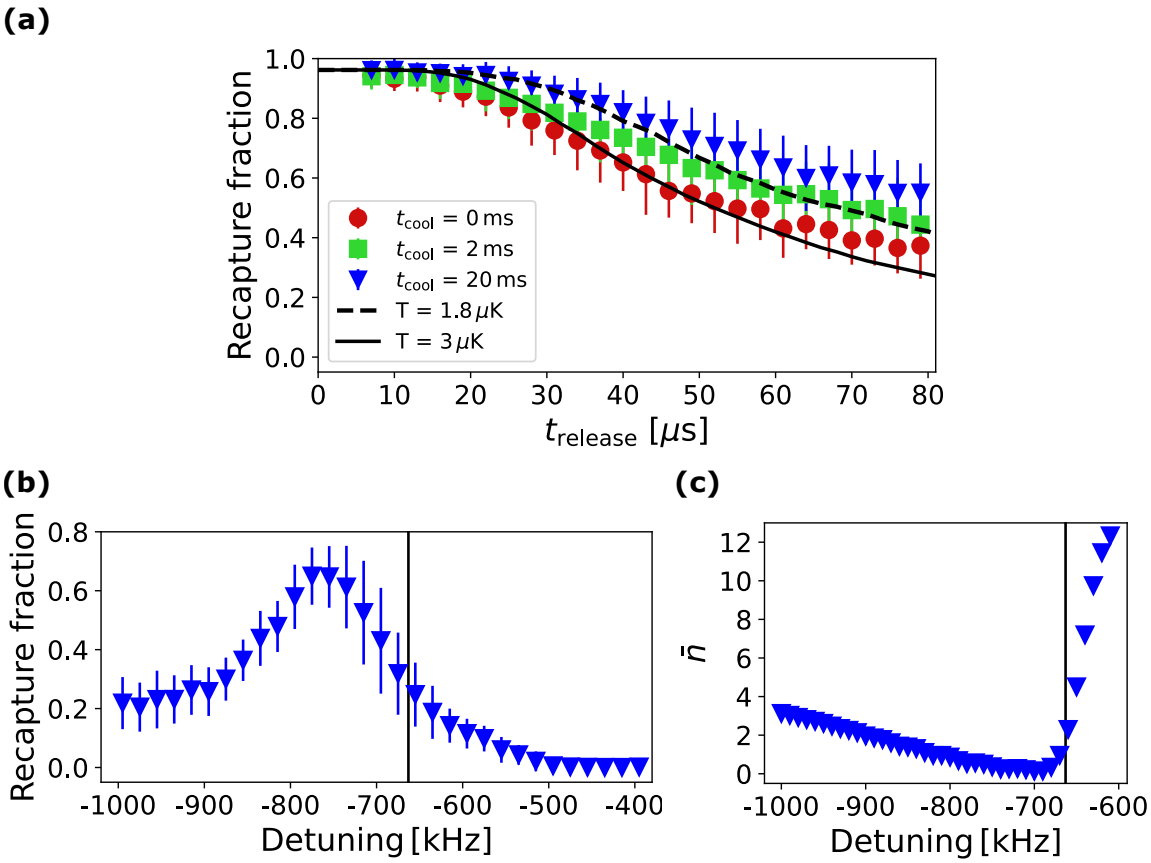

FIGURE 2.2: **(a)** Temperature measurements using the release and recapture method for three different cooling times, t_{cool}, after taking an image. The red circles show an atom directly after an image ($t_{\text{cool}} = 0$ ms), green squares show a briefly cooled atom ($t_{\text{cool}} = 2$ ms), and blue triangles show an optimally cooled atom ($t_{\text{cool}} = 20$ ms). Error bars show the standard deviation calculated over the 36 atom array. All other errors fall well inside these error bars. The dashed (solid) lines show the results of Monte Carlo simulations for temperatures of 1.8 μK (3 μK) respectively. As discussed in Sec. 2.4(C), we use an interlaced imaging/cooling technique that ends with 1.5 ms of cooling. The time t_{cool} starts after the final 1.5 ms of cooling at the end of the first image, so t_{cool} is the amount of additional cooling. **(b)** Recapture fraction of a single atom versus the cooling frequency for $t_{\text{cool}} = 20$ ms and $t_{\text{release}} = 60$ μs. Here we vary the cooling frequency both during the period t_{cool} and during the brief cooling phases interlacing the imaging process. The vertical line shown at -663 kHz indicates the approximate Stark shifted resonance of the cooling transition. **(c)** Average motional quanta $\bar{n}$, obtained by numerical simulation, in dependence of cooling light detuning at optimal intensity. The cooling transition is indicated as in (b).

for a frequency of -775 kHz from the free space resonance and an intensity of $\sim 88\ I_{\text{sat}}$ (Rabi frequency $\sim 2\pi \times 50$ kHz). Note that for frequencies blue of the Stark shifted resonance, atoms are heated out of the tweezer, causing the zero and one atom signals in the histogram to merge. To still distinguish zero and one atom we keep the threshold determined for histograms using optimal detection parameters (our 'standard' threshold).

We compare the experimentally determined optimal parameters and the temperature with results of a numerical simulation of the cooling process. The simulation is based on solving the steady state of a Lindblad master equation for a two-level atom in a pair of 1D quantum harmonic oscillators (QHO), one for each internal state $|g\rangle$, $|e\rangle$. The ratio of the QHO frequencies is given by $\omega_g/\omega_e = \sqrt{\alpha_g/\alpha_e} = 0.899$, with $\alpha_{g,e}$ the dynamic polarizabilities at the tweezer wavelength. Choosing a traveling wave for the Sisyphus cooling laser, the transition dipole moments between vibrational states of different QHO's are calculated as $d_{eg} \langle m| e^{ikx} |n\rangle$, with $|m\rangle$, $|n\rangle$ the vibrational states for internal states $|g\rangle$ and $|e\rangle$, respectively, and d_{eg} the transition dipole moment of the $^1S_0$ - $^3P_1$ transition.

We find the optimal parameters and the minimum temperature to be in good agreement (10%) with the experimentally found ones. In Fig. 2.2(c) we show the number of average motional quanta after cooling in dependence of detuning at optimum intensity (all parameters of this simulation are given in Appendix C). At the minimum we obtain $\bar{n} \approx 0.25$, which is in good agreement with measurements using sideband spectroscopy done by another group using the same cooling method [35, 57, 58].

2.4.3 Optimizing the imaging parameters

We now discuss the imaging procedure and optimize its parameters. In a first approach we record the fluorescence of atoms while cooling. We find that the parameters that are optimal for cooling lead to a low scattering rate. The rate increases if the imaging beam frequency is chosen such that the atom is hotter. In the following we determine the imaging frequency and intensity that lead to highest scattering rate. We then explore a method to increase the fraction of atoms that survive imaging: interlacing imaging with brief cooling stages.

The imaging frequency that leads to maximal scattering is found to be near the Stark shifted resonance (trap bottom). The scattering rate increases with imaging beam

intensity approaching the theoretical maximum of ~ 23 kHz at our chosen operating intensity $I \sim 350\, I_{\text{sat}}$. Deviations of $\pm 50\%$ from this value have barely any effect on the scattering rate where lower intensities than this range cause a detectable decrease in the scattering rate away from the saturated regime. Higher intensities cause unnecessary heating of the atom and excess camera background noise during detection. To clearly distinguish one atom from zero atoms, we image for 90 ms (see Sec. 2.4(D)).

The scattering rate is maximized for different conditions than the ones leading to optimum cooling. The optimum cooling frequency is not close to the Stark shifted resonance, but approximately 2-3 radial motional sidebands to the red of the shifted resonance. This behavior is consistent with the fluorescence being suppressed once the atom is cooled and there are no longer motional quanta to remove, leaving the laser off resonance. The optimum cooling intensity ($\sim 88\, I_{\text{sat}}$) is much lower than the intensity used for imaging. Imaging is therefore accompanied by sub-optimal cooling, leading to a higher equilibrium temperature than optimum cooling, and potentially to higher atom loss.

We attempt to increase the fraction of atoms that survive imaging by interlacing imaging with cooling pulses. A similar approach of interlaced imaging and cooling was demonstrated for blue imaging in [45]. In order to determine how much cooling is needed we execute a single imaging pulse with the full duration needed for reliable single atom detection (90 ms) followed by cooling. We estimate the temperature change during cooling by measuring the recapture fraction for a release time of 60 μs, see Fig. 2.3(a). Cooling proceeds quickly for a few milliseconds, then approaches the steady-state for $t_{\text{cool}} \gtrsim 8$ ms. This indicates that about 10% of the total imaging time should be spent on cooling to maintain a low temperature.

To keep the temperature low during the imaging process, we interlace the 90 ms of imaging time with eight cooling pulses of 1.5 ms duration, i.e. we alternate eight times between 11 ms of imaging and 1.5 ms of cooling, each time changing frequency and intensity. This is the standard imaging timing sequence for all images in this work, unless stated otherwise. The duration of one cooling pulse was chosen to allow significant cooling while not wasting time at a low scattering rate for marginal additional cooling, see Fig. 2.3(a). The cooling pulse time is much longer than the timescales determining a single Sisyphus cooling cycle (axial and radial trap period, excited state lifetime, and inverse scattering rate) and allows the atom to scatter ≤ 34 photons.

We now reoptimize the imaging frequency to maximize the fraction of detected

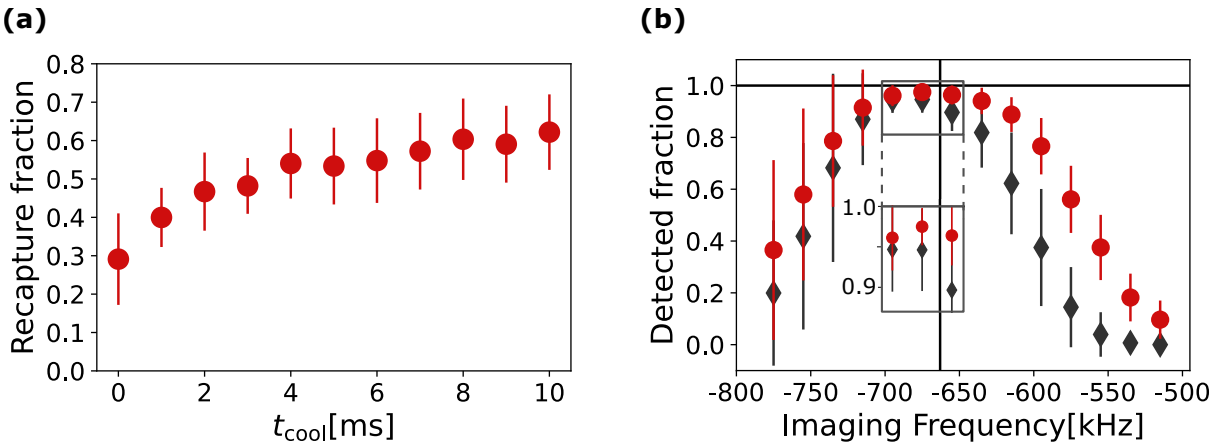

FIGURE 2.3: **(a)** Determination of cooling time scale. After heating the atoms for 90 ms with imaging light only (detuning of -675 kHz and $I \sim 350\, I_{\mathrm{sat}}$), we cool them for the time t_{cool} and then measure the survival fraction after release and recapture. We use a fixed release time of $t_{\mathrm{release}} = 60\,\mu$s. **(b)** Detected atom fraction in a second image versus imaging frequency. The cooling frequency is fixed at -775 kHz from free space resonance of the $^1S_0$ - $^3P_1$ transition. Red circles show data recorded using imaging interlaced by 1.5-ms-duration cooling pulses using an optimized duty cycle of 88% imaging and 12% cooling. Grey diamonds show data recorded using imaging without interlaced cooling and instead a 12 ms cooling stage at the end of the image. The detuning is plotted with respect to the free space resonance of the $^1S_0$ - $^3P_1$ transition. The vertical solid line shows the approximate Stark shifted resonance of the transition. The inset displays a vertical zoom onto the three points of best performance. The point at -675 kHz shows the highest survival probability of 0.97(2).

atoms using imaging interlaced with cooling. This fraction is measured by preparing a sample of single atoms using interlaced imaging with optimized operating parameters (see Sec. 2.3), and then determining how many atoms are also detected on a second interlaced image in dependence of the imaging frequency used for that image, see Fig. 2.3(b) (red circles). We also show the detected fraction without interlacing imaging with cooling (Grey diamonds).

The best performance is reached for a detuning of -675 kHz from the free space resonance (-12 kHz from the Stark shifted resonance), with a detected fraction of 0.97(2). We use this detuning for all images in this work unless stated otherwise. The benefit of imaging interlaced by cooling is that the survival probability is $\sim$3% higher than what we could obtain without interlaced cooling. This can be clearly seen in the inset of Fig. 2.3(b) where we zoom in on the points of best performance.

At the points highlighted by the inset, the detected fraction of atoms in the second picture is equivalent to the survival probability. However we specifically choose this alternate label because the reduction in the detected fraction for higher and lower detuning is due to different mechanisms. For blue detuning from the optimum value (right hand side of the plot in Fig. 2.3(b)) the reduction is dominated by the probability of an atom to be lost during imaging as evident from an increased variation in collected photon number. The blue detuned light can heat the atom out of the tweezer before sufficient photons can be scattered for detection. In the region red detuned of the optimum value (left hand side of the plot) the poor detected fraction is instead dominated by insufficient scattering rate as evident from a decreased average number of collected photons. The reduction in scattering rate also leads to the drastically increased error bars at further red detuned frequencies. For frequencies more than 50 kHz away from optimum the zero and one atom signals merge. Again, we use our standard threshold to distinguish zero and one atom.

We compare the temperature after our imaging process (which ends in a 1.5 ms cooling stage) to the one obtained after a long cooling time (20 ms additional cooling) using release and recapture measurements, see Fig. 2.2(a). Directly after the imaging process the data is well described by a simulation assuming 3 μK (red circles and solid line). This is not much above the temperature obtained after long cooling of about 1.8 μK (blue triangles and dashed line).

2.4.4 Detection fidelity, survival probability and minimum tweezer depth

To distinguish tweezers containing one or zero atoms on fluorescence images we use a photon count detection threshold. We now illustrate this method and determine the optimum detection threshold and the detection fidelity. We measure the fraction of atoms that survive imaging and discuss its dependence on tweezer trap depth. Finally, we compare the lifetime of atoms under cooling and imaging conditions.

Figure 2.4(a) shows a histogram of the number of collected photons in a tweezer ROI, where the average offset from background photons and camera noise is subtracted. Two distinct peaks are visible: one around zero photons, corresponding to no atom in the tweezer, and another around 50 photons, corresponding to the fluorescence count of a single atom. As is standard procedure [30, 32, 34, 44, 46, 76, 77], we postulate that an atom is present if the photon count is above a detection threshold, marked as dashed vertical line in the histogram. It may happen that randomly very few photons are scattered despite an atom being present in the tweezer or vice versa, leading to a wrong detection result. The detection fidelity is the probability of the detection to be correct. We determine it by calculating the overlap between a skewed Gaussian (fit to the zero atom peak) and a Gaussian (fit to the one atom peak) following the procedure outlined in [77]. As a double check, we calculate the fidelity following the procedure outlined in [45], which does not rely on fitting the histogram. Both methods agree within our quoted uncertainty. Using the detection threshold as an optimization parameter, we obtain a maximum detection fidelity of 0.9991(4) for a 135(20) μK trap depth.

The duration of images can be decreased to 50 ms with only a small loss in detection fidelity (fidelity reduced to 0.985). The loss is dominated by misidentifying a filled tweezer as empty at the optimal threshold, and is limited by background light on the camera and not by camera electronic noise. In particular the stray light of the repump lasers contributes to misidentification (the band pass filter in front of the camera insufficiently filters their light). In fact, we obtain a better detection fidelity without using the repump lasers, also because optical pumping to metastable states happens rarely during imaging for our optical tweezer intensities. This is the reason why we do not use the repump lasers during our imaging process for shallow traps.

To determine the probability of an atom to survive the imaging process we record

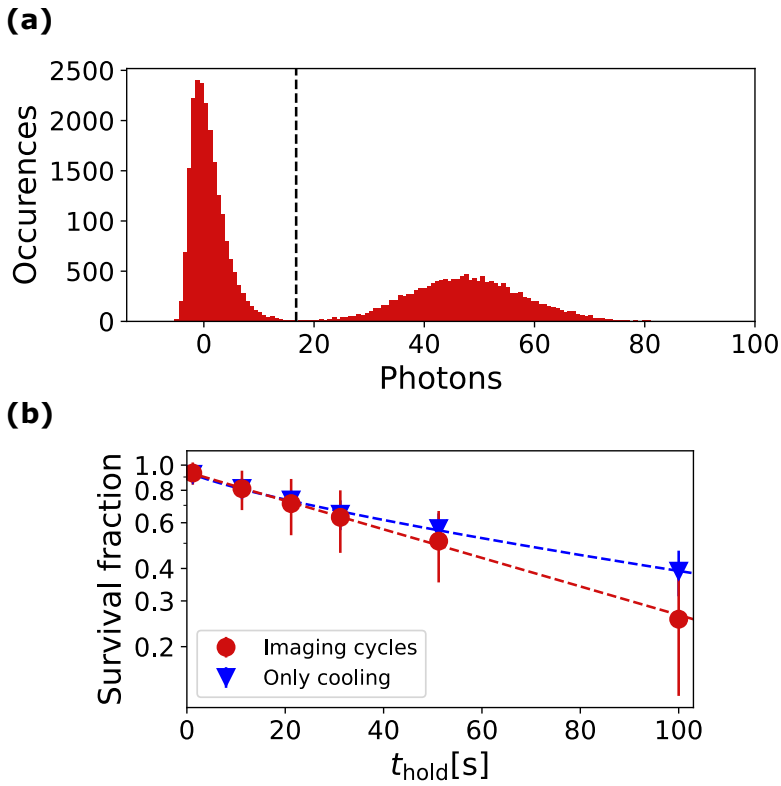

FIGURE 2.4: **(a)** A histogram showing fluorescence photon counts from ROIs around single tweezers during imaging. This histogram combines the results of 1000 experimental runs using a 6×6 tweezer array. The clear separation of the peaks highlights the uniform scattering over the array. The EMCCD counts per ROI have been converted to the number of incident photons. We use a bin size of 0.79 photons (150 EMCCD counts). The dashed line indicates the threshold separating the 0 atom peak (left) from the one atom peak (right). The EMCCD camera has a quantum efficiency of 92% at 689 nm. Fluorescence is collected for 100 ms during which we perform 8 cycles consisting of 11 ms of imaging light followed by 1.5 ms of cooling light. **(b)** The survival fraction versus the time spent under optimized imaging cycles (red circles) and under optimal cooling (blue triangles). The dashed lines show fits to the data (see text).

two images in sequence. The probability to detect an atom on the second image if it was present on the first is 0.97(2).

The trap depth can be reduced to 99(15) μK without sacrificing detection fidelity. However, once the tweezer trap depth is decreased below the $\sim$135 μK level, the chance of recovering the atom on a second image starts to decrease. For example we measure a decrease in survival probability to 0.926(65) for a trap depth of 99(15) μK.

Survival probability is reduced for trap depths below $\sim$135 μK because one of the Sisyphus cooling criteria outlined in Sec. 2.4(A) is not met. For such low trap depths, the excited state $axial$ trap frequency becomes lower than the natural linewidth of the transition ($\sim$ 7.4 kHz). When the axial trap frequency becomes that small the cooling process does not sufficiently compensate fluorescence recoil heating in the axial direction. This is supported qualitatively by our Sisyphus cooling simulation when we set the trap frequency to the axial value. As the trap frequency is varied to lower values, we see that cooling quickly deteriorates for values below the natural linewidth. This analysis also shows there is still something to be gained in cooling performance from a higher axial trap frequency.

The fact that Sisyphus cooling works for higher trap depths highlights the ability of the single radial cooling beam to remove energy from all directions simultaneously. Imaging at even lower trap depths could be achieved by using closer to spherically symmetric potentials as those in [36] or in a 3-D lattice [56], allowing reliable imaging at even lower trap depths. Already the achieved trap depth of 135 μK for reliable imaging is three times less than obtained with blue imaging in 813-nm tweezers [32], making it possible for us to obtain three times more tweezers for a given 813-nm laser source power. We note that [44] uses similar trap depths (200 μK) to those in our work albeit at a different tweezer wavelength of 515-nm. At this wavelength and with the higher NA microscope objective used in [44], much higher trap frequencies are obtained. Because of this, we predict that in such a system a similar reduction in trap depth should be possible.

In Figure 2.4(b) we show the survival probability over time t_{hold} when continually imaging or when just cooling. For these long measurements we turn on the repump lasers and close the atomic beam shutter. We fit the data by $e^{-(t/\tau)^{\alpha}}$, where α and τ are fit parameters. For continual imaging cycles the fit provides α=1 and a 1/e lifetime of τ=79(3) seconds, allowing for hundreds of pictures to be taken of a single atom. This decay of the survival fraction is equivalent to p_1^N, where N is the number of elapsed 100

ms long images and $p_1 = 0.9986(4)$ [32]. For continuous cooling the fit provides α=0.8 and τ=116(5) seconds. The deviation from a pure exponential decay might be due to slowly improving vacuum quality over the course of each measurement, triggered by the atomic beam shutter closure. When analysing individual tweezers, we find that some tweezers have the same lifetime under cooling and imaging conditions.

The discrepancy between the value of p_1 and our quoted survival probability for a single image is still unknown to us, however we hypothesize a few causes. One cause might be the slowly improving vacuum as mentioned above. Another might be technical issues during the process of recording an image. Such an image recording error would not contribute much to p_1, as images are only recorded at the beginning and end of N imaging durations. If such hypotheses are true, p_1 would be the more accurate value for the survival probability and achievable for single pictures with technical improvements.

The finite lifetime can have a variety of origins. We verify that the temperature of the atoms stays constant under both investigated conditions, excluding a slow process heating the atoms out of the trap. We find that the lifetime depends on the vacuum quality, as lifetime degrades over months and increases to the values stated above only after flashing titanium sublimation pumps. The decrease in lifetime from cooling to imaging conditions for most tweezer sites indicates that the small trap depth variation between tweezers of 3% make it impossible to optimize cooling and imaging for all tweezers.

We observe day to day changes of the survival probability originating from drifts away from ideal conditions, in particular magnetic field drifts. Magnetic field drifts on the $\sim$20 mG level affect the single image survival probability significantly ($\sim$ 2% reduction).

2.5 Site selective imaging

Our imaging technique provides an additional advantage. Using an easily achievable differential Stark shift, one can tune a certain tweezer out of resonance with the imaging light used for the rest of the array. This allows for selective imaging of either the remaining tweezers of the array or of the single shifted tweezer. The ability to selectively readout a single atom from the array is a necessary step for error correction in many quantum computation algorithms [78, 79].

To demonstrate the ability to select (or dark out) an atom from the image, we use a tweezer created by the crossed AODs to create a deeper potential for a single tweezer site in a 3×3 tweezer array. To characterize site selective images, we record four consecutive images in one experimental run, see Fig. 2.5. The first image (Fig. 2.5(a)) is taken directly after single atom preparation, as described in Sec. 2.3. The AODs are then turned on for the second and third image (Fig. 2.5(b,c)), in which we image the single shifted tweezer and the rest of the array respectively. To record atoms in the shifted tweezer, we increase the imaging detuning to -2 MHz (i.e. 1.325 MHz to the red of the usual imaging detuning). In the fourth image we turn off the additional tweezer and again image the entire array (Fig. 2.5(d)).

We can image the single site such that it is detected in image two with a survival probability of 0.96(2), and never appears in image three. Moreover, the entire atom array survives this 'dark out' measurement with a probability of 0.95(2).

The lower survival probability, in comparison to the value obtained in Sec. 2.4, is due mainly to worse balancing of the trap intensities for the nine trap array used for this measurement. Here the traps were only balanced to about 7% (the value we tend to get from calculated phase patterns before any additional balancing is performed). This variation is larger than the frequency tolerance that we see for our imaging process of about 3.8% i.e. a 12.5 kHz frequency difference for our Stark shift. Additionally, the cooling frequency and intensity in the deeper single tweezer were not fully optimized. We note that the AC Stark shift chosen here is too small to fully protect quantum information of the remaining atoms but provides an initial proof of concept. However a stronger AC Stark shift, on the order of 20 MHz, could make this feasible.

2.6 Conclusion

In conclusion, we have demonstrated the detection of single Sr atoms in shallow tweezers with high fidelity (0.9991(4)) and survival probability (0.97(2)). Detection is based on imaging on the red, narrow linewidth $^1S_0$ - $^3P_1$ $(|m_j| = 1)$ transition. We show that with proper frequency and intensity modulation a high scattering rate can be maintained while keeping the temperature of the atoms low.

Our red imaging technique works for a wide range of trap depths, and for shallow traps, red imaging is advantageous over blue imaging. We need slightly (∼2-fold) increased imaging times (100 ms instead of 50 ms) in comparison to blue imaging on

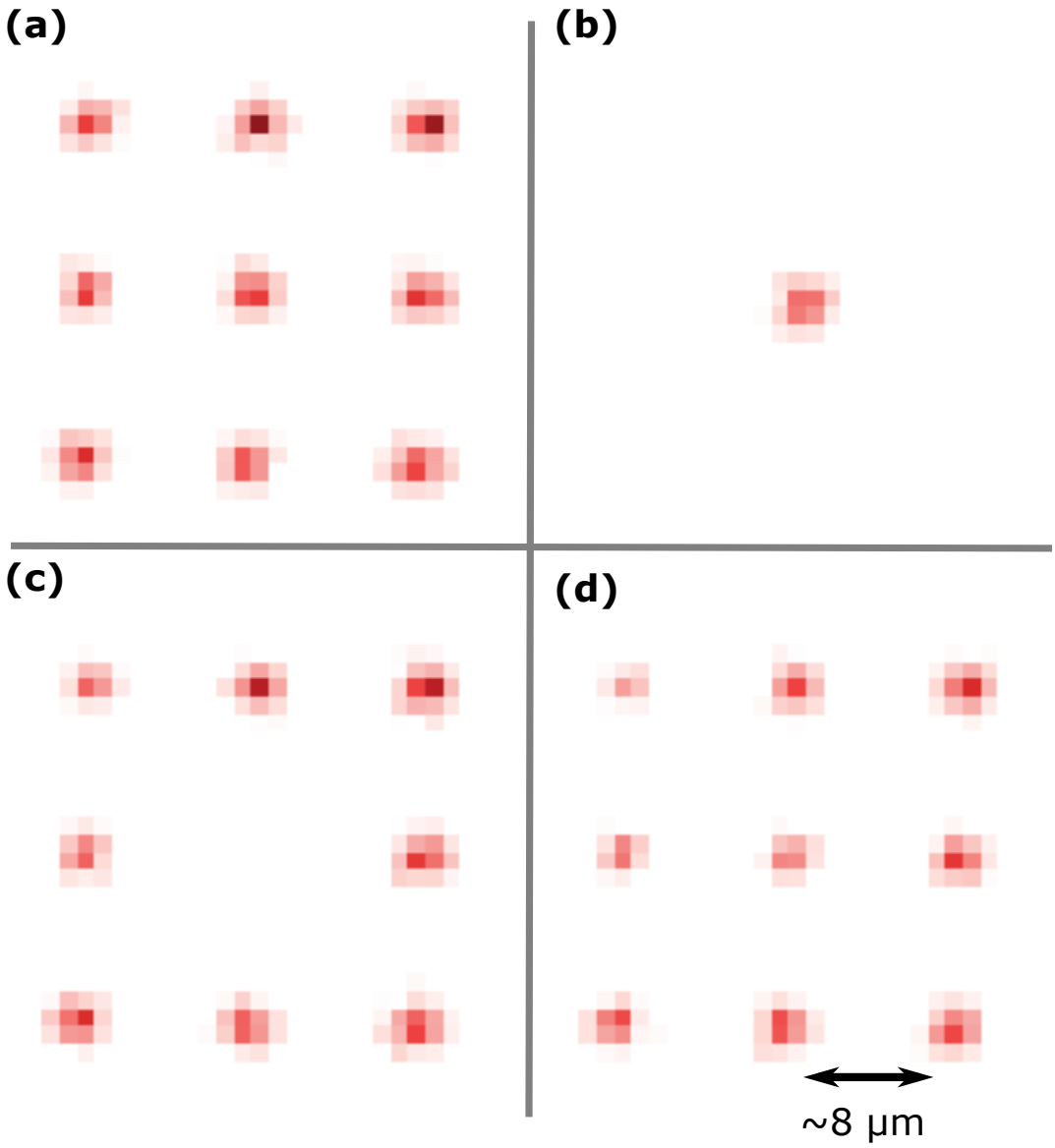

FIGURE 2.5: Site selective imaging using an additional tweezer to apply a differential Stark shift to one tweezer. **(a)** A first image is recorded to check loading. **(b-c)** After turning on the AOD tweezer on top of the center tweezer, we image first only the center tweezer and then the rest of the array by using respectively appropriate imaging and cooling detunings. **(d)** When the AODs are turned off, all traps are visible in a final image using the normal imaging detuning. The images show the average fluorescence from 300 experimental realizations.

the broad linewidth $^1S_0$ - $^1P_1$ transition in deep traps (450 μK depth) [32]. However, in shallow traps blue imaging is limited by the cooling rate, leading to excessive imaging times in comparison to red imaging [56].

In contrast to blue imaging, red imaging avoids optical pumping of ground state atoms into the metastable states (via $^1D_2$). Imaging in shallow traps reduces off-resonant scattering of trap light by metastable state atoms ($^3P_{0,2}$), leading to longer coherence times. Red imaging in shallow traps combines both advantages and enables high-fidelity shelving into metastable states for state specific detection or clock readout.

We show that, with a small additional Stark shift, we can isolate a single tweezer of the array from the imaging process. This allows us to selectively image (or hide) a single atom of the array. Through application of a bias field of $\sim$50 G, this selective imaging technique could be further extended to *state-selective* imaging for hyperfine ground states in the fermionic isotope. This opens the possibility of imaging more than two hyperfine ground states without disturbing the others. This will be a useful tool for quantum simulations or qudit style quantum computing [41, 80, 81].

It should be possible to extend red imaging to situations beyond the specific one examined here. The small potential wells containing the atoms can also be created by optical lattices, or other tightly confining dipole traps, making it possible to use the technique in quantum gas microscopes or 3D lattice clocks. This detection technique should work at nearly all tweezer wavelengths where one of the m_J states of $^3P_1$ is stronger trapped than the ground state. In particular, using 515-nm tweezers would be an appealing option. This is because red imaging avoids the leakage channel through $^1D_2$ from which blue imaging suffers [30, 44]. Tweezers at this wavelength are also likely to trap most Rydberg states [60, 61, 82]. The large polarizabilities at this wavelength, small diffraction limit of the tweezer light, and shallow required trap depth of red imaging would allow for the creation of $\geq$ 1000 strontium atom tweezer arrays with current laser technology.

Acknowledgments

We thank the other members of the Strontium Quantum Gasses group at the University of Amsterdam for useful discussions and debugging tips. We also thank the Eindhoven quantum computing group led by Servaas Kokkelmans and Edgar Vredenbregt for stimulating discussions. This project is supported by the Netherlands Organization

for Scientific Research (NWO) under the Gravitation grant No. 024.003.037, Quantum Software Consortium, and under grant No. FOM-153. This work is supported by the Dutch Ministry of Economic Affairs and Climate Policy (EZK), as part of the Quantum Delta NL programme.

2.7 Appendix A: Experimental Sequence

We utilize a unique technique for loading our narrow linewidth MOT in order to create optical access for the microscope objective. First, ^{88}Sr atoms from an $\sim 500°\mathrm{C}$ oven are slowed using a Zeeman slower operating on the $2\pi \times 30$ MHz wide $^1S_0$ - $^1P_1$ transition at 461 nm. The slowed atoms are then further cooled and compressed by a four beam 'blue' MOT, also using the $^1S_0$ - $^1P_1$ transition, in a 3D quadrupole field to milli-Kelvin temperatures. This blue MOT consists of two sets of retro-reflected beams ($1/e^2$ waist of $\sim$ 12 mm) that are perpendicular to each other and horizontal. Refraining from implementing the usual third MOT beam pair allows us to place the microscope objective along the gravity axis without complications from that beam pair, as shown in Fig. 2.6(a). This blue MOT is an incomplete trap as it provides no confinement against gravity. However the blue MOT is able to quickly cool and confine the atoms in the horizontal plane, which comprises the only dimension along which atoms entering from the Zeeman slower are fast. A significant fraction of atoms are then trapped in the quadrupole magnetic field (52 G/cm gradient in the axial direction, which is vertical) of the MOT by optical pumping to low-field seeking states of the $^3P_2$ manifold. This optical pumping is naturally happening when atoms rapidly scatter MOT light and decay from $^1P_1$ through the 5s4d $^1D_2$ state to $^3P_2$.

After quadrupole trap loading, all blue lasers are switched off and the magnetically trapped atoms are repumped back to the ground state, using a 497 nm laser resonant with the $^3P_2$-$^3D_2$ transition. Simultaneously the quadrupole field gradient is reduced to 0.63 G/cm in the vertical direction. The atoms are then loaded into a five beam narrow linewidth "red" MOT operating on the $^1S_0$ - $^3P_1$ transition. Four of the five red MOT beams are overlapped with the blue MOT beams and the fifth beam ($1/e^2$ waist of $\sim$6 mm) is propagating vertically upwards.

There is no need for a downwards propagating beam because the upward radiation pressure force is limited by the narrow linewidth and the MOT quadrupole field

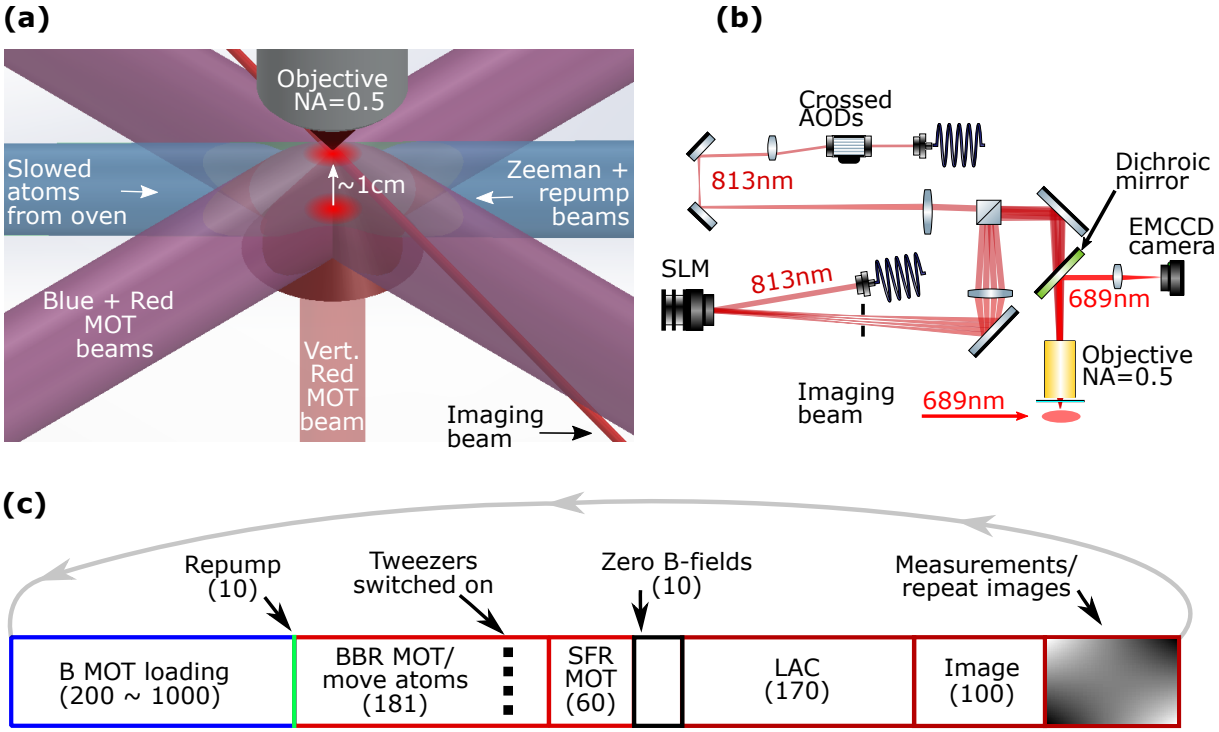

FIGURE 2.6: **(a)** Detailed sketch of crucial elements of the experimental setup. The arrow from the left indicates the beam of slowed atoms from the oven. The Zeeman slower and repump beams are shown in blue. The horizontal, overlapping blue and red MOT beams are shown in purple. An additional vertically upwards propagating red MOT beam (shown in pale red) provides confinement against gravity. The initial and final red MOT positions are shown as intense red spots. The red MOT is moved vertically 1 cm into the focus of the microscope objective. The 679 nm and 707 nm repump lasers co-propagate with the cooling/imaging beam. **(b)** Schematic of the tweezer setup. The main tweezer array is generated using an SLM. An additional tweezer can be created using a pair of crossed AODs. The SLM and AOD tweezers are combined using a polarizing beam splitter. Both systems are imaged through an NA= 0.5 objective onto the atoms. Fluorescence light from the atoms is separated from the tweezer light using a long pass dichroic mirror. The fluorescence is then sent onto an EMCCD camera (Andor Ixon 897). **(c)** Experimental sequence (numbers in brackets give time spans in ms). The figure uses acronyms for blue MOT (B MOT), broadband red MOT (BBR MOT), single frequency red MOT (SFR MOT) and light-assisted collisions (LAC).

to a small phase-space region. This force is counter-balanced by gravity. The atoms settle into a cloud on the lower part of a shell of equal B-field magnitude below the quadrupole centre. This shell is defined by the detuning of the MOT beams being equal to the Zeeman shift induced by the B-field. This trap scheme again does not need a beam going through the microscope objective.

The red MOT beams are initially frequency modulated in order to create a comb of frequencies from -60 to -3000 kHz detuning with 20 kHz spacing. The modulation range and intensity of this broadband red MOT are decreased over 181 ms, while a bias field of ∼0.6 G against gravity is ramped on, raising the atoms by 1 cm, from the centre of the vacuum chamber to the focal plane of the microscope objective, by shifting the center of the quadrupole field. An additional small bias field produced by three orthogonal coil pairs is ramped while the MOT position is raised and used to finely position the red MOT onto the tweezer array. The frequency modulation is then switched off and single frequency red MOT beams, with a detuning of -100 kHz and intensity of $8\,I_{\mathrm{sat}}$, are used to load the tweezers.

We optimize all parameters of the experiment up to this point on achieving the desired red MOT atom number in a reliable way and in a short time. We find that for MOTs (with our selected detuning) of 5×10^4 to 3×10^6 atoms, the entire tweezer array can be loaded with ≥ 1 atom per site, where on the low end we get slightly below unity filling. On the high end the high density of atoms in the tweezers leads to less than half of the tweezers being filled with atoms, presumably because of additional *non*-pairwise losses during the light-assisted collision step. Because of this robustness to atom number fluctuations, we load the magnetic reservoir for a variable amount of time at the end of an experimental sequence ($\sim$ 200 ms). The exact time is determined by the need to store data of the last run on the data analysis computer and the need to prepare the next experimental sequence in the experiment control computer. This procedure creates a MOT of approximately 5×10^5 atoms at a temperature $\leq$ 1.5 μK in the focal plane of our objective.

Slightly before the MOT is switched to single-frequency operation, the tweezers are switched on, see also next Appendix. After the red MOT has reached its final position we wait for 50 ms to load the tweezers. Then we switch off the MOT lasers and quadrupole field, and ramp the bias magnetic fields to 0 G at the position of the tweezers.

Single-atom detection only worked properly once we spectrally filtered the 689-nm

laser light used to induce fluorescence. The source of all 689-nm light is an external cavity diode laser (ECDL) that is short-term stabilized on a reference cavity with a linewidth of 35 kHz, which in turn is long-term stabilized (in length) on a spectroscopy signal. Light from the ECDL is amplified by injection locked lasers and then used on the experiment. Initially we used light from the ECDL directly to inject the amplifying diodes. This ECDL light is spectrally broadened by servo bumps from the locking electronics and amplified spontaneous emission and we found it impossible to prepare and detect single atoms. We then used the light that is transmitted through and therefore filtered by the reference cavity to inject the amplifying diodes, allowing us to achieve the single atom preparation and detection results presented here. The red MOT behavior did not noticeably change when switching from unfiltered to filtered light.

The light used for light-assisted collisions, imaging, and cooling is sent onto the tweezer array via a single beam with a polarization perpendicular to both the tweezer propagation axis and the tweezer polarization, and a $1/e^2$ waist of $\sim$1 mm. We find robust single atom preparation of $\sim$50% for a detuning of approximately -100 kHz from the Stark shifted resonance (-750 kHz from free space resonance). We change the intensity of the beam from low ($I \sim 88\, I_{\text{sat}}$ for 10 ms) to high ($I \sim 700\, I_{\text{sat}}$ for 150-200 ms) then back to low ($I \sim 88\, I_{\text{sat}}$ for 10 ms) in order to cool the loaded atoms into the tweezer, induce light-assisted collisions [30, 69], and cool the single atom before taking the first image of an experimental run.

2.8 Appendix B: tweezer creation

The 813.4-nm laser light used for the optical tweezers in our experiment is generated by an external cavity diode laser, which is amplified to 1.7 W using a tapered amplifier (TA). The output of the TA is divided into two optical paths, a main path to create the tweezer array using an SLM (Meadowlark P1920 1920×1152) and a second path for a movable tweezer using AODs (AA opto-electronic DTSXY-400-800), see Fig. 2.6(b). The main output path is sent through a dispersive prism in order to filter out any amplified spontaneous emission from the TA and is then sent through an acousto-optic modulator for intensity control before being coupled into a fibre. The second path is sent without further filtering into an optical fibre.

The optical tweezers are created by imaging an array of beams through a microscope objective (NA= 0.5, Mitutoyo 378-848-3). An almost arbitrary and stationary pattern of tweezers is created using the SLM. In order to calculate the phase pattern of the desired tweezer pattern we use the weighted Gerchberg-Saxton algorithm [83]. The phase imprinted onto the incident beam by the SLM is a sum of phases including the tweezer array pattern phase, a lens phase to Fourier transform the phase to a real image, a grating phase to separate the zeroth order, and a factory correction phase.

The sum of these phases creates an array of foci ~ 180 cm from the SLM. This array is imaged through the microscope objective (effective focal length $f = 4$ mm) with a field lens of $f = 500$ mm taking care that the array of beams is conjugated onto the aperture of the microscope objective. In this work all results shown have been performed with the SLM creating a square 6×6 array of tweezers unless otherwise noted.

Additional balancing of the tweezer trap depths can be achieved by fine tuning the SLM pattern. As a first step we spectroscopically measure the depth of each tweezer by inducing heating on the $^1S_0$ - $^3P_1$ $(m_j = 0)$ transition, which is weaker trapped than the ground state. The loss feature is then fit with a Gaussian, and the center frequency is extracted for each tweezer. The detuning of this frequency from the free-space resonance is proportional to the tweezer intensities. The amplitude of each tweezer, in the pattern to be calculated, is then weighted based on these measured center frequencies. The tweezer phase pattern is then recalculated using these new weights. This procedure allows us to balance the trap depths across the 6×6 array to a standard deviation of approximately 3% [30, 75, 76]. This procedure was not executed for the 3×3 array used in Sec. 2.5.

We characterize the depth of our tweezers using spectroscopic method explained above. The error in our trap depth determination has two sources. The choice of either the blue edge frequency or center frequency, based on if a purely thermally broadened line shape or a purely power broadened line shape is fit respectively, provides 15 μK of error [30]. An additional 5 μK uncertainty comes from the 3 % standard deviation of the optimized SLM pattern. For the tweezers used throughout the paper, we estimate a waist of ~ 0.84 μm and an optical power on the atoms of ~ 2.33 mW per tweezer.This is in good agreement with our externally measured waist of $\sim$0.78 μm. The microscope transmission is also characterized externally to be $\sim$36%.

The AC Stark shifts depend not only on the light intensity, but also on the polarization of the light and the magnetic field. To zero the magnetic field, we collect fluorescence induced on the $^1S_0$ - $^3P_1$ $(m_j = \pm 1)$ transitions from many atoms trapped in a tweezer. We assume the frequency with the maximum fluorescence to be near the bottom of the trap. We then apply B-fields along each Cartesian axis separately and look for the zero crossing point where a single fluorescence feature can be seen in the scan of imaging frequency. We measure the tweezer polarization to be linear directly before the microscope objective, and with zero B-field see that the measured lines are in good agreement with our polarizability calculations for linearly polarized tweezers ($\alpha(^1S_0)$= 286 a.u., $\alpha(^3P_1\,(|m_j| = 1))$= 355 a.u., and $\alpha(^3P_1\,(m_j = 0))$= 199 a.u.). We note that a more robust characterization of the trap depth would also include trap frequency measurements as those in [30, 35, 44, 45], but we have not yet performed such measurements due to either lack of the required laser or technical limitations in our system.

An additional tweezer (or tweezers) can be created using a crossed pair of acousto-optic deflectors (AODs) whose position in the focal plane can be controlled through radio frequency tones sent to the AODs. Unlike the SLM's slow refresh rate, this tweezer can move at speeds sufficient for sorting atoms into defect free arrays, or for quickly applying an additional tweezer for isolating one tweezer from the rest of the array (see Sec. 2.5).

2.9 Appendix C: Sisyphus cooling simulation parameters

For the Sisyphus cooling simulation we consider a trap depth of $k_B \times 135\,\mu$K = $h \times 2.8$ MHz. For our estimated waist of 0.84 μm, this gives a *radial* trap frequency of 43 kHz for the ground state. We calculate the $^1S_0$ (α_g) and $^3P_1\,(|m_j| = 1, \alpha_e)$ polarizabilities to be 286 a.u. and 355 a.u. respectively. For the results presented in Fig. 2.2(c), we use a Rabi frequency of $2\pi \times 42$ kHz. We include 15 harmonic oscillator levels in our calculation.

Chapter 3

Theory

3.1 Polarizability in the presence of a magnetic field

In the past few decades, optical dipole traps have become a powerful tool for ultracold atom experiments. These traps rely on interaction between atoms and a far off resonant laser. The potential created by the interaction of an atom and an oscillating electric field, such as those of a continuous wave laser, is referred to as the AC Stark shift, the optical dipole potential or simply the light shift [3, 84, 85]. The dipole potential was first used to trap atoms in 1986 by Chu et al. [6], where a single strongly focused Gaussian laser beam tuned to far below the D_1 resonance in sodium is used to trap sodium atoms.

For a given internal state of the atom, the radial potential[1] of an optical dipole trap created by a single focused laser beam can be calculated using the expression

$$U_0 = -\frac{1}{2\epsilon_0 c} I_0(r)\alpha(\lambda_\mathrm{L}) = -\frac{P_\mathrm{L}}{\epsilon_0 c \pi w_0^2} \mathrm{e}^{-2r^2/w_0^2} \alpha(\lambda_\mathrm{L}), \tag{3.1}$$

where ϵ_0 is the vacuum permittivity, c is the speed of light, $I_0(r)$ is the intensity of the trapping laser, r is the distance from the center of the focus, $\alpha(\lambda_\mathrm{L})$ is the polarizability of the atomic state at the trapping laser wavelength (λ_L), P_L is the laser power, w_0 is the waist of the tweezer beam[2]. The polarizability is the proportional constant between light intensity and light shift. It is related to the detuning from atomic transitions of the state of interest and the polarization of the light. For the ground state of alkali and

[1] For the axial potential, the expression in Eqn. (3.1) changes the intensity profile from the Gaussian focus to the evolution along the propagation of the beam using instead $I_0(z) \propto 1 + (\lambda_\mathrm{L} z/\pi w_0^2)^2$, where λ_L is the trapping laser wavelength.

[2] The polarizability is most often reported in atomic units. The conversion factor $4\pi\epsilon_0 a_0^3$ can be used to convert from atomic units to SI units (F m^2)).

alkaline-earth atoms, considering the effect from the most dominate transition gives a reasonable estimation of the strength of the polarizability, however for excited states where there are many transitions of similar lifetimes, a more detailed calculation is needed [85]. Here, we will outline a technique for calculating the polarizability for different states of strontium. We will compose a polarizability operator, which will be used to calculate of the polarizability of the sublevels of a desired internal state. For completeness, we will refer to the Hamiltonian consisting of this operator and the prefactors in Eqn. (3.1) at $r = 0$ as the light shift Hamiltonian.

Atomic state sublevels can also be shifted by external magnetic fields. This is known as the Zeeman Effect. The shift of the sublevels of a given atomic state by magnetic fields provides an extra tuning knob for changing the energy of the sublevels. Separating these sublevels in energy allows for the use of unique laser frequencies and intensities for addressing different sublevel transitions between two atomic states. This is very useful for forming complex atom-light coupling Hamiltonians for use in quantum simulation and computation, such as in the example outlined in Section 3.4. We briefly introduce the Zeeman Hamiltonian, which will be used for determining the splitting between internal sublevels, focusing mainly on the triplet $^3P_{1,2}$ states.

In optical tweezers, the Zeeman shift of magnetic sublevels at small magnetic fields on the order of a few Gauss and the light shift from the tweezer laser can be similar. This similarity in energy scales makes it important to include the light shift Hamiltonian and Zeeman Hamiltonian in the determination of energy shifts, because the total energy shift can be significantly altered compared to simply adding up the effect of the individual Hamiltonians. However, in general the eigenstates of the Zeeman Hamiltonian are not the same as those of the light shift Hamiltonian. Therefore, the Zeeman shifts and light shifts are not additive. Small changes to the shift can have adverse effects on certain processes like cooling or could affect our trap depth characterization, see Section 2.8. However, the combined shift can provide a useful tool for tuning two internal states of an atom to a so-called magic condition where the energy of the two states is equal and first-order insensitive to variations of laser intensity or magnetic field amplitude [34, 44]. The usual approach for calculating the polarizability is to decompose it into scalar, tensor, and vector contributions. Here we use a different method for calculating the polarizability that is more practical for combining with the Zeeman shift.

This section is outlined as follows. First we will describe a tensor method for calculating the polarizability for the bosonic (^{88}Sr) and fermionic (^{87}Sr) isotopes of strontium. Second, we will briefly outline the Zeeman Hamiltonian, again for both isotopes. Third we will conclude with some specific results, including results for ellipticity tuning of the polarizability, magic angles between the magnetic field and tweezer polarization, and magic wavelength estimations for the $^1S_0$ - $^3P_2$ transition [40].

3.1.1 Polarizability

To calculate the polarizability, we use the method outlined in [86] adapted to strontium. We start by defining polarization unit vectors in the Cartesian basis,

$$\vec{\boldsymbol{u}}_{\sigma^-} = \frac{1}{\sqrt{2}}\begin{pmatrix} 1 \\ -\mathrm{i} \\ 0 \end{pmatrix}, \vec{\boldsymbol{u}}_{\sigma^+} = \frac{1}{\sqrt{2}}\begin{pmatrix} -1 \\ -\mathrm{i} \\ 0 \end{pmatrix}, \vec{\boldsymbol{u}}_{\pi} = \begin{pmatrix} 0 \\ 0 \\ 1 \end{pmatrix}, \tag{3.2}$$

$$\vec{\boldsymbol{u}}_{x} = \begin{pmatrix} 1 \\ 0 \\ 0 \end{pmatrix}, \vec{\boldsymbol{u}}_{y} = \begin{pmatrix} 0 \\ 1 \\ 0 \end{pmatrix}, \vec{\boldsymbol{u}}_{z} = \begin{pmatrix} 0 \\ 0 \\ 1 \end{pmatrix}, \tag{3.3}$$

where we have chosen our basis such that $\vec{\boldsymbol{u}}_\pi = \vec{\boldsymbol{u}}_z$, defining this as the quantization axis, which will be a convenient choice later when a magnetic field along the z-axis is introduced.

We can construct two additional unit vectors describing elliptical polarizations,

$$\vec{\boldsymbol{u}}_\gamma = (\sin\gamma, -\mathrm{i}\cos\gamma, 0), \tag{3.4}$$

and for considering an angle between the linear polarization of a laser propagating along the y-axis and a magnetic field oriented along the z-axis,

$$\vec{\boldsymbol{u}}_\theta = (\sin\theta, 0, \cos\theta). \tag{3.5}$$

The unit vector $\vec{\boldsymbol{u}}_\gamma$ is constructed such that the angle γ represents the ellipticity of the polarization, where $\gamma = 0, -\pi/4, \pi/4$ are equivalent to linear[3] left hand circular, and

[3]The linear polarization at $\gamma = 0$ is equivalent to the superposition of $\sigma^+ + \sigma^-$, which is equivalent to π-polarization in the absence of magnetic field.

right hand circular-polarizations respectively. Here, we have arbitrarily chosen z as the propagation axis of our tweezer and y as the major axis. The unit vector $\vec{\boldsymbol{u}}_\theta$ is constructed such that the angle θ is the angle between a magnetic field defining the quantization axis along z and the linear polarization of the trapping laser, which means the relevant range of θ is from $\theta = 0$ (parallel) to $\theta = \pi/2$ (perpendicular). Here, we have chosen y as the propagation axis of the tweezer and z as the major axis for convenient combination with the Zeeman Hamiltonian when a magnetic field is applied along the z-axis. This second unit vector ($\vec{\boldsymbol{u}}_\theta$) allows one to calculate the effect of a magnetic field on the potentials of different excited state sub-levels in strontium as well as being a valuable tool for finding so-called magic angles between a B-field and polarization where the differential light shift between two states vanishes [34, 44].

To use the defined polarization unit vectors to extract the proper polarizability terms for the dipole allowed transitions, we must convert to a spherical basis. This is done using

$$\vec{\boldsymbol{e}}_{\text{sph}} = U^{-1} \cdot \vec{\boldsymbol{u}}_{\text{Cart}} = \begin{pmatrix} 1/\sqrt{2} & \mathrm{i}/\sqrt{2} & 0 \\ 0 & 0 & 1 \\ -1/\sqrt{2} & \mathrm{i}/\sqrt{2} & 0 \end{pmatrix} \cdot \vec{\boldsymbol{u}}_{\text{Cart}} \tag{3.6}$$

where we have chosen the basis $\{\sigma^-, \pi, \sigma^+\}$ for $\vec{\boldsymbol{e}}_{\text{sph}}$. These unit vectors allow for the proper selection of matrix elements from the polarizability operator that we will construct.

With the polarization unit vectors defined in spherical coordinates, we can now begin to construct the polarizability operator. To calculate the polarizability we must use the electric dipole operator, d_q, to calculate the transition dipole moment (TDM) for a given transition between two states, $|J, m\rangle$ and $|J', m'\rangle$ [87]. To calculate the TDM, we can use the Wigner-Eckart theorem. This theorem allows for the decomposition of any matrix element of an irreducible spherical tensor operator with respect to a $|J, m\rangle$ basis into the angular momentum vector space created by $|J, m\rangle$ into the product of two terms. One term is a Clebsch-Gordan coefficient and the other is a common factor shared by all matrix elements independent of angular momentum orientation. Using the Wigner-Eckart theorem, we can express the TDM as

$$\langle J', m'|d_q|J, m\rangle = \frac{1}{\sqrt{2J'+1}} \langle J'\|d\|J\rangle C_{J,m}^{J',m+q}, \tag{3.7}$$

where $\langle J'\|d\|J\rangle$ is the reduced transition dipole moment (RDM) from initial state J to

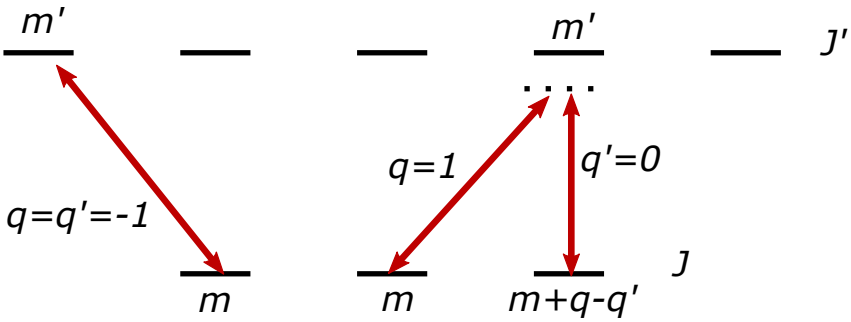

FIGURE 3.1: Illustration of the quantum numbers used in the polarizability calculation. J and J' represent the fine structure levels for the ground and excited states of the atomic transition of interest. Each state contains $(2J+1)$ m_J sublevels; m and m' which are depicted for two different cases. For case one (left most arrow), a pure σ^- polarization is displayed leading to $q = q' = -1$ defining the levels m and m' as shown. For case two (right two arrows), elliptical polarization leads to components of both σ^+ and π light resulting in $q = 1$ and $q' = 0$ and defining m and m' as shown. Such effects lead to off-diagonal terms in the polarizability matrix of Eqn. (3.11).

excited state J' in a.u., $C_{J,m}^{J',m+q}$ is the Clebsch-Gordan coefficient for the dipole transition, $|J, m\rangle \rightarrow |J', m+q\rangle$ where $q = (-1, 0, 1)$ corresponds to the light polarization of $(\sigma^-, \pi, \sigma^+)$ respectively, and $m' = m + q$ [87]. In Fig. 3.1, we have included a simple diagram that helps to better illustrate these different quantum number.

From here we can calculate the polarizability operator for a given transition $J \rightarrow J'$ using

$$\begin{aligned}\hat{\alpha}_{q,q'}(J, J', \lambda) = \frac{1}{\beta}\frac{\alpha_{\mathrm{FS}}}{\pi}\frac{|\langle J'\|d\|J\rangle|^2}{2J'+1}\frac{\tilde{\nu}_{J'} - \tilde{\nu}_J}{(\tilde{\nu}_{J'} - \tilde{\nu}_J)^2 - \tilde{\nu}_\lambda^2} \\ \times \sum_m C_{J,m+q-q'}^{J',m+q} C_{J,m}^{J',m+q} \times |J, m+q-q'\rangle \langle J, m|\end{aligned} \tag{3.8}$$

where α_{FS} is the fine structure constant, $\tilde{\nu}_{J',J}$ are the energy of the respective states expressed in cm^{-1}, and $\tilde{\nu}_\lambda$ is the trapping laser wavelength also expressed in cm^{-1} [86]. The prefactor, $\beta = 5.29 \times 10^{-9}$ cm, allows for the energies $\tilde{\nu}$ to be expressed in cm^{-1} while maintaining a.u. for the polarizability. This is a convenient choice for using tabulated data such as from the NIST atomic database and other publications [30, 88, 89]. We have also introduced the term q' for the explicit case where two different

polarizations of light are present. Such situations can lead to a change in m by off-resonant coupling as depicted in Fig. 3.1. This provides a polarizability tensor operator of the form $|J, m+q-q'\rangle \langle J, m|$ with matrix elements

$$\hat{\alpha}^{(4)}_{m_\mathrm{i},m_\mathrm{f},q,q'}(J, J', \lambda) = \langle J, m_\mathrm{f}|\hat{\alpha}_{q,q'}(J, J', \lambda)|J, m_\mathrm{i}\rangle, \tag{3.9}$$

where m_i and m_f represent the initial and final m_J state of the atom respectively. This provides a rank-4 tensor with indices m_i, m_f, q, and q' of size $(2J+1)\times(2J+1)\times 3\times 3$.

The rank-4 tensor can be combined with the spherical basis polarization unit vectors, with polarization given by Eqn. (3.6). This constructs a rank-2 tensor where the different polarizabilities of specific sublevels can be extracted with the two indices m_i and m_f. This rank-2-tensor is

$$\hat{\alpha}^{(2)}_{m_\mathrm{i},m_\mathrm{f}}(J, J', \lambda) = \sum_{q,q'} e^*_q \cdot \hat{\alpha}^{(4)}_{m_\mathrm{i},m_\mathrm{f},q,q'}(\lambda) \cdot e_{q'} = \vec{\boldsymbol{e}}^{\,*}_\mathrm{sph} \cdot \hat{\alpha}^{(4)}_{m_\mathrm{i},m_\mathrm{f},q,q'}(J, J', \lambda) \cdot \vec{\boldsymbol{e}}_\mathrm{sph}, \tag{3.10}$$

with size $(2J+1)\times(2J+1)$. For pure σ^-, π, or σ^- polarizations, we have $q = q'$ and $m_\mathrm{i} = m_\mathrm{f}$, but in the case of elliptical polarization or when an angle is present between the quantization axis and polarization, this is not necessarily the case and we obtain "Raman" coupling terms between two m_J sublevels of the same J in the polarizability operator.

To calculate the total polarizability, we then take the sum of all contributions for transitions from a given initial state J,

$$\hat{\alpha}_{m_\mathrm{i},m_\mathrm{f},\mathrm{tot}}(J, \lambda) = \alpha_\mathrm{other}(J, \lambda) + \sum_{J'} \hat{\alpha}^{(2)}_{m_\mathrm{i},m_\mathrm{f}}(J, J', \lambda) \tag{3.11}$$

where $\alpha_{J,\mathrm{other}}$ accounts for the grouped together contributions from all other non-dominant transitions and the ionic-core polarizability. The latter is a small contribution consisting of two factors, the polarizability of the ionic core and a small change due to the presence of the valence electron [90]. These contributions are taken to be scalar, tend to vary smoothly with wavelength, and are generally small in comparison to the other transitions [30, 88, 89, 90]. We model $\alpha_{J,\mathrm{other}}$ as a function of the form

$$\alpha_\mathrm{other}(J, \lambda) = a + \frac{b}{\lambda - c} \tag{3.12}$$

with free parameters $a, b,$ and c fitted to literature data listed as 'other' of transition J [30, 88, 89]. We use additional literature data around our tweezer wavelength of 813.4 nm to optimize the results of the fit near this wavelength [34, 35, 36, 77]. The uncertainty in this function is the dominant discrepancy between the values obtained here and by other works mentioned, but this is usually below a few percent and even lower when compared with numbers like differential shifts between internal states, magic wavelengths, and magic angles [30, 32, 34, 35]. For the $^3P_2$ state the case is even simpler since we have only a single value for the other and core contributions. In that case $\alpha_{J,\text{other}}(\lambda)$ is purely defined by a global correction a and is a leading source of any possible error in our $^3P_2$ calculations presented later. In Tab. 3.1, we present the values of the free parameters for different internal states of strontium.

Eqn. (3.11) is a matrix whose eigenvalues can be seen as the polarizabilities of different m_j levels of a given state J for our effective quantization axis. The polarizability includes all contributions of higher excited states (and sublevels). The choice of polarization unit vector used in $\vec{\boldsymbol{e}}_{\text{sph}}$ allows for us to calculate the polarizability for different polarizations including for elliptical polarizations using Eqn. (3.4).

State	a [a.u.]	b [nm $\times$ a.u.]	c [nm]
$^1S_0$ [30]	11.57	45.88	470.61
$^3P_0$ [88]	25.2832	2173.54	322.64
$^3P_1$ [30, 34]	35.03	6011.86	355.61
$^3P_2$ [89]	46.8	0	0

TABLE 3.1: Fit parameters of $\alpha_{J,\text{other}}(\lambda)$ for $^1S_0$ and $^3P_{0,1,2}$. The fit is done using λ expressed in nanometers. Reference data citations are presented in the table for each state. These fits are not necessarily unique and other fits could provide similar results. Aside from the references mentioned, the fits for $^1S_0$, $^3P_0$, and $^3P_1$ were optimized around 813-nm to mimic the reported differential shift results of other experiments [32, 34, 35].

Polarizability for ^{87}Sr

To extend the calculation of the polarizability to ^{87}Sr, where $I = 9/2$, we must include the hyperfine splitting induced by the nuclear spin plus spin-orbit coupling $(\hat{J} \cdot \hat{I})$. This can be by done using Condon and Shortley normalization for the reduced matrix

element, which gives according to the Wigner-Eckart theorem

$$\langle F'(J',I),m'|\hat{d}_q|F(J,I),m\rangle = C^{F',m+q}_{F,m}\langle F'(J',I)\|d\otimes\hat{1}_I\|F(J,I)\rangle, \tag{3.13}$$

where $\hat{1}_I$ is the unit operator acting on the nuclear spin subspace [86, 91]. This expression can be further reduced by using the coupling law for the reduced matrix element, which gives

$$|\langle F'(J',I)\|d\otimes\hat{1}_I\|F(J,I)\rangle|^2 = f_{F',F}|\langle J'\|d\|J\rangle|^2, \tag{3.14}$$

where

$$f_{F',F} = (2J'+1)(2F+1)\left|\left\{\begin{array}{ccc} F' & I & J' \\ J & 1 & F \end{array}\right\}\right|^2 \tag{3.15}$$

is the relative oscillator strength for decay from $|F'\rangle \to |F\rangle$ [86, 91].

This allows for us to rewrite Eqn. (3.8) as

$$\begin{aligned}\hat{\alpha}_{m_\mathrm{i},m_\mathrm{f},q,q'}(F,J,J',\lambda) = \frac{1}{\beta}\frac{\alpha_{FS}}{\pi}\frac{|\langle J'\|d\|J\rangle|^2}{(2J_e+1)}\frac{\tilde{\nu}_{J'}-\tilde{\nu}_J}{(\tilde{\nu}_{J'}-\tilde{\nu}_J)^2-\tilde{\nu}_\lambda^2} \\ \times\sum_{F'}\sum_{m} f_{F',F}C^{F',m+q}_{F,m'-q'}C^{F',m+q}_{F,m}\times|F,m+q-q'\rangle\langle F,m|,\end{aligned} \tag{3.16}$$

where we have included the summation over all the hyperfine excited state manifolds [86]. The derived expression holds for detunings that are much larger than the hyperfine splitting. In the case of a near resonant laser, it would be required to include the F' specific detunings into the summation, however this is only a minor correction in the far-off-resonant conditions considered here. The same procedure as outlined above can be used to calculate the rank-2 tensor product in Eqn. (3.10), and to calculate the total polarizability $\hat{\alpha}_{m_\mathrm{i},m_\mathrm{f},\mathrm{tot}}(F,J,\lambda)$ in Eqn. (3.11), where the same fit values from Tab. 3.1 are used in Eqn. (3.12) for the $\alpha_{J,\mathrm{other}}(\lambda)$ contributions.

3.1.2 Zeeman Hamiltonian

For the simpler case of ^{88}Sr where there is no nuclear spin, the calculation of the magnetic field shift is trivial. It can be written in the standard fashion

$$H_B = \frac{\mu_B}{h}g_J\vec{J}\cdot\vec{B}, \tag{3.17}$$

where $g_J \simeq 1.5$ is the Landé g-factor for both the $^3P_1$ and $^3P_2$ states and μ_B is the Bohr magneton [92].

Calculating the Zeeman shifts for ^{87}Sr is slightly more complicated. We briefly outline the procedure used in [92]. The Zeeman interaction Hamiltonian in the presence of a weak magnetic field B along the z-axis is given by

$$H_z = (g_s S_z + g_L L_z + g_I I_z)\frac{\mu_B}{h}B, \tag{3.18}$$

where $g_s \simeq 2$, $g_L = 1$, and S_z, L_z, I_z are the z components of the electron spin, orbital, and nuclear spin angular momentum, respectively, and h is Planck's constant [92]. The nuclear spin g factor, g_I, is calculated using the expression

$$g_I = \frac{\mu_I(1-\sigma_d)}{\frac{\mu_B}{h}|I|}. \tag{3.19}$$

Here $\mu_I = -1.0924(7)\mu_N$ is the nuclear magnetic moment for ^{87}Sr, where μ_N is the nuclear magneton[93]. The diamagnetic correction is $\sigma_d = 0.00345$ for ^{87}Sr [92].

To extend the Hamiltonian to arbitrary field strengths for ^{87}Sr we can consider the hyperfine and Zeeman interaction together using a spin-orbit mixed state basis [92]. Although we will only present the result of this process here, an interested reader can see [92] for further details on this technique. In short it allows for us to write the total Zeeman Hamiltonian as the sum of Eqn. (3.18), hyperfine effects H_A and quadrupole effects H_Q.This gives

$$\hat{H}_{\mathrm{ZT}} = H_z + H_A + H_Q = H_z + A\vec{I}\cdot\vec{J} + Q\frac{\frac{3}{2}\vec{I}\cdot\vec{J}(2\vec{I}\cdot\vec{J}+1) - IJ(I+1)(J+1)}{2IJ(2I-1)(2J-1)}, \tag{3.20}$$

where the values for A and Q can be found listed in Tab. 3.2 for the $^3P_1$ and $^3P_2$ states [92]. Although not much work was done with fermions in tweezers for this thesis, this Hamiltonian will be important for a few calculations considered in the following (sub)sections. We briefly look at the influence that a small magnetic field would have on the trap depths of the $^3P_1$, $F = 11/2$ sublevels in the following subsection as well as later in 3.4, where diagonalization of this Hamiltonian is required to extract the proper magnitude of the transition dipole matrix elements, since the mixing of hyperfine levels will depend on the magnitude of the magnetic field used.

State	A (MHz)	Q (MHz)
$^3P_1$	-260	-35
$^3P_2$	-212.765	67

TABLE 3.2: Quantities of A and Q in the total Zeeman Hamiltonian (Eqn. (3.20)) for the $^3P_{1,2}$ states, taken from [92].

3.1.3 Polarizability results

Now that we have outlined the process for calculating both the polarizability and Zeeman Hamiltonian, we can start to look at some results. We can substitute the total polarizability matrices, $\hat{\alpha}_{m_\mathrm{i},m_\mathrm{f},\mathrm{tot}}(J,\lambda)$ and $\hat{\alpha}_{m_\mathrm{i},m_\mathrm{f},\mathrm{tot}}(F,J,\lambda)$ for ^{88}Sr and ^{87}Sr respectively, into Eqn. (3.1) to calculate the light shift Hamiltonian, giving

$$\hat{H}_E = -\frac{4P_L a_0^3}{c w_0^2}\hat{\alpha}_{m_\mathrm{i},m_\mathrm{f},\mathrm{tot}}(J,\lambda), \tag{3.21}$$

and

$$\hat{H}_E = -\frac{4P_L a_0^3}{c w_0^2}\hat{\alpha}_{m_\mathrm{i},m_\mathrm{f},\mathrm{tot}}(F,J,\lambda), \tag{3.22}$$

respectively, where we use the subscript E for electric field. Here, we have included the conversion factor from a.u. to Joules ($4\pi\epsilon_0 a_0^3$) and use the peak intensity at $r = 0$. Here we will present a few results for different states of interest. To keep the discussion independent of trap power and waist, we will present all results as polarizabilities in atomic units. The RDMs along with energies $\tilde{\nu}_J$ and $\tilde{\nu}_{J'}$ for transitions between initial states J and final states J' can be found for the $J \equiv {}^1S_0$, $^3P_0$, $^3P_1$, and $^3P_2$ states in Tab. 3.3. We will use these values to evaluate the polarizability using Eqn. (3.11). We will start with polarizability plots of different pure polarizations for the bosonic case. We will continue with results for the fermionic isotope ^{87}Sr. To finish, we will consider tuning the polarizability by varying the trap polarization ellipticity, which will enable us to tune the polarizability.

Bosonic strontium polarizability

In Figure 3.2 the polarizability versus trapping wavelength is plotted for the $^1S_0$, $^3P_2$, and $^3P_0$ states of ^{88}Sr and for pure σ^-, σ^+, and π polarizations. Looking at the plots for $\sigma_\pm$, we see that close to the magic wavelength of the clock state, at 813.4 nm, there is also a near magic crossing with the $^3P_2$, $m_j = 0$ sublevel. Such a magic wavelength

Initial state (J)	Final state (J')	$\tilde{\nu}_J$	$\tilde{\nu}_{J'}$	RDME
5s^2, $^1S_0$ [30]	5s5p, $^3P_1$	0	14504.3	0.151
5s^2, $^1S_0$	5s5p, $^1P_1$		21698.5	5.248
5s5p, $^3P_0$ [88]	5s4d, $^1D_2$	14317.5	18159.0	2.607
5s5p, $^3P_0$	5s6s, $^3S_1$		29038.8	1.962
5s5p, $^3P_0$	5s5d, $^3D_1$		35006.9	2.450
5s5p, $^3P_0$	5p^2, $^3P_1$		35400.1	2.605
5s5p, $^3P_0$	5s7s, $^3S_1$		37424.7	0.516
5s5p, $^3P_0$	5s6d, $^3D_1$		39685.8	1.161
5s5p, $^3P_0$	5s8s, $^3S_1$		40761.4	0.302
5s5p, $^3P_0$	5s7d, $^3D_1$		41864.4	0.822
5s5p, $^3P_0$	5s9s, $^3S_1$		42451.2	0.270
5s5p, $^3P_0$	5s8d, $^3D_1$		43070.3	0.820
5s5p, $^3P_1$ [30]	5s^2, $^1S_0$	14504.3	0	0.151
5s5p, $^3P_1$	5s4d, $^3D_1$		18159.0	2.322
5s5p, $^3P_1$	5s4d, $^3D_2$		18218.8	4.019
5s5p, $^3P_1$	5s4d, $^1D_2$		20149.7	0.190
5s5p, $^3P_1$	5s6s, $^3S_1$		29038.8	3.425
5s5p, $^3P_1$	5s6s, $^1S_0$		30591.8	0.045
5s5p, $^3P_1$	5s5d, $^1D_2$		34727.4	0.061
5s5p, $^3P_1$	5s5d, $^3D_1$		35006.9	2.009
5s5p, $^3P_1$	5s5d, $^3D_2$		35022.0	3.673
5s5p, $^3P_1$	5p^2, $^3P_0$		35193.4	2.657
5s5p, $^3P_1$	5p^2, $^3P_1$		35400.1	2.362
5s5p, $^3P_1$	5p^2, $^3P_2$		35674.6	2.865
5s5p, $^3P_1$	5p^2, $^1D_2$		36960.8	0.228
5s5p, $^3P_1$	5p^2, $^1S_0$		37160.2	0.291
5s5p, $^3P_1$	5s7s, $^3S_1$		37424.7	2.657
5s5p, $^3P_2$ [89]	5s4d, $^3D_1$	14898.5	18159.0	0.603
5s5p, $^3P_2$	5s4d, $^3D_2$		18218.8	2.335
5s5p, $^3P_2$	5s4d, $^3D_3$		18218.8	5.538
5s5p, $^3P_2$	5s4d, $^1D_2$		20149.7	0.104
5s5p, $^3P_2$	5s6s, $^3S_1$		29038.8	4.508
5s5p, $^3P_2$	5s5d, $^1D_2$		34727.4	0.362
5s5p, $^3P_2$	5s5d, $^3D_1$		35006.9	0.462
5s5p, $^3P_2$	5s5d, $^3D_2$		35022.0	1.96
5s5p, $^3P_2$	5s5d, $^3D_3$		35045.0	5.00
5s5p, $^3P_2$	5p^2, $^3P_1$		35400.1	3.00
5s5p, $^3P_2$	5p^2, $^3P_2$		35674.6	5.12
5s5p, $^3P_2$	5p^2, $^1D_2$		36960.8	0.683

TABLE 3.3: Tabulated values of reduced transition dipole matrix elements (RDMEs, in a.u.) for the ground state ($^1S_0$) and three metastable triplet states of strontium ($^3P_{0,1,2}$) along with the energies (in cm^{-1}) of the initial (J) and final (J') states of each transition. The citation in which the values for each state can be found is given after the first term of each state.

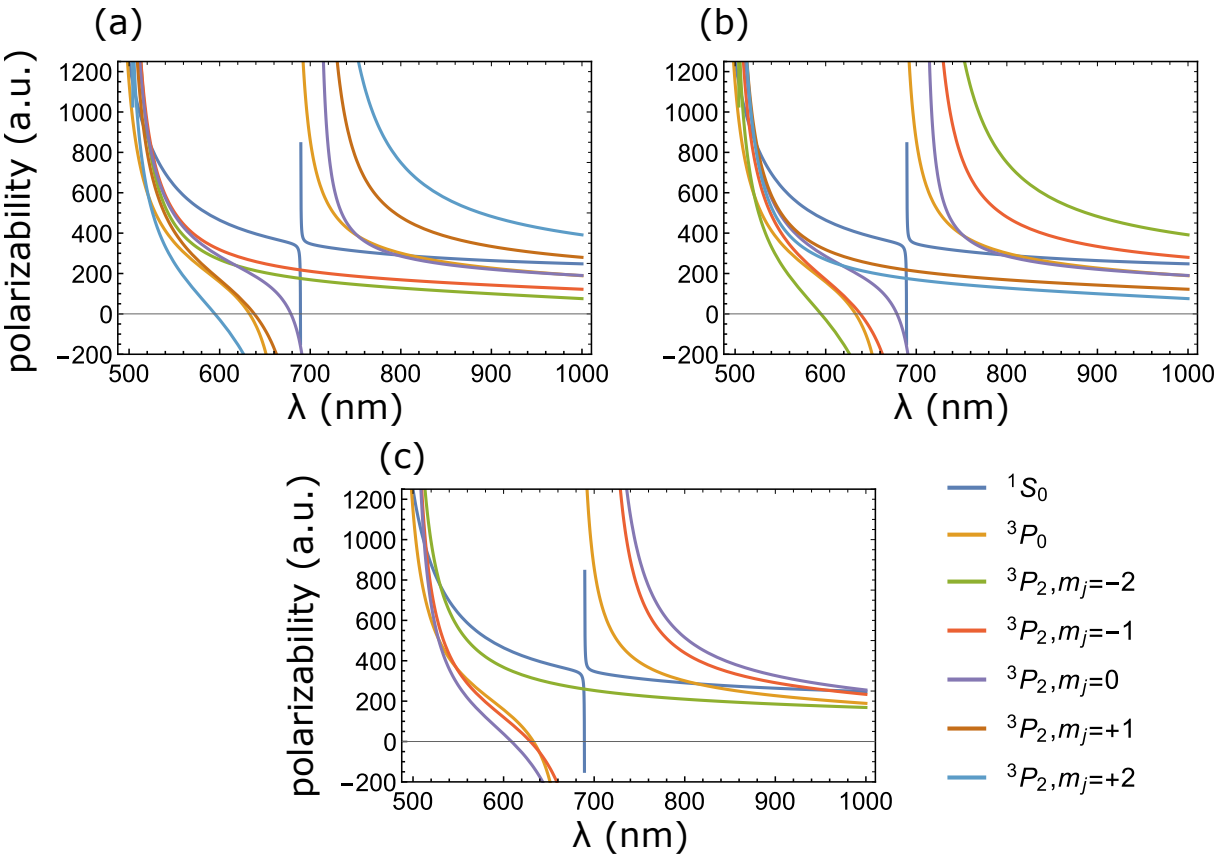

FIGURE 3.2: Polarizability of the $^1S_0$, $^3P_0$, and $^3P_2$ states of ^{88}Sr for trapping light with **(a)** σ^--, **(b)** σ^+-, and **(c)** π- polarizations. The labels in the bottom right corner are for all three graphs. In graph (c), the $^3P_2$ $m_J = +1$ and $m_J = +2$ sublevels are degenerate with $m_J = -1$ and $m_J = -2$ sublevels respectively. Because of this, we only plot $m_J = +1$ and $m_J = +2$ sublevels for (c). We find a magic wavelength crossing between $^3P_0$ and $^3P_2$, $m_J = 0$ at 750 nm for $\sigma^\pm$ polarized trapping light. For all polarizations, a magic wavelength is present between $^3P_0$ and $^3P_2$, $|m_J| = 1$ around 550-600 nm.

could be useful either for direct interrogation of the $^1S_0$ - $^3P_2$ transition or for constructing a qubit by off resonant coupling of the metastable $^3P_0$ and $^3P_2$ states [94]. For σ^- and σ^+ polarized light there exists a magic wavelength between $^3P_0$ and $^3P_2$, $m_j = 0$ around 750 nm.

Another important state to know the polarizability for is the $^3P_1$ state. The transition between this state and the ground state is used for cooling in all strontium tweezer experiments, and in our case also for imaging [30, 32, 34, 44, 45, 46]. The narrow linewidth imaging procedure that we have developed relies on one of the m_J sublevels of $^3P_1$ experiencing a stronger trapping potential than the ground state (see Chapter 2 for details). To find the wavelengths at which this occurs, we have plotted the polarizability versus wavelength, again for all three pure polarizations, in Fig. 3.3. We see that for the range of 700-900 nm and around 515 nm, one of the m_J sublevels experiences a stronger trapping potential than the ground state.

Fermionic strontium (^{87}Sr) polarizability

We continue with presenting the results for the polarizability of $^3P_2$ in ^{87}Sr. For a few theoretical projects, we were interested to know if a magic wavelength arose for the $^1S_0$ - $^3P_2$ transitions in strontium [41, 95]. At first thought, it would seem unlikely that the tensor shifts for all the m_F sublevels of a given $^3P_2$ hyperfine manifold would be comparable to each other. Contrary to this expectation, we did find that such a condition exists for the $F = 11/2$ manifold! In Fig. 3.4, we show the polarizability of the the $F = 11/2$ manifold versus wavelength for σ^-, σ^+, and π polarizations. Coincidentally, we see that for π-polarized light the m_f specific shift nearly disappears over the whole spectrum! The unexpected uniformity results from the summation of the different Clebsch-Gordan coefficients in Eqn. (3.16). We see for all the cases with $J = 2$, $F = 11/2$, and π-polarized trap light, the allowed transitions ($J = 2 \rightarrow J' = (1, 2, 3)$) have uniform polarizability for all m_F sublevels. Interestingly, if we look at different values of I, we see that this always happens for states with $J = 2$ and $F = I + 1$. Other than this mathematical origin, we have no explanation for why this occurs, however it could prove to be a useful tool in future experiments.

We predict two near magic wavelengths for $^1S_0$ - $^3P_2$, $F = 11/2$ around 517.7 nm and 881.7 nm. At these two wavelengths the polarizabilities of different m_F levels have deviations of at most $\pm 0.7\%$ and $\pm 1.1\%$ respectively. The difference in deviation of these

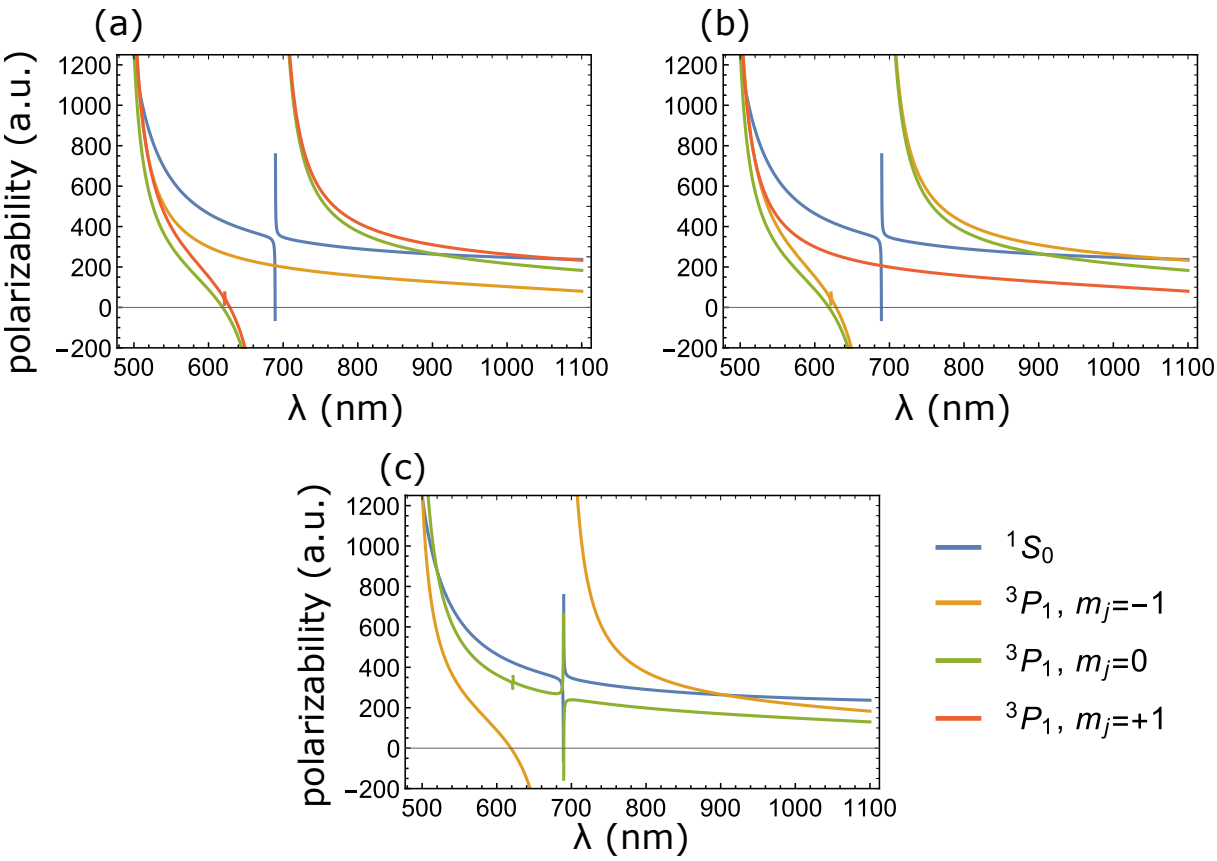

FIGURE 3.3: Polarizability for the $^1S_0$, and $^3P_1$ m_J sublevels for **(a)** σ^-, **(b)** σ^+, and **(c)** π- polarization. For π-polarization, the $m_j = \pm 1$ sublevels are degenerate so only the $m_j = -1$ sublevel is visible. The legend is valid for all three graphs.

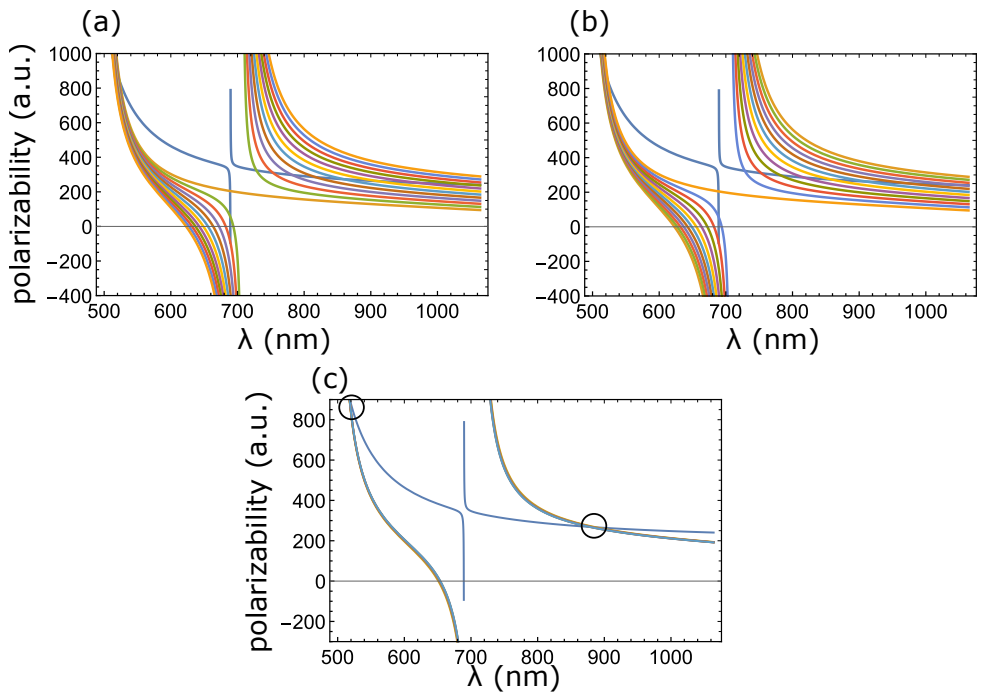

FIGURE 3.4: Polarizability versus trapping wavelength for the 12 m_F sublevels of the $^3P_2$, $F = 11/2$ hyperfine manifold. We have included $^1S_0$ polarizability as well for reference. It is worth noting that all 10 m_F levels of $^1S_0$ are degenerate in the absence of magnetic field. The polarizability is shown for **(a)** σ^-, **(b)** σ^+, and **(c)** π- polarized trap light. We see that for π-polarization all m_F sublevels have near equal polarizability over the whole wavelength range leading to m_f state independent near magic wavelengths at 517.7 nm and 881.7 nm (black circles in (c)). We do not include a legend because the specific m_F sublevels labeling is not relevant here and the main message is the variation between different sublevels. $^1S_0$ is the same color as in all polarizability plots.

two wavelengths comes mainly from the magnitude of the polarizability and distance from a transition. It is also worth noting that the 881.7 nm crossing will be more sensitive to small variations in the other contribution, Eqn. (3.12). Since the crossing is far from any transitions, small changes could lead to shifts of even 20 nm in the magic crossing point. For $\sigma_\pm$ polarizations, the m_f specific crossing spreads out over 100's of nm as shown by the other two plots in Fig. 3.4. For completeness, and to highlight the uniqueness of this effect, we plot the polarizability around 900 nm for the three most relevant hyperfine manifolds, $F = 11/2, 9/2,$ and $7/2$, for π-polarization in Fig. 3.5. We also show a zoom for both magic wavelength crossings of the $F = 11/2$ manifold in the same figure.

Next, to see if it is feasible to use our narrow linewidth imaging procedure with ^{87}Sr, we calculate the polarizability of the $^3P_1$, $F = 11/2$ manifold. This is because only this manifold has a cycling transition between the $m_F = \pm 11/2$ and the stretched ground states. Although the region around 515 nm is no longer ideal for our narrow linewidth imaging procedure (i.e. a deeper trapped $^3P_1$, $m_F = \pm 11/2$ state), we do find that the same range of 700-900 nm will still work nicely for narrow line imaging in ^{87}Sr which includes both the clock magic wavelength and the $^1S_0$ - $^3P_2$ magic wavelength estimated above, see Fig. 3.6.

Using elliptical polarization for tuning the polarizability

The last results for the polarizability that we will present are for the case of elliptical polarization. We can study the effect of the ellipticity on the polarizability of the states. For reference, an ellipticity angle of $\gamma = 0$ is equivalent to linear polarized light, while $\gamma = \pm\pi/4$ is equivalent to $\sigma^\pm$ respectively [30]. Using this method of polarization tuning, we can induce state mixing between different m_J sublevels to shift the polarizability. This can be useful for finding magic wavelength conditions. Here we will present results starting first with the bosonic case and finishing with one example for the fermionic case.

To find an exact magic wavelength crossing between the two metastable states, $^3P_0$ and $^3P_2$, and the ground state, $^1S_0$, we calculate the polarizability versus ellipticity angle γ of the trapping light at the clock magic wavelength of 813.4272 nm [34]. The results of this calculation are shown in Fig. 3.7(a), where we use the labelling of $|\phi_a\rangle$-$|\phi_e\rangle$ for the 5 eigenstates of $^3P_2$ since they are no longer pure m_J sublevels. At the

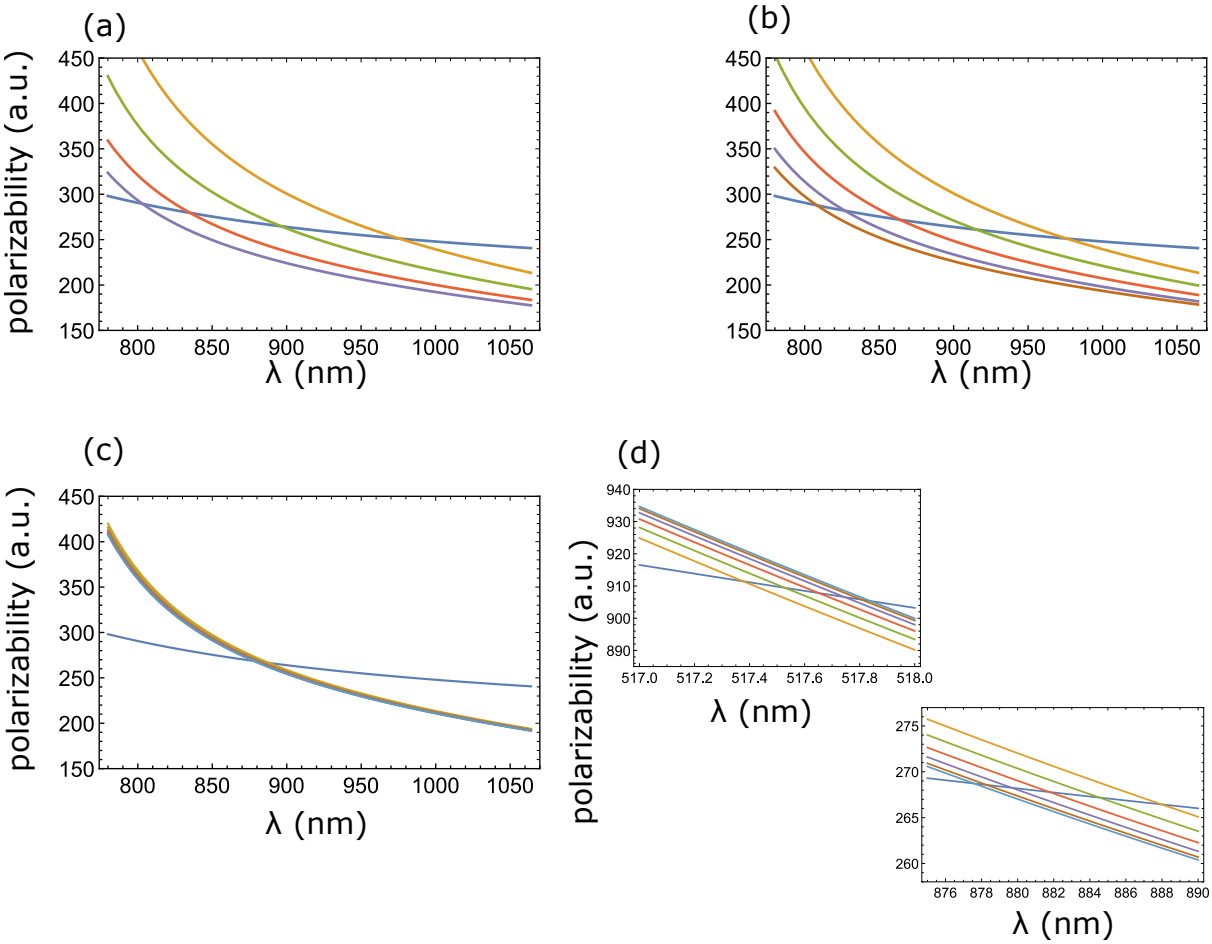

FIGURE 3.5: Polarizability for π-light at different wavelengths around 900 nm for the different F-manifolds of $^3P_2$ where **(a)** $F = 7/2$, **(b)** $F = 9/2$, and **(c)** $F = 11/2$. We have included two additional zooms of $F = 11/2$ around the two predicted magic wavelengths of 517.7 nm and 881.7 nm.

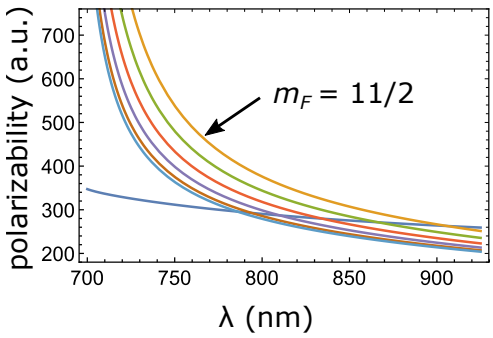

FIGURE 3.6: Polarizability for the different m_F sublevels of $^3P_1$, $F = 11/2$ for π- polarized light, where again the plus and minus m_f levels of the same quantum number are degenerate, leading to 6 unique curves. For a guide we have additionally included the polarizability of $^1S_0$ and identified the $|m_F| = 11/2$ sublevel with an arrow. The $|m_F| = 11/2$ states remain deeper trapped than the ground state until over 900 nm. This means that narrow linewidth imaging should work nicely at both the $^1S_0$ - $^3P_0$ and $^1S_0$ - $^3P_2$ ($F = 11/2$) magic wavelengths.

center of the plot the polarization is equivalent to the superposition of $\sigma^+ + \sigma^-$, which is equivalent to π-polarization in the absence of magnetic field, and the color code matches that of the m_J sublevels in Fig. 3.2. At the edge of the plot where $\gamma = \pm\pi/4$, the eigenstates are again pure m_J sublevels of $^3P_2$, however the colors no longer match the previous figure. For instance, the m_j=0 state is now equivalent to $|\phi_b\rangle$. We find the magic ellipticity angle for the $^1S_0$, $^3P_2$, and $^3P_0$ states at $\gamma = \pm 27°$ (0.151π).

A similar analysis is done for a magic wavelength between $^1S_0$ and $^3P_2$ for a trapping wavelength of 515 nm. There is no magic ellipticity angle between $^3P_0$ and $^3P_2$ at this wavelength unfortunately, but a magic angle between $^1S_0$ and $^3P_2$ offers some advantages aside from the qubit candidate of an ultra-narrow linewidth transition at magic conditions. These advantages include the large polarizability ($\sim$ 950 a.u.), the short wavelength leading to small diffraction-limited tweezer spots, and the trapping of Rydberg states at this wavelength. The results are shown in Fig. 3.7(b), where we see two magic angles of $\gamma = \pm 8°$ (0.04π) and $\gamma = \pm 33°$ (0.183π) for two different sublevels.

We can also perform ellipticity tuning for the $^3P_1$ state, where a magic condition between $^1S_0$ and one of the m_J sublevels of $^3P_1$ could be useful for sideband cooling of an atom in a tweezer. We have included the plots for this tuning at 515 nm and at 813.4 nm in Fig. 3.8(a) and (b) respectively. We see that at 515 nm such a condition exists for the angle $\gamma = 22.7°$ (0.126π), but no such angle exists for 813.4 nm. We will see in the

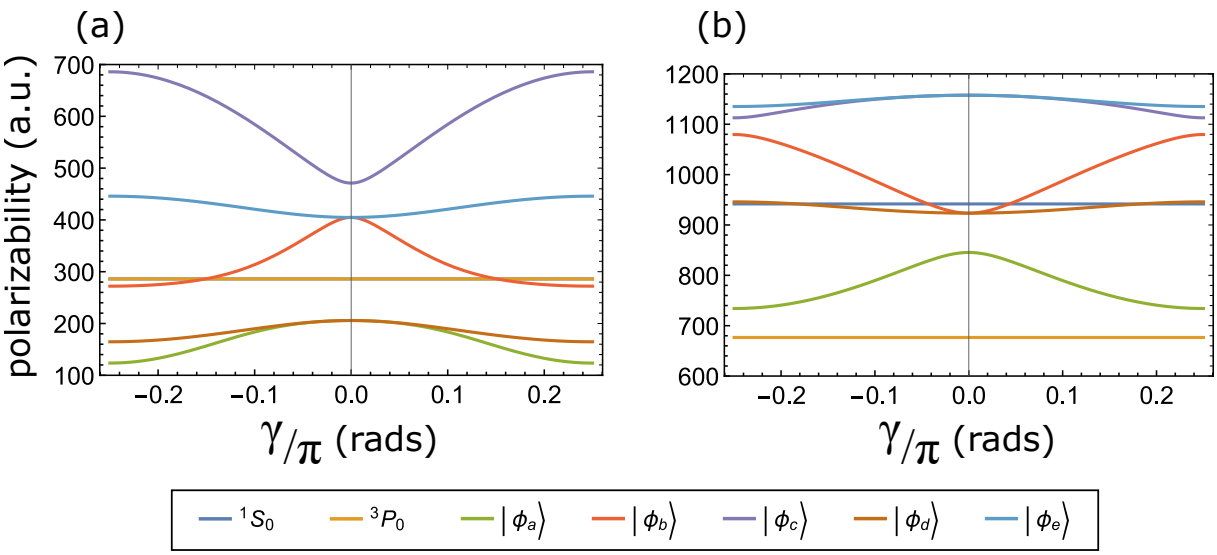

FIGURE 3.7: **(a)** Polarizability versus ellipticity angle γ for the $^1S_0$, $^3P_0$ and the five $^3P_2$ m_J sublevels at 813.42 nm (note that $^1S_0$ and $^3P_0$ have equal polarizability at this wavelength). We find a magic ellipticity angle between $^1S_0$, $^3P_0$ and $^3P_2$ at $\gamma = \pm 27°$ (0.151π). **(b)** same as (a) but at 515.2 nm. We find no magic angle between $^3P_0$ and $^3P_2$, but we find two magic angles for $^1S_0$ and two different sublevels of $^3P_2$ at $\gamma = \pm 8°$ (0.04π) and $\gamma = \pm 33°$ (0.183π).

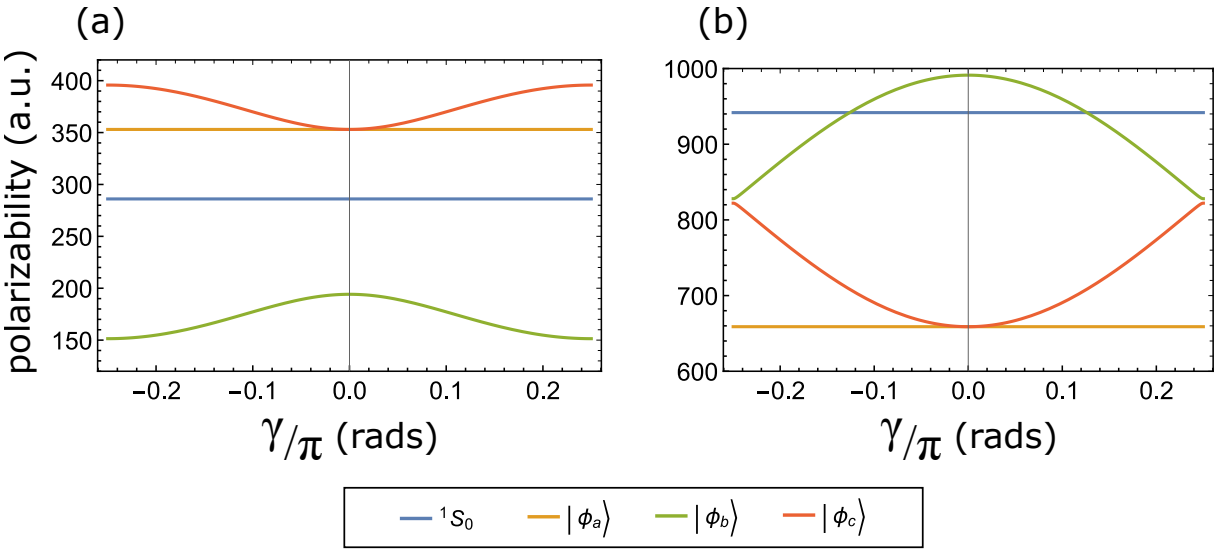

FIGURE 3.8: (a)Polarizability versus ellipticity angle for the $^1S_0$ and the three $^3P_1$ m_J sublevels at 813.42 nm. (b) Polarizability versus ellipticity angle for the same states as the previous plot, but at 515.2 nm. We find a magic ellipticity angle of $\gamma = \pm 22.7°$ (0.126π).

following section that a different tuning method can still be used for tuning to magic conditions at this wavelength.

We conclude this discussion with results for ellipticity tuning of the $^3P_1$, $F = 11/2$ state in ^{87}Sr at 813.4 nm as shown in Fig. 3.9. This plot shows how the picture becomes much more complicated with the additional hyperfine sublevels. We include this plot mainly for completeness but it is worthwhile to note how polarization impurity in the tweezer beam could lead to state specific shifts. We see small ellipticity angles should have little to no effect on the cooling/imaging transition where one of the stretched sublevels are used. Again it is important to note that the pure sublevels can only be found at the three points in this plot, where the strongest (weakest) polarizability corresponds to the $m_f = -11/2(+11/2)$ sublevels at $\gamma = \pi/4$ and vice versa at $\gamma = -\pi/4$.

3.1.4 Combining the light shift and Zeeman Hamiltonian

Finally, we consider how an angle between the magnetic field and the polarization affects the overall shift. To do this we must evaluate the full Hamiltonian, which is the sum of the light shift and Zeeman Hamiltonian,

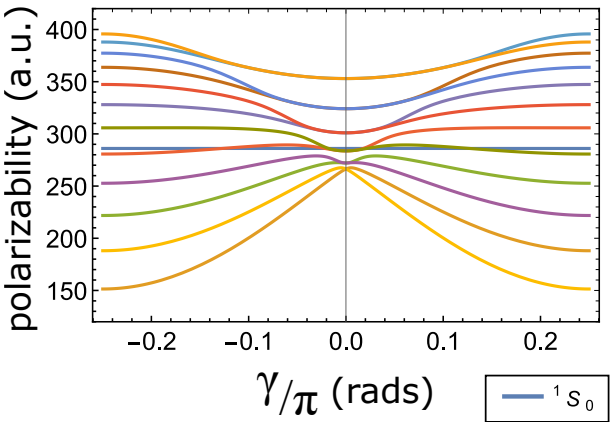

FIGURE 3.9: Polarizability versus ellipticity angle for the $^1S_0$ and the 12 m_F sublevels of $^3P_1$, $F = 11/2$ at 813.42 nm. We plot this mainly to show the effect of polarization impurity on the m_F dependent polarizability.

$$\hat{H}_{\text{full}} = \hat{H}_{B,\text{ZT}} + \hat{H}_E, \tag{3.23}$$

where the choice of Zeeman Hamiltonian corresponds to the choice of polarizability matrix used in $\hat{H}_E$[4]. We here consider a linearly polarized laser beam (typically the tweezer beam) propagating orthogonal to a magnetic field, with an angle θ between the magnetic field direction and the polarization. The results presented here will focus on using the polarization unit vector $\vec{\boldsymbol{u}}_\theta$ from Eqn. (3.5) to calculate the combined shift when there is an angle between the magnetic field and the linear tweezer polarization.

Starting again from the simpler case of ^{88}Sr using H_B, we present some brief results to highlight the agreement between our method and the measured magic angles from previous publications. A magic angle for the $^1S_0$ - $^3P_1$ transition has been measured at both 515 nm [44] and at 813.4 nm [34]. We are able to reproduce these results obtaining the magic angles of $\theta = 23°$ (0.128π) at 515 nm and $\theta = 49°$ (0.272π) at 813.4 nm as shown in Fig. 3.10 (a,b). Magic polarization angles with respect to a magnetic field tend to be a more robust way for cancelling differential shift between two states. This is because paraxial effects at the tight focal points of tweezers, along with the small angles of the different tweezer beams on the waveplate required for ellipticity tuning, could affect the uniformity of polarization across the tweezer volume and thereby the differential light shift cancellation. Additionally, we have included a plot for the same tweezer in the presence of a weak magnetic field (250 mG) in Fig. 3.10(c) to highlight

[4]One should use $\hat{H}_B$ for ^{88}Sr with Eqn. (3.21) and $\hat{H}_{\text{ZT}}$ for ^{87}Sr with Eqn. (3.22).

how stray fields can cause undesired shifts and splittings and emphasize the importance of good magnetic field zeroing.

Since magic angle tuning can be a more robust method for canceling the differential shift, we also examine if a magic angle exists for one of the $^3P_2$ sublevels and the $^1S_0$ and $^3P_0$ states at 813.42 nm. We find that a such a magic angle does exist at $\theta \simeq 75°$ (0.417π) as shown in Fig. 3.11. In the same figure we have also include the B-field dependence of this magic angle in order to determine the required field strength to cancel out the differential shift. We see for a trap depth of approximately -6 MHz a field strength of about 3 G is required. In the final plot we show how the magic condition can be saturated as the power of the trapping laser is increased. For example, a 5 G field is able to suppress the shift up to $\simeq 10$ mW of power for a 0.8μm waist tweezer. Converting back to trap depth, this gives a relation between trap depth and magnetic field strength of approximately 2 MHz/G.

Finally, in Fig. 3.12, we present the total shift for the m_F sublevels of the $^3P_1$, $F = 11/2$ hyperfine manifold versus the angle between a small magnetic field of $B = 500$ mG and linear polarization. This calculation is valid for low fields where the Zeeman shift is still linear and F remains a good quantum number [87]. The state labeling is even harder to keep track of in this plot because of the unique Zeeman and light shifts for different m_F sublevels and the angle dependent state mixing. An important note to make though, is that when the B-field and polarization are aligned ($\theta = 0, \pi$) the polarizability matrix is composed of pure m_F sublevels. This allows for simple calculation of the total shift for a given state by addition of the polarizability and Zeeman shift. This is an important consideration for state specific narrow linewidth imaging on the $^1S_0$ - $^3P_1$ transition in ^{87}Sr.

3.2 *n*-level coupling Hamiltonian with dissipation

In order to understand both how laser cooling works for an atom in an optical tweezer, and how the internal states of an atom can be used as qubit or qudit states, we must first compose a coupling Hamiltonian describing describing the coupling between $^1S_0$ and ^3P_J. Since for both applications the ingredients of this Hamiltonian are the same, we start by outlining its derivation and the corresponding master equation (Section 3.2), before using it for the two applications mentioned (Section 3.3 and Section 3.4).

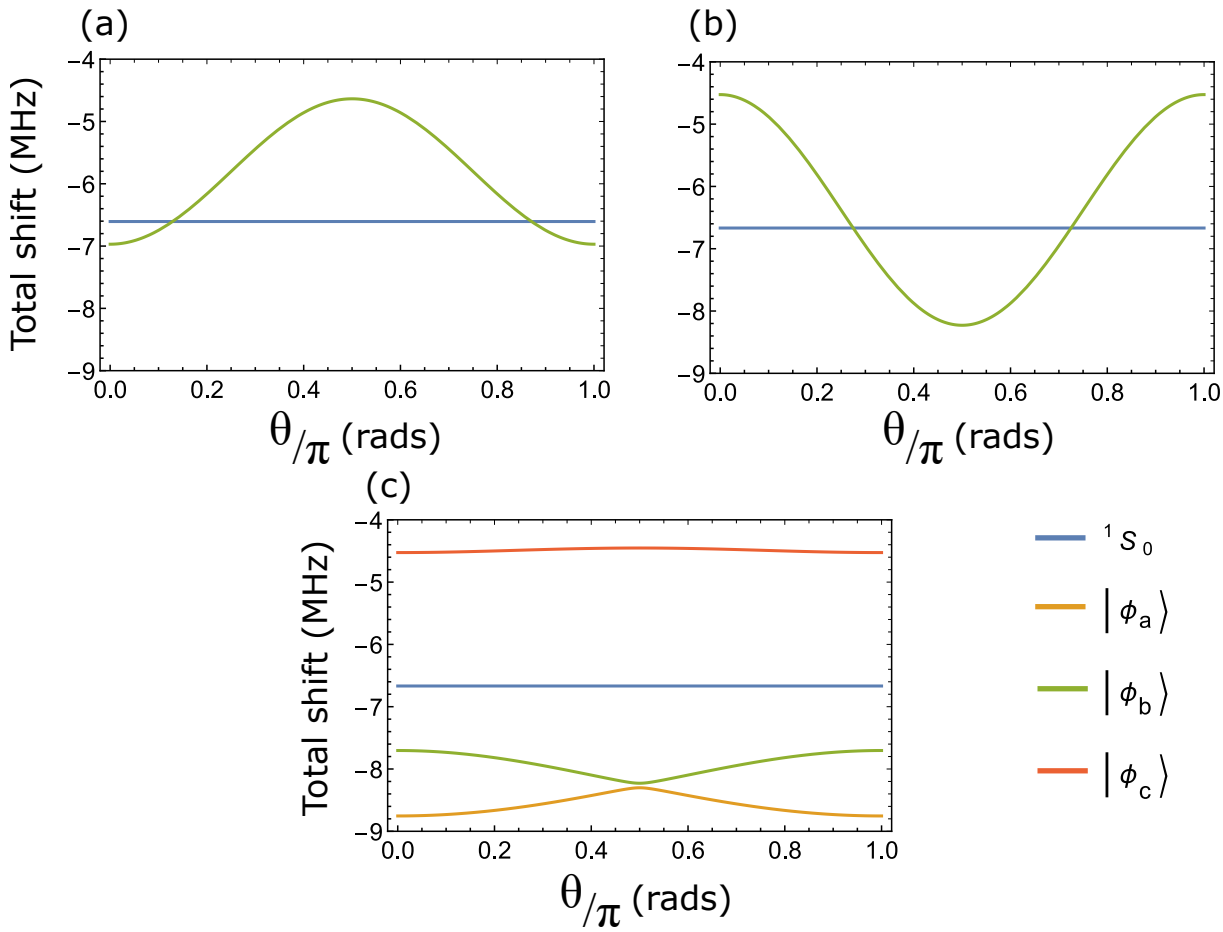

FIGURE 3.10: Total shift for different angles between magnetic field and linear polarization for $^3P_1$ with the light shift of $^1S_0$ included for reference with **(a)** 515 nm trap light, 1.5 mW laser power, 0.8 μm waist, and 20 G field **(b)** 813 nm trap light, 5 mW laser power, 0.8 μm waist, and 20 G field, and **(c)** 813 nm trap light, 5 mW laser power, 0.8 μm waist, and 0.25 G field. In plots (a) and (b) the other $^3P_1$ sublevels have been shifted out of the plot area by the magnetic field. The last plot highlights angle dependence of a stray magnetic field on changing the total shift of the $^3P_1$ sublevels. These small shifts can significantly affect the performance of the cooling process, highlighting the importance of properly zeroing the field or at least properly choosing the angle between an applied field and the polarization. As expected we see that there is a symmetry around $\pi/2$ for all of these graphs.

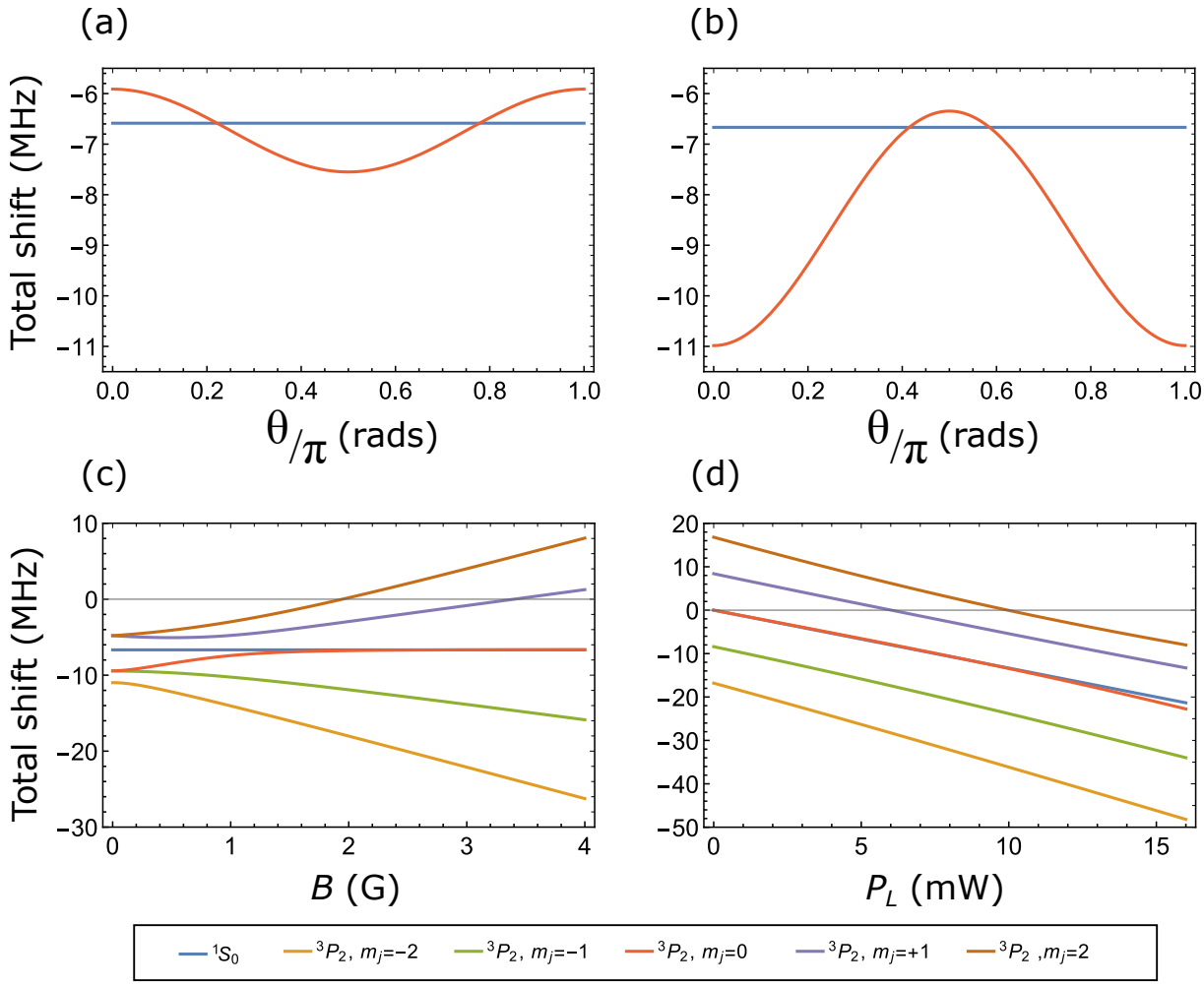

FIGURE 3.11: **(a)** Total shift vs angle between the magnetic field and linear polarization for $^3P_2$ with the light shift of $^1S_0$ included for reference at a trap wavelength of 515.2 nm using $P_L = 1.5$ mW, $w_0 = 0.8\mu$m, and $B = 20$ G. We find a magic angle of $\theta = 40°$ (0.222π). **(b)** Same as (a) at a trap wavelength of 813.4 nm using $P_L = 5$ mW. We find a magic angle at $\theta = 75°$ (0.417π). In plots (a) and (b) the other $^3P_2$ sublevels have been shifted out of the plot area by the magnetic field. **(c)** Total shift vs strength of magnetic field at a trap wavelength of 813.4 nm and with $\theta = 75°$ (0.417π) and the same parameters used in the previous plot. We see that a field strength greater than 2.5 G is sufficient for $^3P_2$, $m_J = 0$ differential Stark shift cancellation at this trap depth. **(d)** Total shift vs tweezer laser power. We plot the results for a low B field ($B = 5$ G) so that the deviation from magic is visible at a low intensity (≤ 12 mW). All other parameters are the same as the previous plots ($\theta = 75°$, $w_0 = 0.8\,\mu$m). The legend at the bottom applies to all graphs and is assigned in the basis where the magnetic field defines the quantization axis.

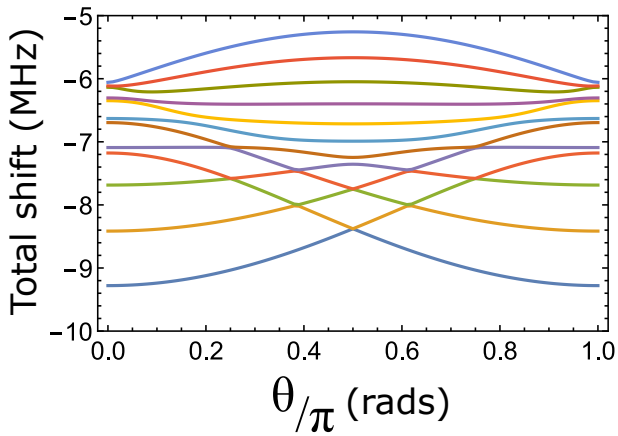

FIGURE 3.12: Total shift vs angle between magnetic field and the linear polarization of the trap light for the m_f sublevels of the $^3P_1$, $F = 11/2$ hyperfine manifold. We use $P_L = 5$ mW, $w_0 = 0.8\mu$m, and trapping wavelength 813.4 nm with magnetic field strength of 500 mG.

The strength of coupling between a $^1S_0$ state $|i\rangle$ and a ^3P_J state $|f\rangle$ by light is described by

$$\Omega = \frac{a_0 e E_0}{2\hbar} \langle f| d |i\rangle , \tag{3.24}$$

where Ω is the Rabi frequency, E_0 is the magnitude of the electric field, and $\langle f| d |i\rangle$ is the TDM between f and i in atomic units (see Eqn. (3.7)). We note that here we use the TDM for which the Clebsch-Gordan coefficient is defined for i to f with q equal to the desired coupling. For a given transition, the Hamiltonian describing the atom light interaction is

$$\hat{H}_0 = \hbar\omega_a \hat{\sigma}_{ff} + \frac{\hbar\Omega}{2}(\hat{\sigma}_{fi} + \hat{\sigma}_{if})(\mathrm{e}^{\mathrm{i}\omega_L t} + \mathrm{e}^{-\mathrm{i}\omega_L t}), \tag{3.25}$$

where ω_a is the frequency of the atomic transition, $\hat{\sigma}_{ff} = |f\rangle\langle f|$, $\hat{\sigma}_{fi} = |f\rangle\langle i|$, $\hat{\sigma}_{if} = |i\rangle\langle f|$, and ω_L is the frequency of the laser driving the transition. Transforming to the interaction picture using a unitary transformation $\hat{U} = \mathrm{e}^{-\mathrm{i}\hbar\omega_a\hat{\sigma}_{ff}}$, the Hamiltonian becomes

$$\hat{H}_0^I = \hat{U}^\dagger H_0 \hat{U} - \hbar\omega_a\hat{\sigma}_{ff} = \frac{\hbar\Omega}{2}(\sigma_{fi}\mathrm{e}^{\mathrm{i}(\omega_a+\omega_L)t} + \sigma_{if}\mathrm{e}^{\mathrm{i}\Delta t} + \sigma_{fi}\mathrm{e}^{-\mathrm{i}\Delta t} + \sigma_{if}\mathrm{e}^{-\mathrm{i}(\omega_a+\omega_L)t}), \tag{3.26}$$

where $\Delta = \omega_L - \omega_a$. The interaction Hamiltonian can be further reduced using the rotating wave approximation to neglect the fast rotating terms, and a second unitary

transformation with $\hat{U} = \mathrm{e}^{-\mathrm{i}\hbar\Delta\hat{\sigma}_{ff}t}$ to give

$$\hat{H} = \hat{U}^{\dagger}\hat{H}_0\hat{U} - \hbar\Delta\hat{\sigma}_{ff} = -\hbar\Delta\hat{\sigma}_{ff} + \frac{\hbar\Omega}{2}(\hat{\sigma}_{if} + \hat{\sigma}_{fi}). \tag{3.27}$$

$\hat{H}$ describes the coupling between two given states of the atom. From here we can describe a larger system using the summation over all relative states,

$$\hat{H}_{\mathrm{tot}} = \hbar\sum_{i=0}^{d_i-1}\sum_{f=0}^{d_f-1} -\Delta_f\hat{\sigma}_{ff} + \frac{\Omega_{if}}{2}(\hat{\sigma}_{if} + \hat{\sigma}_{fi}), \tag{3.28}$$

where $i \neq f$, $d_{i,f}$ is the number of states/dimension of the qudit in the respective state and $d = d_i + d_f$, and Δ_0=0. Expressed in matrix form this becomes

$$\hat{H}_{\mathrm{tot}} = \frac{\hbar}{2}\begin{pmatrix} 0 & \Omega_{0,1} & \Omega_{0,2} & \dots & \Omega_{0,d-1} \\ \Omega_{1,0} & -2\Delta_1 & \Omega_{1,2} & \ddots & \vdots \\ \Omega_{2,0} & \Omega_{2,1} & -2\Delta_2 & \ddots & \vdots \\ \vdots & & \ddots & \ddots & \Omega_{d-2,d-1} \\ \Omega_{d-1,0} & \dots & \dots & \Omega_{d-1,d-2} & -2\Delta_{d-1} \end{pmatrix}. \tag{3.29}$$

Here it is worth noting that the off-diagonal couplings may not follow the same elimination of fast rotating terms after applying the rotating wave approximation. Based on their relative detunings with respect to the leading diagonal coupling's detunings, this effect can be accounted for by additional AC Stark shifts or by keeping time dependent Ω_{if}'s for these terms. Based on the desired calculation, Δ_f can take on two representations. To construct the Hamiltonian for laser cooling, Δ_f can represent the change in energy for different quantum harmonic oscillator levels (QHOs) along with the QHO specific detunings between the ground and excited state, see Section 3.3. To construct the multiple state coupling Hamiltonians in Section 3.4, Δ_f is the detuning of the laser from the specific transition i to f where $i = f - 1$. Many of the Rabi frequencies displayed in the matrix of $\hat{H}_{\mathrm{tot}}$ will go to zero based on either the absence of a laser coupling between the two states, or because they are forbidden by selection rules.

Using density matrix formalism, we can evaluate the evolution under this Hamiltonian in the presence of laser noise and finite excited state lifetime using the Lindblad

master equation,

$$\dot{\rho}(t) = -\frac{\mathrm{i}}{\hbar}[\hat{H}_{\mathrm{tot}}, \hat{\rho}(t)] + \mathcal{L}_L + \mathcal{L}_D, \tag{3.30}$$

where $\dot{\rho}(t)$ is the time derivative of the density matrix $\hat{\rho}$, $\mathcal{L}_L$ is the Lindblad super operator for dephasing from laser noise,

$$\mathcal{L}_L = \frac{\Gamma_L}{2}\sum_{\mathrm{trans}}(2\hat{S}_{\mathrm{trans}}\hat{\rho}\hat{S}_{\mathrm{trans}} - \hat{S}^2_{\mathrm{trans}}\hat{\rho} - \hat{\rho}\hat{S}^2_{\mathrm{trans}}), \tag{3.31}$$

$\hat{S}_{\mathrm{trans}} = |i\rangle\langle i| - |f\rangle\langle f|$ is the collapse operator for a laser resonant with the transition i to f and Γ_L is the spectral linewidth of the laser. $\hat{S}_{\mathrm{trans}}$ describe the effect of dephasing from each coupling laser [96]. $\mathcal{L}_D$ is the Lindblad super operator for excited state decay,

$$\mathcal{L}_D = \frac{\Gamma_d}{2}\sum_{if}(2\hat{C}_{if}\hat{\rho}\hat{C}^\dagger_{if} - \hat{\rho}\hat{C}^\dagger_{if}\hat{C}_{if} - \hat{C}^\dagger_{if}\hat{C}_{if}\hat{\rho}), \tag{3.32}$$

with Γ_d is the excited state decay rate and collapse operator $\hat{C}_{if}$ ($\hat{C}^\dagger_{if}$) which can take two forms based on the specific application [97]. In the case of laser cooling, $\hat{C}_{if} = |n_g\rangle\langle m_e|$ ($\hat{C}^\dagger_{if} = |m_e\rangle\langle n_g|$) and describes the relevant decay processes from e to g with QHOs m and n respectively. In the case of the multiple state coupling Hamiltonian, $\hat{C}_{if} = |i\rangle\langle f|$ ($\hat{C}^\dagger_{if} = |f\rangle\langle i|$) describes the relevant decay channels from an excited state sublevel to the correct ground state sublevels.

3.3 Laser cooling in optical tweezers

Laser cooling of strontium in optical tweezers relies on the near harmonic potential created by the Gaussian focus of the tweezer beam as shown in Fig. 3.13(a). Two different cooling methods have been demonstrated for strontium atoms in tweezers. Both of these methods utilize the narrow $^1S_0$ - $^3P_1$ transition.

The first cooling method is known as sideband cooling. This method has also been used in a variety of other systems aside from optical tweezers [98, 99, 100, 101]. For strontium, sideband cooling can take place when the ground and excited state potentials, U_g and U_e respectively, are equivalent. The laser detuning can then be set to $\Delta_{mn} = -\omega_g$, where ω_g is the ground state trap frequency, such that the atom is excited to the $n-1$ harmonic oscillator level of the excited state. For large enough trap frequencies the atom decays with high probability back down to the $n-1$ ground state,

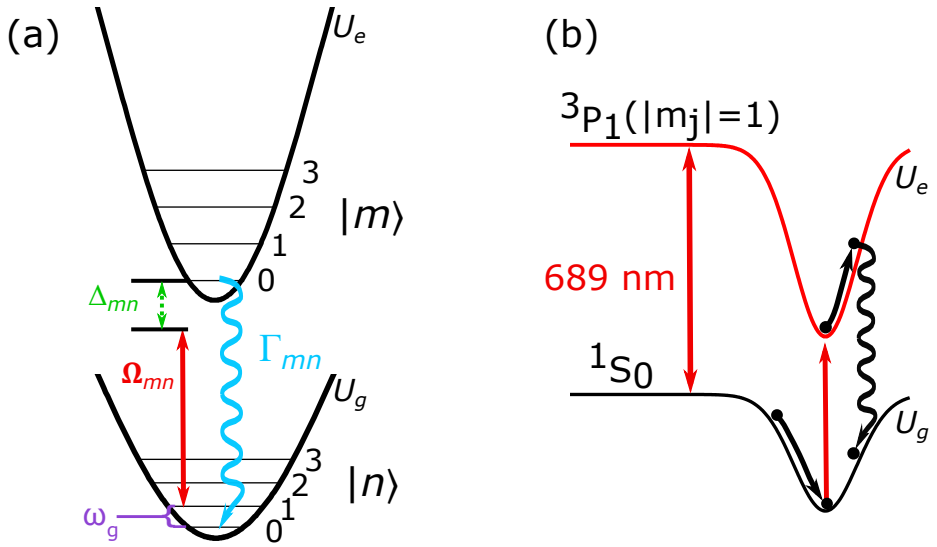

FIGURE 3.13: **(a)** Sketch of the two Harmonic oscillators created for the ground (U_g) and excited states (U_e) deep within the Gaussian potential of the tweezer. Laser cooling of strontium atoms in optical tweezers relies on such potentials. We have included some labels for terms that will be used throughout the following subsection. These include the vibrational levels of the ground ($|n\rangle$) and excited states ($|m\rangle$), Rabi Frequency (Ω_{mn}), decay rate (Γ_{mn}), detuning (Δ_{mn}), and trap frequency (ω_g). Δ_{mn} is defined as the detuning from the mth excited state QHO to the nth ground level QHO of the trap, thus because of the way the arrow of Ω_{mn} is drawn, the gap indicated in the image is Δ_{01}. **(b)** A sketch of the Sisyphus cooling process. The tweezer potential is deeper for the excited state ($^3P_1$) than for the ground state ($^1S_0$). The order of events for a cooling cycle is shown from left to right. The atom initially rolls down the ground state potential where it is preferentially excited near the bottom of the potential. The atom then rolls up the steeper excited state potential before decaying back to the ground state at a lower energy. This leads to a reduction in energy per scattered photon related to the trap depth mismatch [32, 67].

such that an absorption emission cycle leads to the removal of one vibrational quantum. Since the excited state trap frequency, ω_e is equal to ω_g, this process works for any level n such that the atom can be cooled to the motional ground state of the trap with a single detuning. For this process to work, one must be in the resolved sideband regime where $\omega_g \gg \Gamma$ and the Lamb Dicke regime [99]. The first requirement makes sure atoms can be excited from a specific harmonic oscillator level because the trap frequency is much larger than the radiative decay rate of the excited state and the second ensures that the recoil energy of the cooling photon will not lead to a change

in motional state of the atom. This method of cooling is used not only with optical tweezers but also with ions [98, 99], neutral atoms in optical lattices [56, 100, 101], and even micro-mechanical oscillators [102].

The second method, which has only been demonstrated in strontium, is a form of Sisyphus cooling that relies specifically on a difference in potential depths for the ground and excited state [30, 31, 32]. We will focus the discussion on the case of *attractive* Sisyphus cooling as this is the method currently used in our experiment [32].

Attractive Sisyphus cooling relies on the same trap frequency parameters as outline above but instead of equal trap depths relies on a trap depth mismatch of $U_g < U_e$, see Fig. 3.13(b). In a classical picture, the hot atom can be seen as a particle oscillating inside the trap. The cooling laser is tuned such that the atom is selectively excited from the bottom of the potential. When the trap frequency is larger than the radiative decay, the atom is more likely to decay from its turning point of motion through the trap. Because the excited state potential is steeper, the atom 'climbs' the excited state potential only up to a point that is closer to the center of the trap compared to the turning point of the initial ground state oscillations. The atom then decays back down to the ground state having lost energy related to trap depth mismatch. In addition, the non-magic trapping causes the harmonic oscillator levels of $|e\rangle$ and $|g\rangle$ to be non-orthogonal, for both the radial and axial directions, allowing for a single cooling beam to remove energy from all directions [32, 67].

In the quantum picture both cooling processes can be seen to be more or less the same with only a small difference related mainly to the ratio of the trap depths. For the simulation outlined here, we will focus mainly on the attractive Sisyphus cooling example as that is what is used in our experiment, however, the same technique can be easily used to calculate sideband cooling or *repulsive* Sisyphus cooling ($U_g > U_e$) as well.

3.3.1 Cooling simulation

The simulation is based on solving the Lindblad master equation, see Eqn. (3.30), for a two-level atom in a pair of 1D QHOs, one for each internal state $|g\rangle$, $|e\rangle$. We use 1D QHOs in the calculation for simplicity and ignore the anharmonicity of the Gaussian potential. Additionally, we consider an infinite trap depth but truncate the calculation to a finite number of harmonic oscillator levels. The ratio of the QHO frequencies

is given by $\omega_g/\omega_e = \sqrt{\alpha_g/\alpha_e}$, with $\alpha_{g,e}$ the dynamic polarizabilities at the tweezer wavelength. At our tweezer wavelength of 813.4 nm, we calculate this ratio to be ∼0.899.

To construct the desired coupling Hamiltonian, we start by choosing a traveling wave for the Sisyphus cooling laser. The transition dipole moments between vibrational states of different QHOs are calculated as $d_{eg} \langle m| e^{ikx} |n\rangle$, with $|m\rangle$, $|n\rangle$ the vibrational states for internal states $|g\rangle$ and $|e\rangle$, respectively, and d_{eg} the transition dipole moment of the $^1S_0$ - $^3P_1$ transition. This allows us to write the Rabi frequency between vibrational states as

$$\Omega_{mn} = \frac{ea_0 d_{eg} E_0}{2\hbar} \langle m_e|\mathrm{e}^{\mathrm{i}k\hat{x}}|n_g\rangle, \tag{3.33}$$

where $E(x) = E_0 \mathrm{e}^{\mathrm{i}kx}$ is the travelling wave of the cooling laser. We can also calculate the decay from a given oscillator level, Γ_{mn}, as

$$\Gamma_{mn} = \Gamma_{^3P_1} |\langle m_e|\mathrm{e}^{\mathrm{i}k\hat{x}}|n_g\rangle|^2, \tag{3.34}$$

where $\Gamma_{^3P_1}$ is the radiative decay rate of $^3P_1$.

We see that both of these terms require us to calculate the integral $\langle m|\mathrm{e}^{\mathrm{i}k\hat{x}}|n\rangle$. One might think that direct calculation of this integral should be possible as done in [103], but in practice we find this to be numerically slow and unstable. Instead we can split the integral into two parts

$$\langle m_e|\mathrm{e}^{\mathrm{i}k\hat{x}}|n_g\rangle = \sum_{i_g} S_{mi} D_{in} \tag{3.35}$$

where S_{mi} is the squeezing operator and D_{in} is the displacement operator with known matrix elements for each and i_g goes over all vibrational levels of $|g\rangle$.

To split the integral in half we start by inserting an identity matrix from the ground state, $\hat{I} = \sum_{i_g} |i_g\rangle\langle i_g|$, to give us

$$\langle m_e|\mathrm{e}^{\mathrm{i}k\hat{x}}|n_g\rangle = \langle m|\hat{I}\mathrm{e}^{\mathrm{i}k\hat{x}}|n\rangle = \sum_{i_g} \langle m_e|i_g\rangle\langle i_g|\mathrm{e}^{\mathrm{i}k\hat{x}}|n_g\rangle. \tag{3.36}$$

Here $S_{mi} = \langle m_e|i_g\rangle$ and $D_{in} = \langle i_g|\mathrm{e}^{\mathrm{i}k\hat{x}}|n_g\rangle$ and the subscripts g and e have been added to label the ground and excited Fock states respectively. As shown in Fig. 3.14, we can

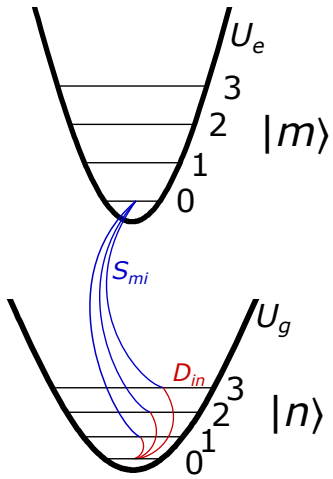

FIGURE 3.14: Visualization of splitting of the integral $\langle m|\mathrm{e}^{\mathrm{i}k\hat{x}}|n\rangle$ into two parts. This figure illustrates how the displacement operator (D_{in}) corresponds to a change in the harmonic oscillator level of the ground state, whereas the squeezing operator (S_{mi}) relates to the Franck-Condon overlap between an excited QHO state and the ground QHO states.

see that the displacement operator corresponds to a change in the harmonic oscillator level of the ground state, whereas the squeezing operator relates to the Franck-Condon overlap between an excited QHO state and the ground QHO states.

To solve for the matrix elements of the displacement operator, we consider the relation between the position operator, $\hat{x}$, and the momentum operator, $\hat{p}$. $\hat{x}$ and $\hat{p}$ are conjugate variables with commutator $[\hat{x}, \hat{p}] = \mathrm{i}\hbar$. This can be seen as $\hat{x}$ being the generator of displacement in $\hat{p}$ and vice versa. More explicitly, the operator $\mathrm{e}^{\mathrm{i}k\hat{x}}$ is the displacement by $\hbar k$ in momentum space giving us

$$\mathrm{e}^{\mathrm{i}k\hat{x}} = \mathrm{e}^{\mathrm{i}kx_0(a+a^\dagger)} = \mathrm{e}^{\mathrm{i}\eta_g(a+a^\dagger)} \tag{3.37}$$

where $a^\dagger$ and a are the creation and annihilation operators respectively, and we have substituted the Lamb Dicke parameter of the ground state, $\eta_g = kx_0 = \sqrt{\omega_R/\omega_g}$ where $\hbar\omega_R$ is the recoil energy from the emission of a photon. By expressing the displacement operator as such, we can use the results of Cahill and Glauber [104] for a harmonic oscillator in which they calculate the matrix elements for the displacement operator $D(\xi) = \mathrm{e}^{(\xi a^\dagger - \xi^* a)}$. After substituting $\mathrm{i}\eta_g$ for ξ, the solutions to the matrix elements are given by

$$\langle m|D(\mathrm{i}\eta_g)|n\rangle = (n!/m!)^{1/2}(\mathrm{i}\eta_g)^{m-n}\mathrm{e}^{-\eta^2/2}L_n^{(m-n)}(\eta_g^2), \tag{3.38}$$

where n and m are the integer values of the oscillator levels, and L_n is the generalized Laguerre polynomial. This expression gives correct numbers for $m > n$ but goes wrong numerically in Mathematica, if $m < n$ and $n - m$ gets large. In that case, we can use the symmetry $\langle m|D(\mathrm{i}\eta_g)|n\rangle = \langle n|D(\mathrm{i}\eta_g)|m\rangle$ to remove this issue from the calculation.

To obtain tractable expressions for the squeezing operator, S_{mi}, we can use the results on squeezed number states from Albano et al. [105]. The states in the excited level QHO are spatially compressed by a ratio $\beta = \eta_e/\eta_g = \sqrt{\omega_g/\omega_e}$, such that $\beta < 1$ when the upper trap is the deeper one. The Franck-Condon overlaps for different Fock states can be calculated with the squeezing operator $S(r)$,

$$S(r) = \exp\left[\frac{r}{2}\left(\hat{a}^2 - (\hat{a}^\dagger)^2\right)\right]. \tag{3.39}$$

where $r = -\ln\beta$. The squeezing operator defined here is in fact a Bogoliubov transformation:

$$S\hat{a}S^\dagger = \cosh(r)\hat{a} + \sinh(r)\hat{a}^\dagger. \tag{3.40}$$

Using this transformation on the position or momentum operator gives

$$\begin{aligned} S\hat{x}S^\dagger &= \mathrm{e}^{-r}\hat{x}, \\ S\hat{p}S^\dagger &= \mathrm{e}^{r}\hat{p}, \end{aligned} \tag{3.41}$$

which shows how the squeezing operator acts as mechanical squeezing of the trap to a stiffer one in position and a spread in momentum space consistent with a squeezed state picture. We can rewrite the first half of the split integral, S_{mi} as

$$S_{mi} = \langle m_e|i_g\rangle = \langle m_g|S(r)|i_g\rangle \equiv \langle n|m,r\rangle, \tag{3.42}$$

allowing us to use the solution outlined in [105],

$$\langle n|m,r\rangle = \frac{(m!n!)^{1/2}}{\cosh(r)^{(m+n+1)/2}} \times \sum_k^{\min(m,n)} \left(\frac{\sinh(r)}{2}\right)^{(m+n-2k)/2} \frac{(-1)^{(n-k)/2}}{k!\,\frac{(m-k)!}{2}\,\frac{(n-k)!}{2}} \tag{3.43}$$

$$k = \begin{cases} 0,2,4,6\ \ldots & n,m \text{ even} \\ 1,3,5,7\ \ldots & n,m \text{ odd}, \end{cases}$$

to extract the required matrix elements for the calculation. With this we have the two terms required to solve Eqn. (3.35).

To evaluate the cooling performance under different parameters, we can now use the Lindblad master equation, Eqn. (3.30) with $\Gamma_d = \Gamma_{mn}$. For this simple simulation we neglect the laser noise super operator.

3.3.2 Results

To analyse the performance of cooling we can integrate the Lindblad master equation out to different times. We choose a single motional level of the ground state as the starting condition, v_i, and set a maximum number of motional levels, v_{max}, to be included along with the parameters r, η_g, ω_g, Δ, Ω, and U_g. We present the results for such a calculation in Fig. 3.15, where we use the parameters $v_i = 15$, $v_{\text{max}} = 30$, $r = 0.054$, $\eta_g = 0.326$, $\omega_g = 2\pi \times 45$ kHz, $\Delta = -2\pi \times 710$ kHz, $\Omega = 2\pi \times 30$ kHz, and $U_g = 2\pi \times 2.8$ MHz and calculate the populations for 125 μs steps. We plot the population of each of the QHO levels of both the excited and ground states in Fig. 3.15(a), where we have highlighted the most interesting levels. After a few milliseconds of cooling, we see that the initial state of 16_g is no longer populated and there is only a significant population remaining in 3 levels, the lowest motional level of the ground state (0_g), excited state (0_e), and first excited motional level of the ground state (1_g). The sum of 0_g and 0_e give us the true motional ground state population of $\sim 95.1\%$ as the 0_e population will decay with high likelihood to 0_g after the cooling laser is switched off. The only other state with a significant population is 1_g where $\sim 3.5\%$ remains. This shows that an atom in the tweezer can be cooled in a few milliseconds down to the motional ground state

To simplify the results, we can look at the average motional level, $\bar{n}$, of the atom, as shown in Fig. 3.15(b), where the average motional level vs time under the same conditions is plotted. This shows the atom is cooled to near the motional ground state in approximately 3 ms, however we note that the time it takes for the atom to be cooled is related to the initial state/temperature of the atom, but the initial cooling rate of approximately 10 quanta/ms remains fairly constant with fixed conditions independent of initial state. This simulation shows the great potential performance of the cooling method and can be used for final optimizations, especially when attempting to reduce

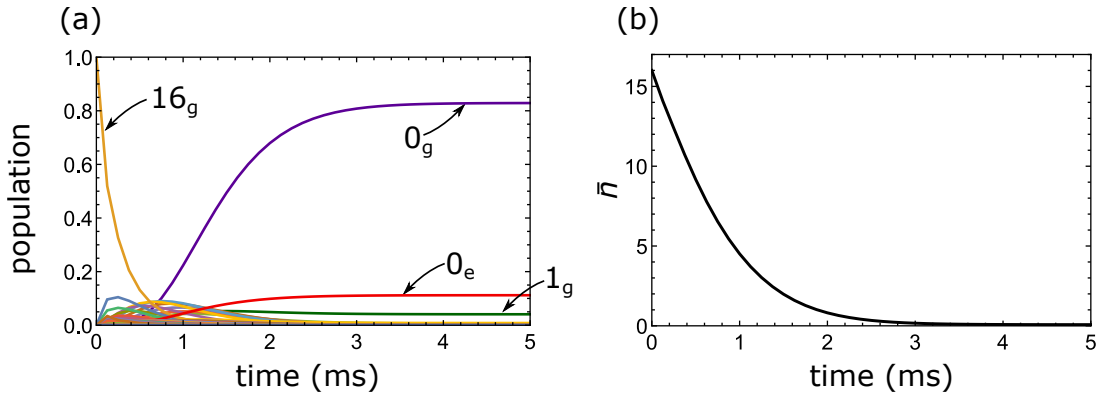

FIGURE 3.15: Time evolution of attractive Sisyphus cooling. We evaluate the Lindblad master equation using the parameters $v_i = 16$, $v_{\max} = 20$, $r = 0.0532$, $\eta_g = 0.333$, $\omega_g = 2\pi \times 43$ kHz, $\Delta = -2\pi \times 700$ kHz, $\Omega = 2\pi \times 30$ kHz, and $U_g = 2\pi \times 2.8$ MHz as outlined in the main text. We calculate the populations of each state at 125 μs steps using the previous result as the initial state. **(a)** The evolution of the state population for each motional level. Since there are a total of 40 levels considered in the calculation (20 ground and 20 excited QHO levels), we label the four most relevant states in place of a legend. States are labelled with their QHO level and subscript related to which internal state the atom is in (g $\equiv {}^1S_0$ and e $\equiv {}^3P_1$). Under these conditions we find a ground state fraction of $\sim 94\%$. **(b)** Evolution of the average motional level, $\bar{n}$, of the atom under the same conditions. We see the atom is cooled from the 16th motional level to the near motional ground level in approximatly 3 ms.

cooling timescales in our system. However, the simulation takes a significant amount of time to calculate and instead a more efficient method can be used for optimization.

As an alternative to the system evolution under the Hamiltonian, we can instead solve for the steady-state populations of each state. Since after a few milliseconds the state populations are already constant, we can consider the steady-state solutions of the Lindblad master equation setting $\dot{\rho}(t) = 0$. We can then plot the average motional level after cooling to steady-state and use this as a faster method for determining final parameters. As examples of such optimizations, we present in Fig. 3.16 the steady-state populations for varying the detuning (Δ), Rabi frequency (Ω), ground state trap frequency (ω_g).In addition Fig. 3.16(d) shows the pop of all motional levels under the optimal conditions mentioned above.

In Fig. 3.16(a), we show the average motional level of the atom versus the detuning. The vertical dashed line indicates the calculated Stark shifted resonance of the transition from 0_g to 0_e for the given trap depth. We find the best cooling happens for a detuning of -690 to -750 kHz where a value of $\bar{n} < 0.3$ is obtained. This range includes the detunings related to the first (-709 kHz) and second (-753 kHz) red motional sidebands. This is consistent with the explanation that in the quantum picture Sisyphus cooling and sideband cooling can be seen as the same cooling mechanism. As the cooling laser is even further red detuned (left of the plot), we see that the cooling performance decreases. As the atom is cooled, there are no longer higher order motional transitions that can take place. This leaves the laser far detuned from the low motional sidebands, effectively decreasing the scattering rate of the cooling laser as it becomes far off resonant in comparison to the transition linewidth. This is also why we choose to modulate the laser in order to maximise fluorescence from the $^1S_0$-$^3P_1$ transition during the imaging process as explained in Chapter 2.

In the next plot, Fig. 3.16(b), we present the average motional level versus the Rabi frequency of the cooling laser. The two different data sets show the performance at two different detunings, -690 kHz and -740 kHz, related to the range defined by the detuning scan. We see that in both cases as the intensity of the cooling laser is decreased, the average motional level also decreases. More specifically, we see that for Rabi frequencies below 75 kHz, the average motional level is $\bar{n} \leq 0.5$. In the shallow tweezers considered throughout this section we see that the cooling saturates at low intensities and similar performance is achieved over a range of Rabi frequencies. At higher trap depths (not shown here), we see that an optimal intensity exists, and as

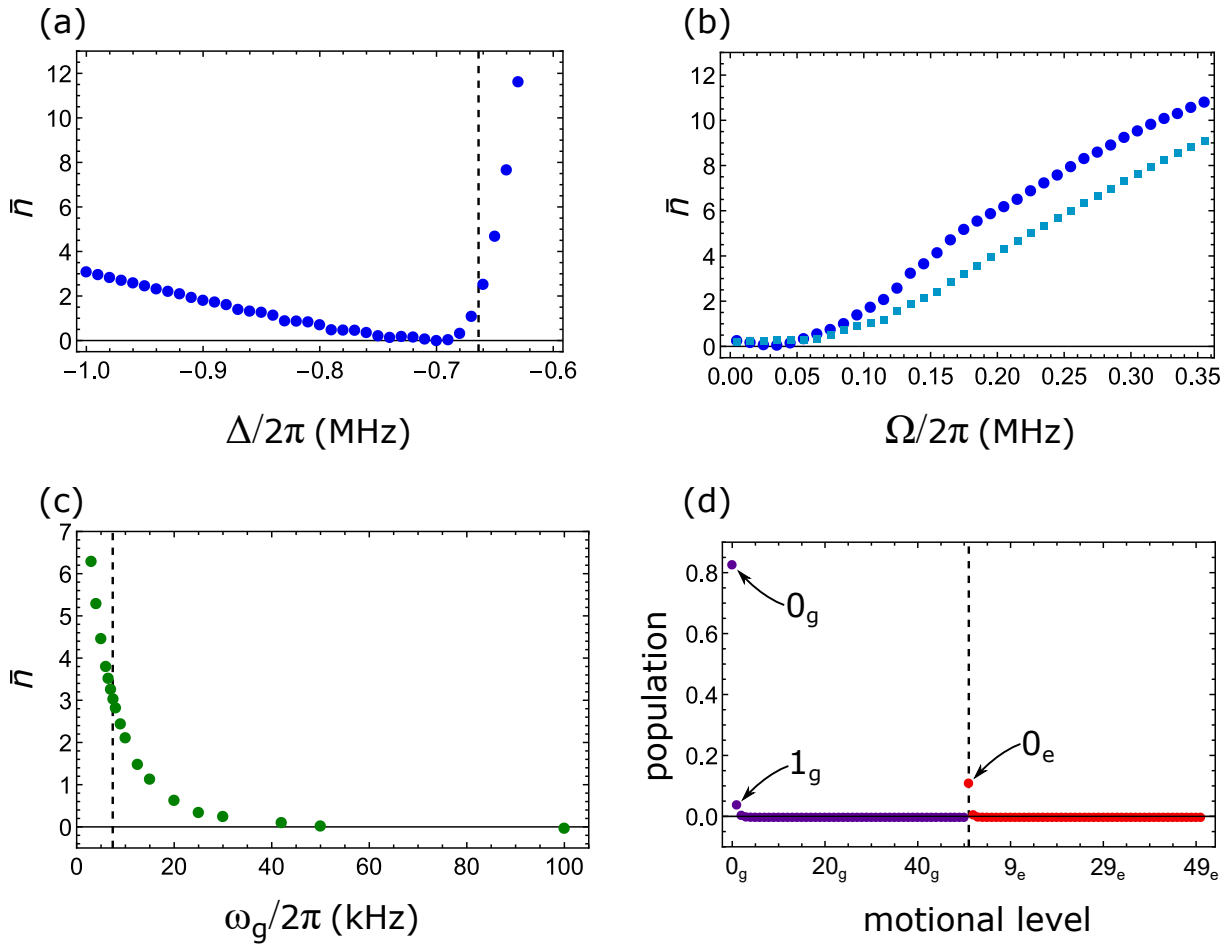

FIGURE 3.16: Steady state results of the Lindblad master equation for **(a)** detuning, **(b)** Rabi frequency, and **(c)** ground state trap frequency. All other parameters are the same as in Fig. 3.15 except we use $v_{\max} = 30$ ($r = 0.0532$, $\eta_g = 0.333$, $\omega_g = 2\pi \times 43$ kHz, $\Delta = -2\pi \times 700$ kHz, $\Omega = 2\pi \times 30$ kHz, and $U_g = 2\pi \times 2.8$ MHz). **(b)** We have included two different detunings in this plot, $\Delta = -2\pi \times 690$ kHz (blue circles) and $\Delta = -2\pi \times 740$ kHz (teal squares). **(c)** Here both ω_g and η_g are varied since $\eta_g = \sqrt{\omega_R/\omega_g}$. The veritcal dashed line shows the point where $\omega_g = \Gamma_{^3P_1}$. **(d)** For completeness, we include the steady state solution of all states under the optimized conditions used in Fig. 3.15, where we have increased the number of harmonic oscillator levels to 50. The results are the same as those of the evolution after 5 ms, confirming that the 20 QHO levels used in the evolution calculation were sufficient.

the intensity is further decreased the cooling performance again deteriorates related to inadequate power broadening of the transition in comparison to the spacing between motional levels.

In the experiment, we observe a minimal trap depth for high fidelity imaging of $U_g = 2.8$ MHz, see Chapter 2. We relate this minimum to the point where the Sisyphus cooling is no longer able to compensate for heating in the axial direction. At shallower trap depths, the excited state *axial* trap frequency is less than the natural linewidth of the transition. In the classical picture of the steeper hill for the excited state potential, this trap depth is where the atom is no longer more likely to decay away from the center of the trap, which reduces the energy lost per cooling photon absorbed [67].

To better understand the effect of the trap frequency on the cooling performance we calculate the average motional level for different trap frequencies while keeping the trap depth fixed as shown in Fig. 3.16. At trap frequencies comparable to our *radial* trap frequency and higher we see great cooling performance that asymptotically approaches $\bar{n} = 0$ as the trap frequency increases. Although there are still improvements to the cooling performance as we go to a 30 kHz trap frequency, the rate of improvement for higher frequencies decreases significantly. For lower trap frequencies we see that the cooling performance gets worse as more motional sidebands remain after cooling. The vertical dashed line shows the point where $\omega_g = \Gamma_{^3P_1}$. We see that as we approach this value, and go to even lower trap frequencies, the rate of cooling degradation accelerates significantly, consistent with our simple picture. This also highlights how methods that use a more spherically symmetric trap, or smaller waists can still have high quality cooling performance in even shallower traps [36, 44, 56].

Finally, we plot the steady-state solution of the Lindblad master equation under optimal conditions in Fig. 3.16(d). These results reproduce the populations of all states in Fig. 3.15(a) at times after about 4 milliseconds. This also shows that all motional states greater than one for both the ground and excited states are not populated with any significant fraction. To summarize the results, we find the lowest temperature for a detuning of 1-2 motional sidebands red of the Stark shifted resonance, at an intensity $\Omega \leq \omega_g$, and a trap frequency $\omega_g \gg \Gamma_{^3P_1}$.

The current calculation already shows good agreement to the results seen in our experiment, see Chapter 2. We can nicely estimate cooling times and experimental parameters such as intensity and detuning for the cooling laser within easily scanned ranges. The calculation even gives nice qualitative results supporting the minimum

trap depth that we measure in the experiment. However, the calculation could of course be improved with some additions outlined here. We could add the true 3D potential of the tweezer created from the Gaussian focus of the beam. This will give us more information on how well a single beam from the radial direction cools the atom in all directions. The non-magic trapping present in the Sisyphus cooling scheme presented here causes the harmonic oscillator states of $|e\rangle$ and $|g\rangle$ to be non-orthogonal, for both the radial and axial directions. Extending the calculation to 3D would thus provide more direct information on the axial cooling performance. Additionally, by considering a 3D trap, we could manipulate the angle between the cooling beam and the radial plane of the tweezer to understand if this helps improve cooling in the axial direction. We could also examine how multiple cooling frequencies or even frequency sweeps could help to improve our cooling and more importantly our narrow-linewidth imaging process (Chapter 2). Finally, we could also include the Lindblad super operator for dephasing from laser noise in Eqn. (3.31). This would be a valuable addition, since we see the effect of laser noise on the cooling process already, see Chapter 2.

3.4 Qudits with strontium

The following subsection is related to the publication [41].

In this section we describe a proposed implementation of qudits using ^{87}Sr. While most current experimental efforts focus on the use of qubits, neutral atoms are a natural platform for qudits and we specifically focus on the example of fermionic strontium, ^{87}Sr [29, 68, 106]. The reason is that it possesses a nuclear spin $I = 9/2$ that is decoupled from the electronic spin in the $^1S_0$ ground state. Consequently this state features $d_{\max} = 2I+1 = 10$ hyperfine sublevels, which are relatively insensitive to electric and magnetic field fluctuations. Moreover, by using strontium, one can make use of the long-lived excited states from the ^3P_J manifold, which has been exploited in a recent experiment to create a Bell state with fidelity reaching 99% [57].

We present a full stack approach from algorithm to implementation in [41]. We study the correlation clustering problem using the quantum approximate optimization algorithm (QAOA) and qudits, which constitute a natural platform for such non-binary problems. Specifically, we consider a neutral atom quantum computer including Hamiltonian formulation of the algorithm, analysis of its performance, identification of a suitable level structure for ^{87}Sr and specific gate design. We show the qudit

implementation is superior to the qubit encoding as quantified by the gate count. The majority of this large collaborative project falls beyond the scope of this thesis, but we will briefly mention the main ingredients before proceeding with the single qudit formulation that will be the focus of this section.

In QAOA, some combinatorial optimization problem is encoded into a cost Hamiltonian H_C, a mixing Hamiltonian H_M, and some initial quantum state $|\psi_0\rangle$ [107]. The cost Hamiltonian encodes the cost function to be optimized meaning that it must act diagonally on the n-qudit computational basis states and is related to the two-qudit operations, which in our case would be induced through Rydberg excitation. The mixer Hamiltonian is usually taken to be the transverse field Hamiltonian $H_M = \sum_j \Sigma_j^x$, where Σ_j^x is the Pauli X operator generalized to spin 9/2 acting on the jth qudit. The mixer acts on the single qudit subspace and defines the connectivity, which determines how many unique states of the qudit are coupled to each other. The initial quantum state $|\psi_0\rangle$ is usually equivalent to a uniform superposition of all computational states in the single-qudit Hilbert space. QAOA creates a parameterized quantum state by alternating between the application of $\beta_k H_M$ and $\gamma_k H_C$ starting from the initial state $|\psi_0\rangle$ for a predetermined number of rounds (indicated by subscript k), where β_k and γ_k are the optimization parameters. The state is then measured in the computational basis to return a candidate solution. The cost function can then be estimated through the repetition of state preparation and measurement [107]. Here we will focus on the formulation and characterization of the single qudit mixer, H_M, in ^{87}Sr.

For completeness, we now briefly mention some details of the correlation clustering problem. Generally, the objective of clustering problems is to group elements into a family of subsets, named clusters, such that the elements within a cluster are more similar to one another than elements in different clusters. In case of the correlation clustering problem, we would like to cluster based only on given pairwise relations and without specifying the number of clusters in advance based only on pairwise relations. The problem was introduced by Bansal et al. [108] to the theoretical computer science community and has applications amongst others in social psychology, statistical mechanics and biological networks.

Instances of correlation clustering problems are commonly represented as a graph problem, where the nodes are the elements to be grouped in clusters and edge weights represent similarities between these elements. Correlation clustering is then formally defined in the following way: let $G(V, E)$ be an undirected graph, where V, E denotes

the sets of nodes (also known as vertices) and edges, respectively. Let N be the total number of nodes, i.e. $N = |V|$. Every edge $(u, v) \in E$, where $u,\ v \in V$ are the vertices connected by the edge, is labelled either '+' or '−', depending on whether the elements are similar or dissimilar, respectively. For more details, see [41].

In this section we will outline a series of steps needed to formulate the desired single qudit mixer. First we will briefly present the mixer Hamiltonian that we need for the problem. Second, we will present the chosen coupling scheme for implementing the mixer, and outline the determination of the parameters of the system, such as transition dipole moments (TDMs), maximum Rabi frequencies, and magnetic field strengths. Third, we continue on to a more specific example of results for a $d = 4$ qudit. Fourth, we present investigations of the initial state preparation and error sources that apply to any dimension qudit quantifying the results such that they are easily compared with the fidelity of other *qubit* schemes. Fifth, we will conclude with a discussion of the experimental implementation of this coupling scheme.

3.4.1 Mixer Hamiltonian

In short, we wish to compose a coupling Hamiltonian that can mix over the single qudit subspace. Such a Hamiltonian was given in the work by Hadfield et al. [107], where the following single-qudit mixing Hamiltonian is proposed

$$h_M(r) = \sum_{i=1}^{r} \left((\Sigma^x)^i + (\Sigma^{x\dagger})^i \right), \tag{3.44}$$

where $r \in \{1, \ldots, d-1\}$, a parameter determining the connectivity of the mixer and Σ^x is the generalized Pauli X-operator, given by

$$\Sigma^x = \begin{pmatrix} 0 & & & 1 \\ 1 & & & \\ & \ddots & & \\ & & 1 & 0 \end{pmatrix}. \tag{3.45}$$

This defines how many qudit states are coupled, acting similar to a qudit shift register. One observes that for $r = 1$, the single-qudit mixer is equal to

$$h_M(r=1) = \begin{pmatrix} 0 & 1 & & & 1 \\ 1 & & \ddots & & \\ & \ddots & & \ddots & \\ & & \ddots & & 1 \\ 1 & & & 1 & 0 \end{pmatrix} \tag{3.46}$$

such that every level is connected to its nearest neighbours, including periodic boundary conditions. The full mixing Hamiltonian is then

$$H_M = \sum_{u \in V} h_M, \tag{3.47}$$

where u specifies a specific qudit from the set of all qudits V, i.e., all nodes of the graph in the correlation clustering problem. We can pick any value of $r \in \{1, \ldots, d-1\}$, where the special cases at the boundary are called the single-qudit ring mixer for $r = 1$ and the fully-connected mixer for $r = d-1$. In the following subsections, we will focus specifically on the $r = 1$ case.

3.4.2 Single qudit coupling scheme for *r = 1* mixer

The relevant level scheme of $^{87}\mathrm{Sr}$ is sketched in Fig. 3.17(a). As stated above, the ground state manifold, which we denote with a slight abuse of notation as $|\mathbb{S}\rangle \equiv |^1S_0,\ F = \frac{9}{2}\rangle$, consists of $d = 2F + 1 = 10$ m_F-sublevels, $m_F \in \{-9/2, \ldots, 9/2\}$. We also denote $|\mathbb{P}\rangle \equiv |^3P_2, F = \frac{11}{2}\rangle$ the excited state manifold, which we will use to implement the single and two qudit gates [40]. Here we choose the $^3P_2$ manifold in particular due to its long lifetime, which allows for a resonant excitation to the Rydberg state, and resonant qudit excitations as described below. In our QAOA example, Rydberg excitations are used for the implementation of the cost Hamiltonian. These two qudit operations will not be discussed here, but details can be found in [41].

The choice of the $\mathbb{P}$-manifold is motivated by the fact that, unlike the other possible choices such as $|^3P_2, F = \frac{7}{2}\rangle$ or $|^3P_2, F = \frac{9}{2}\rangle$, it possesses a *magic* wavelength $\lambda_{\text{tweezer}} \approx$

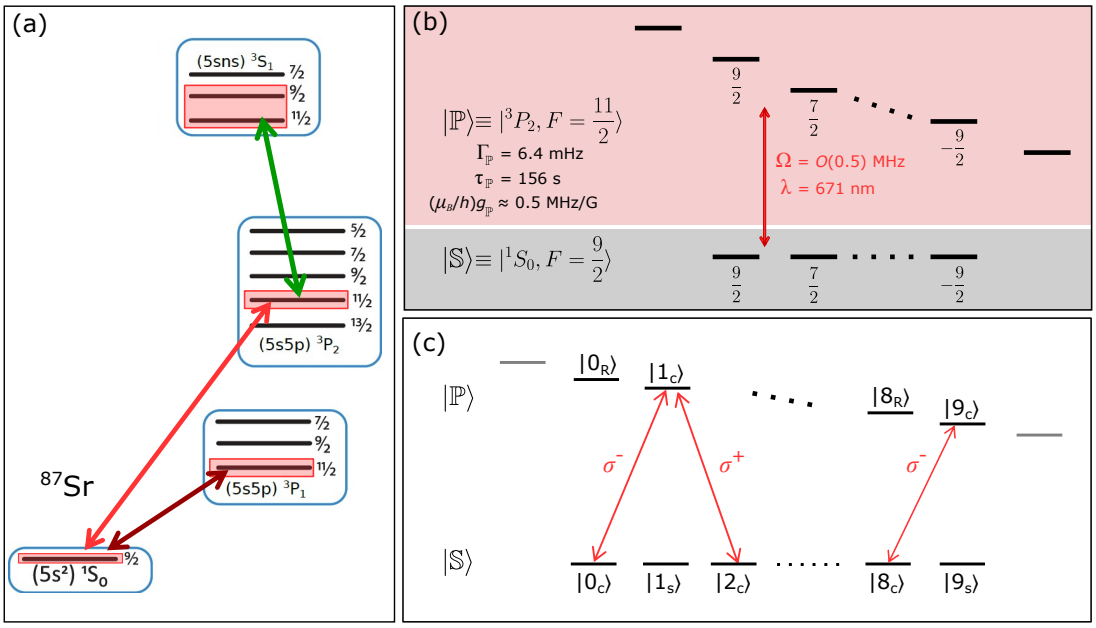

FIGURE 3.17: **(a)** Relevant level scheme of ^{87}Sr. The proposed qudit states are realized by the ground state manifold $|\mathbb{S}\rangle = |^1S_0, F = 9/2\rangle$. The two-qudit gates are realized by exciting the states from $|\mathbb{S}\rangle$ to a Rydberg manifold $|\mathbb{R}y\rangle = |\mathrm{n}^3S_1\rangle$ through an intermediate state from the $|\mathbb{P}\rangle = |^3P_2, F = 11/2\rangle$ manifold (red and green arrows). The dark red arrow indicates the transition to the $|^3P_1, F = 11/2\rangle$ manifold used for measurement of the quantum state. **(b)** Parameters of the manifolds $|\mathbb{S}\rangle, |\mathbb{P}\rangle$ relevant for the single qudit operations: transition wavelengths λ, typical Rabi frequencies Ω, decay rates Γ and the associated lifetimes τ from the excited $|\mathbb{P}\rangle$ manifold and the Landé g-factor quantifying the Zeeman splitting of the magnetic sublevels. The values of $\Gamma_{\mathbb{P}}, \tau_{\mathbb{P}}$ are taken from [109]. The $\mathbb{P}$-manifold states are used to realize the single qudit gates such as the mixing unitaries, which are shown in **(c)** for $r = 1$. We have included state labeling for computational and storage states using the subscripts c and s respectively. As explained in the main text, these storage states can be used to extend the time before a tweezer photon is scattered, an effect that can cause decoherence. Two qudit operations, such as the implementation of the cost Hamiltonian, require computational states of $|\mathbb{S}\rangle$ to be transferred to the same m_F level of $|\mathbb{P}\rangle$. These states have been labelled with the subscript R for Rydberg.

$881\,\mathrm{nm}$, for which the transition frequencies $|\mathbb{S}, m_F\rangle - |\mathbb{P}, m_{F'}\rangle$ are approximately independent of the intensity of the tweezer light for all m_F and $m_{F'}$ sublevels, which ensures a position independent addressing frequency of the individual sublevels as discussed in Section 3.1 (Fig. 3.5).

The actual addressing relies on the Zeeman splitting of the $\mathbb{P}$-manifold and has been experimentally demonstrated using ^{173}Yb [39]. Applying moderate values of the magnetic field B results in linear Zeeman splitting with an energy shift between the adjacent $m_{F'}$ sublevels of $\mu_B g B/h$, where μ_B and h is the Bohr magneton and the Planck constant respectively and g is the Landé g-factor. The Zeeman shift in the m_F sublevels of $|\mathbb{S}\rangle$ comes purely from the nuclear Landé g factor, g_I, whereas the shift in the m_F sublevels of $|\mathbb{P}\rangle$ comes primarily from the spin-orbital Landé g factor, g_J. Since $g_J \gg g_I$, the frequency of the laser needed for each qudit transition is unique, reducing unwanted couplings and off resonant scattering in the system. We calculate the Zeeman shift for the $|\mathbb{P}\rangle$ state following the procedure outlined above in Section 3.1. For the $\mathbb{P}$-manifold, $g \approx 0.36$ and $\mu_B g/h \approx 0.5\,\mathrm{MHz/G}$ [92]. This provides a splitting of $\approx 50\,\mathrm{MHz}$ between adjacent $m_{F'}$ sublevels for a magnetic field amplitude of $100\,\mathrm{G}$, allowing for both resonant and off-resonant addressing as discussed in [41]. Here we will focus specifically on the resonant $r = 1$ case. We have summarized the relevant parameters in Fig. 3.17(b).

To create the $r = 1$ single qudit mixer, we consider resonant excitation between adjacent m_F sublevels of the $|\mathbb{S}\rangle$ and $|\mathbb{P}\rangle$ manifolds of ^{87}Sr, see Fig. 3.17(c). The excited state $|\mathbb{P}\rangle$, used for every other qudit state, is a metastable state with a minutes long lifetime in the absence of the trapping light, however, this lifetime will be limited by scattering of the trap light from the $|\mathbb{P}\rangle$ - $^3S_1$ transition. This will occur at a rate of 1 Hz and is the limiting time scale for a sequence of gates. This time scale can be further increased by transferring the $|\mathbb{P}\rangle$ states down to the $|\mathbb{S}\rangle$ of the same m_F in between operations, which is limited by scattering of tweezer photons off the $|\mathbb{S}\rangle$ - $^1P_1$ transition and by background gas collisions at a rate of < 0.1 Hz. For example, phase coherence times well over 10 seconds have been demonstrated in nuclear spin encoded qubits of ^{87}Sr [46]. This coupling scheme adds two additional types of pulse sequences to a gate sequence. Atoms can be moved to a storage state by transferring the $|\mathbb{P}\rangle$ computational states down to their respective $|\mathbb{S}\rangle$ sublevels. For two qubit operations, the $|\mathbb{S}\rangle$ computational states can be transferred to the $|\mathbb{P}\rangle$ sublevels of the same m_F. We have added additional state labels to Fig. 3.17(c) to clarify the difference between these states.

The unique addressing frequencies allow for balancing the strength of the different Rabi frequencies in the system by using unique powers for each coupling laser. To estimate the power needed for each beam, we must calculate the TDMs for the different transitions involved at the magnetic field that will be used. At zero field,

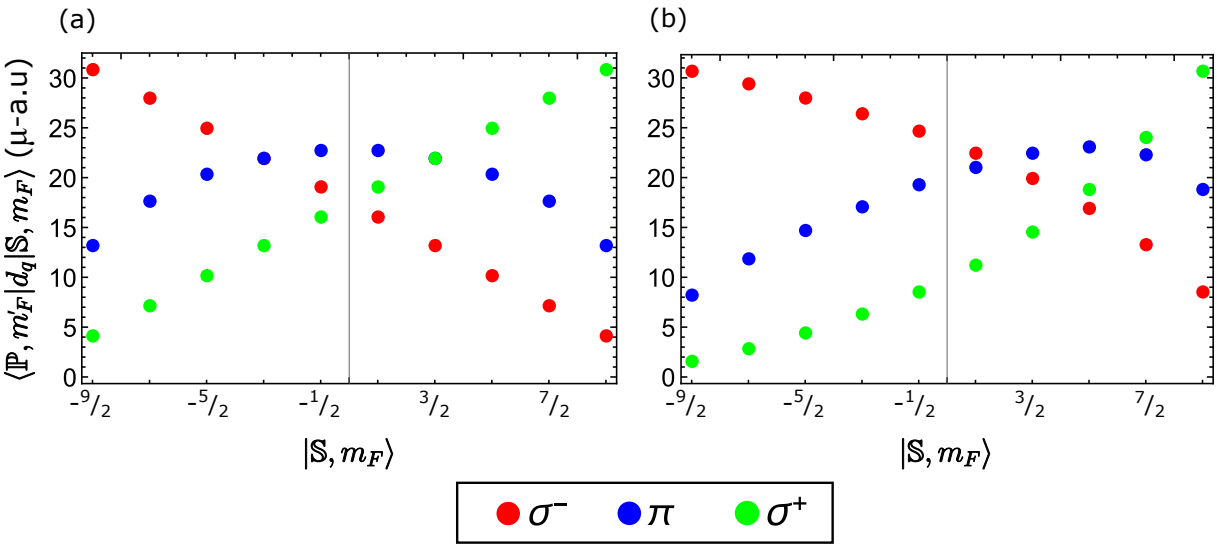

FIGURE 3.18: Transition dipole matrix elements from $|\mathbb{S}\rangle$ to $|\mathbb{P}\rangle$. The horizontal axis is the $|\mathbb{S}, m_F\rangle$ state of the transition. The values of the TDMs are presented in μ-a.u. and results are shown for σ^- (red), π (blue), and σ^+ (green) at both **(a)** 0 G and **(b)** 160 G. We chose the value of 160 G because this is the near maximum field at which the separation between hyperfine manifolds is still larger than the separation between m_F sublevels of the same manifold. We see that a strong field also helps to balance the TDMs for positive m_F sublevels while increasing the variation for negative m_F sublevels. Because of this a smaller field might be favorable for a $d = 10$ qudit, whereas a large (160 G) field may be more favorable for smaller values of d.

the TDMs are proportional to the Clebsch-Gordan coefficient for the transition. However, as a magnetic field is applied, F is no longer a good quantum number causing non-negligible contributions from the other $^3P_2$ F-manifolds to be present [87]. We calculate the TDMs for the $|\mathbb{S}\rangle$ - $|\mathbb{P}\rangle$ transitions including contributions from the hyperfine $E1$ transition levels, $F = 11/2$, $9/2$, and $7/2$, by determining the eigenvectors of the full Zeeman Hamiltonian of $^3P_2$, see Eqn. (3.20), and using the decay rates from [109][5]. The results for 0 G and 160 G can be seen in Fig. 3.18. The value of 160 G is the maximum field strength before the separation between neighbouring F-manifolds becomes insignificant in comparison to the detuning between m_F sublevels of the same manifold. It is worth noting that in this scheme the largest qudit possible might be limited to a dimension of $d < 10$ because of the imbalance of the TDMs. This effect can be slightly mitigated by using smaller Rabi frequencies and magnetic fields (see Fig. 3.18, the most even couplings over all 10 sublevels is at 0 G). However, reducing the speed of the qudit couplings and magnetic field strength can cause more adverse effects from different decoherence sources of the system, such as unwanted couplings, laser dephasing and finite excited state lifetime, making it hard to find reasonable parameters for a full $d = 10$ qudit. In this case the mixers could be implemented in a step-wise fashion by means of the Givens rotations [111].

To consider the speed limit with which we can drive the transition before unwanted decoherence from the coupling laser, we must consider a few sources of decoherence. Mainly, we must consider the off-resonant scattering of the coupling laser off of the broadest transitions of the qudit states of interest. For $|\mathbb{S}\rangle$ this is the 30 MHz broad $|\mathbb{S}\rangle$ - $^1P_1$ transition at 461 nm, and for $|\mathbb{P}\rangle$ this is the 7 MHz broad $|\mathbb{P}\rangle$ - $^3S_1$ transition at 707 nm. The latter transition from $|\mathbb{P}\rangle$ is the more dominant decoherence mechanism with an off resonant scattering rate that is more than an order of magnitude larger. For a Rabi Frequency of $\Omega = 2\pi \times 500$ kHz between adjacent states and considering a $d = 4$ qudit, the off resonant scattering from the $|\mathbb{P}\rangle$ - $^3S_1$ transition is approximately $\Gamma_{\text{sc}} = 22$ Hz or a time of $\tau_{\text{sc}} = 45.5$ ms before a dephasing photon is likely to have been scattered off the unwanted transition. Taking the ratio $\Gamma_{\text{sc}}/\Omega$ allows for us to estimate the infidelity from such events to be on the order of 8×10^{-5} per 2π-pulse (between adjacent states). This should allow for a high number of operations to be performed

[5]The decay rate can be converted to the reduced transition dipole moment using the expression $a_0 e\langle J'\|d\|J\rangle = \sqrt{3\pi\epsilon_0\hbar c\Gamma/\omega^3}$ [87, 110]. The TDMs are calculated with Eqn. (3.7), summing over the different F contributions.

before such a decoherence event occurs. A similar analysis can be done for $\mathbb{S}$ giving an order of magnitude lower infidelity. An additional consideration is the off-resonant scattering of the coupling laser from a different $|\mathbb{S}, m_F\rangle$ - $|\mathbb{P}, m_{F'}\rangle$ transition. We discuss this further in the following subsection using a more explicit example.

Finally, we briefly discuss the implementation of the mixing unitary $U_M(\beta_k) = \exp[-i\beta_k H_M]$ for the $r = 1$ case. We propose to implement the $r = 1$ case as shown in Fig. 3.17(c). Here, the subscript k refers to the size of the time step used in the QAOA computation.

Starting with all qudit states in their $|\mathbb{S}, m_F\rangle$ sublevels i.e., from a uniform superposition over the m_F sublevels of $|\mathbb{S}\rangle$ such that the $|\mathbb{P}\rangle$ computational states are in their respective storage states, we apply the following sequence of pulses:

1. Apply $\lfloor \frac{d}{2} \rfloor$ π-polarized π-pulses on the states $\{1, 3, \ldots, l\}$, $l = 2\lfloor \frac{d}{2} \rfloor - 1$, on the $|\mathbb{S}\rangle - |\mathbb{P}\rangle$ transition, which brings them from $|\mathbb{S}\rangle$ to $|\mathbb{P}\rangle$. Here d ranges from 1 to d and l is the computational qudit states as labeled in Fig. 3.4.5(c).

2. Apply the Rabi frequencies $\Omega_{\ell,\ell+1}$ connecting nearest-neighbour qudit states for time τ_k.

3. Repeat step 1 to bring the $\lfloor \frac{d}{2} \rfloor$ levels from $|\mathbb{P}\rangle$ back to $|\mathbb{S}\rangle$. Or

4. Perform step 1 on the states $\{0, 2, \ldots, l\}$ to bring the computational states into their respective two-qudit computational states in preparation for application of a cost Hamiltonian. See [41] for further details.

In Fig. 3.17(c), the choice of couplings is depicted by the red arrows and the coupling Hamiltonian reads

$$\Omega h_\Omega = \Omega \begin{pmatrix} 0 & c_{0,1} & & \\ c^*_{0,1} & & \ddots & \\ & \ddots & & c_{d-2,d-1} \\ & & c^*_{d-2,d-1} & 0 \end{pmatrix}. \tag{3.48}$$

When the individual Rabi frequencies $\Omega_{\ell,\ell'}$ are adjusted such that $c_{\ell,\ell'=\ell+1} = 1 \ \forall \ell$, $h_\Omega \to h_M$ and the sequence 1-3 corresponds to the mixing unitary U_M, with the mixing parameter $\beta_k = \Omega\tau_k$ where τ_k is the step size of the operation in the QAOA sequence.

One important remark is in order: the mixing Hamiltonian, Eqn. (3.46), implements a "periodic boundary condition" in that it couples the levels 0 and $d-1$ (and similarly for higher r). Such coupling is typically not native to a physical qudit, which instead corresponds to an "open boundary condition" as is apparent from Eqn. (3.48). We discuss the difference between using Eqn. (3.48) in place of Eqn. (3.46) in more detail in [41] where we see that our hardware specific mixer is not expected to result in a significant decrease in performance.

3.4.3 *d*=4 qudit example

To consider a more concrete example, we can examine the qudit coupling for the $r = 1$ and $d = 4$ case. An illustration of the coupling scheme is presented in Fig. 3.19. The coupling lasers alternate between σ^- and σ^+ polarization for couplings from $|\mathbb{S}\rangle$ - $|\mathbb{P}\rangle$ and $|\mathbb{P}\rangle$ - $|\mathbb{S}\rangle$ respectively. We will leave all coupling matrices in the form of $\hat{H}_{\text{tot}}$ (Eqn. (3.29)) instead of the qudit mixer mentioned above.

With only the desired couplings included, the Hamiltonian takes the form of

$$\hat{H}_{\text{tot}} = \frac{\hbar}{2}\begin{pmatrix} 0 & \Omega_{0,1} & 0 & 0 \\ \Omega_{1,0} & -2\Delta_1 & \Omega_{1,4} & 0 \\ 0 & \Omega_{4,1} & -2\Delta_4 & \Omega_{4,5} \\ 0 & 0 & \Omega_{5,4} & -2\Delta_5 \end{pmatrix}, \tag{3.49}$$

for states $|0\rangle = |\mathbb{S}, 9/2\rangle$, $|1\rangle = |\mathbb{P}, 7/2\rangle$, $|2\rangle = |\mathbb{S}, 5/2\rangle$, $|3\rangle = |\mathbb{P}, 3/2\rangle$. However, for proper consideration of all off resonant couplings, decay channels, and laser noise, the Hamiltonian

$$\hat{H}_{\text{tot}} = \frac{\hbar}{2}\begin{pmatrix} 0 & \Omega_{0,1} & 0 & 0 & 0 & 0 & 0 & 0 \\ \Omega_{1,0} & -2\Delta_1 & \Omega_{1,2} & 0 & \Omega_{1,4} & 0 & 0 & 0 \\ 0 & \Omega_{2,1} & -2\Delta_2 & \Omega_{2,3} & 0 & 0 & 0 & 0 \\ 0 & 0 & \Omega_{3,2} & -2\Delta_3 & \Omega_{3,4} & 0 & \Omega_{3,6} & 0 \\ 0 & \Omega_{4,1} & & \Omega_{4,3} & -2\Delta_4 & \Omega_{4,5} & 0 & 0 \\ 0 & 0 & 0 & 0 & \Omega_{5,4} & -2\Delta_5 & \Omega_{5,6} & \Omega_{5,7} \\ 0 & 0 & 0 & \Omega_{6,3} & 0 & \Omega_{6,5} & -2\Delta_6 & 0 \\ 0 & 0 & 0 & 0 & 0 & \Omega_{7,5} & 0 & -2\Delta_7 \end{pmatrix}, \tag{3.50}$$

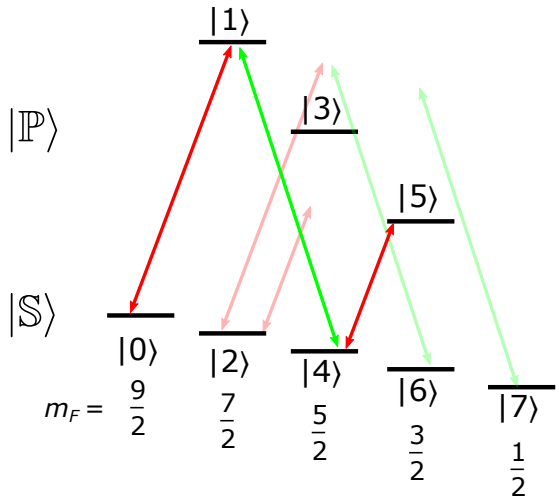

FIGURE 3.19: Coupling scheme for a $d = 4$ qudit with all required coupling lasers present. The states are labelled with both their respective m_F sublevels and state in the 4 level qudit basis where states ($|0\rangle$, $|1\rangle$, $|4\rangle$, $|5\rangle$) compose the computational basis. The m_F labels correspond to vertically aligned sublevels of both $|\mathbb{S}\rangle$ and $|\mathbb{P}\rangle$. σ^- transitions are shown in red and σ^+ transitions are shown in green. the unwanted, but unavoidable, off resonant couplings of each laser are shown as well with less opacity. Zeeman shifts are not to scale.

is needed, where the states $|0\rangle$ to $|7\rangle$ are $|\mathbb{S}, 9/2\rangle$, $|\mathbb{P}, 7/2\rangle$, $|\mathbb{S}, 7/2\rangle$, $|\mathbb{P}, 5/2\rangle$, $|\mathbb{S}, 5/2\rangle$, $|\mathbb{P}, 3/2\rangle$,$|\mathbb{S}, 3/2\rangle$, and $|\mathbb{S}, 1/2\rangle$ respectively. This Hamiltonian shows all allowed couplings in the system. When implementing the desired coupling of Eqn. (3.49), the Rabi frequencies $\Omega_{1,2}, \Omega_{3,4}$, and $\Omega_{5,6}$ can be set to zero with proper choice of polarization while others, $\Omega_{2,3}$, $\Omega_{3,6}$, and $\Omega_{5,7}$,, will still be present with a large detuning caused by the Zeeman shift of the $|\mathbb{P}\rangle$ levels in the presence of a magnetic field. Additionally, with proper tuning of the laser frequencies to resonance, certain detunings can also be set to zero, specifically Δ_1, Δ_4, and Δ_5. Considering equal Rabi frequencies for all desired couplings for Eqn. (3.49) and after setting the proper terms to zero, we can rewrite

Eqn. (3.50) as

$$\hat{H}_{\text{tot}} = \frac{\hbar}{2}\begin{pmatrix} 0 & \Omega & 0 & 0 & 0 & 0 & 0 & 0 \\ \Omega & 0 & 0 & 0 & \Omega & 0 & 0 & 0 \\ 0 & 0 & 0 & \Omega_{2,3} & 0 & 0 & 0 & 0 \\ 0 & 0 & \Omega_{3,2} & -2\Delta_3 & 0 & 0 & \Omega & 0 \\ 0 & \Omega & 0 & 0 & 0 & \Omega & 0 & 0 \\ 0 & 0 & 0 & 0 & \Omega & 0 & 0 & \Omega \\ 0 & 0 & 0 & \Omega & 0 & 0 & 0 & 0 \\ 0 & 0 & 0 & 0 & 0 & \Omega & 0 & -2\Delta_7 \end{pmatrix}, \tag{3.51}$$

giving us the Hamiltonian of the four-level-qudit.

A plot of the evolution under this Hamiltonian using the Lindblad master equation (Eqn. (3.30)) is shown in Fig. 3.20. Rabi frequencies of $\Omega = 2\pi \times 500$ kHz, laser noise of $\Gamma_L = 2\pi \times 100$ Hz, $\Delta_3 = -2\pi \times 20$ MHz and $\Delta_7 = 2\pi \times 40$ MHz (Zeeman shifts induced by $B \approx 40$ G) have been used to create these plots and all others, unless otherwise specified. The only Rabi frequencies that differ from Ω is $\Omega_{2,3}$ ($\Omega_{3,2}$). Instead we set this Rabi frequency to $2.415\,\Omega$ because two beams off resonantly affect this transition as shown in Fig. 3.19. The deviation of this Rabi frequency from two accounts for the different TDMs of each transition[6]. The detunings of these two beams are equal up to a sign (one is +20 MHz and the other is -20 MHz due to Zeeman splitting), so we set the detuning to the blue detuned frequency of the m_F splitting induced by the magnetic field (corresponding to Δ_3= 20 MHz). With these parameters, we have observed coherent oscillations for well over $300\,\mu$s between the four computational states with no population being transferred to the unwanted m_F sublevels outside the computational basis.

To further examine the fidelity of the mixing Hamiltonian, we calculate the fidelity after a 2π-pulse using

$$F \equiv \text{tr}\sqrt{\rho^{1/2}\sigma\rho^{1/2}}, \tag{3.52}$$

where ρ is the density matrix after the evolution of the Lindblad master equation and

[6]At the chosen magnetic field, the ratio of TDMs are $\langle \mathbb{P}, 5/2 \| d_q \| \mathbb{S}, 7/2\rangle / \langle \mathbb{P}, 7/2 \| d_q \| \mathbb{S}, 9/2\rangle = 1.691$ and $\langle \mathbb{P}, 5/2 \| d_q \| \mathbb{S}, 7/2\rangle / \langle \mathbb{P}, 3/2 \| d_q \| \mathbb{S}, 5/2\rangle = 0.724$. The sum of these ratios gives the value $2.415\,\Omega$. A similar method could be used for the off resonant σ^+ beams. However since the TDMs of these transitions are weaker than the transition being addressed, we instead overestimate the error by leaving them at Ω.

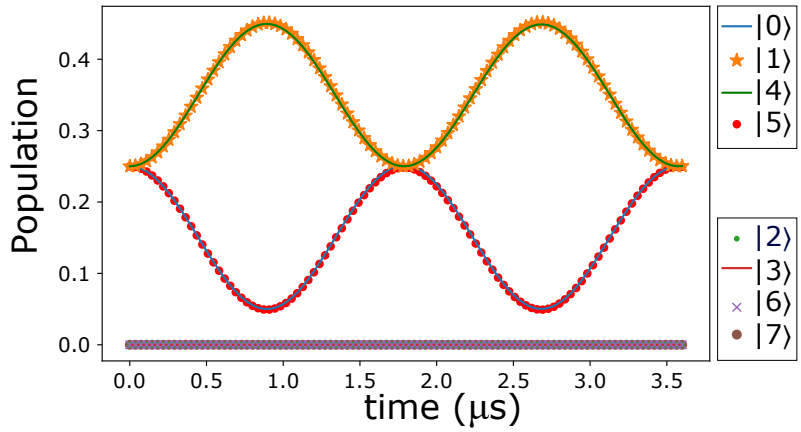

FIGURE 3.20: Evolution of Lindblad master equation for a 4 level qudit using the Hamiltonian in Eqn. (3.51) and the levels outlined in Fig. 3.19. The initial state is a superposition over all four qudit states. We use the parameters $\Omega = 2\pi\times500$ kHz, laser noise of $\Gamma_L = 2\pi\times100$ Hz, $\Delta_3 = 2\pi\times20$ MHz and $\Delta_7 = 2\pi\times40$ MHz to make this plot. We set all Rabi frequencies equal to $\Omega_{l,l'} = \Omega$ except for $\Omega_{2,3}$ ($\Omega_{3,2}$) which is set to 2.415Ω. We observe coherent evolution over several oscillations and no unwanted coupling to states outside the computational basis throughout the evolution. The fidelity after a 2π-rotation is $F = 0.9998$ under these conditions. See text for further details.

σ is the density matrix for an ideal superposition of the four computational states [19]. With the parameters used for Fig. 3.20, we find a fidelity of $F = 0.9998$ after a 2π-pulse (1.795μs). The limiting factor on the fidelity for these parameters is laser noise which, with state of the art technology, can be reduced significantly lower than the $2\pi \times 100$ Hz considered here. In the absence of laser noise we find a fidelity of $F = 0.999993$. We have preformed similar calculations to check the required magnetic field strength and find the 40 G field used here to be sufficient and even with the maximum field of 160 G (see Fig. 3.18), the fidelity on increases by 1.5×10^{-6}.

3.4.4 Initial state preparation, state isolation, and off resonant scattering

A few additional situations must be considered to understand the fidelity of the state preparation and the qudit coupling. The three remaining effects we will consider here are the fidelity of a $\pi-$pulse for the two level case, which quantifies the fidelity in a way comparable to a single qubit rotation, the required field for isolating the individual

m_F sublevels from each other, and the effect of off resonant scattering from the $|\mathbb{P}\rangle$ - $^3S_1$ transition. We note that even more analyses could be done to further understand gate fidelity, such as including polarization purity, laser intensity noise, and magnetic field noise into the calculations, some of which we will also briefly comment on in the following subsection.

To analyse the state preparation fidelity, we consider all the relevant levels of a three state qudit coupling scheme and examine the situation of a single laser driving the $|0\rangle$ to $|1\rangle$ transition, i.e. a qubit like drive scheme, as shown in Fig. 3.21(a). We include the third state to model all possible decay channels. An evolution of the Lindblad master equation is shown in Fig. 3.21(b). We see that a fidelity of well over 99% is preserved even after 10 oscillations (infidelity of 1×10^{-4} per $\pi-$pulse, see inset). For preparing the required superposition we will use a number of fractional $\pi-$pulses where each one achieves the same coherence as the evolution illustrated by this coupling, limiting the need for individual examination. See Section 3.4.5 for further details on the state preparation.

To examine the protection of off resonant scattering from the wrong m_f by the coupling beams, we use the same Hamiltonian as Fig. 3.21, but place half of the initial population into the $|2\rangle$ ($|\mathbb{S}, 7/2\rangle$) state and see if any population is transferred to the $|3\rangle$ ($|\mathbb{P}, 5/2\rangle$) state, see Fig. 3.22. This allows us to determine the magnetic field required to mitigate any depopulation of neighboring m_F sublevels via off resonant coupling. The required magnetic field to keep the fidelity unchanged is approximately ~ 80 G/MHz of Rabi frequency to prevent such scattering events from occurring. We consider only the effect of the coupling laser on the nearest m_F state because subsequent states will be even further detuned by the Zeeman shifts leading to smaller effects.

Finally, we examine the effects of decoherence from off resonant scattering of the $|\mathbb{P}\rangle$ - $^3S_1$ transition using a 3 level Hamiltonian with states $|0\rangle = |\mathbb{S}, 9/2\rangle$, $|1\rangle = |\mathbb{P}, 7/2\rangle$, and $|2\rangle = {}^3S_1$. We calculate the effect of direct off resonant coupling using the laser power of the coupling beams to calculate the Rabi frequency of this transition, and the difference of the $|\mathbb{P}\rangle$ - $^3S_1$ (707 nm) and the $|\mathbb{S}\rangle$ - $|\mathbb{P}\rangle$ (671 nm) transitions as the detuning. We calculate by considering all off resonant scattering rates of this transition as a loss channel out of $\mathbb{P}$. The effect is negligible (1×10^{-6}) on the time scales of interest with the chosen parameters.

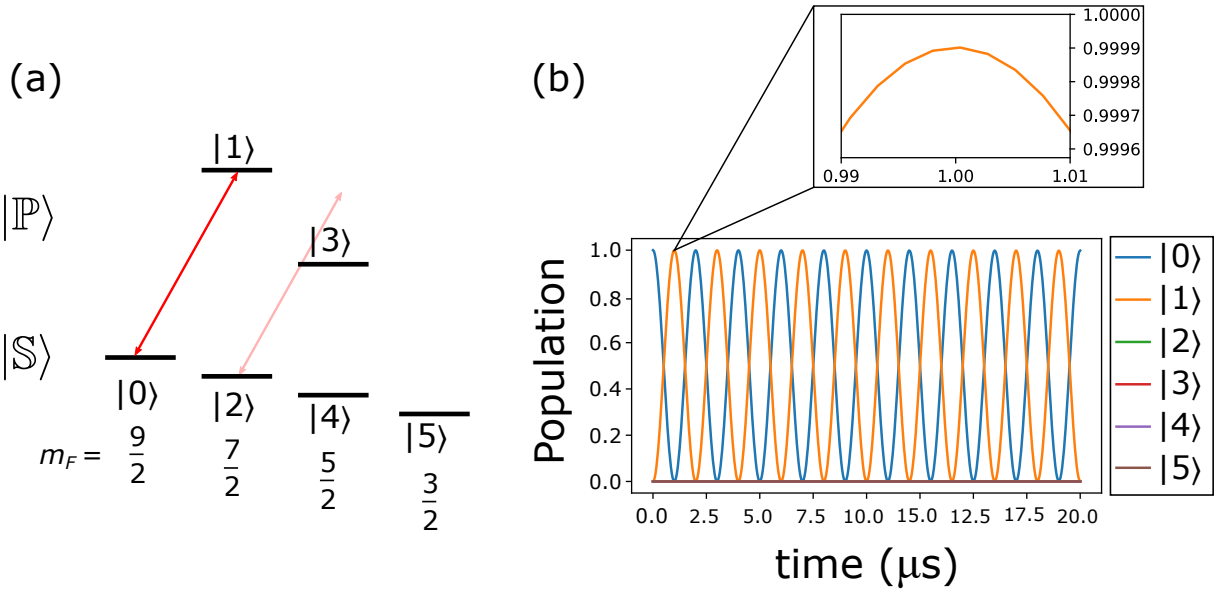

FIGURE 3.21: **(a)** Level scheme for a $d = 3$ qudit. The states are labelled with both their respective m_F sublevels and state number in the 3 level qudit basis. The m_F labels correspond to vertically aligned sublevels of both $|\mathbb{S}\rangle$ and $|\mathbb{P}\rangle$. We start with the atom in the $|0\rangle$ state and apply a single coupling laser between states $|0\rangle$ and $|1\rangle$ to characterize the evolution of this qubit like system for state preparation. **(b)** Evolution of the Lindblad master equation for the system described in (a). We use this to evaluate the performance of the fractional pulses required for superposition state preparation. We see that over 10 full rotations can be completed with a nearly negligible infidelity. Specifically, we observe an infidelity of 1×10^{-4} per $\pi-$pulse as shown in the inset. All parameters are the same as specified for Fig. 3.20.

3.4.5 Experimental Implementation

The proposed experiment begins with the preparation of single ^{87}Sr atom trapped in optical tweezers formed by laser beams at $\lambda = 881$ nm imaged through a microscope objective to create a static array of traps, see Chapter 2 and Chapter 4. A defect free array of tweezers can be made using an additional movable tweezer, see Section 4.5. The choice of wavelength comes from the near magic wavelength condition for the $|\mathbb{S}\rangle$ - $|\mathbb{P}\rangle$ transition in which a differential Stark shift of at most $\pm$ 125 kHz/mK trap depth is expected for certain m_F sublevels[7], see Section 3.1. Trap depths on the order of $200\mu K$ are required during the imaging process and gate operation to remain in the Lamb

[7]This separation is for the furthest separated m_F states in a d=10 qudit, where the levels $|\mathbb{P}, |m_F| = 7/2\rangle$ and $|\mathbb{P}, |m_F| = 1/2\rangle$ are the furthest separated for linear polarization, see Fig. 3.5.

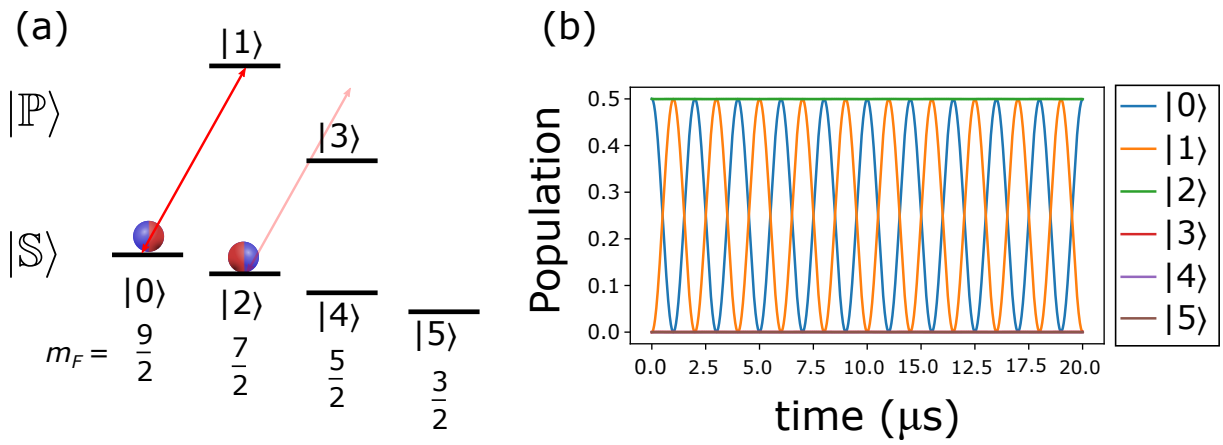

FIGURE 3.22: **(a)** To examine the protection by the Zeeman shift of the neighboring m_F state from unwanted scattering of the coupling laser, we use the same system as described in Fig. 3.21, but instead use an initial state with an equal superposition of $|0\rangle$ and $|2\rangle$. **(b)** Evolution of the Lindblad master equation of the system described in (a). The protection comes from Zeeman shift induced by the applied magnetic field. We find that a ratio of ~ 80 G/MHz for $B-$field strength to Rabi frequency provides adequate protection of $|2\rangle$. The field strengths here are $B = 40$ G and all other parameters are the same as in Fig. 3.20.

Dicke regime for the axial confinement of the tweezer. This means the m_F specific differential light shifts are negligible when the tweezer trap depths are balanced to a few percent, see Section 4.4, and when considering Rabi frequencies above 0.5 MHz where unwanted detunings of ± 25 kHz only affects the fidelity on the 10^{-5} level.

For imaging the atoms in the tweezers, scattered light from the cycling transition of $|\mathbb{S}, 9/2\rangle$ - $|^3P_1, F = 11/2, m_F = 11/2\rangle$ can be collected onto an EMCCD camera through the microscope objective. Although the length of time required for an image increases due to the low scattering rate of this transition when compared to current methods, this scheme has the advantage of simultaneously cooling the atoms while light is being collected allowing for shallower traps to be used during the imaging process, see Chapter 2. Furthermore, this method allows for state specific detection of individual m_F sublevels in the presence of a large (> 50 G) magnetic field. Only atoms in the $|\mathbb{S}, 9/2\rangle$ sublevel will be imaged in this case after which each additional state can be transferred to $m_F = 9/2$ state using optical pumping, or via stimulated Raman adiabatic passage or Raman coupling. This imaging method allows for storage of the qudit states in the m_F sublevels of $|\mathbb{S}\rangle$ which reduces the chance of off resonant scattering

while the other m_F sublevels are being imaged. It also allows for imaging of all 10 m_F sublevels within the expected tweezer lifetimes of $\gg 10$ seconds in the absence of cooling. This time is limited mainly by background gas collisions and can be increased further by improving vacuum quality. The initial image and post-sorting confirmation image can both be done in the absence of a magnetic field and will directly initialize all atoms into the $|\mathbb{S}, 9/2\rangle$ sublevel[8].

Two different magnetic fields are required for all of the single and two qudit operations. One coil will create a bias magnetic field, $B_{\|}$, along the propagation axis of the tweezers for use during the single qudit operations. The second coil creates a magnetic field, $B_{\perp}$, perpendicular to the propagation of the tweezers, and along the axis of the imaging/cooling beam. The second coil allows for the necessary $\pi-$polarization from the coupling beams for de-excitation of $|\mathbb{P}\rangle$ computational states to their respective storage states, or for excitation of the $|\mathbb{S}\rangle$ computational states to their respective $|\mathbb{P}, m_F\rangle$ sublevel for Rydberg excitation. Additionally, $B_{\perp}$ allows for the imaging light to be pure σ^+ polarization, which is required for state specific detection of the different m_F sublevels. The time required for changing between these two magnetic fields could be a significant source of dead time since the field needs to be switched anytime we transfer between computational states and storage states.

A final consideration for the magnetic fields is the required stability. The necessary stability for the fields is dependent on the shift per Gauss of the different m_F sublevels of $|\mathbb{P}\rangle$ which will determine the required laser frequencies for each coupling laser. The Zeeman shift for these sublevels fall into the range of ~ 500 kHz/G meaning a magnetic field stability of ~ 10 mG will be sufficient for the Rabi frequencies we consider as long as the field varies slowly with respect to the duration of the algorithm.

A series of fractional $\pi-$pulses from the individual coupling lasers can prepare the desired initial superposition across all qudit states. The length of each pulse takes the form of $(d-i-1)\pi/(d-i)$ where d is the number of qudit levels and i is the initial state of the pulse ranging from $i = 0$ (for $|0\rangle$) to $i = d-1$ (for $|d-1\rangle$). For example, to prepare an initial super position over all 10 computational qudit states a series of pulses with magnitude $9\pi/10$, $8\pi/9$,..., $\pi/2$ are used. Comparing this with the $\pi-$pulse fidelity determined from Fig. 3.21 and other error sources outlined above, we see the superposition state can be prepared with a fidelity exceeding 0.999. An

[8]If σ^+ polarized-light is used for the cooling beam, the Clebsch-Gordan coefficients of the $|^3P_1, F = 11/2\rangle$ state will lead to all atoms being pumped to the stretched state.

additional five π-polarized $\pi-$pulses would be required to transfer the computational states down to their respective storage states.

After this initialization step, all coupling frequencies can be turned on for the single qudit gate or pulses can be serialized. The magnetic field can then be switched from the $B_{\parallel}$ to the $B_{\perp}$ configuration for transferring the $^3P_2$ qudit states to their storage states, or for exciting the $^1S_0$ qudit states to their respective $^3P_2$ sublevels in preparation for a two qudit gate. Once the entire gate sequence is completed, all qudit states are transferred to their $^1S_0$ sublevels and imaging can be performed in presence of a high magnetic field as explained above. Since the state transfer during imaging can also swap out the atoms already in $m_F = 9/2$, once an atom is detected in a specific site, its m_F sublevel assignment is fixed and will not change even if it disappears or reappears in a later image.

For engineering site selective qudit couplings, a similar system to the one described in [46] can be used. The coupling beams for the different qudit transitions can be created using the sideband of an EOM with multiple drive frequencies from an arbitrary waveform generator to create the necessary frequencies and intensities for each transition. Ideally, a method for filtering of the unwanted sidebands and carrier frequencies should be used. The unwanted sidebands and the carrier will induce off resonant scattering on the $|\mathbb{P}\rangle$-$^3S_1$ transition, which limits the number of gates. Due to the significant power required for the coupling beams, this could significantly reduce the time available for the algorithm. One possibility to remove these unwanted frequencies would be to instead use an AOM in a double-pass configuration with multiple frequencies.

The coupling light is divided into two separate paths of perpendicular linear polarizations, with each path going to a pair of perpendicularly aligned acoustic optic deflectors (AODs) allowing for single site addressing of each tweezer. By using two separate pairs of AODs the available laser power can be most efficiently used and unwanted laser frequencies/polarizations can be avoided. The two paths are recombined using a polarizing beamsplitter before being sent through a Pockels cell for conversion to the required $\sigma^{\pm}$ polarization for the coupling beams. The Pockels cell offers the additional advantage of fast switching of the polarization when $\pi-$polarized light is required. Both paths are constructed in a $4f$ configuration through the microscope and aligned with the tweezers similar to shown in Fig. 4.4. We have briefly analysed the purity of the polarization by adding unwanted couplings. We observe that a polarization impurity of 1% only affects the gate infidelity on the 10^{-4} level.

The described coupling setup also allows for one to control which two tweezer sites are involved in a two qudit operation since the $|\mathbb{P}\rangle$ - $|\mathbb{R}y\rangle$ transition is used for the two qudit coupling. If all tweezers are placed into their $|\mathbb{S}\rangle$ storage states (as opposed to their $|\mathbb{P}\rangle$ computational states), we can selectively choose which tweezer sites and which qudit states to entangle by using the coupling beam as the first photon in the two photon excitation to the Rydberg state.

Chapter 4

Experimental setup and tweezer results

Our starting point was a Sr quantum gas machine that was able to produce both Bose Einstein condensates and degenerate Fermi gases with the intent of moving towards quantum simulation experiments and eventually to a quantum gas microscope. We decided to change strategy and instead make a tweezer experiment due to the versatility, fast repetition rate, and powerful capabilities of these experiments for both quantum simulation and quantum computing [46, 47, 49, 50, 57, 64]. In the following sections we will cover the developments to the experimental setup involved in switching from a quantum gas machine to a tweezer machine along with some additional tweezer results. This includes initial results of loading atoms into the tweezers, our first single atom signals along with the ingredients that we found most helpful in obtaining this signal, further optimizations to near unity survival rates, and results of site selective imaging and sorting.

An in depth description of the strontium apparatus and laser systems used in this experiment can be found in the PhD theses of O. Onishchenko [62] and S. Piatchenkov [63]. Some additional details on our first tweezer setup and a great discussion of microscope objective properties and characterization can be found in the master thesis of I. Knottnerus [112].

Similar to other groups in the field of optical tweezers for strontium [30, 44, 45], our first attempts at preparing single strontium atoms were with 515-nm and 532-nm tweezers (green tweezers). We never managed to make these tweezers work. We had many suspicions for what the problem could be, and the main one was our tweezer light source.

By this time, other groups were presenting new results with 813-nm tweezers [32, 34]. The benefits of better imaging survival rates and much longer lifetimes [32] motivated us to switch to a similar tweezer wavelength. Here we will discuss some results

with 785-nm tweezers and mainly the results with 813-nm tweezers (NIR tweezers).

This section is ordered as follows. We will begin with a brief outline of the experimental setup and our unique procedure for making a μK cloud of strontium atoms at the focal plane of the microscope objective (Section 4.1). Next we will discuss the NIR tweezer system including characterization of the relevant parameters externally and alignment onto the experimental setup (Section 4.2). We continue by outlining the procedure for single atom preparation and detection in optical tweezers including our first results and the limiting factors that prevented us from seeing these results sooner (Section 4.3). In Section 4.4 we discuss the optimizations performed to reach high fidelity preparation, detection, and survival of single atoms in larger tweezer arrays and the limit on minimum trap depth that we observe. Finally, as an important initial step to quantum computation and simulation experiments, we finish with our results on sorting single strontium atoms into defect free arrays in Section 4.5.

4.1 Overview of experimental setup

The experimental setup used in this thesis was originally constructed to be a quantum gas microscope, however we later decided to pursue tweezer arrays instead. A detailed description of the design of this machine can be found in [62, 63]. After completing the work on $^1S_0$ - $^3P_2$ spectroscopy [40], we began the conversion to a tweezer machine. Here we will discuss the changes to the machine since this publication, skipping the green tweezers and instead focusing on the upgrade to NIR tweezers. In addition to this information, an overview of the experiment and additional details on the experimental procedure used for preparing a red MOT can be found in Section 2.3 and Section 2.7 respectively.

In Fig. 4.1, a picture of the experimental setup along with a CAD drawing of the vacuum chamber is shown. In the picture, we show the tweezer optical setup on the upper most breadboard, the objective mount assembly hanging down to the main chamber, and the tweezer fluorescence imaging system. The CAD drawing shows the placement of the tweezer objective inside of the MOT coils along with the path of the atoms from the oven.

The tweezer fluorescence imaging system images the fluorescence of trapped atoms onto an EMCCD camera (Andor Ixon 897), using the objective that is also used to project tweezers onto the atoms. The fluorescence light is split from the tweezer laser

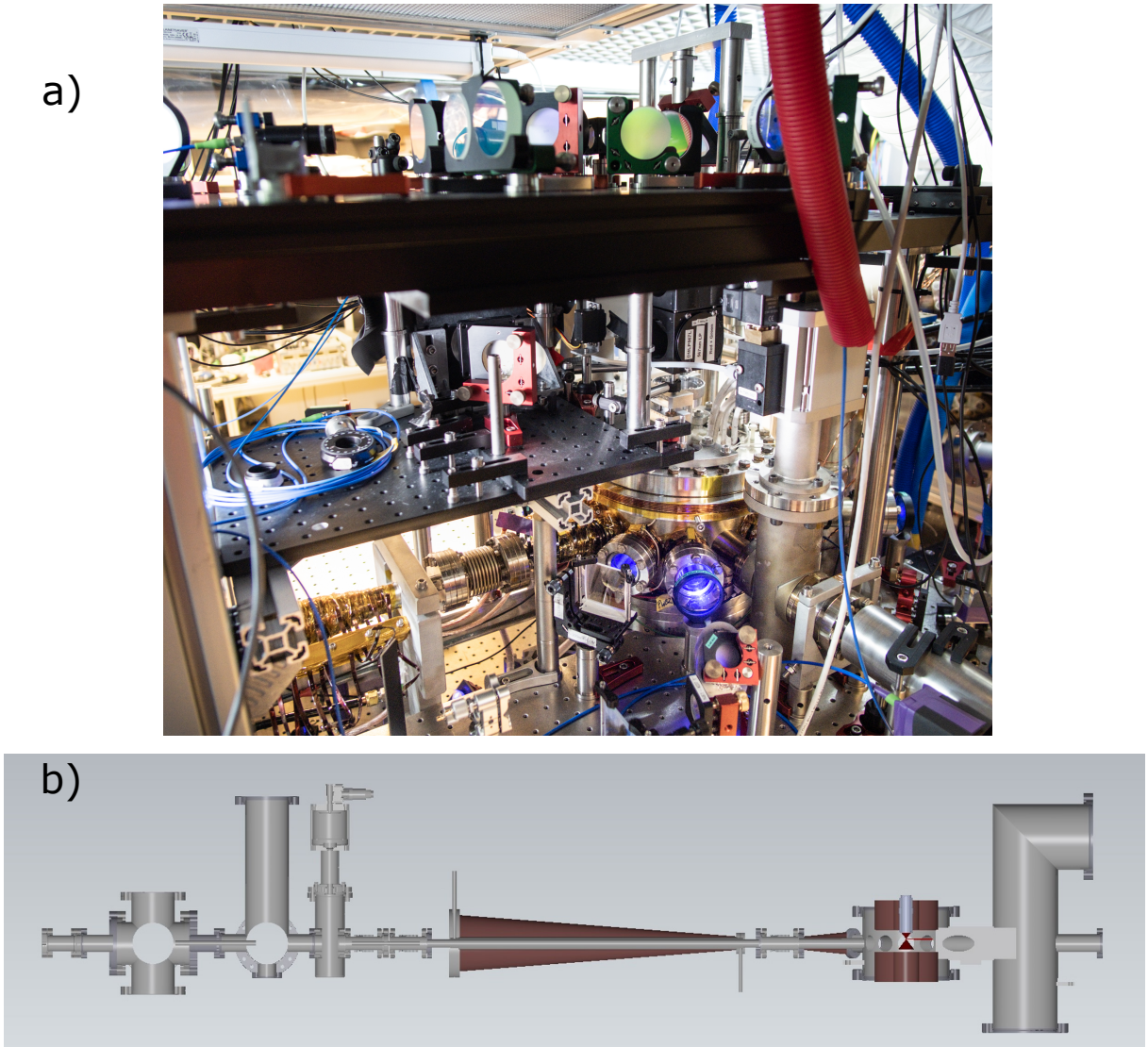

FIGURE 4.1: **(a)** Picture of the experimental setup focusing on the science chamber and tweezer optics. The uppermost breadboard is the tweezer optical setup and the breadboard above the Zeeman slower is the tweezer fluorescence imaging system. The objective mount assembly is also visible hanging down to the main chamber with the microscope objective hidden by the MOT coils (the two black cubes above the main chamber are part of this assembly, see Fig. 4.5). **(b)** CAD drawing of vacuum chamber with the oven, Zeeman slower, MOT coils and tweezer objective visible. For further details on the vacuum chamber and electromagnetic coil designs see [62, 63].

path with a dichroic mirror placed inside one of the mounting cubes, visible in both Fig. 4.1 and Fig. 4.5. Originally, we used a long pass dichroic mirror with a 505-nm cutoff wavelength (Thorlabs, DMLP505L) for splitting the 461 nm fluorescence from the green or NIR tweezers. Once we obtained single atoms, we swapped the dichroic to one with a 750-nm cutoff wavelength (Edmund optics, $\#34 - 745$) to enable collection of 689 nm fluorescence light with a high efficiency. This dichroic still works for blue imaging, although it has a few percent lower reflectance than the previous dichroic at 461 nm. We use an $f = 80\,\mathrm{mm}$ achromatic doublet lens on a translation stage as the field lens for focusing the light from the infinity corrected objective onto the camera chip, giving a magnification of 20. Due to space limitations, the lens is placed further away than the ideal position at the sum of the field lens focal length plus the effective focal length of the objective. Since the objective is infinity corrected, this translates mainly to a reduced field of view for the fluorescence imaging system. The magnification is chosen such that a single tweezer (diameter $\sim$1.6 μm) is the size of a few pixels of the Andor 897 EMCCD camera used for imaging (pixel size of 16 μm, which corresponds to 0.8 μm in the tweezer plane with our chosen magnification of 20). In a trade off between resolution and signal-to-noise (with higher magnification, the resolution becomes better, but the readout noise increases as there are more pixels in the area of one tweezer's fluorescence), this choice optimizes the imaging system for signal to noise ratio over resolution. Finally, two filters are always placed on the camera, one band pass filter centered around the imaging wavelength (461 nm during blue imaging and 689 nm during red imaging) to remove any stray light in the lab and a cutoff filter to specifically eliminate any possible tweezer light.

By installing the tweezer objective along the vertical axis we block the retro reflection of the upward propagating MOT beams. At first we expected additional optics above the objective to be required for sending collimated beams back through the objective, however this was not the case. First, for the red MOT the downward propagating vertical MOT beam of the red MOT provides little confinement due to the radiative pressure of the upward propagating beam vs the force of gravity pushing down [42]. Because of this, the downward propagating red MOT beam could be removed with almost no effect on the red MOT atom number or temperature. This is not the case for the blue MOT beam though. When trying to add a single upward propagating blue MOT beam, we see nearly no fluorescence from the blue MOT, meaning that atoms

are pushed out of the central capture zone. When we remove the vertical beam entirely we see a blue MOT that resembles a 2D MOT (with the difference of using a 3D quadrupole magnetic field). Although this "MOT" does not provide any confinement against gravity, the blue light still pumps atoms to the $^3P_2$ state via the leakage decay channel through the $^1D_2$ state. We expect that some of these magnetic atoms will be trapped in the 3D quadrupole field of the MOT. The observation of a blue MOT without vertical MOT beam gave us the idea to try loading the red MOT from the magnetic reservoir loaded by this blue MOT. This leads to greater than an order of magnitude reduction in atom number in comparison to the normal 3D blue MOT operation, however we are still able to capture over 10^6 atoms per second into the red MOT.

One of our colleagues, Dr. B. Pasquiou from the SrPAL experiment, had an idea to increase the number of atoms that ended up in the $^3P_2$ reservoir. This became an interesting bachelor thesis project that deserves to at least quickly be mentioned. The proposed idea was to pump atoms from the $^1P_1$ state to the 5s5d $^1D_2$ state during the blue MOT instead of relying on the natural decay that occurs through 5s4d $^1D_2$ state. This proved to be possible, and allowed for us to see a greater than three-fold increase in red MOT atom number quite easily. More specifically, we use a laser near-resonance with the 5s5p $^1P_1$ - 5s5d $^1D_2$ transition at 767 nm and with an intensity of approximately $2I_{\mathrm{sat}}$. The laser light is sent to the experiment with a non-polarization maintaining multi-mode fiber. The beam was collimated to a waist of 3 mm as to sufficiently illuminate the whole blue MOT and it was retro-reflected to increase the intensity on the atoms and to minimize momentum kicks. This light is then shone onto the atoms during the blue MOT loading phase at different frequencies and the red MOT atom number is measured.

Results from this quick experiment to improve our red MOT loading are shown in Fig. 4.2 for different frequencies of the 767-nm laser. Even with this simple setup, we saw an increase in atom number from 1.3×10^6 to 5×10^6. A number of improvements could possibly increase this atom number even further, such as better frequency stabilization of the 767-nm laser, polarization maintaining of the fiber, examination of different polarizations, and more accurate scans of the intensity and frequency.

At the moment, we also still do not fully understand the underlying mechanism as to why this increased decay to the $^3P_2$ reservoir occurs. However, we were unable to reproduce the same increase on another experiment with a 3D MOT. This points to the simple conclusion that we speed up the decay to $^3P_2$ before atoms can be lost

due to a lack of confinement against gravity. In a 3D MOT this loss process is not present. Each atom has plenty of opportunity to be pumped into $^3P_2$ and accelerating this process shouldn't make much of a difference. We note that the red MOT loading rate with the 767-nm laser present is still below what was achieved in our machine with a 3D MOT. Our experimental sequence is not currently limited by loading time when using ^{88}Sr, as mentioned in Section 2.7, which lead to a pause on the investigations into improved loading. However, this increased loading could prove to be a very useful tool for other isotopes in our system, where the increased loading efficiency would be a useful ingredient to keep cycle times down.

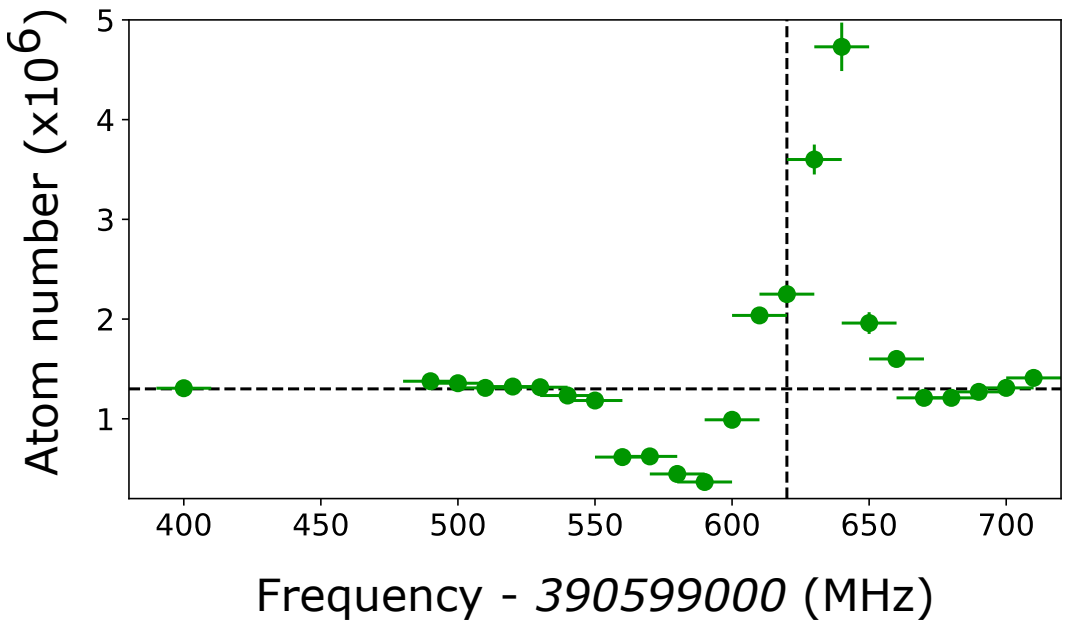

FIGURE 4.2: Atom number in final red MOT stage vs 767-nm laser frequency. The 767-nm laser is on throughout the entire experimental sequence. The frequency range is displayed in MHz after subtracting the offset frequency (390599000 MHz). We use a HighFinesse WS-30 wavemeter referenced to our 689-nm laser to measure the laser frequency. The horizontal dashed line indicates our normal average atom number without 767-nm light and the vertical dashed line indicates our estimation of the $^1P_1$ - $^1D_2$ transition frequency.

The red MOT position must be moved vertically approximately 1 cm in order to load the tweezers. This movement is necessary because the MOT is centred in a vacuum chamber that has more than twice the height of the microscope objective working distance. Placing the blue MOT quadrupole centre above the centre of the vacuum

chamber during loading was not possible due to lack of a strong enough coil to offset by this distance. Additionally, we did not explore this option because a change in vertical offset field of ∼100 mG already begins to reduce the loading flux. With the large red MOT beams that we use, moving the red MOT is easily accomplished by applying a bias field along the vertical direction, shifting the quadrupole center upwards. We use a quadrupole field strength of 0.63 G/cm, which means a bias field of 0.63 G will shift the center by 1 cm.

We have worked hard to minimize any fluctuations in the red MOT position since the position stability is crucial for loading the tight focus of the tweezers especially in the vertical axis. The power supply driving the MOT coils during the red MOT phase, and the small additional bias field coil have been replaced with high precision current drivers originally designed for laser diode drivers. These power supplies provide 1 A of power with sub mA precision, which is sufficient for both coil sets. Since the two coils have sensitivities of 1 G/cm/A and 1 G/A for the quadrupole and bias coils respectively, these power supplies provide sub mG precision on these coils. Our red MOT position stability was further improved with better polarization stability of the red MOT vertical beam. A polarizing beamsplitter is placed after the optical fiber that delivers light to the experiment in order to clean the MOT beams' polarizations. This beamsplitter converts poor polarization stability of the fiber into intensity fluctuations in the MOT beam, which lead to significant fluctuations in the red MOT position. Additionally, overcoming a small experimental sequence problem also helped to improve the repeatability of our red MOT position. The DDS we use for the red MOT (Analog Devices AD9852) allows for frequency modulation, which we use to create the broadband red MOT (see Section 2.7 for details on our sequence). When we started working with tweezers, we would leave some modulation on all the time in order to try to slightly increase the size of our red MOT. However, we used a frequency span that was the same as the modulation frequency, which is outside the DDSs specifications and provoked erratic behavior, with sometimes only a single frequency somewhere in the desired frequency span being produced. This erratic behavior led to a shot-to-shot fluctuation in red MOT position as well. Switching the DDS to single frequency operation before tweezer loading alleviated this problem. After these improvements to the position stability, the center of the red MOT fluctuates by less than $\pm 25\,\mu$m throughout the course of a day of operation with a drift of less than 50 nm/10 minutes.

The last important improvements were to the camera and control software of the

experiment. With tweezer experiments the fast repetition rate of the experiment and number of experimental runs needed for data sets required some small upgrades to the way we take and save pictures as well as to the control software. In many ultracold atom experiments, including the others in our lab and even our experiment before the conversion to a tweezer machine, multiple computers are used to operate the experiment. Specifically, in our experiment two separate computers were used. One for creating the command sequence for all of the electronics and DDSs, and one for the camera servers and image processing. The main issue with this system is that the time wasted in communication between the two computers can sometimes approach or even greatly surpass the duration of an experimental sequence for preparing and detecting single atoms. With ultracold atom experiments this dead time is rather negligible since the experiments take 10's of second in comparison to our near once per second repetition rate. A main ingredient slowing down this transfer was the image processing being done by our imaging software. This can be extremely useful but causes a delay before the next experimental run can take place. To mitigate these problems we upgraded our camera software to directly save the pictures itself and moved to a single computer for camera and control software. This has an added benefit for when we sort the atoms, because in this case the camera software needs to quickly send the atom number in each tweezer back to the control software. The control software needs this information to determine good moves for atom sorting, see Section 4.5.

We have developed a new image viewer software which is independent from the control and camera software. It simply reads the images that the camera software stored on an SSD (solid state disk) and analyzes them in parallel to the execution of experiments. This viewer actively checks the data folder, analyzes all new data, and updates all the plots we ask for, providing us with a nearly real time view of what is happening on the experiment. We have tailored this viewer more specifically towards tweezer style experiments as well by including options such as choices between number of counts or a normalized number of occurrences above a given threshold (occurrences/runs), analysing individual tweezers or averaging over the array, viewing multiple pictures from the same sequence and directly calculating the survival rate between different images, along with plotting the data for a parameter being scanned and displaying the single shot images and averaged image for a given data point. The back end code of the viewer is written in python and the GUI was designed with Qt

designer. An image of the GUI interface is shown in Fig. 4.3.[1]

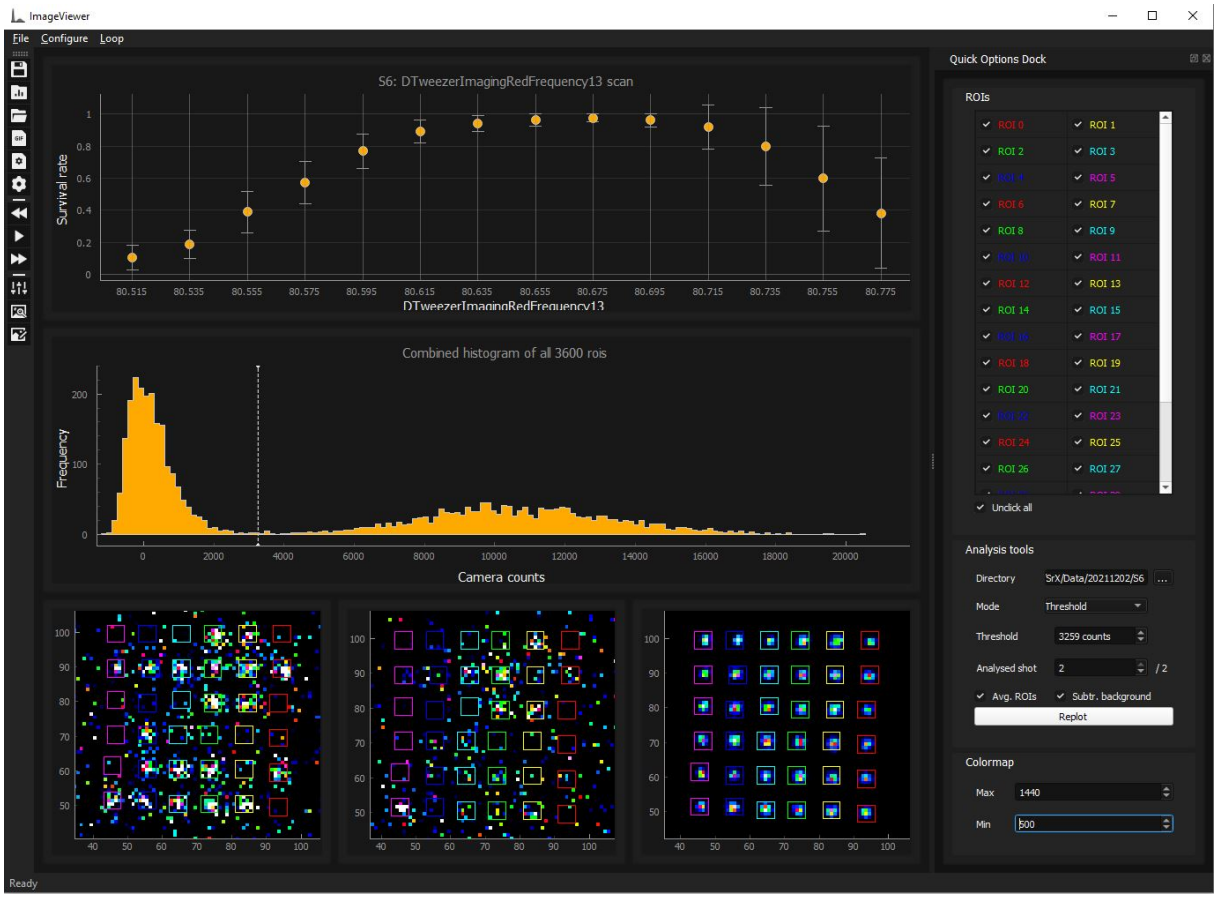

FIGURE 4.3: A screenshot of the GUI of our image viewer software. In the upper left we have a number of buttons for functions. In the center three panels we have the plot of the data set for the selected image number, the histogram of the selected data point and imagenumber, and three tweezer array images. The three images are the last two images taken (of the same experimental run) and an average image for the selected data point and image number. The data set displayed here is one of the data sets from Fig. 2.3. On the right side we have the list of ROIs to be included along with additional quick options for plotting the results.

[1]The back end and GUI coding for this viewer was done primarily by I. Knottnerus.

4.2 Tweezer production, characterization, and alignment

Single atom tweezer experiments always contain two main ingredients. The first is some method for creating arrays of tightly focused optical dipole traps (known as tweezers) in which to capture atoms. The second is some method for high resolution detection, which is usually done by collection of atomic fluorescence. Both of these ingredients require a high resolution imaging system created from either a microscope objective or an aspherical lens (or pairs of those on opposite sides of the tweezer plane). Here we will discuss the creation of tweezer arrays in our experimental setup and the imaging system used for tweezer characterization (characterization imaging system).

We began our journey into the preparation of single strontium atoms with a very simple system consisting of a single acousto-optic modulator (AOM) and a choice from two different green laser sources, a diode-pumped solid state 532-nm laser (Thorlabs DJ532-40) or a free-running 515-nm laser diode (Nichia NDG4216) to make our tweezers. For creating the tweezers and imaging, we used our home built NA = 0.44 microscope objective [113]. This objective was originally designed for use in a quantum gas microscope with the primary application being collection of fluorescence at 461-nm from the broad $^1S_0$ - $^1P_1$ transition. For green tweezers, the chromatic aberrations (which leads to a focal shift for different colors) is small enough that the imaging plane of the 461-nm light can be shifted with the field lens to match the focal position of the tweezers [112]. Some more details on this setup can be found in [63] and [112].

When we struggled to produce clean results with this system, we theorized on a number of problems that could be the cause of this system failing. However once one finds the true problem, the theories one came up with along the way become irrelevant. We will not comment on these theories here, and instead eliminate the anticipation of an interested reader by briefly mentioning that the problem with this system was most likely frequency noise on the cooling laser, see Section 4.3. However as stated above, we decided to switch to NIR tweezers before a doubt-free single atom signal was obtained.

Once the decision to switch from green to NIR tweezers was made, a number of changes and upgrades were done to the experimental setup. First, the NIR laser light source is an external cavity diode laser, which is amplified using a tapered amplifier (TA). Due to lab logistics, we started with a spare 785-nm laser source before eventually

switching to an 813-nm laser source. Second, due to the poor performance and large focal shift of our home built objective at near-infrared wavelengths, we decided to switch to a commercial NA=0.5 objective (Mitutoyo 378-848-3). Due to the design of our vacuum chamber and the working distance of the microscope objective, the atom cloud must be moved vertically by 1 cm into the focal position of the microscope. Because of this asymmetry, we only installed a single objective on the machine, which is used for both imaging and tweezer production, see Section 4.1. Third, we upgraded from an Andor Luca to an Andor iXon 897 camera in order to reduce the charge-induced current noise during imaging. Finally we upgraded from a single AOM to two different methods of tweezer production. We now use a pair of crossed acousto-optic deflectors (AODs) for creating fast movable tweezers and a spatial light modulator (SLM) for creating arbitrary 2D arrays of tweezers.

4.2.1 Tweezer production

Our initial optimizations and first experiments with NIR tweezers were performed with a TA at 785-nm. The choice of this over the clock magic wavelength at 813-nm was based purely on laser availability. Since another experiment in our lab foresaw the need for the available 813-nm TA, we instead started off using a spare TA for rubidium cooling at ∼780 nm. This TA was tuned to 785-nm without any loss in output power (max output of 1.8 W). Our cooling simulations supported that the attractive Sisyphus cooling at this wavelength would work as well as at the previously demonstrated wavelength of 813-nm. The choice to change to 813-nm tweezers was done during the debugging process due mainly to a worry of off-resonant scattering from the $^1P_1$-5s5d $^1D_2$ transition at 767-nm during fluorescence imaging using the $^1S_0$ - $^1P_1$ transition (again, the actual problem was most likely due to frequency noise on the cooling laser). The main output path is sent through a dispersive prism in order to filter out any amplified spontaneous emission from the TA. We have always operated with the prism in the path of the main tweezer array.

For creating the tweezer arrays, we started first with a pair of AODs (AA opto-electronic DTSXY-400-800). The AODs work exactly like an AOM but are designed for beam deflection over frequency shifting [114]. This is done by the selection of a crystal that uses a slower speed of sound leading to a larger deflection angle for a given radio frequency. The radio frequencies required for the AODs were produced

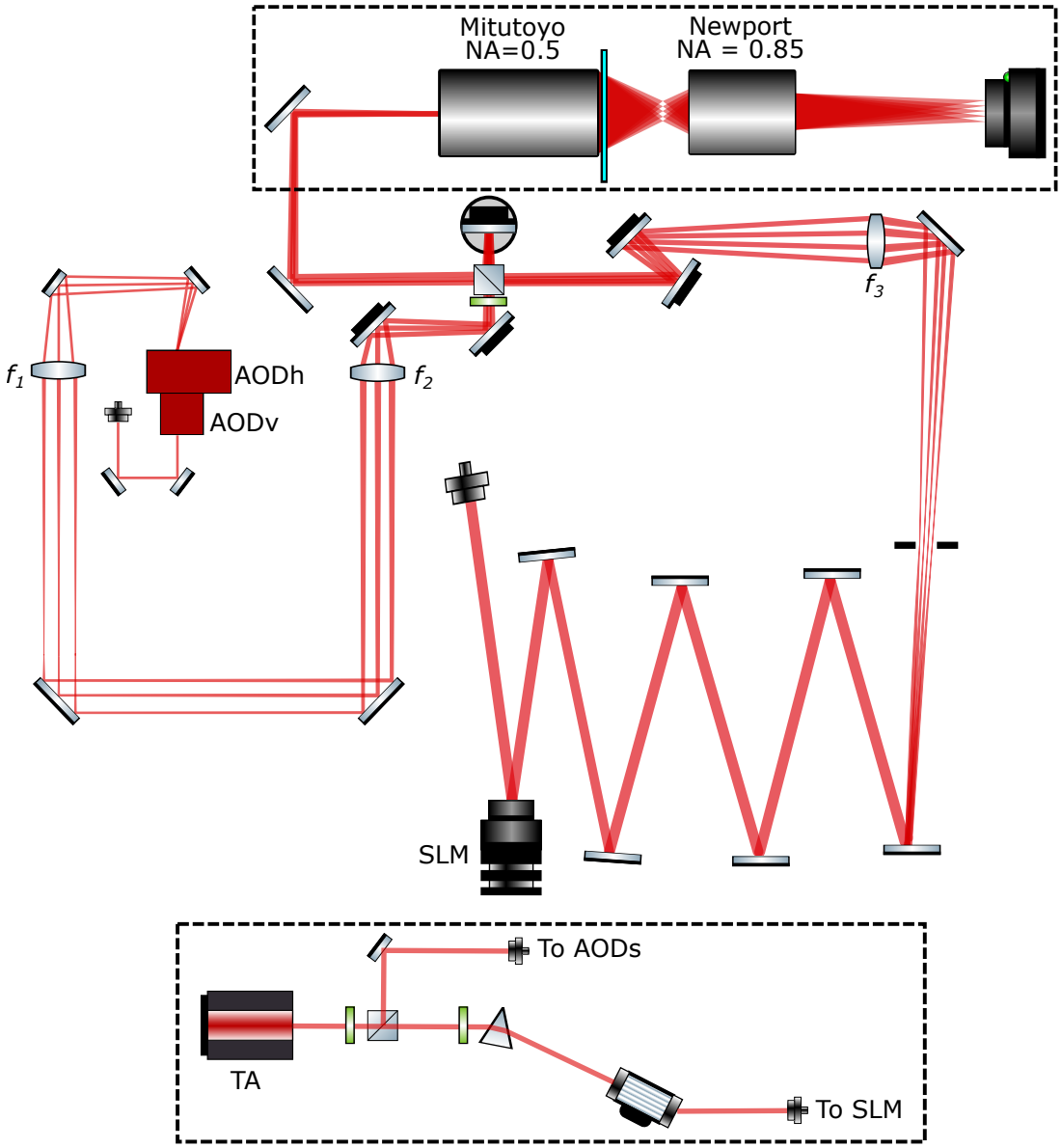

FIGURE 4.4: A schematic of the tweezer optical setup. On the left, the AOD path is shown. The region inbetween lens f_1 and f_2 the beams are focusing to create the pre-image of the tweezer array. The SLM setup is also visible in the main picture. Since the SLM is used as the focusing lens for the pre-image, the individual tweezer beams continue to diverge after the pre-image. Because of this the field lens f_3 must be placed further from the microscope objective than f_3. The top inset shows the characterization imaging system (not to scale). The second objective provides the resolution to image the tweezer foci. The bottom inset shows the tweezer laser path from the TA to fibers that bring the light to the tweezer optical setup (not to scale). This includes a dispersive prism for filtering the amplified spontaneous emission of the TA and AOM for global intensity control of the SLM array.

by a number of DDSs that are mixed together to form multiple first order diffraction spots from the AODs. The two AODs are placed perpendicular to each other such that a 2D array of tweezer spots can be made. The size of the array that can be created with the AODs is limited to the number of radio frequencies sent to each AOD. Later on, this configuration also allows for a single tweezer to be scanned over the field of view of the microscope focal plane, which is useful for sorting and site-selective imaging. A simple sketch of the AOD setup can be seen in Fig. 4.4.

The AOD setup must be aligned in a $4f$ configuration for proper transmission of all beams through the aperture of the microscope objective. We send a collimated beam (w_0 = 1.1 mm) into the AODs. The AODs are placed directly against each other with the second AOD aligned to the Bragg angle of the first.[2] The diffracted, but still collimated, beams begin to expand away from each other like rays in a geometrical optics picture. Each beam is controlled by two frequencies, one from the vertical AOD (AODv) and one from the horizontal AOD (AODh). By placing the first lens (f_1= 250 mm) of the setup a distance f_1 away from the AODs, we collimate the rays with respect to each other. This fixes the distance between neighboring beams while creating a focused image at a distance f_1 from the lens. The beams expand and a second lens (f_2 = 600 mm) is placed at a distance f_2 away from the initial image plane. This creates an array of beams with waist $w_0 \approx$ 2.5 mm, which is larger than the microscope aperture radius of 2 mm. Ideally, the ratio of waist to aperture should be ≈1 for the most efficient use of the optical power and largest trap frequencies for a given input power [77]. However, we chose to make the waists larger in favor of less sensitivity to misalignment over most efficient power usage. The collimating lens f_2 again causes the individual collimated beams to begin 'converging' in the geometrical optics picture. Placing the microscope at a distance f_2 away from the second lens allows for equal transmission of all beams through the microscope aperture. The choice of lenses for this system comes mainly from the limitation of how close we can get to the microscope objective while still having room for two adjustment mirrors, for a PBS cube to combine the SLM and AODs, a dichroic mirror to split off imaging light, and without significant changes to

[2]This method leads to slight deviations from perfect alignment for different frequencies on the first AOD, however this effect is small for the array sizes considered in this thesis. A more robust method would be to use an additional $4f$ configuration for imaging the first AOD onto the second AOD [30, 44, 115]. We did not find this to be necessary and instead saved our limited optical breadboard space for the addition of our SLM setup. The AODs are used only for sorting or site selective imaging now, but if one wants to make large arrays with the AODs, then one should use this slightly more complicated setup.

the existing experimental setup. A shearing plate interferometer is a very useful tool for checking that the beams are properly collimated before the microscope objective.

After our first successful production of single strontium atoms in tweezers and our first narrow-linewidth imaging results (see Section 4.3), we upgraded the experimental setup to include an SLM enabling the production of larger 2D arrays. An arbitrary wave form generator for the AOD frequencies could have accomplished the same scale up to more tweezers, however, the SLM also has a few added benefits. The SLM is able to create arbitrary tweezer patterns, such as hexagonal, triangular, or kagome arrays just to name a few. The SLM allows for better trap balancing since many pixels of the SLM control a single tweezer unlike the AOD where many tweezers share the same frequency tone(s) in large arrays. With the SLM, the trap light is the same frequency for every tweezer, which can be useful for magic wavelength tuning of the tweezers. For example, in tweezer based clocks the shift of the tweezer frequency away from magic by the AOD(s) can be seen in the $^1S_0$ - $^3P_0$ spectroscopy [34, 35, 36]. After this addition to the setup, the main path with filtering prism is used for the SLM and a second path split off by a PBS from the TA is used for the AODs with no additional filtering.

The phase-only reflective SLM used in our experiment is a device for manipulating the phase of an incident laser beam. By applying a voltage to one (or many/all) of the pixels in the display, the orientation of the liquid crystals inside the pixel change orientation. This changes the refractive index of the pixel and thus the path length the laser travels. In turn the SLM manipulates the phase of the incident laser beam based on the phase pattern applied to the pixels allowing for arrays of foci to be created via a Fourier transform induced by a lens [49, 50, 116].

The SLM setup is also shown in Fig. 4.4. Since the SLM has a slow refresh rate, the path starts with an AOM, before the optical fiber, which brings the light to the optical breadboard of the tweezer setup, for switching and global intensity control of the array (see inset of figure). After the fiber, a collimated beam with waist of 6 mm is sent to the SLM. Because the SLM has an active area of 10.7 mm $\times$ 17.6 mm, we chose to match the beam waist closer to the short axis for a balance of maximizing the area of the SLM used for creating the tweezer pattern while not wasting excess power on clipping the beam on the short axis. The light is reflected off the SLM with the phase pattern imprinted.

The phase pattern contains a number of different contributions summed together.

First, there is the factory correction phase given to us by Meadowlark that is intended to compensate flatness imperfections from the surface of the SLM. Second, we add a grating phase to separate the non-diffracted zeroth order beam from the diffracted fist order. Third, we add a Fresnel lens phase for focusing the array, thereby saving the extra optical path length for a second focusing lens in the optical setup. The effective lens we initially used was the combination of two slightly different focal length vertical and horizontal lenses due to an astigmatism at the focal plane of the lens. This most likely has to do with how the SLM chip is mounted, creating a slight curved cylindrical mirror in one direction, which is not properly removed by the factory correction phase. We later replaced the lens combination by one lens and switched to using a combination of Zernike polynomial phases to remove optical aberrations from the system, see Section 4.4. All of these phases can be easily generated using the Meadowlark SLM software. The final phase pattern added to the SLM is the phase for creating the tweezer array.

To calculate the phase pattern for creating the tweezer array, we use the weighted Gerchberg-Saxton algorithm [83, 117, 118, 119]. The algorithm creates a phase mask to match a desired intensity pattern in the image plane by iteratively looking at the projected light field in the image plane (i.e. the focused tweezers) and diffraction plane (i.e. the incoming Gaussian beam) and applying boundary conditions on the amplitude. The algorithm starts with randomly assigned phases, ϕ_0, from 0 to 2π for each pixel. The phase is then multiplied by the incident amplitude pattern, A_0 (Gaussian beam incident on the SLM) to obtain a starting value for the light field. At each iteration we start with the field after the SLM being defined as $A_0 \mathrm{e}^{\mathrm{i}\phi_n^i}$ and perform a fast Fourier transform (FFT) to convert the phase to an Intensity distribution. This creates a new intensity pattern and phase of $A_n^f \mathrm{e}^{\mathrm{i}\phi_n^f}$. If the calculated intensity pattern, $|A_n^f|^2$, matches the desired array intensity pattern, I_t, we have found a good phase pattern. If it does not match, we multiply the FFT calculated phase, ϕ_n^f, of the pattern by the desired amplitude, $\sqrt{I_t}$, and then perform an inverse FFT bringing us back to the SLM plane. This gives the field $A_{n+1}\mathrm{e}^{\mathrm{i}\phi_{n+1}}$. After setting the amplitudes A_{n+1} to A_0 this field is used as starting point for the next iteration with the new phase ϕ_{n+1} [83]. The process is repeated until the desired convergence of the intensity pattern is reached, which usually occurs in < 100 iterations. Any intensity pattern can be reached by this procedure including tweezer arrays with individual intensities for each tweezer spot. These individual intensities and iterative procedure will be a useful tool for balancing

the trap depths, see Section 4.4.

With the sum of these four phases, the SLM creates a focused pre-image of the array at a distance of ∼183 cm from the SLM. The collimating lens, $f_3 = 500\,\text{mm}$, is placed 500 mm from the focus to collimate the individual beams. The combination of SLM lens phase and the lens f_3 demagnifies the large initial beam to a waist of $\sim 2.2\,\text{mm}$. Unlike in the AOD setup, the individual beams are not propagating parallel to each other at this point but instead are diverging away from each other. To properly transmit all the beams through the objective, the lens must be placed further back than f_3. We calculate the distance with a set of ABCD matrices using the aperture of the objective, focal length of the collimating lens and size of the SLM. This procedure also gives us the distance from the SLM to the pre-image focal plane.

4.2.2 Tweezer characterization and alignment

To characterize tweezer parameters such as waist and microscope transmission, we constructed an external test setup. The setup uses the same technique as outlined in [63, 112, 113]. The procedure to characterize the quality of the tweezer foci created by the main objective uses a characterization imaging system consisting of a second microscope objective (imaging objective), an additional magnification to spread the focus over a sufficient number of pixels to perform an adequate fit, a field lens to focus the image, and a camera. For the analysis presented here, we simplified the characterization imaging system by upgrading to a higher NA finite conjugate objective (Newport M-60×, NA=0.85). The higher NA of this microscope objective removes the need for any deconvolution of the imaging system from the object being measured (in our case the tweezer waist) [112]. The finite conjugation of the objective also means it produces an image with no need for a field lens and the large magnification (quoted specs 60×, measured 80× in setup) eliminates the need for any additional magnification.

For the initial examination of the AOD tweezer arrays, we constructed an external mount for the tweezer production optical setup (Fig. 4.4). This setup was elevated approximately 1 meter above the optical table in order to conveniently send beams through the top of the full objective mount assembly from the experimental setup, see Fig. 4.5, in place of building the test setup directly onto the optical table. We chose to characterize the tweezer system in this way in order to look at the position stability of the tweezers in the actual experimental setup as well as to confirm the ability to blindly

align the objective to the setup since we lack the ability to observe our tweezers in-situ once installed on the experiment.

To start the alignment procedure, the objective mount assembly is placed in position against the optical setup breadboard. The tweezer beam is centered onto the assembly mirror that sends the beams down to the objective. Custom irises (4 mm diameter) are used to center the beam on the two apertures of the mount, one at the top of the mount and one at the top of the microscope holder (75 mm from microscope aperture), see Fig. 4.5 for details. This is usually done with a single beam at the center of the AODs frequency range, but additional beams can prove useful for fine tuning at later steps. Once centered, the irises are removed. The beams of the tweezers are now roughly aligned near the final position.

Before installing the tweezer objective into the test setup, the characterization imaging system needs to be calibrated. For the calibration process, a target must be installed first. The target used for calibration was made at ETH Zurich[3], see Fig. 4.6. It was made with a focused ion beam used to carve pinholes into a Cr-Pt-Pd film on a glass plate. There are 6 patterns on the target, each with 6 holes in a unique 20 μm square, where the specific pattern we use has holes with diameters of 200 nm. These small holes act like point sources when light is transmitted through them. Since the small holes are hard to find, additional 20 μm squares are used to locate the spot pattern. These squares can even be seen by eye and allow us to roughly position the desired pattern inside the beam. A single beam at the center of the AOD frequencies is used to illuminate the target pattern. The Cr-Pt-Pd film acts nicely as a mirror allowing for us to make sure the target, which will define our calibrated imaging plane, is perpendicular to the incoming beam. The target is placed as close as possible to the expected tweezer objective focal plane to avoid changing the characterization imaging system when we switch to measuring tweezers.

Once the target has been installed, the characterization imaging system can be aligned. As briefly mentioned above, the imaging objective is a finite conjugate objective, meaning we only need the objective and a camera for the imaging system. The one downside of this objective is its extremely short working distance (0.48 mm). Therefore our adjustable objective mount can easily be moved too far, pushing the objective against the target and damaging it. To avoid this danger, special care must be taken during alignment. We use a Gimbal mirror mount (Thorlabs GM100) with an

[3]We thank Joakim Reuteler for the manufacture of the target

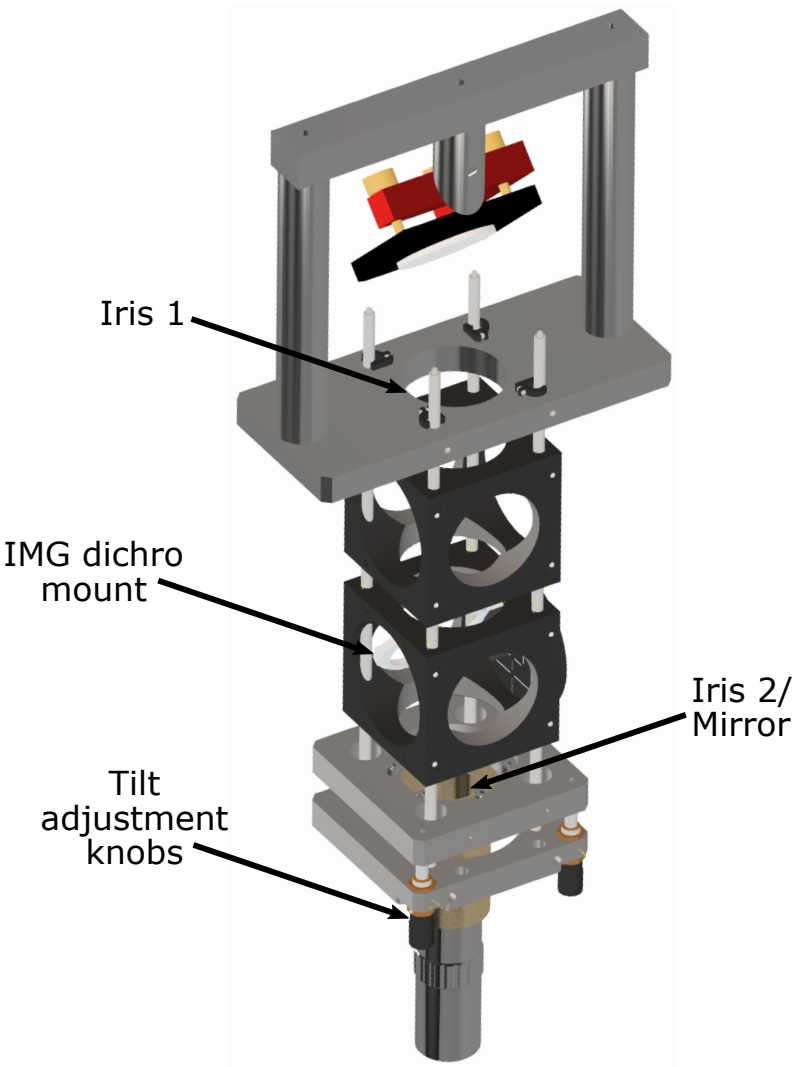

FIGURE 4.5: CAD drawing of the objective mount assembly. We have indicated with arrows the positions at which we place the alignment irises (Iris1 and Iris 2), the mirror used to retro-reflect the tweezer beam during alignment (Mirror), and the dichroic mirror mount of the tweezer fluorescence imaging system (IMG dichro mount). We also indicate one of the three tilt adjustment knobs used for aligning the tilt of the tweezer objective to the stationary window of the vacuum chamber and for moving the objective closer to the window. The microscope mount is depicted in gold to make it more easy to identify. The microscope objective and the objective mount are inside the MOT coils once installed on the machine, see Fig. 4.7.

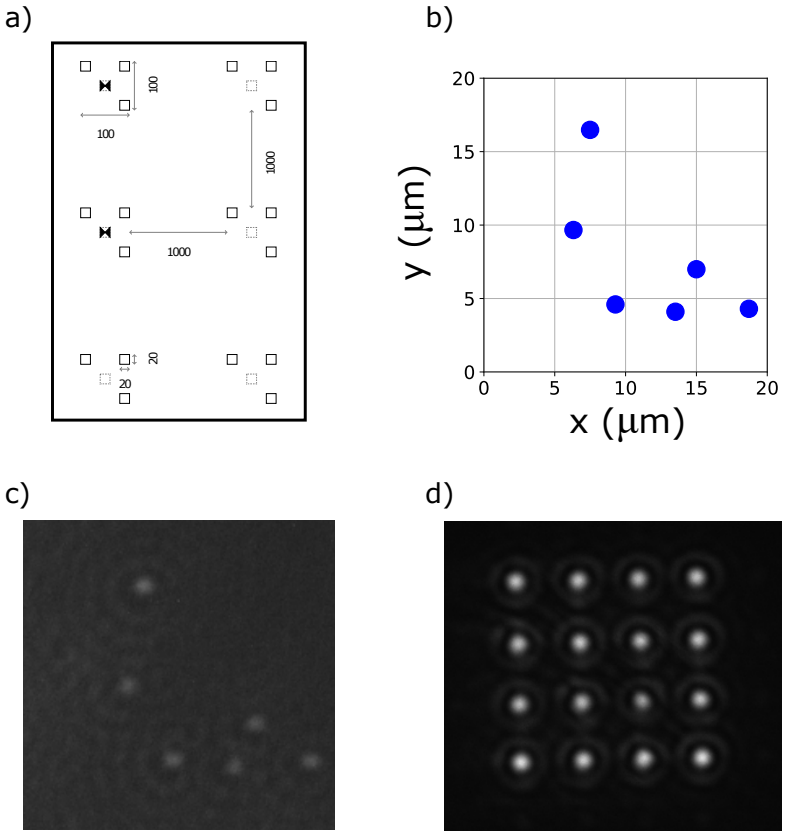

FIGURE 4.6: **(a)** Schematic of the characterization target. The squares for rough alignment and finding the individual patterns are shown. All dimensions are in μm. **(b)** Target pattern used for all characterization. **(c)** Picture of pattern illuminated with 785 nm light. This gives a resolution of σ_{fit}=0.27(3) μm. **(d)** Picture of AOD tweezer array in the test setup showing a waist of 0.81(2) μm.

additional tube to mount the objective such that the tilting plane of the mount is as close as possible to the focal plane while still having enough space to get close to the target. The Gimbal mount is connected to a set of three translation stages, one for each Cartesian axis. A mirror reflects the transmission of the imaging objective to the camera. The camera is also mounted to a translation stage along the imaging axis to compensate for any adjustments needed to the focal plane of the objective. An example image of the calibrated characterization imaging system is shown in Fig. 4.6(c), where we measure σ_{fit} = 0.27(3) μm corresponding to a resolution of 0.78(9) μm and a magnification of 14.1 pixels/μm[4]. The fits suggest that we do not reach the diffraction limit of the imaging objective (resolution of 0.57 μm), however the resolution and magnification are sufficient to provide an estimate of the tweezer waists.

With a calibrated characterization imaging system we can measure the tweezer waists. We first install a vacuum chamber viewport under the tweezer objective in order to reproduce the beam distortion that the tweezer beam experiences in the experimental apparatus. This viewport was left out of the test setup so far because it is not required for calibration of the characterization imaging system or for the initial alignment to the center of the tweezer microscope objective. We adjust the window such that the incoming tweezer beam is retro-reflected. An IR viewer can be useful in seeing the weak reflection. This step is crucial because angles between tweezer objective and window significantly affects the quality of the tweezer foci produced by the tweezer objective. Once the window is in place, the tweezer objective can no longer be screwed into its mount. Because of this, the objective mount assembly position is marked using blocks such that we can can lift up the assembly, install the tweezer objective into the mount, and place the assembly back in the same position. A mirror is then placed on top of the objective mount and the angle of the mount is adjusted such that the beam is again retro reflected. During the first attempts the final adjustments can be done using the characterization imaging system to confirm the alignment is good. Once the process is complete and the $1/\mathrm{e}^2$ waists of AOD tweezer array in the test setup are measured to be 0.81(2) μm. This is approximately 20% higher than the

[4]We define the terms σ_{fit} and resolution based on those defined in [112]. The former is related to the normal Gaussian distribution, $\propto \mathrm{e}^{-\frac{1}{2}(\frac{x}{\sigma_{\text{fit}}})^2}$, and related to NA through $\sigma_{\text{fit}} = 0.21\lambda/\text{NA}$. In a perfect imaging system, the Airy disk is the point spread function of a point source. The diffraction limit is defined as the distance from the principal maximum of the Airy disk to the first minimum, given by $a_0 = 0.61\lambda/\text{NA}$. The resolution is defined as the conversion of the Gaussian distribution to the diffraction limit giving $r_0 \approx 2.9\sigma_{\text{fit}}$. See [112] for an extensive explanation of these terms.

expected diffraction limited spot size of the tweezer objective. The deviation from optimal is most likely due to the difference between the designed cover glass thickness (3.5 mm) and the one on our experimental setup (3.175 mm on the machine, however for the test setup a window of 3.2 mm is used). This most likely causes additional spherical aberrations limiting the quality of our focus. After the alignment of the tweezers is finalized, the characterization imaging system magnification and resolution can be recalibrated with the target to confirm that the adjustments did not significantly alter either value.

We confirm that the tweezer objective is properly aligned with respect to the collimating lens (f_1) by looking at the transmission of individual tweezer beams. The system is properly aligned to the objective when all beams of the array show not only similar waists but also the same transmission. For the tweezer beams used, we measure a transmission of 50% for 785 nm and 36% for 813 nm.

The external alignment allowed for us to check the position stability of the tweezers, which we were worried about since the objective mount assembly acts as a long lever arm. We saw that external influences were causing a significant jitter on the array position. To alleviate this, we added some additional supports attached to the assembly below the imaging dichroic cube and going to the more sturdy support system of the experimental setup. Shortening the lever arm in this simple way sufficiently dampened any oscillations.

The SLM was also initially characterized externally. For simplicity this characterization was done with optics on an optical breadboard instead of optics integrated in the elevated test setup. As a consequence the optical setup around the SLM was constructed twice, once for the test and once in the experimental setup. To transfer the alignment of the SLM's optical setup from test breadboard to apparatus, we traced all the optics poles and mounts onto the optical breadboard and then transferred the pattern to a clear plastic film. We cut out the individual component placements and used this template to place the optics onto the final optical breadboard of the experimental setup. We added the characterization imaging system shown in Fig. 4.4 to the optical layout on the machine, allowing for us to look at the overlap between the AODs and the SLM. We have observe that this characterization imaging system is not an exact reproduction of the tweezers on the atoms. For example, using images of the tweezer array to perform trap depth balancing does not directly correlate to balanced trap depths for the atoms. However, this additional characterization imaging system

is a powerful tool for debugging purposes.

Alignment to the experimental setup

FIGURE 4.7: A close up picture of the tweezer objective mounted inside the MOT coil. The objective must be aligned orthogonal to the window and suspended just above the window (0.9 mm from the front face of the objective to the window) such that the tweezers can be aligned to the red MOT. We had to modify the objective mount assembly in order for it to pass the MOT coils.

With satisfactory tweezer waists measured externally, the tweezer optical setup is installed on the experimental apparatus, using the alignment procedure outlined next. This procedure is complicated by the fact that the vacuum chamber window is fixed and that the microscope objective must be mounted inside the MOT coils, seeFig. 4.7. To help us align the microscope objective orthogonal to the window, we first install the objective mount assembly and tweezer breadboard on the machine, but without the objective. We use the two mirrors after the collimating lens to adjust the beam position such that the central beam of the array is aligned with both irises placed onto the mount and the beam is retro-reflected by the window. The windows on the machine are AR coated making the reflection from the window very weak, but it is still visible with an IR viewer. Once this alignment is completed, we place a mirror on top of the objective mount and retro-reflect the beam using the mount adjustment knobs. The position of the objective mount assembly is then marked with blocks before we remove it to add the tweezer objective. Once the tweezer objective and the mount assembly are reinstalled, the irises and retro-reflection mirror on top of the mount are used for fine

adjustment of the beams to compensate for any slight displacement from reinstalling the objective mount assembly. This procedure was characterized externally by many repetitions of the process after slight displacements of the window. The idea for this alignment procedure came from a similar method used in [120].

Once the system is aligned we still need to find the focal position of the tweezers and overlay the MOT with this position. This can feel like looking for a needle in a hay stack, but we found one very helpful trick to ease the search. To find the focal point of the objective, we send light resonant with the $^1S_0$ - $^1P_1$ transition along the imaging path such that it is reflected off the dichroic mirror and is co-propagating with the NIR tweezer beam entering the tweezer objective. Since the path from our oven to our science chamber is a straight long path, we have a nearly collimated beam of fast travelling atoms going through the location of the tweezers when no laser cooling light is on. However, the long path of the Zeeman slower allows only atoms with relatively low radial velocity (few 10 m/s) to pass into the science chamber. The resonant beam through the objective, which is perpendicular to the atomic beam, is inducing fluorescence in atoms with low radial velocity. The short lifetime of the excited state of the transition allows for the atoms to rapidly scatter photons as they pass through the beam. This allows us to see the tweezer focal position in the chamber with our MOT imaging system under long camera exposure as shown in Fig. 4.8(a).

The placement of the objective was initially too high above the chamber, which required us to move it closer to the window. The tweezer objective is mounted inside the MOT coils eliminating the direct line of sight to the distance between the tweezer objective and the window. To make sure we didn't press the objective into the window and possibly ruin our vacuum, we made the simple origami tool displayed in Fig. 4.8(b). We folded the paper a number of times to create a given thickness(measured with a caliper). The paper can then be slid underneath the objective to confirm that such a gap is still present between the objective and window as shown in Fig. 4.8(c). The objective can then be lowered with the adjustment knobs of the objective mount taking into account the threads per mm of the adjustment screws. We used this process to go from 3 mm away from the window down to approximately 0.9 mm.

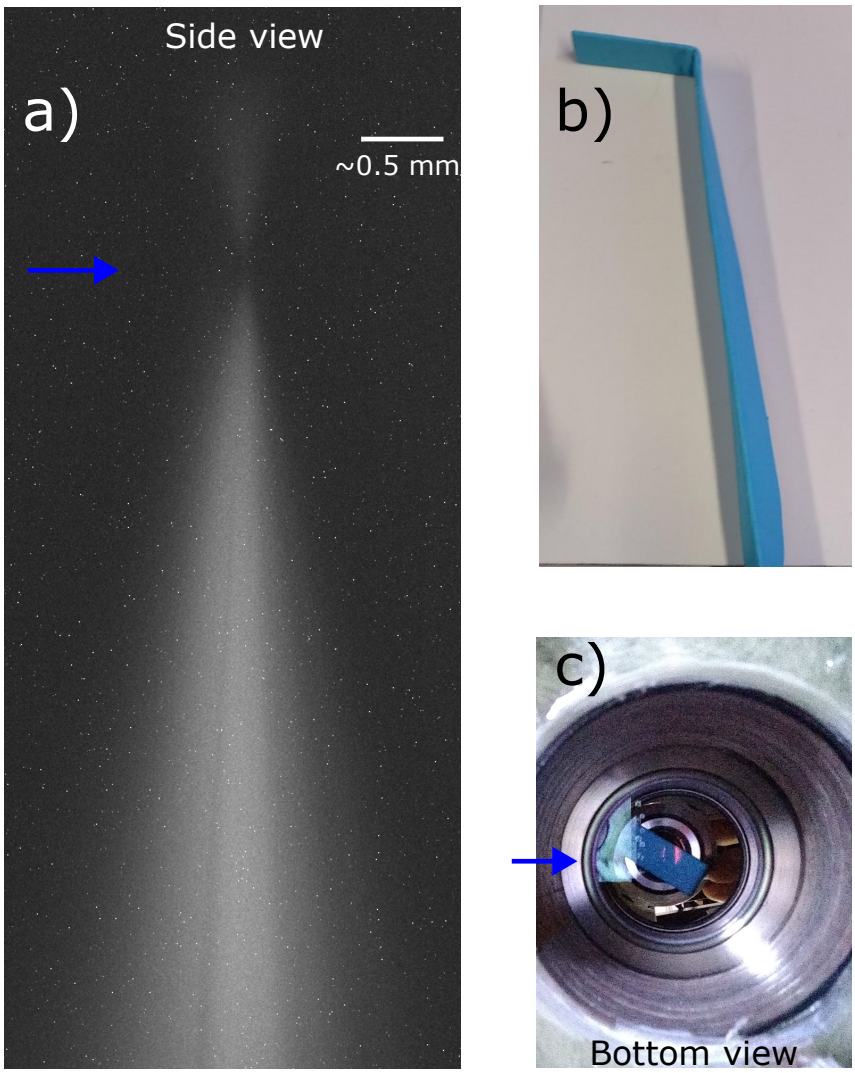

FIGURE 4.8: **(a)** Atomic fluorescence from a 461-nm beam sent through the microscope objective and co-propagating with the tweezer beam. The 461-nm beam is resonant with the $^1S_0$ - $^1P_1$ transition and propagates perpendicular to the atomic beam coming from the oven. The direction of the incoming beam is indicated with a blue arrow and a scale bar has been included for reference. The image is taken with an exposure time of 3 seconds. This method was used to locate the tweezer traps in order to properly position the red MOT. **(b)** An origami tool made for moving the tweezer objective closer to the vacuum window. **(c)** A picture of the origami tool in practice taken from below the vacuum chamber. The window diameter is 50.8 mm and the direction of the incoming atomic beam from the oven is again indicated with blue for reference. We use the thickness of the folded paper to determine the distance between the objective and window. After determining the distance, the objective is lowered with the tilt adjustment knobs. We remove layers from the origami tool until it again fits. The process can be repeated until the desired distance is achieved.

4.3 Initial tweezer loading and single atom preparation

In this section we will present the initial results for loading tweezers, cooling and single atom preparation including our initial red imaging results. The main purpose of this section is to discuss some details and observations that lead to our first single atom signal and that are not included in Section 2.4. It is more intended to highlight the problems and first signs that allowed for us to achieve the nice results shown in Chapter 2, in order to help others to achieve similar results faster. We will start by discussing our initial results with a 2×2 array of AOD tweezers and then continue to our more recent results with the SLM tweezers.

4.3.1 With AOD tweezers

Initially we started the search for atoms loaded in tweezers using imaging light resonant with the $^1S_0$ - $^1P_1$ transition, also referred to as blue imaging throughout this thesis. The fluorescence of the atoms in tweezers was induced by two independent collimated beams each with their own AOM control. The unique AOM for each path allows for the frequency of the beams to be tuned independently as to avoid a standing wave and to allow for the intensity of the beams to be balanced. The beams are aligned such that they are both coupled back into each other's optical fibers bringing them to the experiment to make sure they are retro reflected. This alignment is done to minimize momentum kicks from the imaging beams. The imaging beams are also aligned perpendicular to the tweezer objective to concentrate the heating from photon recoils of the imaging light to the radial axis. The blue imaging beams polarization are linear (horizontal) and also perpendicular to the tweezer propagation to maximise fluorescence, similar to what is done in Chapter 2. The same repumper and cooling/red imaging beams mentioned in Chapter 2 are also already present, with the exception that the cooling beam polarization was placed parallel to the tweezer propagation (vertical). With the original AODs tweezer configuration, there was still a 30° angle between the cooling beam propagation and tweezer polarization. Choosing vertical polarization thus maximises the power available for cooling by placing the polarization perpendicular to

the quantization.[5] Blue imaging provided the advantage of allowing for images of the red MOT to be used for aligning the atoms below the tweezer objective, as shown in Fig. 4.9.

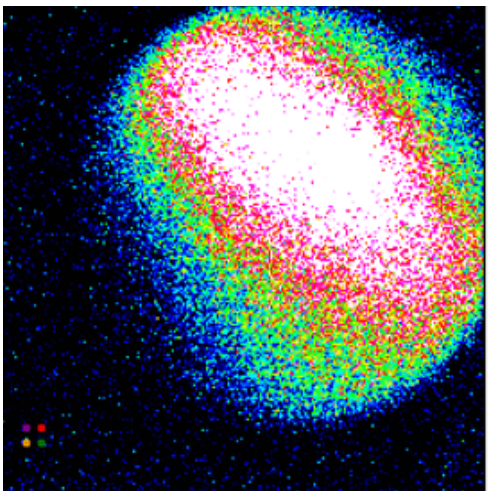

FIGURE 4.9: In-situ fluorescence of the red MOT imaged through the tweezer objective. We induce fluorescence on the $^1S_0$ - $^1P_1$ transition. We have included four tweezer ROIs at the separation used with the AOD tweezer array in the bottom left for a scale comparison.

With the red MOT positioned below the tweezer objective, we began to load the 785 nm tweezers and try to image them. We find an important ingredient to produce reliable results is to start from uniform loading of the array, i.e., all tweezers loaded with at least one atom. An example of the fully loaded array plus the histogram it produces is shown in Fig. 4.10(a) where a single broad peak shows an unknown number of atoms has been loaded into each tweezer, leading to at least some fluorescence before either cooling or imaging light begins to kill pairs of atoms or even heat out single atoms. This is also where MOT stability is critical because poor MOT loading stability can be mistaken for single atom preparation in extreme cases[6].

[5]Since we operate the tweezers at zero magnetic field, the $m_J = \pm 1$ states are degenerate and addressed with $\sigma\pm$-polarized light respectively. By placing the linear polarization of the cooling beam perpendicular to the quantization axis defined by the tweezer polarization, we maximize $\sigma\pm$-polarization of the light.

[6]If you only load the tweezers approximately 50% of the time, the histogram of occurrences vs counts look very similar to a single atom histogram. Two main differences can be an inconsistent number of counts from different tweezers, and a non randomized loading, i.e. all tweezers loaded or no tweezers loaded instead of 50% of the traps randomly loaded in each shot.

Once the tweezers were loaded, we began with scanning the 689-nm cooling laser looking for the frequency where we see the Sisyphus cooling working as evident by the increase in fluorescence counts since the cooling is now compensating some of the heating of the 461-nm fluorescence. An example of such a scan is shown in Fig. 4.10(b). The detuning of the best cooling was found to be around -5.25 MHz from free space resonance for the trap depths being used at this time. From this measurement we estimated the trap depth to be approximately 650μK[7] deep by assuming the best cooling frequency will be near equivalent to the Stark shifted resonance.

After the first signs of cooling, we began to look at how long atoms survived in the presence of cooling light and how much imaging light it would take to heat the atoms out of the trap. We began to see a significant lifetime in the presence of cooling exceeding a few seconds, meaning that the cooling light was at least not killing the atoms[8]. However, we still had a poor survival in the presence of 461-nm light even for very low scattering rates of 10-20 kHz. With this performance we attempted to look for a balance of interleaved 461-nm imaging light with 689-nm cooling light to try collecting enough blue photons before the atom was heated out. An example of such a run is shown in Fig. 4.11.

Even these long images did not produce a single atom signal fully separated from the zero atom signal. This led to two ideas of why we were struggling so much with the imaging process. Either cooling was not working sufficiently well or off resonant scattering of the tweezer light was accelerating our loss to $^3P_2$ or another metastable state. Since a fairly exhaustive search of all cooling parameters had been done, we chose to first look into the latter. One possibility for such a loss channel would be off resonant excitation via the 5s5p $^1P_1$-5s5d $^1D_2$ transition at 767 nm when the atom is in the excited state during imaging. As mentioned above, once this $^1D_2$ state is populated, the atom is very likely to decay to $^3P_2$. Because of this we tried adding different repumpers for depopulating both the $^3P_2$ and $^3P_0$ states but saw no significant change. A reason for this could have been anti trapping of the $^1D_2$ state causing heating or even direct atom loss before the desired decay can occur. This would be similar to the behavior seen for the 5s4d $^1D_2$ state in 515-nm tweezers [30, 44].

To further reduce the chance of off resonant scattering of the tweezer light, we chose

[7]Disclaimer: As we will mention later in the chapter, The actual trap depth was 400 μK.

[8]We note that this is still not a truly clear sign of cooling but at least we knew we were surviving the 689-nm light for extended periods

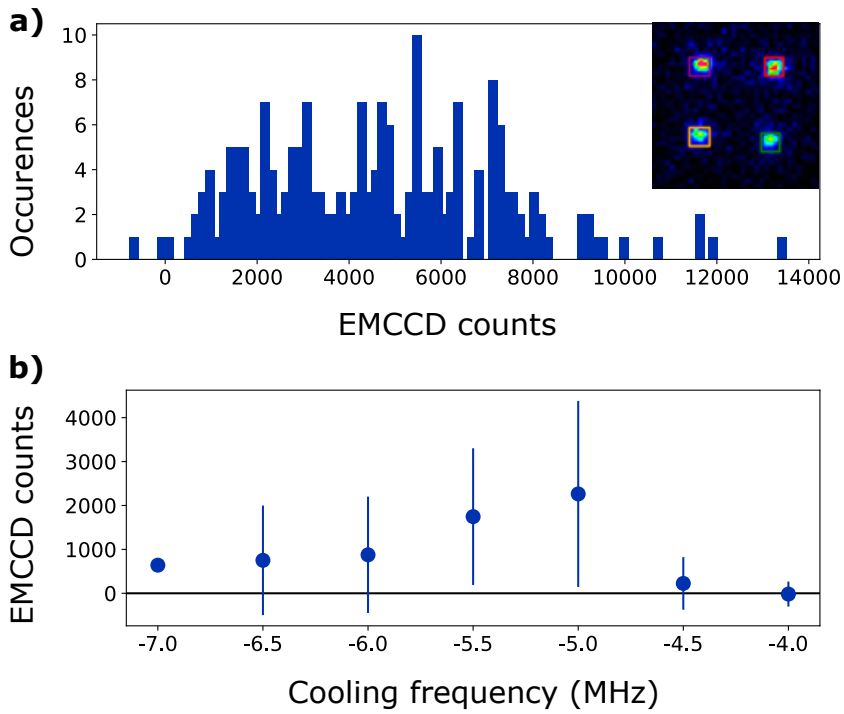

FIGURE 4.10: **(a)** A histogram of the number of occurrences vs EMCCD counts per ROI for 785 nm AOD tweezers loaded with at least one atom. A single broad peak above zero counts shows that at least one atom per tweezer has been loaded in every image. The data is for all four tweezer ROIs. The inset image shows the average image of all experimental runs used to make the histogram. **(b)** Scan of the 689-nm cooling laser frequency during imaging. The frequency is plotted as the detuning from the free-space resonance of the $^1S_0$ - $^3P_1$ transition. The increase in average EMCCD counts around -5 MHz indicates the cooling is working because the atoms are able to scatter more 461-nm photons before being lost from the tweezer. Throughout this section all data plotted in blue was taken using the blue imaging technique [32]. All data plotted in red was taken using our red imaging technique, see Chapter 2.

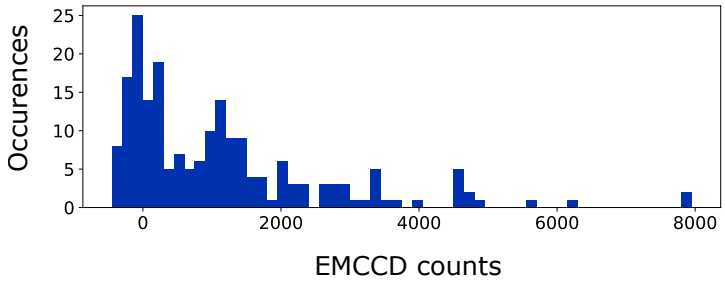

FIGURE 4.11: A histogram of the number of occurrences vs EMCCD counts per ROI for a long duration image of the 785 nm AOD tweezers. A combination of MOT light, cooling light, and 461-nm light were used before the image to try inducing light assisted collisions. The lack of two distinct peaks is indicative of a loss process or pumping to a metastable state before a sufficient number of photons were collected per atom.

to switch the tweezer laser source to 813-nm light. This choice was supported with the numerous nice results that had already been reported at this tweezer wavelength [32, 34, 35, 36, 57]. The tweezer optical setup was constructed with all achromatic lenses specifically for an easy conversion to this further detuned wavelength. With small realignments we were quickly able to recover the same signal.

With the new tweezer wavelength we again scanned the cooling frequency and found the best cooling around -3.5 MHz as shown in Fig. 4.12(a). This Stark shift is consistent with the smaller differential Stark shift of the $^1S_0$ - $^3P_1$ transition for 813-nm vs 785-nm, see Section 3.1. With the new tweezer laser the cooling performance still seemed insufficient to compensate for the heating induced by the 461-nm light. We again examined the situation of interleaved blue light ($\leq$1 ms at a time at 20-30 kHz scattering rate) followed by a long cooling cycle ($\leq$50 ms) for imaging, but for even longer images ($\sim$2 seconds) and less total blue light($\sim$30). With the right settings we began to see a stretch of what we assumed to be the single atom signal but still a lack of separation, see Fig. 4.12(b). At this point the only remaining issue could be from the cooling performance.

As mentioned in Section 2.7, the source of all 689-nm light is an external cavity diode laser (ECDL) that is short-term stabilized on a reference cavity with a linewidth of 35 kHz, which in turn is long-term stabilized (in length) on a spectroscopy signal. Light from the ECDL is amplified by injection locked lasers and then used on the experiment. The data presented in this section so far is done with the light directly from the ECDL.

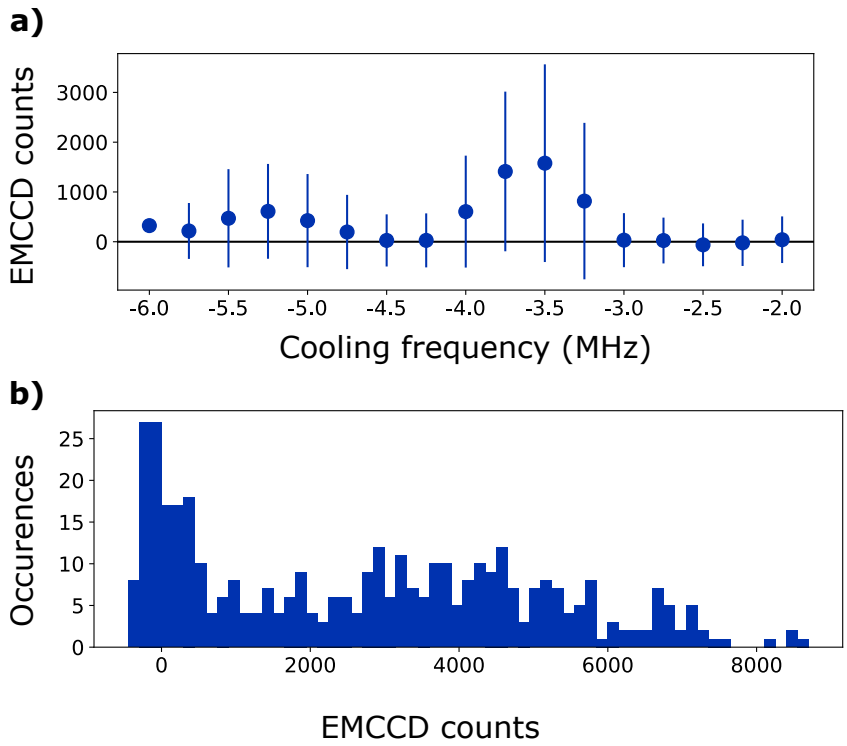

FIGURE 4.12: **(a)** Cooling frequency scan in 813 nm AOD tweezers. The frequency is plotted as the detuning from the free-space resonance of the $^1S_0$ - $^3P_1$ transition. The frequency has shifted with respect to Fig. 4.10 because of the change in differential Stark shift. **(b)** A histogram of the number of occurrences vs EMCCD counts per ROI for a long duration image of the 813 nm AOD tweezers. The lack of separation still points to a problem with cooling.

Based on results from our colleagues on the SrPAL team, we knew that there are so called servo bumps on the 689-nm laser [121]. Servo bumps are induced by the locking electronics pushing the noise of the free-running ECDL to a higher frequency outside the bandwidth of the locking electronics. This noise was already seen to have a negative effect on the SrPAL experiment, and the effort to use the very weak cavity transmission to injection lock an amplifying diode (without delocking the primary ECDL) had already been done[9]. Based on the improvement in cooling performance seen by the SrPAL team, we decided to switch the injection light of our amplifying diodes to the cavity-filtered light as well.

With the filtered light, we again went to look at loading and cooling performance. We directly saw better loading even when no cooling was applied. This could have to do with noise on the red MOT light heating atoms as they are loaded into the tweezer. When scanning the cooling frequency, we saw a very different looking plot for cooling, see Fig. 4.13(a). First, the frequency at which cooling starts to work is shifted by nearly two MHz, which is very similar to the edge of the servo bumps observed on the 689-nm ECDL [121]. Based on this observation, we were most likely using the servo bump for cooling as opposed to the carrier! This means that not only a much weaker but also a much noisier laser source for cooling was being used. It also means that our earlier trap depth estimation was wrong, and the actual trap depth was closer to 400 μK. Second, there seems to be a dip in performance around -1.5 MHz detuning. As will be discussed further, this dip is actually the frequency at which light assisted collisions are taking place. Third, the decrease in cooling performance seems to be much more gradual as we move to further red detuned frequencies. This could likely be related to the reduced noise and higher intensity of the cooling laser with the cavity-filtered light.

With the improved cooling performance, we attempted to look for single atoms. With very little effort, we saw our first clean single-atom signal, shown in Fig. 4.13(b). For this histogram the sequence is as follows. Atoms are loaded into the tweezers, the magnetic fields are set to zero at the location of the tweezers, 689-nm light is shone onto the atoms for 300 ms with a detuning of -1.5 MHz with an intensity of ~ 200 I_{sat}. Counter-propagating 461-nm beams are then shone for 2 ms with a detuning of -200 and -210 MHz for each beam with an intensity of 0.03 I_{sat}. The camera is then triggered to begin the fluorescence collection. During the image the cooling light is

[9] Thank you Chun Chia and Rodrigo! See [121] for details.

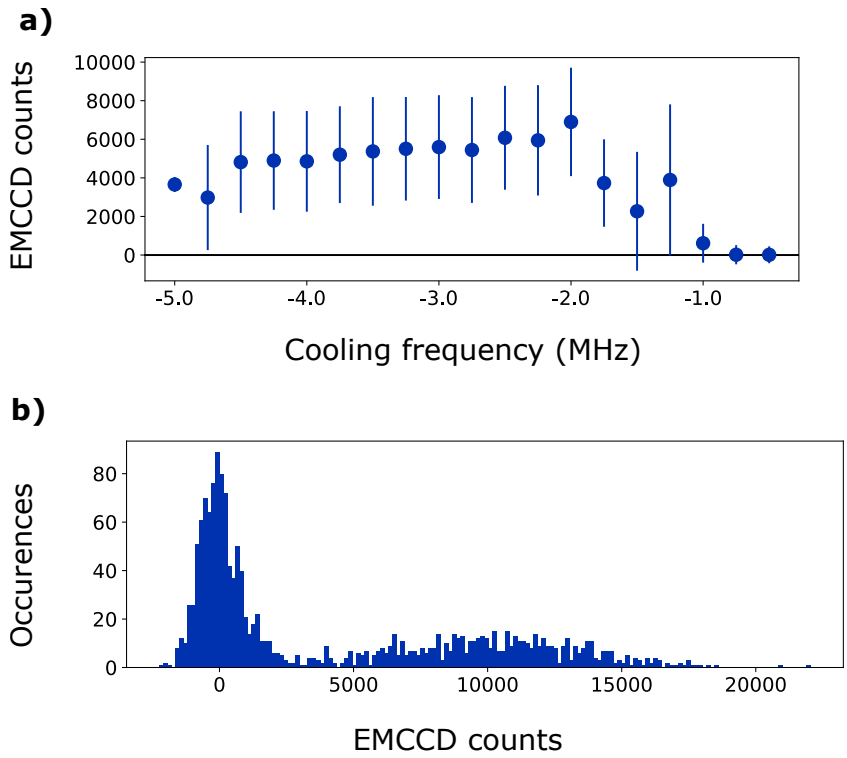

FIGURE 4.13: **(a)** Cooling frequency scan with cavity-filtered 689-nm light in 813 nm AOD tweezers. The frequency is plotted as the detuning from the free-space resonance of the $^1S_0$ - $^3P_1$ transition. The difference between this plot and the one of Fig. 4.12(a) is quite evident. First, even though the same tweezer trap depth is used, the cooling frequency has shifted significantly closer to resonance (-2 MHz instead of -3.5 MHz). Upon further investigation, one can also correlate the feature around -1.5 MHz to the frequency at which light assisted collisions occur, see Fig. 4.14. **b)** Our first histogram clearly indicating single atoms. To make this histogram we perform cooling at a detuning of -1.5 MHz at an intensity of 200 I_{sat} for 300 ms before the image. Counter-propagating 461-nm beams are then shone for 2 ms with a detuning of -200 and -210 MHz for each beam with an intensity of 0.03 I_{sat}. During the image the cooling light is left on continuously while the 461-nm light is blinked on for 1.25 ms every 5 ms for 50 cycles leading to a total image duration of 250 ms. Based on the differential Stark shift, we can estimate the trap depth of the tweezers to be 400 μK.

left on continuously while the 461-nm light is blinked on for 1.25 ms every 5 ms for 50 cycles leading to a total image duration of 250 ms.

After achieving a doubt free single-atom signal, we worked on optimizing the system by characterizing the light-assisted collision step, using the release and recapture method to determine the atom temperature, looking at lifetime under cooling conditions, adding repumper beams, and looking at different imaging parameters to reduce the time for a picture. These scans lead to similar results as presented in Section 2.4. We also estimated our tweezer waists to be about 0.8 μm by measuring the differential Stark shift of the optimal cooling at different trap depths and estimated the tweezer objective transmission for 813 nm to be lower than expected at 36% for our input beam waist. Aside from these quick optimizations and measurements, we did not spend much time on a robust optimization of the blue imaging technique and instead moved directly towards attempting narrow-line imaging with the $^1S_0$ - $^3P_1$ transition (red imaging).

The first step for converting to red imaging was swapping the dichroic mirror and camera filters. As mentioned above, the dichroic mirror for red imaging also supports blue imaging, although the 461-nm reflectance is a few percent lower (still $> 95\%$ reflectance). This allowed for us to swap the dichroic and realign the fluorescence imaging system back quickly with blue imaging. The camera filters on the other hand, specifically the band pass filter to minimize any background light, is unique for each imaging technique. We use a single lens tube with the two filters (one band pass filter and one cutoff filter) for each imaging technique. The filter tube is then screwed directly onto the iXon camera lens mount. The filter tubes can be swapped with minimal effect on the fluorescence imaging system by using the translation stage to move the imaging field lens.

After installing the proper filters on the camera, we began to look at the background noise on the camera. When using the same light for imaging and the final MOT stage, it is important to make sure no light remains on the table from the MOT beams. We place a mechanical shutter blocking all MOT light before the fibers that deliver the light to the experimental setup, instead of using just an AOM to extinguish the MOT beams. On occasions when this shutter has broken, we see that the few nanowatts of residual power from the AOM-attenuated, upward propagating MOT beam is much brighter than any single atom signal. This light could also be harmful as we move to shallower tweezer traps because it could induce heating.

Looking at camera exposures after a normal experimental sequence with all the lasers needed, we saw that every little reflection of red light contributed significantly to the background noise. Examples include badly aligned beams clipping on the chamber, beamsplitters for combining repumpers with the red imaging/cooling beam, the dichroic combining red and blue imaging beams, and reflections of the beam off other optical elements after it travels through the chamber. We were even able to see the remnants of the red MOT beams charging the electron wells of the camera pixels even when the camera was not in exposure mode. These problems were easily solved with better light management, including beam dumps, tented covers over beamsplitters and dichroic mirrors, shuttering off any beams that were not in use, and including an additional shutter in front of the camera to prevent any light from reaching it before exposure. The speed of the camera shutter does prevent imaging of the red MOT since the red MOT beams must be extinguished before the camera shutter is opened causing the MOT to fall and expand out of the focal plane before an image can be taken. This is not a hindrance once the tweezer loading fields are known. Small adjustments to MOT position can then be done by optimizing tweezer loading.

Before looking for a red imaging signal, the polarization of the red imaging/cooling beam needs to be rotated to horizontal (perpendicular to the tweezer propagation) to maximise the fluorescence into the tweezer objective. As mentioned above, at this time there was a 30° angle between the tweezer polarization, which defines the quantization axis, and the cooling beam propagation axis. The tweezer polarization defines the quantization axis since we work at near zero magnetic field as described in Section 3.1. This means the $\sigma^{\pm}$ intensity of the beam is 75% of the actual intensity. We tested this would not cause any issues with cooling performance with blue imaging first.

Our first imaging attempts at the previously characterized best cooling frequency for blue imaging resulted in extremely low counts that were nearly indiscernible from the zero atom signal. After scanning the imaging frequency, we saw the most fluorescence counts around -1.1 MHz as shown in Fig. 4.14(a). At first we thought this had something to do with a misalignment of the tweezers from switching the dichroic mirror, but we quickly realized it was more to do with the poor scattering rate at the optimum cooling frequency. We also saw that we could easily image the many-atom peak without causing light-assisted collisions. We then scanned the frequency of the light-assisted collision step and saw directly quite clean single-atom results, see Fig. 4.14(b) and (c) respectively.

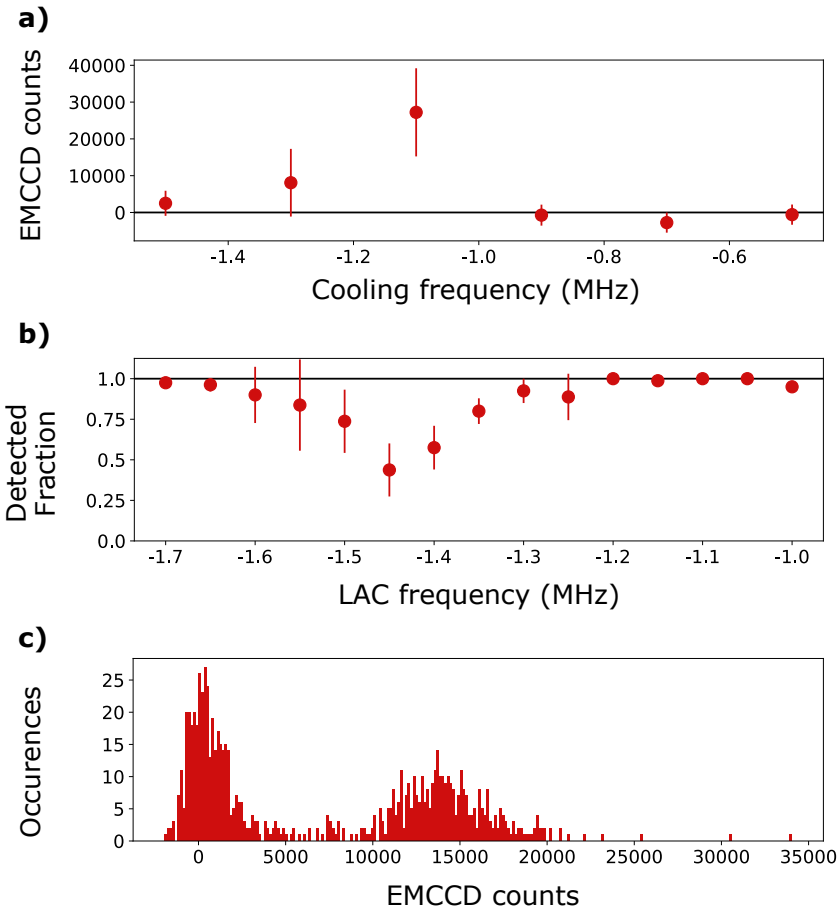

FIGURE 4.14: **(a)** EMCCD counts collected during a red image vs the red imaging frequency used in 400 μK deep tweezers. The imaging beam has an intensity of 200 I_{sat}. The frequency is plotted as the detuning from the free-space resonance of the $^1S_0$ - $^3P_1$ transition. **(b)** Probability of detecting a loaded tweezer (detected fraction) vs frequency used to induce light assisted collisions. At -1.45 MHz we observe a clear dip to 50%. (c) First histogram of red imaged single atoms. This series was taken in the absence of the cut-off filter used to remove reflected tweezer light from the image. This additional noise increases the width of the zero atom peak.

With these nice initial results, we began to further optimize the system. This led to additional observations of certain factors limiting the performance of our system. We noticed that stray magnetic fields have a significant affect on performance and imaging frequency, trap depth balancing will be crucial for best results, and good vacuum quality is important, see Section 4.4. We also began looking at performance at shallower trap depths but struggled to balance the tweezer trap depths sufficiently to have the same results in all tweezers. We assumed the problem with balancing came from either a lack of resolution in the built in DDS attenuators or from the fact that a single rf frequency controls two tweezers[10] making balancing the four traps non-trivial. Later on, when looking at scans of the AOD frequencies for atom sorting, we noticed an interrupted data line in the parallel bus controlling the DDS that could have also been responsible for the struggle to adequately balance trap depths. Nevertheless, it was at this point that we decided to install the SLM since it would not only lead to more tweezers, but also allow for balancing of the trap depths with modifications of the phase pattern sent to the array.

4.3.2 With SLM tweezers

Once we achieved nice red-imaging results, we moved on to installing the SLM. As mentioned above, we first characterized the SLM setup externally before transferring it onto the experimental setup. Once the system was installed, we began to look at larger arrays of tweezers. We noticed that the differential Stark shift of the $^1S_0$ - $^3P_1$ transition was significantly lower than measured for similar power per tweezer using the AODs. Our first assumption was poor alignment to the tweezer objective. After some optimizations we ruled out this as a significant source of the error. We decided to look at the image plane created by the SLM to characterize the initial waist and to look for aberrations. This allowed for us to see the presence of astigmatism in our foci. We corrected for this effect by using two slightly different cylindrical lens phases for the vertical and horizontal axes. Later, we added the external characterization system shown in Fig. 4.4 to the experimental setup allowing for observation of the tweezer

[10]For the four tweezer square grid used at this point, a single rf frequency controls the horizontal or vertical position and amplitude of two tweezers simultaneously. Since there are 4 frequencies and amplitudes and four tweezers, one would think it is possible to perfectly balance the trap depths but this cross talk makes it harder than expected. However, in the end the limiting factor could very well have come from the missing bit in the data sent to the DDSs that could have caused these issues. We did not recheck if the AOD tweezers could be balanced after connecting the data bus correctly.

foci on the machine, although with a copy of the objective[11]. This system is very helpful for additional characterizations of other optical aberrations along with alignment of the AOD tweezer array to the SLM array, especially in the axial direction. This will be discussed further in the following sections.

An additional $\lambda/2$ wave plate is used in the tweezer path. This is done to remove the angle between the tweezer polarization and the propagation direction of the cooling beam. Since a PBS cube is used for combining the two tweezer paths, the polarization of the SLM tweezers is perpendicular to the polarization of the AOD tweezers. This means that without the added waveplate 25% of the cooling beam intensity would be the proper polarization for cooling of SLM tweezers.

To properly align the SLM array through the tweezer objective we used a 10×10 array of tweezers. By measuring the red imaging frequency that induces the maximum fluorescence for each trap, we could align the array such that any gradients in trap depth or clipping due to alignment are removed. We concluded this procedure when the trap depth variation appears more random than patterned. An example of an early image in this alignment procedure along with an image at the end of the procedure is shown in Fig. 4.15.

We began to attempt single-atom preparation in the very shallow traps of this 100-site tweezer array. The maximum achievable trap depth for this array was only on the order of 60 μK. This depth is estimated using the approximately -300 kHz Stark shift of the $^1S_0$ - $^3P_1$ ($|m_j| = 1$) transition. In traps this shallow we were only able to poorly prepare and image single atoms. Atoms are easily lost from such shallow traps where the axial trap frequency is only about 4.8 kHz. Relating this back to our results and interpretations outlined in Section 2.4 and Section 3.3, this axial trap frequency is already significantly lower than the linewidth of the $^1S_0$ - $^3P_1$ transition and even approaches the photon recoil energy of 689-nm photons. Not only does this reduce the cooling performance based on the Sisyphus cooling mechanism, but at this depth we are no longer in the Lamb-Dicke regime. This means the atom is no longer guaranteed to decay to the same motional level. We decided to increase the trap depth by working with a smaller number of traps.

We started focusing on a 7×7 array to move closer to the regime where we knew red imaging still works based on our work with the AODs tweezers. However, even after

[11] There could still be small manufacturer differences between these two objectives. We did not do any direct comparison between the two objectives since the second objective was purchased at a later time

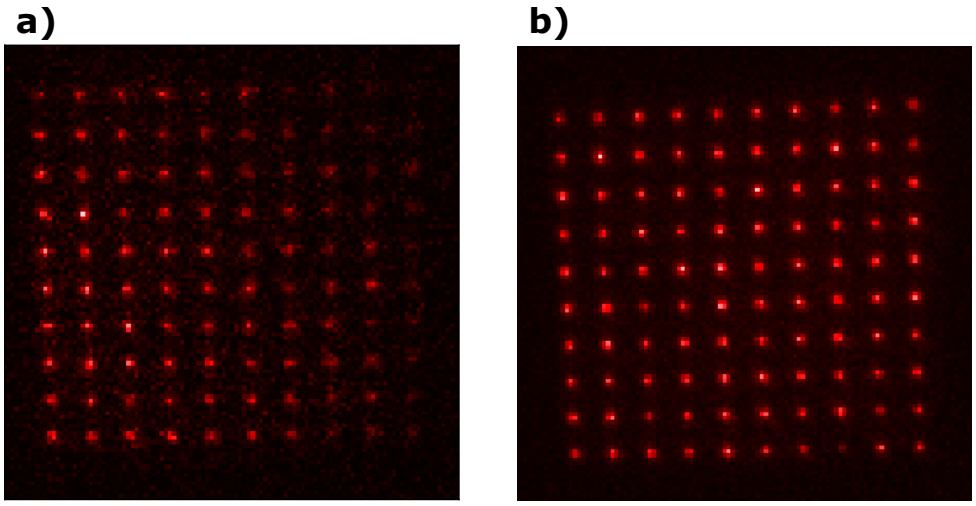

FIGURE 4.15: Averaged fluorescence images of a 10×10 at the **(a)** beginning and **(b)** end of the alignment procedure. The fainter tweezer sites are less regularly loaded or atoms in them more often removed by the imaging light. At the beginning a clear gradient is visible across the array where as at the end the variation in loading is random. The sensitivity of our red imaging technique to trap depths provides a useful tool for aligning and balancing the trap depths.

trap depth balancing (next section) and optimization of all parameters as discussed in Section 2.4, we still found a maximum survival fraction of the atom in a second picture of only 92%, see Section 2.4. We still saw good cooling performance and significantly long lifetimes at these trap depths but still had a loss that we couldn't remove. At this trap depth the axial trap frequency is still below the natural linewidth. Although we had surpassed the photon recoil energy, we came to the conclusion that slightly deeper traps were still required. This led to us switching to the 6×6 array used for the results in Chapter 2.

Aside from the square patterns used for optimizations and the results in Chapter 2, we have also made other SLM patterns and used them for trapping atoms in different geometries. In Fig. 4.16 we show examples of fluorescence images for different tweezer patterns. Some of these examples could be useful for quantum simulations while others were just for fun.

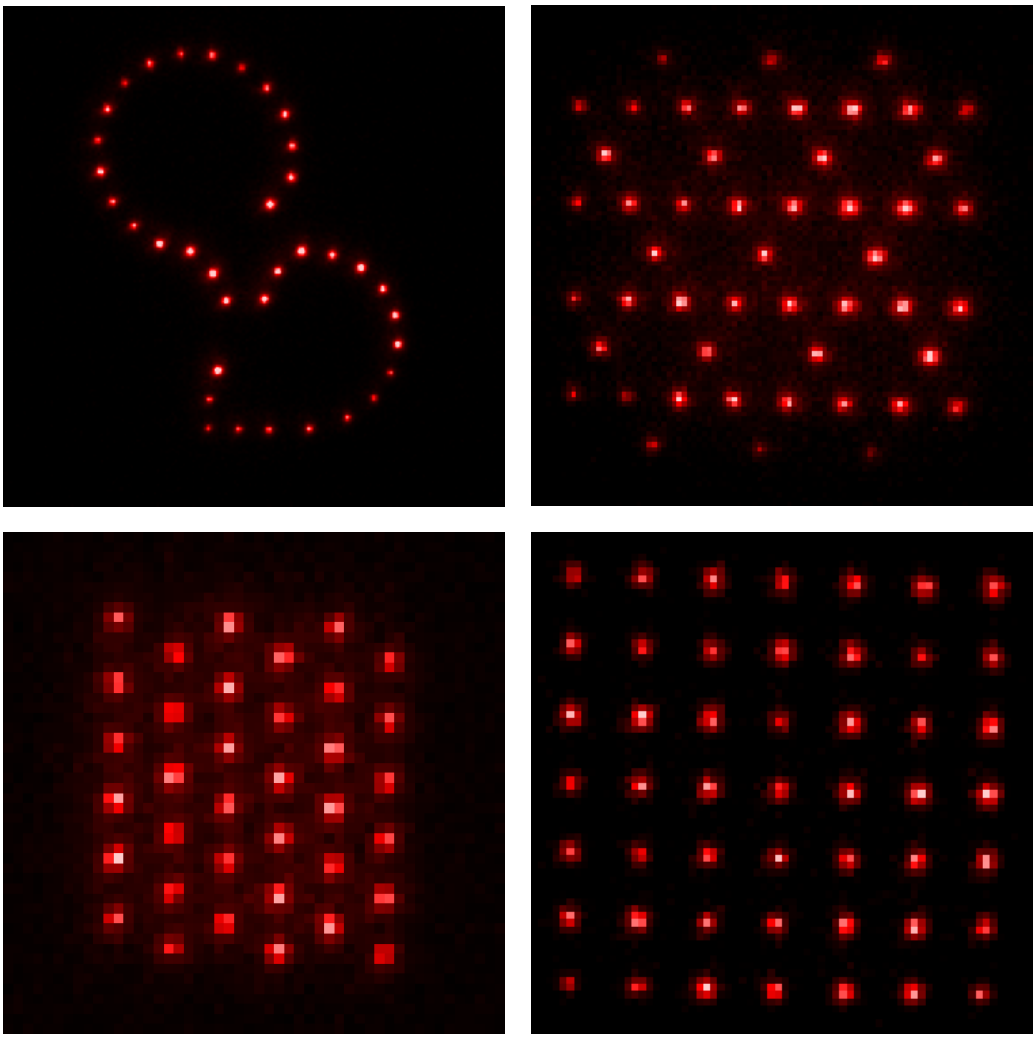

FIGURE 4.16: Atomic fluorescence images of atoms trapped in different SLM tweezer arrays. All images presented here are the average of many preparations and made using our red imaging technique. We have included the Quantum Delta NL logo that demonstrates nicely the ability to create an arbitrary pattern, a kagome lattice, a triangular lattice and a 7×7 square lattice.

4.4 Optimizations of tweezer performance

During the optimization of our single-atom survival in tweezers we have noticed a few critical elements that have helped us to achieve the best results. We have found three main parameters that must be optimized to achieve the highest survival rate aside from trap depth, and the frequency and intensity of the 689-nm laser during light-assisted collisions, cooling, and imaging steps. These three additional parameters are vacuum quality, magnetic field zeroing, and trap depth balancing.

We have found the vacuum quality to have a significant effect on the single-atom survival under imaging and cooling conditions even at the 10^{-10} mBar level. With pressure gauges built into our ion pump we are able to measure the pressure down to 1×10^{-10} mBar. Even after a few months of normal operation, the ion pump current was so low that we only can give this limit as upper estimation of the vacuum pressure. However, we do see that over this time period the single-atom lifetime in the tweezers had a significant decrease on the order of a factor of two. The vacuum quality in our science chamber can be improved by the use of titanium sublimation pumps installed on the apparatus. By coating the vacuum chamber with titanium, a getter material, we see an increase in the vacuum lifetime to the values reported in Chapter 2 without seeing a change in the ion pump current. Because of this increase in performance, we routinely fire the titanium sublimation pumps at least once a month when operating the experiment to maintain the best performance.

Our red imaging technique is a fantastic tool for both zeroing stray magnetic fields and for trap depth balancing of the tweezers. One disadvantage of using narrow-linewidth imaging on a Stark shifted resonance is that small variations in the field or traps can noticeably shift the imaging frequency. However, this can also be seen as an advantage during optimization since it provides a lot of information with a quick scan of the imaging frequency. We are able to gain this information just from the imaging frequency with highest fluorescence counts even with many atoms in the array. This is very useful for initial optimizations when the stray fields or trap depth variation can prevent or seriously affect single-atom production.

Zeroing magnetic fields at the location of the tweezers can be extremely tricky at low fields of a few hundred mG up to even 1 G because of competing quantization axes between the Zeeman and Stark shifts on the transition frequencies as discussed in Section 3.1. The differential shifts of the $|m_j| = 1$ sublevels of $^3P_1$ are also sensitive

to the angle between the magnetic field and tweezer polarization. Our method for zeroing the magnetic field components starts with applying a significant offset field of a few hundred mG along one Cartesian axis. With this biased field, we image tweezers filled with multiple atoms at different imaging frequencies. We then vary the field to minimize the splitting between the $|m_j| = 1$ resonances. The process is then repeated for each Cartesian axis which allows for us to determine the approximate magnetic field required for each axis to zero the magnetic field at the location of the tweezers.

Once the rough estimation of the best field is finished, we perform higher precision scans on single atom samples. The field is set to the assumed zero as the red MOT is shut off before the parity projection and a subsequent imaging process, where two back to back images are taken. We have found the survival fraction between first and second image to be the most sensitive parameter to the zero field calibration. We then scan the individual x, y, and z components of the magnetic field independently to find the highest survival fraction. This procedure is done in an iterative manner until we are satisfied with the final field and we see that the field has stabilized. We see an initial magnetization of our machine and small drift of the magnetic field throughout the day mainly in the z-axis (tweezer propagation axis). We usually perform these precision magnetic field scans every few hours to make sure the field stays at near zero. A more robust method would be to use the system development next door by the RbSr team for field monitoring and calibration. After the initial field zeroing process, we confirm the zeroing of the fields by the single, as narrow as possible, $|m_j| = 1$ line and by confirming that the relation between the $m_j = 0$ and $|m_j| = 1$ matches our calculations for the polarizability at zero magnetic field.

To balance the trap depths of the SLM we use a similar procedure as with the magnetic field zeroing. We find the initial calculated phase patterns usually have a standard deviation of around 7% for the tweezer trap depths measured on the atoms. We have found the same rough optimization as with the magnetic field zeroing procedure works well for the first iteration. We again use a sample of many atoms prepared in each tweezer and scan the imaging frequency to find the frequency of the maximum fluorescence. We use this frequency as an estimate of the trap depth and determine the deviation of each trap depth from the average. We use this deviation to modify the weights used for recalculating the tweezer pattern with the weighted Gerchberg Saxton algorithm as described in Section 4.2.

Further trap balancing is then done with spectroscopy of the weaker trapped $^3P_1$

m_j=0 state. Since this excited state is weaker trapped, there is a less significant broadening of the detected signal due to cooling[12]. At first, when the variation is still significant, scans can be done with 20 to 50 kHz precision. However, as the uniformity of the array increases, the precision of the scan should be increased. The deviation from the average center frequency is used to determine the weights for the next iteration of the phase pattern. An example of this procedure is shown in Fig. 4.17, where we show the deviation in center frequency after each iteration along with scans of the $^1S_0$ - $^3P_1$ m_j=0 spectroscopy for the initial phase pattern and final phase pattern after four iterations. We find the intensity converges down to the 1% level after only a few iterations. This is even better than what we report in the red imaging paper (Chapter 2) due mainly to some small technical changes such as better fit functions for the signal, finer resolution scans, and faster iteration from the fast Fourier transform code.

Finally, we have found the addition of Zernike polynomial phases to the calculated phase pattern helps us to reduce any aberrations from the tweezer optical system [122]. This additional step helps us to improve the waists of the tweezers instead of just balancing the intensity in each tweezer. Specifically, we use the rectangular Zernike polynomials outlined in [123]. To find the proper Zernike polynomials, we started with the external characterization imaging system. By taking images of the tweezers and fitting the tweezer waists for different polynomial phases we can reduce the size of the waists of the tweezers as measured by the characterization imaging system. Unfortunately this external calibration did not translate directly to the actual traps measured with atoms. The initial optimization did provide a good estimation and sign of the polynomials.

We again turn to many atoms trapped in tweezers to further optimize the values of the Zernike polynomials. We perform scans of the imaging frequency for different polynomials looking for the largest differential shift on the imaging frequency. This procedure has noticeably improved the size of our waists leading to a nearly 10 % decrease in size of the waist. This procedure could also be partially responsible for the improved uniformity that we can now achieve on the system since it has also been done to our patterns with highest uniformity.

We have found four polynomials to have the most significant contribution. The first two relate to the astigmatism from the SLM mentioned above in Section 4.2. More

[12]This is also because we look at a detected fluorescence signal on the $m_j = 1$ state instead of loss spectroscopy as done with the $m_j = 0$ spectroscopy.

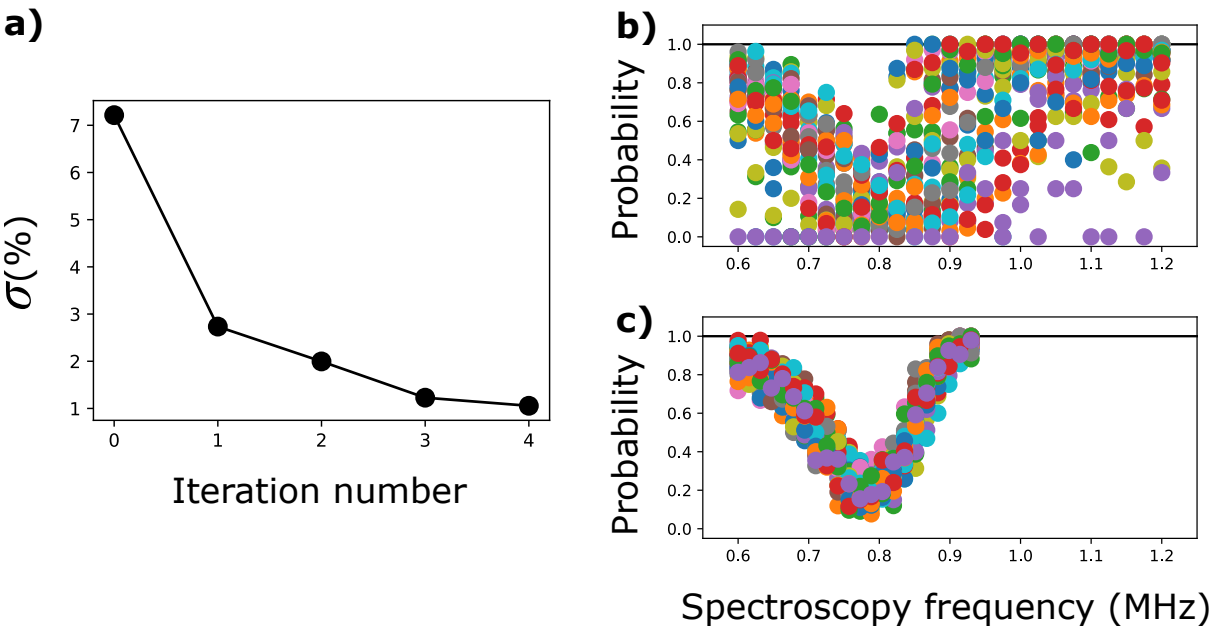

FIGURE 4.17: **(a)** Iteration number vs standard deviation of the center frequency of the loss spectroscopy feature. By using the measured center frequencies we can alter the weights of the weighted Gerchberg Saxton algorithm to balance the tweezer trap depths. After four iterations the deviation is less than 1% over the 36 tweezer sites. **(b)** Plot of the probability of detecting the atom in a second shot after the spectroscopy laser pulse vs spectroscopy frequency for a tweezer pattern before any additional balancing (Iteration zero). Because of the variation in trap depth it is hard to see a distinct line with all 36 tweezers plotted. The frequency is plotted as the detuning from the free-space resonance of the $^1S_0$ - $^3P_1$ transition. **(c)** Same as (b) but after four iterations. We now see a single loss feature for all traps.

specifically, if we use a normal Fresnel lens phase instead of the two cylindrical lens phases mentioned above, we find the contributions of astigmatism in x and y to be -0.8λ and 1.1λ respectively[13]. The other two significant contributions relate to the deviation in thickness between the vacuum window in our apparatus and the designed cover glass thickness (3.125 mm vs 3.5 mm respectively). This deviation causes primary spherical aberrations of the tweezers. We find the smallest waist for the primary spherical polynomial phase of magnitude 3λ[14]. This correction also causes a shift in the focal position since primary spherical aberrations are a focal position varying with radius at the pupil plane. To correct for the change in focus position, an additional defocus polynomial can be added as well. The magnitude of the defocus should be 1.5 times that of the spherical polynomial based on the formulas for the Zernike polynomials, see [123]. The individual Zernike polynomial phases that give the best results along with the sum correction phase are presented in Fig. 4.18.

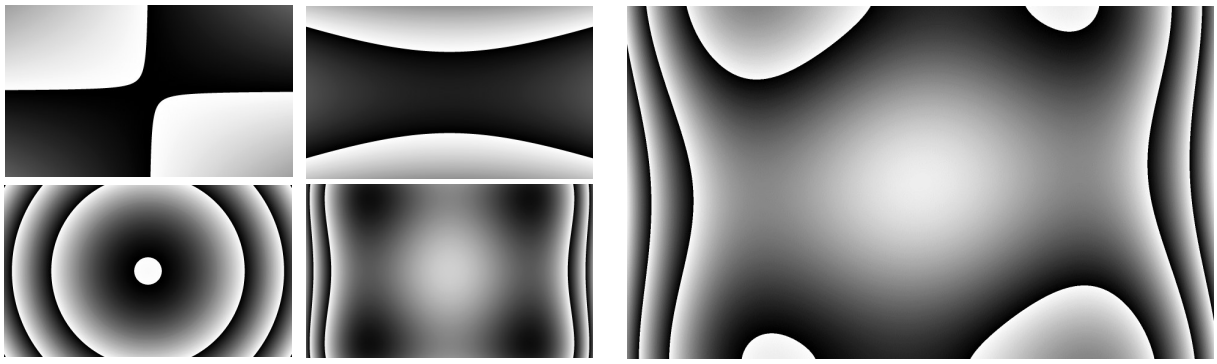

FIGURE 4.18: The four smaller images show the Zernike polynomial phases resulting from our Zernike polynomial optimization of the tweezer trap depths, see text for details. The top row has the x (left) and y (right) Astigmatism phases, and the bottom row has the primary spherical (left) and defocus (right) phases. The large image shows the sum of these four phases and is the correction phase used in our experiment.

[13]Aberrations of the optical system introduce wave front distortion, $W(x, y)$. The distortion can be quantified to a change in the wavefront phase using $\Delta\phi(x, y) = kW = 2\pi(W(x, y)/\lambda)$ [122]. We report the aberration correction phases in units of the period λ as is the common convention, see [112, 122] for more details. A negative λ correction shifts the focusing axis back to the proper focal plane and vice versa for positive λ.

[14]The positive correction phase corrects for inadequate focusing of the peripheral rays.

4.5 Site selective imaging and sorting

For both the site-selective imaging presented in Section 2.5 and sorting the randomly filled tweezer array into a defect-free array, we use the AODs to create an additional movable tweezer. This tweezer can be used to increase the Stark shift of a given tweezer site allowing for selective imaging of a given tweezer site. The movable tweezer can also be used to grab an atom from an SLM tweezer and drag it to a different SLM tweezer for sorting. In this section we will go over some initial observations from optimizing the site selective imaging along with our first results with sorting the tweezer array.

4.5.1 Site-selective imaging

Before either site-selective imaging or sorting could be performed, we needed to align the AODs relative to the SLM array. The characterization imaging system in Fig. 4.4 was used for this alignment. After aligning we chose frequencies for the AODs such that the tweezer from the AODs would overlap with a tweezer site of the SLM. At first we were only concerned with choosing a single site for studying site-selective imaging. The high resolution of the characterization imaging system also made alignment of the SLM and AODs foci along the propagation axis possible.

For our first attempts with site-selective imaging, we were only concerned if we could hide a single atom from the array. With the majority of the optical power going to the SLM array (the same trap depth of 135(20) μK as in Chapter 2 is used), we measured a maximum fluorescence of the AODs tweezer at a frequency of -700 kHz from the free space resonance of the $^1S_0$ - $^3P_1$ transition. By aligning the AOD tweezer to an SLM site and imaging at the normal SLM imaging frequency (-675 kHz), we directly saw that the site aligned to the AODs tweezer could be removed from the set of imaged tweezers, without losing the atom from the hidden trap. A series of three pictures in Fig. 4.19 shows an example of this result.

However, when attempting to image the hidden atom at the expected shifted imaging frequency (the sum of the shift of the two tweezers) we saw nothing even though the atom was still present in a third picture after the AODs have been switched off. A more thorough scan of the imaging frequency allowed us to see the atom, but at a frequency nearly half of what we expected for a single tweezer at -350 kHz from the

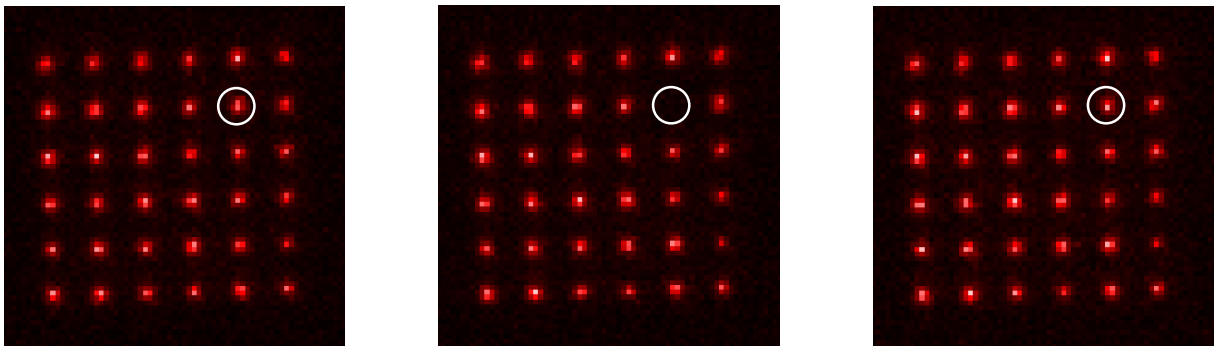

FIGURE 4.19: First time hiding an atom from the image. From left to right, the images show averaged images over 100 experimental runs for **(a)** the initially loaded array **(b)** the array with one site removed from the image by the addition of an AOD tweezer to that site, and **(c)** the final confirmation image with the AOD tweezer removed such that the whole array is again visible.

free space resonance, not even close to the expected shift for the sum of the two tweezers at -1.375 MHz. Although we are not sure why this effect happens, one hypothesis could be that the perpendicular polarization of the two tweezers with respect to each other leads to competing quantization axes. Because of this effect, we image the atoms using some super position of the $|m_j| = 1$ and $m_j = 0$ states of $^3P_1$. Before introducing the Zernike polynomial corrections to the phase pattern, we did not have sufficient power for both to create a 36 tweezer SLM pattern and to make the AODs tweezer deep enough to observe a further shifted imaging frequency. To combat this effect we sent more power to the AOD by reducing the power to the SLM. To still maintain deep enough tweezers we used a smaller 3×3 array instead of the usual 6×6 array. After introducing the Zernike polynomial phases onto the SLM the traps are now deep enough to make a 6×6 array and have a deep enough AODs tweezer.

4.5.2 Sorting

Sorting atoms into defect-free arrays is an important tool for quantum simulation and computation experiments in optical tweezers since the primary method for introducing interactions into the system is with Rydberg interactions. Since the strength of the Rydberg interaction is $\propto 1/r^6$, the interaction strength is highly sensitive to the spacing r between the atoms. Because of this, the randomly filled array after initial single atom preparation would not be well suited for most quantum simulation and computation

experiments. However, this problem has been circumvented through the use of an additional movable tweezer to sort atoms from tweezers that contain an atom but don't need one into sites that need an atom but don't have one in the pattern desired for the experiment [124, 125]. Here we will discuss the implementation of sorting in our system and present our first results of defect free arrays.

For sorting, we began with a full mapping of AOD frequencies to tweezer locations using the characterization imaging system. While performing this mapping, we observed jumps in the AOD tweezer position that were not smooth with changing frequency. This led us to examining the data transfer to the DDSs controlling the AOD frequencies. It was at this point that we found the disconnected parallel bus data line that sometimes occurred with the data being sent to the DDSs. This was easily fixed by exchanging the cables connecting the DDSs to the control system data bus.

After calibrating the AOD frequencies to tweezer positions, we could begin to try moving atoms to different sites. To simplify the initial tests, we moved a single row of atoms out of the traps and then moved the rest of the rows down one row as shown in Fig. 4.20. This tested our tweezer position calibration and ability to move atoms from all sites without having to worry about errors such as identifying which tweezer is filled, assigning locations or ordering moves. Once we confirmed that atoms could be moved we could then move on to modifying the control and camera software to perform the sorting.

We chose to implement the Hungarian algorithm for identifying the moves used in sorting the atoms [125, 126]. The Hungarian algorithm was developed as a solution to the assignment problem. It allows for us to calculate the cost of moving each atom to the desired location [126]. By minimizing the total cost of all moves, we can determine near optimal moves. To minimize the distance that atoms must travel, we use distance squared as the cost. The Hungarian algorithm does have a poor scaling with the number of sites considered. With the small arrays used in our system this is not a problem, however, with larger arrays other algorithms could be more beneficial[124].

The sorting procedure goes as follows. First we prepare single atoms and take an initial image. The camera server then analyses the number of counts in the predetermined ROIs of each tweezer and, based on an assigned threshold of EMCCD counts, decides whether each trap is empty or filled. The list of trap assignments is then sent to the control software. The trap assignments are used along with the Hungarian algorithm and desired pattern to assign the best moves. Once the best moves have been

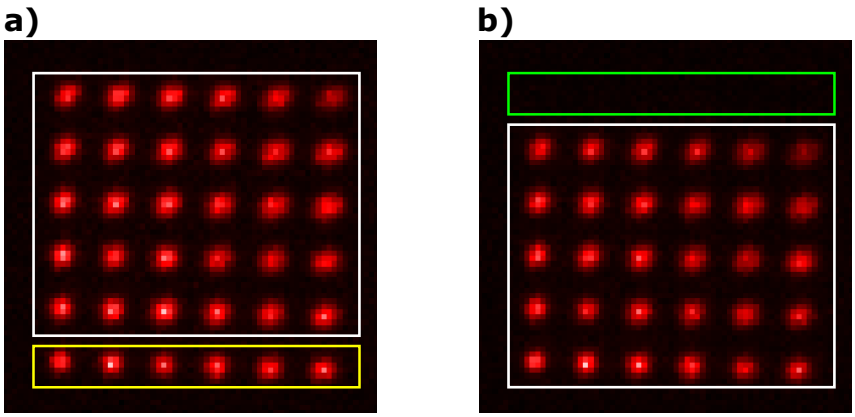

FIGURE 4.20: Averaged images from a test of our calibration of SLM tweezer locations to AOD frequencies. The first image on the left is to see which tweezer sites were loaded with an atom. The AOD tweezer is then used to remove any atoms from the tweezers in the yellow box. Atoms in the white box are then moved down to the row below one at a time in order to avoid accidentally placing two atoms in the same trap. The confirmation image on the right shows that the atoms have been moved down and the top row of traps (green box) are now empty. This procedure allowed for us to test moving the atoms without worrying about the calculation of moves.

assigned, the list of moves must be reordered to avoid any collisions during the sorting process that could lead to multiple atoms in a tweezer site and inevitably atom loss from light-assisted collisions during the confirmation image. The sorted list is then converted to AOD frequency sweeps using the previously calibrated frequency mapping. The required frequency sweeps of the AODs are then performed on the tweezer array to execute the sorting. A confirmation image is taken after all moves are completed to confirm the desired array has been prepared. An example of such a sorting can be seen in Fig. 4.21.

To optimize the survival of atoms during the sorting procedure we have examined survival in dependence of the speed of ramping the sorting tweezer on and off as well as the speed at which we move the atoms, see Fig. 4.22. These parameters are also dependent on the trap depth of our movable tweezer. For these results we use the maximum trap depth obtainable with our available power for the AOD tweezer, which is currently limited to about 400 μK ($\sim$ 3 times deeper than the tweezer array), see Section 2.5. We found that survival was more sensitive to the tweezer ramp on and off time than to the tweezer movement speed. For our tweezer trap depths (135 μK

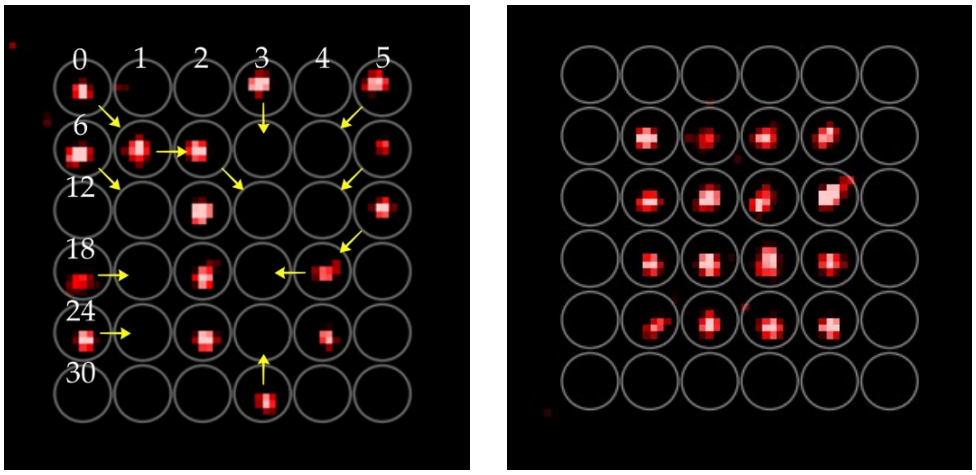

FIGURE 4.21: Two pictures providing an example of the sorting procedure in our experiment. The first image is used to determine which traps are filled. We use the Hungarian algorithm to assign the correct moves and then sort the moves to avoid any collisions. The moves are shown as yellow arrows, and the tweezer ROI numbers are shown in white. After the sorting is completed, we take a second image to confirm that the sorting has been successful.

for the array and 400 μK for the movable tweezer), we need to ramp on and off the sorting tweezer in about 1 ms and we can move the atom at a speed of 40 nm/μs for the best results defined as highest probability to detect the desired atom pattern on a verification image. The movement speed is most likely limited by the depth of the sorting tweezer. With these parameters we obtain a probability of preparing an atom in a desired trap of 0.97. This means, for the 16 filled trap pattern presented here, we prepare a defect free array 61% of the time, which is comparable to results shown by other groups [49, 124].

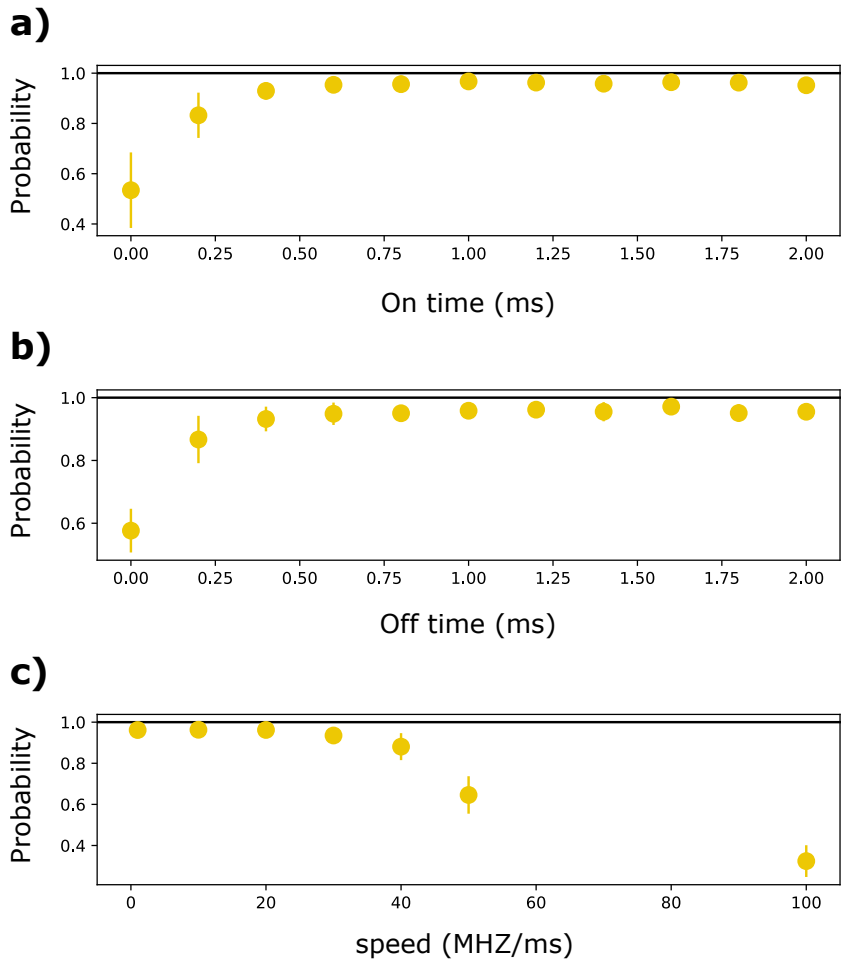

FIGURE 4.22: **(a)** Probability of preparing an atom in a desired trap vs AOD tweezer ramp on time. After approximately 1 ms the probability reaches its maximum of 0.97. **(b)** Same as (a) but for AOD tweezer ramp off time. **(c)** Probability of preparing an atom in a desired trap vs speed of the moving tweezer. The x-axis is plotted for change in rf-frequency of the AOD per ms. The frequency can be converted to a distance giving a max speed of 40 nm/μs (20 MHz/ms) before the speed affects the probability of performing the desired move.

Conclusion and outlook

In this thesis we have presented our results on constructing a defect-free array of single ^{88}Sr atoms in optical tweezers. This includes a detailed discussion and characterization of our narrow-linewidth imaging technique along with extra details of the experiment and our work on preparing defect-free arrays via atom sorting. We have also presented the theoretical calculations that helped us to characterize our system along with one of our theoretical ideas for future work of a possible qudit coupling scheme in ^{87}Sr.

Our experimental setup is able to consistently produce single atoms in arbitrary arrays, and sort the atoms into the desired sites. The main component missing in order to perform our first quantum simulation experiments is the ability to perform Rydberg excitation of the atoms for entanglement.

During the course of this thesis, Thies Plaßmann constructed a UV laser for exciting atoms from one of the ^3P_J states to either the $5sns\ ^3S_1$ or $5snd\ ^3D_J$ Rydberg series for states $n = 40$ to $n = 80$ [127]. The laser is constructed to be tunable from 316 - 324 nm in order to perform with this level of versatility. To accomplish this high level of tunability, the laser consists of two IR-fiber amplifiers seeded with external cavity diode lasers. The two lasers plus amplifiers are tunable from 1060-1090 nm and 1570-1600 nm, respectively, while still producing 5 W each. The light from the two amplifiers is then combined using sum frequency generation in order to produce light from 632 - 648 nm, which is then frequency-doubled via second harmonic generation to produce the required UV-light. The red light is also locked to an optical cavity whose length is controlled via our 689-nm laser in order to remove any long term drift in the cavities length. The cavity lock is able to reduce the short term linewidth of the laser to 11 kHz at 632-nm. For more details see Thies' thesis [127]. Thies was also awarded the 2022 Master thesis award by the Division of Atomic, Molecular, and Optical Physics of the Netherlands' Physical Society (NNV AMO).

With this laser, we can already explore quantum simulations taking advantage of a ground state to Rydberg qubit by either using one of the metastable $^3P_{0,2}$ states [57, 58],

or by excitation through the $^3P_1$ state [47, 60]. The UV laser system has now been installed into the experimental setup along with all (re)pump lasers for preparing atoms in a given metastable state (using lasers resonant with the $5s6s\ ^3S_1$ transitions) and the 408-nm laser for addressing the ion core transition for auto ionization [57] or for controlling the two qubit gate [47].

One possible extension of our experimental setup is the addition of 515 nm optical tweezers. Commercial laser sources at this wavelength can be purchased for up to 10 W. By utilizing our narrow-linewidth imaging technique, we could eliminate the loss channel exhibited by the blue imaging technique (loss via decay to the anti-trapped $^1D_2$ state) and perform high-fidelity imaging in trap depths as low as 80μK while still maintaining an axial trap frequency larger than the $^3P_1$ decay rate. Due to the large polarizability of the $^1S_0$ and $^3P_1$ states at 515 nm, tweezers with this trap depth would only require a few hundred μW per trap, making the production of several thousands of tweezer sites feasible, even with significant loss of laser power from optical components such as the SLM and microscope objective. New problems, such as the microscope field of view or loss of efficiency of the SLM for increasing deflection angles from the 0th order [49], would instead be the limiting factors for the number of tweezers. Tweezers at 515 nm would also trap atoms in Rydberg states as the ion core polarizability is less than the ponderomotive polarizability of the electron [61, 77] as already demonstrated in Yb [60]. As shown in Section 3.1, a magic angle between magnetic field and polarization exists for the $^1S_0$ - $^3P_2$ transition at 515 nm, which could be utilized for single qubit operations.

Another logical extension of our experimental capabilities would be to implement the necessary components in order to prepare and detect single ^{87}Sr atoms in tweezers. Our experimental setup is already able to produce a red MOT at the focal position of the microscope objective. We only lack certain magnetic field coils required for detection [46]. This would allow for us to analyse the performance of our narrow-linewidth imaging technique for nuclear-spin-state-specific detection and is a necessary step for implementing the qudit coupling scheme proposed in Section 3.4.

Finally, through our new collaboration with the Technische Universiteit Eindhoven through the Quantum Delta NL ecosystem, we plan to help investigate one- and two-qubit coupling schemes for use in a variational quantum eigensolver [128].

Bibliography

[1] A. Ashkin, *"Optical trapping and manipulation of neutral particles using lasers"*, Proc. Natl. Acad. Sci. USA **94** , 4853, 1997.

[2] A. Ashkin, *"Acceleration and Trapping of Particles by Radiation Pressure"*, Phys. Rev. Lett. **24** , 156, 1970.

[3] A. Ashkin, *"Trapping of Atoms by Resonance Radiation Pressure"*, Phys. Rev. Lett. **40** , 729, 1978.

[4] S. Chu, *"Cold atoms and quantum control"*, Nature **416** , 206, 2002.

[5] H. J. Metcalf and P. van der Straten, *"Laser cooling and trapping of atoms"*, J. Opt. Soc. Am. B **20** , 887, 2003.

[6] S. Chu, J. E. Bjorkholm, A. Ashkin, and A. Cable, *"Experimental Observation of Optically Trapped Atoms"*, Phys. Rev. Lett. **57** , 314, 1986.

[7] A. Ashkin and J. M. Dziedzic, *"Optical trapping and manipulation of viruses and bacteria"*, Science **235** , 1517, 1987.

[8] A. Ashkin, J. M. Dziedzic, and T. Yamane, *"Optical trapping and manipulation of single cells using infrared laser beams"*, Nature **330** , 769, 1987.

[9] A. Ashkin and J. M. Dziedzic, *"Internal cell manipulation using infrared laser traps"*, Proc. Natl. Acad. Sci. USA **86** , 7914, 1989.

[10] F. Schreck and K. van Druten, *"Laser cooling for quantum gases"*, Nat. Phys. **17** , 1296, 2021.

[11] M. H. Anderson, J. R. Ensher, M. R. Matthews, C. E. Wieman, and E. A. Cornell, *"Observation of Bose-Einstein condensation in a dilute atomic vapor"*, Science **269** , 198, 1995.

[12] I. Bloch, J. Dalibard, and S. Nascimbène, *"Quantum simulations with ultracold quantum gases"*, Nat. Phys. **8** , 267, 2012.

[13] F. Schäfer, T. Fukuhara, S. Sugawa, Y. Takasu, and Y. Takahashi, *"Tools for quantum simulation with ultracold atoms in optical lattices"*, Nat. Rev. Phys. **2** , 411, 2020.

[14] C. Gross and I. Bloch, *"Quantum simulations with ultracold atoms in optical lattices"*, Science **357** , 995, 2017.

[15] R. P. Feynman, *"Simulating physics with computers"*, Int. J. Theor. Phys. **21** , 467, 1982.

[16] D. Deutsch, *"Quantum theory, the Church-Turing principle and the universal quantum computer"*, Proc. R. Soc. Lond. A. **400** , 97, 1985.

[17] J. L. Brylinski and R. Brylinski, *"Universal quantum gates"*, Mathematics of Quantum Computation , 98, 2002.

[18] T. D. Ladd, F. Jelezko, R. Laflamme, Y. Nakamura, C. Monroe, and J. L. O'Brien, *"Quantum computers"*, Nature **464** , 45, 2010.

[19] M. A. Nielsen and I. L. Chuang, *"Quantum Computation and Quantum Information: 10th Anniversary Edition"*, Cambridge University Press 2011.

[20] D. Jaksch, J. I. Cirac, P. Zoller, S. L. Rolston, R. Côté, and M. D. Lukin, *"Fast Quantum Gates for Neutral Atoms"*, Phys. Rev. Lett. **85** , 2208, 2000.

[21] M. D. Lukin, M. Fleischhauer, R. Cote, L. M. Duan, D. Jaksch, J. I. Cirac, and P. Zoller, *"Dipole Blockade and Quantum Information Processing in Mesoscopic Atomic Ensembles"*, Phys. Rev. Lett. **87** , 037901, 2001.

[22] N. Schlosser, G. Reymond, I. Protsenko, and Philippe Grangier, *"Sub-poissonian loading of single atoms in a microscopic dipole trap"*, Nature **411** , 1024, 2001.

[23] A. Gaëtan, Y. Miroshnychenko, T. Wilk, A. Chotia, M. Viteau, D. Comparat, P. Pillet, A. Browaeys, and P. Grangier, *"Observation of collective excitation of two individual atoms in the Rydberg blockade regime"*, Nat. Phys. **5** , 115, 2009.

[24] E. Urban, T. A. Johnson, T. Henage, L. Isenhower, D. D. Yavuz, T. G. Walker, and M. Saffman, *"Observation of Rydberg blockade between two atoms"*, Nat. Phys. **5** , 110, 2009.

[25] T. Wilk, A. Gaëtan, C. Evellin, J. Wolters, Y. Miroshnychenko, P. Grangier, and A. Browaeys, *"Entanglement of two individual neutral atoms using rydberg blockade"*, Phys. Rev. Lett. **104** , 010502, 2010.

[26] M. Saffman, T. G. Walker, and K. Mølmer, *"Quantum information with Rydberg atoms"*, Rev. Mod. Phys. **82** , 2313, 2010.

[27] A. Browaeys and T. Lahaye, *"Many-body physics with individually controlled Rydberg atoms"*, Nat. Phys. **16** , 132, 2020.

[28] M. Morgado and S. Whitlock, *"Quantum simulation and computing with Rydberg-interacting qubits"*, AVS Quantum Sci. **3** 2021.

[29] S. Stellmer, F. Schreck, and T. C. Killian, *"Degenerate quantum gases of strontium"*, Annual Review of Cold Atoms and Molecules, World Scientific , 1, 2014.

[30] A. Cooper, J. P. Covey, I. S. Madjarov, S. G. Porsev, M. S. Safronova, and M. Endres, *"Alkaline-Earth Atoms in Optical Tweezers"*, Phys. Rev. X **8** , 041055, 2018.

[31] C. C. Chen, S. Bennetts, R. González Escudero, F. Schreck, and B. Pasquiou, *"Sisyphus optical lattice decelerator"*, Phys. Rev. A **100** , 023401, 2019.

[32] J. P. Covey, I. S. Madjarov, A. Cooper, and M. Endres, *"2000-Times Repeated Imaging of Strontium Atoms in Clock-Magic Tweezer Arrays"*, Phys. Rev. Lett. **122** , 173201, 2019.

[33] C. C. Chen, R. González Escudero, J. Minář, B. Pasquiou, S. Bennetts, and F. Schreck, *"Continuous Bose–Einstein condensation"*, Nature **606** , 683, 2022.

[34] M. A. Norcia, A. W. Young, W. J. Eckner, E. Oelker, J. Ye, and A. M. Kaufman, *"Seconds-scale coherence on an optical clock transition in a tweezer array"*, Science **366** , 93, 2019.

[35] I. S. Madjarov, A. Cooper, A. L. Shaw, J. P. Covey, V. Schkolnik, T. H. Yoon, J. R. Williams, and M. Endres, *"An Atomic-Array Optical Clock with Single-Atom Readout"*, Phys. Rev. X **9** , 041052, 2019.

[36] A. W. Young, W. J. Eckner, W. R. Milner, D. Kedar, M. A. Norcia, E. Oelker, N. Schine, J. Ye, and A. M. Kaufman, *"Half-minute-scale atomic coherence and high relative stability in a tweezer clock"*, Nature **588** , 408, 2020.

[37] M. A. Norcia, J. R. K. Cline, J. A. Muniz, J. M. Robinson, R. B. Hutson, A. Goban, G. E. Marti, J. Ye, and J. K. Thompson, *"Frequency Measurements of Superradiance from the Strontium Clock Transition"*, Phys. Rev. X **8** , 021036, 2018.

[38] T. Bothwell, C. J. Kennedy, A. Aeppli, D. Kedar, J. M. Robinson, E. Oelker, A. Staron, and J. Ye, *"Resolving the gravitational redshift across a millimetre-scale atomic sample"*, Nature **602** , 420, 2022.

[39] S. Taie, Y. Takasu, S. Sugawa, R. Yamazaki, T. Tsujimoto, R. Murakami, and Y. Takahashi, *"Realization of a* $\mathrm{SU}(2) \times \mathrm{SU}(6)$ *System of Fermions in a Cold Atomic Gas"*, Phys. Rev. Lett. **105** , 190401, 2010.

[40] O. Onishchenko, S. Pyatchenkov, A. Urech, C.C. Chen, S. Bennetts, G. A. Siviloglou, and F. Schreck, *"Frequency of the ultranarrow* $^1\mathrm{S}_0 -^3 \mathrm{P}_2$ *transition in* $^{87}\mathrm{Sr}$*"*, Phys. Rev. A **99** , 052503, 2019.

[41] J. R. Weggemans, A. Urech, A. Rausch, R. Spreeuw, R. Boucherie, F. Schreck, C. J. M. Schoutens, J. Minář, and F. Speelman, *"Solving correlation clustering with QAOA and a Rydberg qudit system: a full-stack approach"*, Quantum **6** , 687, 2022.

[42] S. Stellmer, *"Degenerate quantum gases of strontium"*, Ph.D. Thesis, University of Innsbruck 2013.

[43] S. Saskin, J. T. Wilson, B. Grinkemeyer, and J. D. Thompson, *"Narrow-Line Cooling and Imaging of Ytterbium Atoms in an Optical Tweezer Array"*, Phys. Rev. Lett. **122** , 14302, 2019.

[44] M. A. Norcia, A. W. Young, and A. M. Kaufman, *"Microscopic Control and Detection of Ultracold Strontium in Optical-Tweezer Arrays"*, Phys. Rev. X **8** , 041054, 2018.

[45] N. C. Jackson, R. K. Hanley, M. Hill, F. Leroux, C. S. Adams, and M. P. A. Jones, *"Number-resolved imaging of* ^{88}*Sr atoms in a long working distance optical tweezer"*, SciPost Phys. **8** , 038, 2020.

[46] K. Barnes, P. Battaglino, B. J. Bloom, K. Cassella, R. Coxe, N. Crisosto, J. P. King, S. S. Kondov, K. Kotru, S. C. Larsen, J. Lauigan, B. J. Lester, M. McDonald, E. Megidish, S. Narayanaswami, C. Nishiguchi, R. Notermans, L. S. Peng, A. Ryou, T. Y. Wu, and M. Yarwood, *"Assembly and coherent control of a register of nuclear spin qubits"*, arXiv:2108.04790 2021.

[47] S. Ma, A. P Burgers, G. Liu, J. Wilson, B. Zhang, and J. D Thompson, *"Universal gate operations on nuclear spin qubits in an optical tweezer array of* ^{171}*Yb atoms"*, arXiv:2112.06799 2021.

[48] A. Jenkins, J. W. Lis, A. Senoo, W. F. McGrew, and A. M. Kaufman, *"Ytterbium nuclear-spin qubits in an optical tweezer array"*, arXiv:2112.06732 2021.

[49] S. Ebadi, T. T. Wang, H. Levine, A. Keesling, G. Semeghini, A. Omran, D. Bluvstein, R. Samajdar, H. Pichler, W. W. Ho, S. Choi, S. Sachdev, M. Greiner, V. Vuletić, and M. D. Lukin, *"Quantum phases of matter on a 256-atom programmable quantum simulator"*, Nature **595** , 227, 2021.

[50] P. Scholl, . Schuler, H. J. Williams, A. A. Eberharter, D. Barredo, K. N. Schymik, V. Lienhard, L. P. Henry, T. C. Lang, T. Lahaye, A. M. Läuchli, and A. Browaeys, *"Quantum simulation of 2D antiferromagnets with hundreds of Rydberg atoms"*, Nature **595** , 233, 2021.

[51] K. N. Schymik, B. Ximenez, E. Bloch, D. Dreon, A. Signoles, F. Nogrette, D. Barredo, A. Browaeys, and T. Lahaye, *"In situ equalization of single-atom loading in large-scale optical tweezer arrays"*, Phys. Rev. A **106** , 022611, 2022.

[52] K. N. Schymik, S. Pancaldi, F. Nogrette, D. Barredo, J. Paris, A. Browaeys, and T. Lahaye, *"Single Atoms with 6000-Second Trapping Lifetimes in Optical-Tweezer Arrays at Cryogenic Temperatures"*, Phys. Rev. App. **16** , 034013, 2021.

[53] D. Bluvstein, H. Levine, G. Semeghini, T. T. Wang, S. Ebadi, M. Kalinowski, A. Keesling, N. Maskara, H. Pichler, M. Greiner, V. Vuletić, and M. D. Lukin, *"A quantum processor based on coherent transport of entangled atom arrays"*, Nature **604** , 451, 2022.

[54] T. M. Graham, Y. Song, J. Scott, C. Poole, L. Phuttitarn, K. Jooya, P. Eichler, X. Jiang, A. Marra, B. Grinkemeyer, M. Kwon, M. Ebert, J. Cherek, M. T. Lichtman, M. Gillette, J. Gilbert, D. Bowman, T. Ballance, C. Campbell, E. D. Dahl, O. Crawford, N. S. Blunt, B. Rogers, T. Noel, and M. Saffman, *"Multi-qubit entanglement and algorithms on a neutral-atom quantum computer"*, Nature **604** , 457, 2022.

[55] A. Urech, I. H. A. Knottnerus, R. J. C. Spreeuw, and F. Schreck, *"Narrow-line imaging of single strontium atoms in shallow optical tweezers"*, Phys. Rev. Research **4** , 023245, 2022.

[56] N. Schine, A. W. Young, W. J. Eckner, M. J. Martin, and A. M. Kaufman, *"Long-lived Bell states in an array of optical clock qubits"*, arXiv:2111.14653 2021.

[57] I. S. Madjarov, J. P. Covey, A. L. Shaw, J. Choi, A. Kale, A. Cooper, H. Pichler, V. Schkolnik, J. R. Williams, and M. Endres, *"High-fidelity entanglement and detection of alkaline-earth Rydberg atoms"*, Nat. Phys. **16** , 857, 2020.

[58] J. Choi, A. L. Shaw, I. S. Madjarov, X. Xie, J. P. Covey, J. S. Cotler, D. K. Mark, H. Y. Huang, A. Kale, H. Pichler, F. G. S. L. Brandão, S. Choi, and M. Endres, *"Emergent Randomness and Benchmarking from Many-Body Quantum Chaos"*, arXiv:2103.03535 2021.

[59] A. W. Young, W. J. Eckner, N. Schine, A. M. Childs, and A. M. Kaufman, *"Tweezer-programmable 2D quantum walks in a Hubbard-regime lattice"*, Science **377** , 885, 2022.

[60] J. T. Wilson, S. Saskin, Y. Meng, S. Ma, R. Dilip, A. P. Burgers, and J. D. Thompson, *"Trapping Alkaline Earth Rydberg Atoms Optical Tweezer Arrays"*, Phys. Rev. Lett. **128** , 033201, 2022.

[61] T. Topcu and A. Derevianko, *"Divalent Rydberg atoms in optical lattices: Intensity landscape and magic trapping"*, Phys. Rev. A **89** , 023411, 2014.

[62] O. Onishchenko, *"Ultracold atomic gases of strontium: production and narrow-line spectroscopy"*, Ph.D. Thesis, University of Amsterdam 2020.

[63] S. Piatchenkov, *"A versatile ultracold strontium apparatus: from construction to new tools for quantum simulation"*, Ph.D. Thesis, University of Amsterdam 2020.

[64] M. J. Martin, Y. Y. Jau, J. Lee, A. Mitra, I. H. Deutsch, and G. W. Biedermann, *"A Mölmer-Sörensen Gate with Rydberg-Dressed Atoms"*, arXiv:2111.14677 2021.

[65] W. B. Cairncross, J. T. Zhang, L. R.B. Picard, Y. Yu, K. Wang, and K. K. Ni, *"Assembly of a Rovibrational Ground State Molecule in an Optical Tweezer"*, Phys. Rev. Lett. **126** , 123402, 2021.

[66] S. Burchesky, L. Anderegg, Y. Bao, S. S. Yu, E. Chae, W. Ketterle, K. K. Ni, and J. M. Doyle, *"Rotational Coherence Times of Polar Molecules in Optical Tweezers"*, Phys. Rev. Lett. **127** , 123202, 2021.

[67] V. V. Ivanov and S. Gupta, *"Laser-driven Sisyphus cooling in an optical dipole trap"*, Phys. Rev. A **84** , 063417, 2011.

[68] S. Stellmer, B. Pasquiou, R. Grimm, and F. Schreck, *"Production of quantum-degenerate strontium gases"*, Phys. Rev. A. **87** , 013611, 2013.

[69] N. Schlosser, G. Reymond, and P. Grangier, *"Collisional Blockade in Microscopic Optical Dipole Traps"*, Phys. Rev. Lett. **89** , 023005, 2002.

[70] T. Zelevinsky, M. M. Boyd, A. D. Ludlow, T. Ido, J. Ye, R. Ciurylo, P. Naidon, and P. S. Julienne, *"Narrow Line Photoassociation in an Optical Lattice"*, Phys. Rev. Lett. **96** , 203201, 2006.

[71] M. Hirsch, R. J. Wareham, M. L. Martin-Fernandez, M. P. Hobson, and D. J. Rolfe, *"A Stochastic Model for Electron Multiplication Charge-Coupled Devices - From Theory to Practice"*, PLoS ONE **8** , e53671, 2013.

[72] A. Bergschneider, V. M. Klinkhamer, J. H. Becher, R. Klemt, G. Zürn, P. M. Preiss, and S. Jochim, *"Spin-resolved single-atom imaging of ^{6}Li in free space"*, Phys. Rev. A **97** , 063613, 2018.

[73] A. Urech, I. H. A. Knottnerus, R. J. C. Spreeuw, and F. Schreck, *"Data Package"* 2022.

[74] R. Taïeb, R. Dum, J. I. Cirac, P. Marte, and P. Zoller, *"Cooling and localization of atoms in laser-induced potential wells"*, Phys. Rev. A **49** , 4876, 1994.

[75] C. Tuchendler, A. M. Lance, A. Browaeys, Y. R.P. Sortais, and P. Grangier, *"Energy distribution and cooling of a single atom in an optical tweezer"*, Phys. Rev. A **78** , 033425, 2008.

[76] K. Singh, S. Anand, A. Pocklington, J. T. Kemp, and H. Bernien, *"A dual-element, two-dimensional atom array with continuous-mode operation"*, arXiv:2110.05515 2021.

[77] I. S. Madjarov, *"Entangling, controlling, and detecting individual strontium atoms in optical tweezer arrays"*, Ph.D. Thesis, California Institute of Technologoy, 2021.

[78] C. Ryan-Anderson, J. G. Bohnet, K. Lee, D. Gresh, A. Hankin, J. P. Gaebler, D. Francois, A. Chernoguzov, D. Lucchetti, N. C. Brown, T. M. Gatterman, S. K. Halit, K. Gilmore, J. Gerber, B. Neyenhuis, D. Hayes, and R. P. Stutz, *"Realization of real-time fault-tolerant quantum error correction"*, Phys Rev. X **11** , 041058, 2021.

[79] I. Sohn, J. Bang, and J. Heo, *"Dynamic Concatenation of Quantum Error Correction in Integrated Quantum Computing Architecture"*, Sci. Rep. **9** , 3302, 2019.

[80] S. Omanakuttan, A. Mitra, M. J. Martin, and I. H. Deutsch, *"Quantum Optimal Control of Nuclear Spin Qudecimals in ^{87}Sr"*, arXiv:2106.13705 2021.

[81] D. Banerjee, M. Bögli, M. Dalmonte, E. Rico, P. Stebler, U. J. Wiese, and P. Zoller, *"Atomic quantum simulation of U(N) and SU(N) Non-abelian lattice gauge theories"*, Phys. Rev. Lett. **110** , 125303, 2013.

[82] R. Mukherjee, J. Millen, R. Nath, M. P.A. Jones, and T. Pohl, *"Many-body physics with alkaline-earth Rydberg lattices"*, J. Phys. B **44** , 184010, 2011.

[83] F. Nogrette, H. Labuhn, S. Ravets, D. Barredo, L. Béguin, A. Vernier, T. Lahaye, and A. Browaeys, *"Single-atom trapping in holographic 2D arrays of microtraps with arbitrary geometries"*, Phys. Rev. X **4** , 021034, 2014.

[84] S. H. Autler and C. H. Townes, *"Stark Effect in Rapidly Varying Fields"*, Phys. Rev. **100** , 703, 1955.

[85] R. Grimm, M. Weidemüller, and Y. B. Ovchinnikov, *"Optical Dipole Traps for Neutral Atoms"*, Adv. At. Mol. Opt. Phys. **42** , 95, 2000.

[86] I. H. Deutsch and Poul S. Jessen, *"Quantum-state control in optical lattices"*, Phys. Rev. A **57** , 1972, 1998.

[87] J. T. M. Walraven, *"Atomic physics lectures"*, Lecture notes, University of Amsterdam 2018.

[88] M. S. Safronova, Z. Zuhrianda, U. I. Safronova, and Charles W. Clark, *"Extracting transition rates from zero-polarizability spectroscopy"*, Phys. Rev. A **92** , 040501, 2015.

[89] M. S. Safronova and S. G. Porsev, *"Properties of the $^3P_2$ state of Sr"*, Internal Communication 2019.

[90] B. Arora, M. S. Safronova, and C. W. Clark, *"Magic wavelengths for the $np-ns$ transitions in alkali-metal atoms"*, Phys. Rev. A **76** , 052509, 2007.

[91] C. Carr, *"Cooperative Non-Equilibrium Dynamics in a Thermal Rydberg Ensemble"*, Durham theses, Durham University, 2013.

[92] M. M. Boyd, T. Zelevinsky, A. D. Ludlow, S. Blatt, T. Zanon-Willette, S. M. Foreman, and J. Ye, *"Nuclear spin effects in optical lattice clocks"*, Phys. Rev. A **76** , 022510, 2007.

[93] L. Olschewski, *"Messung der magnetischen Kerndipolmomente an freien* ^{43}Ca-,^{87}Sr-,^{135}Ba-,^{137}Ba-,^{171}Yb- *und* ^{173}Yb-*Atomen mit optischem Pumpen"*, Z. Physik **249** , 205, 1972.

[94] F. Meinert, T. Pfau, and C. Hölzl, *"Quantum computing device, use, and method"*, EU Patent Application No. EP20214187.5 2021.

[95] A. M. Müller, M. Lajkó, F. Schreck, F. Mila, and J. Minář, *"State selective cooling of $SU(N)$ Fermi gases"*, Phys. Rev. A **104** , 013304, 2021.

[96] D. Plankensteiner, J. Schachenmayer, H. Ritsch, and C. Genes, *"Laser noise imposed limitations of ensemble quantum metrology"*, J. Phys. B: At. Mol. Opt. Phys. **49** 2016.

[97] N. Henkel, *"Rydberg-dressed Bose-Einstein condensates"*, Ph. D. Thesis, Technische Universität Dresden 2013.

[98] F. Diedrich, J. C. Bergquist, Wayne M. Itano, and D. J. Wineland, *"Laser Cooling to the Zero-Point Energy of Motion"*, Phys. Rev. Lett. **62** , 403, 1989.

[99] G. Morigi, J. Eschner, J. I. Cirac, and P. Zoller, *"Laser cooling of two trapped ions: Sideband cooling beyond the Lamb-Dicke limit"*, Phys. Rev. A **59** , 3797–3808, 1999.

[100] S. E. Hamann, D. L. Haycock, G. Klose, P. H. Pax, I. H. Deutsch, and P. S. Jessen, *"Resolved-Sideband Raman Cooling to the Ground State of an Optical Lattice"*, Phys. Rev. Lett. **80** , 4149, 1998.

[101] H. Perrin, A. Kuhn, I. Bouchoule, and C. Salomon, *"Sideband cooling of neutral atoms in a far-detuned optical lattice"*, EPL **42** , 395, 1998.

[102] J. D. Teufel, T. Donner, D. Li, J. W. Harlow, M. S. Allman, K. Cicak, A. J. Sirois, J. D. Whittaker, K. W. Lehnert, and R. W. Simmonds, *"Sideband cooling of micromechanical motion to the quantum ground state"*, Nature **475** , 359, 2011.

[103] K. B. Mo/ller, T. G. Jo/rgensen, and J. P. Dahl, *"Displaced squeezed number states: Position space representation, inner product, and some applications"*, Phys. Rev. A **54** , 5378, 1996.

[104] K. E. Cahill and R. J. Glauber, *"Ordered Expansions in Boson Amplitude Operators"*, Phys. Rev. **177** , 1857–1881, 1969.

[105] L. Albano, D. F. Mundarain, and J. Stephan, *"On the squeezed number states and their phase space representations"*, J. Opt. B: Quantum Semiclass. Opt **4** , 352–357, 2002.

[106] B. J. DeSalvo, M. Yan, P. G. Mickelson, Y. N. Martinez de Escobar, and T. C. Killian, *"Degenerate Fermi Gas of ^{87}Sr"*, Phys. Rev. Lett. **105** , 030402, 2010.

[107] S. Hadfield, Z. Wang, B. O'Gorman, E. G. Rieffel, D. Venturelli, and R. Biswas, *"From the Quantum Approximate Optimization Algorithm to a Quantum Alternating Operator Ansatz"*, Algorithms **12** , 34, 2019.

[108] N. Bansal, A. Blum, and S. Chawla, *"Correlation Clustering."* Machine Learning **56** , 89, 2004.

[109] S. G. Porsev and A. Derevianko, *"Hyperfine quenching of the metastable $^3P_{0,2}$ states in divalent atoms"*, Phys. Rev. A **69** , 042506, 2004.

[110] D. A. Steck, *"Quantum and atom optics"*, Lecture notes, University of Oregon 2007.

[111] D. P. O'Leary, G. K. Brennen, and S. S. Bullock, *"Parallelism for quantum computation with qudits"*, Phys. Rev. A **74** , 032334, 2006.

[112] I. H. A. Knottnerus, *"Tweezer machine for Sr atoms using a homebuilt microscope objective from commercial lenses"*, Master Thesis, University of Amsterdam 2018.

[113] I. H. A. Knottnerus, S. Pyatchenkov, O. Onishchenko, A. Urech, F. Schreck, and G. A. Siviloglou, *"Microscope objective for imaging atomic strontium with 0.63 micrometer resolution"*, Opt. Express **28** , 11106–11116, 2020.

[114] AA opto electronic, *"Acousto-optic Theory Application Notes"* 2013.

[115] A. Kaufman, *"Laser-cooling atoms to indistinguishability: Atomic Hong-Ou-Mandel interference and entanglement through spin-exchange"*, Ph.D. Thesis, University of Colorado 2015.

[116] R. M. W. van Bijnen, *"Quantum engineering with ultracold atoms"*, Ph.D. Thesis, Eindhoven University of technology 2013.

[117] R. Di Leonardo, F. Ianni, and G. Ruocco, *"Computer generation of optimal holograms for optical trap arrays"*, Opt. Express **15** , 1913, 2007.

[118] R. W. Gerchberg and W. O. Saxton, *"A Practical Algorithm for the Determination of Phase from Image and Diffraction Plane Pictures"*, Optik **35** , 237, 1972.

[119] H.Kim, M. Kim, W. Lee, and J. Ahn, *"Gerchberg-Saxton algorithm for fast and efficient atom rearrangement in optical tweezer traps"*, Opt. Express **27** , 2184, 2019.

[120] A. Bergschneider, *"Ultracold few-fermion systems in multiwell potentials"*, Master Thesis, University of Heidelberg 2013.

[121] C. C. Chen, *"An atomic marble run to unity phase-space density"*, Ph.D. Thesis, University of Amsterdam 2019.

[122] K. D. Wulff, D. G. Cole, R. L. Clark, R. DiLeonardo, J. Leach, J. Cooper, G. Gibson, and M. J. Padgett, *"Aberration correction in holographic optical tweezers"*, Opt. Express **14** , 4169, 2006.

[123] P. He, X. Zong, and R. Fu, *"Zernike polymomials for rectangular area and applications in off-axis asphere testing"*, Proc. SPIE 7656, 5th International Symposium on Advanced Optical Manufacturing and Testing Technologies: Optical Test and Measurement Technology and Equipment , 765615, 2010.

[124] K. N. Schymik, V. Lienhard, D. Barredo, P. Scholl, H. Williams, A. Browaeys, and T. Lahaye, *"Enhanced atom-by-atom assembly of arbitrary tweezer arrays"*, Phys. Rev. A **102** , 063107, 2020.

[125] W. Lee, H. Kim, and J. Ahn, *"Defect-free atomic array formation using the Hungarian matching algorithm"*, Phys. Rev. A **95** , 053424, 2017.

[126] F. Bourgeois and J. C. Lassalle, *"An Extension of the Munkres Algorithm for the Assignment Problem to Rectangular Matrices"*, Commun. ACM **14** , 802, 1971.

[127] T. Plaßmann, *"A strontium Rydberg laser for quantum simulation with tweezer arrays"*, Master Thesis, University of Amsterdam 2021.

[128] J. Tilly, H. Chen, S. Cao, D. Picozzi, K. Setia, Y. Li, E. Grant, L. Wossnig, I. Rungger, G. H. Booth, and J. Tennyson, *"The Variational Quantum Eigensolver: A review of methods and best practices"*, Phys. Rep. **986** , 1, 2022.

Summary

Single strontium atoms held in optical tweezers have so far only been imaged using the broad $^1S_0$ - $^1P_1$ transition. For Yb, use of the narrow (183 kHz-wide) $^1S_0$ - $^3P_1$ transition for simultaneous imaging and cooling has been demonstrated in tweezers with a magic wavelength for the imaging transition. We demonstrate high-fidelity imaging of single Sr atoms using its even narrower (7.4 kHz-wide) $^1S_0$ - $^3P_1$ transition. The atoms are trapped in *non*-magic-wavelength tweezers. We detect the photons scattered during Sisyphus cooling, thus keeping the atoms near the motional ground state of the tweezer throughout imaging. The fidelity of detection is 0.9991(4) with a survival probability of 0.97(2). An atom in a tweezer can be held under imaging conditions for 79(3) seconds allowing for hundreds of images to be taken, limited mainly by background gas collisions. The use of a fully closed (cycling) transition for imaging will provide a useful tool for state specific detection. We detect atoms in an array of 36 tweezers using 813.4-nm light and trap depths of 135(20) μK. This trap depth is three times shallower than typically used for imaging on the broad $^1S_0$ - $^1P_1$ transition. Narrow-line imaging opens the possibility to even further reduce this trap depth, as long as all trap frequencies are kept larger than the imaging transition linewidth. Imaging using a narrow-linewidth transition in a non-magic-wavelength tweezer also allows for selective imaging of a given tweezer. As a demonstration, we selectively image (hide) a single tweezer from the array. This provides a useful tool for quantum error correction protocols. This is the main experimental result of this thesis [55].

We continue with some theoretical calculations including calculations that are important for the main experimental result along with a possible future quantum computation scheme based on qudits. These calculations include discussions of how light and magnetic fields affect the internal states of the atom and outline how to calculate the polarizability (light shift) and Zeeman shift for different internal states of strontium including for states of fermionic ^{87}Sr. Calculating these shifts accurately is important for characterizing trap depths, and to find magic-wavelengths between different internal states. We also cover in detail our simulation of the attractive Sisyphus cooling

process mentioned in [55] including additional results and limits of the cooling parameters. The simulation outlined here also works for other types of laser cooling in an optical tweezer, including sideband cooling and *repulsive*-Sisyphus cooling. Finally, the theoretical section concludes with the main theoretical result of this thesis, which was the author's main contribution to the publication "Solving correlation clustering with QAOA and a Rydberg qudit system: a full-stack approach" [41]. Here, we propose a single qudit coupling scheme in ^{87}Sr. We calculate the required transition dipole moments for varying magnetic field strength in order to determine coupling strengths, analyse the dominant error sources and summarize the limits or required parameters, and present a possible method for experimental implementation.

The thesis continues with some additional experimental details and results. This section's primary focus is to give additional details that were excluded from [55] and tries to highlight the methods that we found useful in initially acquiring single atom results. This includes a brief overview of the experimental setup, an outline of the optical setup of the tweezer system including the alignment and characterization procedure along with the alignment to the vacuum chamber, and our initial results with NIR-tweezers including the wavelengths of 785 nm and 813 nm. We focus on our preliminary results and first signs of single atoms in order to help future experiments work through this initial period as fast as possible. We also include our first red imaging results and alignment of the spatial light modulator tweezer array after our first single atom results. We also mention some of the critical parameters that we have found to help significantly improve the performance of our experimental setup and allow for us to achieve the results presented in [55]. We finish the main content of the thesis by presenting some additional information on our site-selective imaging technique and our results on using an additional movable tweezer to sort the atoms into a defect-free array. This process is required for using Rydberg excitation of the atoms for engineering interactions between atoms in different tweezer sites. Finally in the outlook and conclusion we mention our ongoing work towards Rydberg excitation of atoms in the array and conclude.

Samenvatting

Enkele strontium atomen in optische tweezers zijn tot op heden enkel afgebeeld via de brede $^1S_0$ - $^1P_1$ overgang. Voor Yb is de nauwe ((183 kHz-breed) $^1S_0$ - $^3P_1$ overgang gebruikt voor gelijktijdig afkoelen en afbeelden van atomen in tweezers met een magische golflengte voor deze overgang. Wij demonstreren het afbeelden van enkele Sr atomen met hoge fidelity , gebruikmakend van de nog nauwere (7.4 kHz-breed) $^1S_0$ - $^3P_1$ overgang in Sr. De atomen zijn gevangen in niet-magische-golflengte tweezers. We detecteren de fotonen die verstrooid worden tijdens het Sisyphus koelen van de atomen, waardoor de atomen rond de bewegingsgrondtoestand van de tweezer blijven gedurende het afbeelden. De fidelity van het afbeelden is 0.9991(4), waarbij de atomen een overlevingskans hebben van 0.97(2). Een atoom in een tweezer kan 79(3) seconden gehouden worden in de afbeeldingsomstandigheden, waardoor er honderden afbeeldingen gemaakt kunnen worden van het enkele atoom. Dit getal is voornamelijk gelimiteerd door botsingen met overige deeltjes in het vacuum. Het gebruik van een bijna gesloten transitie voor het afbeelden zou nuttig kunnen zijn voor het detecteren van specifieke toestanden. We detecteren atomen in een rooster van 36 tweezers gemaakt van 813.4 nm licht met een valdiepte van 135(20) μK. Deze valdiepte is drie keer kleiner dan gebruikelijk bij het afbeelden met de brede $^1S_0$ - $^1P_1$ overgang. Narrow-line afbeelden staat toe om de valdiepte nog verder te verminderen, zolang alle valfrequenties groter blijven dan lijnbreedte van de overgang gebruikt voor het afbeelden. Afbeelden met een nauwe overgang in een niet-magische tweezer kan ook gebruikt worden als valspecifieke afbeeldingstechniek. Ter demonstratie, verbergen we en beelden we selectief één enkele tweezer uit het rooster af. Dit is een nuttige techniek voor foutencorrectie in quantum computing. Bovenstaande vormt het voornaamste experimentele resultaat van dit proefschrift [55].

We presenteren daarnaast enkele theoretische berekeningen, waaronder berekeningen die belangrijk zijn voor het experimentele werk en een mogelijke implementatie van quantum computing gebaseerd op qudits. Deze berekeningen gaan in op hoe licht- en magneetvelden de interne toestanden van het atoom beïnvloeden en schetsen

hoe de polariseerbaarheid en de Zeeman verschuivingen voor verschillende interne toestanden van strontium, waaronder het fermionische ^{87}Sr, berekend kunnen worden. Het berekenen van deze verschuivingen is belangrijk voor het karakteriseren van valdieptes en om magische golflengtes tussen verschillende interne toestanden. De simulatie van het attractieve-Sisyphus-koelingsproces dat genoemd wordt in [55] wordt uitgebreid behandeld en gepresenteerd met extra resultaten en limieten van de koelingsparameters. Deze simulatie werkt ook voor andere koelprocessen in een optische tweezer, waaronder sideband cooling en repulsive-Sisyphus cooling. De theoretische sectie besluit met het belangrijkste theoretische resultaat in dit proefschrift, namelijk de bijdrage die de auteur heeft geleverd aan het artikel "Solving correlation clustering with QAOA and a Rydberg qudit system: a full-stack approach" [41]. Daarin stellen we een qudit koppelingsschema voor in ^{87}Sr. De benodigde overgangsdipoolmomenten bij veranderende magnetische veldsterkte worden berekend om de koppelingssterkte te berekenen, de grootste oorzaken van fouten worden bestudeerd en de limieten van parameters worden samengevat, en een mogelijke experimentele implementatie wordt gepresenteerd.

Het proefschrift vervolgt met enkele andere experimentele details en resultaten. Het hoofddoel van deze sectie is om details te belichten die niet in [55] aan bod kwamen en er is getracht de methodes toe te lichten die nuttig waren bevonden in het verkrijgen van de eerste resultaten met enkele atomen. Hieronder valt een kort overzicht van de experimentele opstelling, een omschrijving van de optische opstelling van het tweezersysteem met procedures voor uitlijnen en karakterisatie, en de eerste resultaten met tweezers van golflengte 785nm en 813nm. De focus ligt vooral op eerste resultaten en eerste tekenen van enkele atomen, in de hoop dat toekomstige experimentalisten werk bespaard blijft. Daarnaast zijn ook de eerste resultaten met het roodlicht-afbeelden en uitlijnen van de spatial light modulator tweezers na het verkrijgen van de eerste resultaten. Daarnaast worden enkele kritieke parameters genoemd die significant de werking van onze experimentele opstelling verbeterd hebben en het mogelijk maakten om de resultaten in [55] te behalen. Daarna wordt extra informatie gegeven over de valspecieke afbeeldingstechniek en de resultaten van het gebruiken van een extra beweegbare tweezer om de atomen te sorteren tot een compleet gevuld rooster. Dit proces is nodig voor het gebruiken van Rydberg excitaties van de atomen om interacties tussen atomen in verschillende tweezers te genereren. Als laatst worden de vorderingen tot Rydberg excitaties van de atomen besproken en een conclusie

gegeven.

Single strontium atoms held in optical tweezers have so far only been imaged using the broad transition. For Yb, use of the narrow (183 kHz-wide) $^1S_0$ - $^3P_1$ transition for simultaneous imaging and cooling has been demonstrated in tweezers with a magic wavelength for the imaging transition. We demonstrate high-fidelity imaging of single Sr atoms using its even narrower (7.4 kHz-wide) $^1S_0$ - $^3P_1$ transition. The atoms are trapped in *non*-magic-wavelength tweezers. We detect the photons scattered during Sisyphus cooling, thus keeping the atoms near the motional ground state of the tweezer throughout imaging. The fidelity of detection is 0.9991(4) with a survival probability of 0.97(2). An atom in a tweezer can be held under imaging conditions for 79(3) seconds allowing for hundreds of images to be taken, limited mainly by background gas collisions. The use of a fully closed (cycling) transition for imaging will provide a useful tool for state specific detection. We detect atoms in an array of 36 tweezers using 813.4-nm light and trap depths of 135(20) μK. This trap depth is three times shallower than typically used for imaging on the broad $^1S_0$ - $^1P_1$ transition. Narrow-line imaging opens the possibility to even further reduce this trap depth, as long as all trap frequencies are kept larger than the imaging transition linewidth. Imaging using a narrow-linewidth transition in a non-magic-wavelength tweezer also allows for selective imaging of a given tweezer. As a demonstration, we selectively image (hide) a single tweezer from the array. This provides a useful tool for quantum error correction protocols. This is the main experimental result of this thesis [55].

We continue with some theoretical calculations including calculations that are important for the main experimental result along with a possible future quantum computation scheme based on qudits. These calculations include discussions of how light and magnetic fields affect the internal states of the atom and outline how to calculate the polarizability (light shift) and Zeeman shift for different internal states of strontium including for states of fermionic ^{87}Sr. Calculating these shifts accurately is important for characterizing trap depths, and to find magic-wavelengths between different internal states. We also cover in detail our simulation of the attractive Sisyphus cooling process mentioned in [55] including additional results and limits of the cooling parameters. The simulation outlined here also works for other types of laser cooling in an optical tweezer, including sideband cooling and *repulsive*-Sisyphus cooling. Finally, the theoretical section concludes with the main theoretical result of this thesis, which was the author's main contribution to the publication "Solving correlation clustering

with QAOA and a Rydberg qudit system: a full-stack approach" [41]. Here, we propose a single qudit coupling scheme in ^{87}Sr. We calculate the required transition dipole moments for varying magnetic field strength in order to determine coupling strengths, analyse the dominant error sources and summarize the limits or required parameters, and present a possible method for experimental implementation.

The thesis continues with some additional experimental details and results. This section's primary focus is to give additional details that were excluded from [55] and tries to highlight the methods that we found useful in initially acquiring single atom results. This includes a brief overview of the experimental setup, an outline of the optical setup of the tweezer system including the alignment and characterization procedure along with the alignment to the vacuum chamber, and our initial results with NIR-tweezers including the wavelengths of 785 nm and 813 nm. We focus on our preliminary results and first signs of single atoms in order to help future experiments work through this initial period as fast as possible. We also include our first red imaging results and alignment of the spatial light modulator tweezer array after our first single atom results. We also mention some of the critical parameters that we have found to help significantly improve the performance of our experimental setup and allow for us to achieve the results presented in [55]. We finish the main content of the thesis by presenting some additional information on our site-selective imaging technique and our results on using an additional movable tweezer to sort the atoms into a defect-free array. This process is required for using Rydberg excitation of the atoms for engineering interactions between atoms in different tweezer sites. Finally in the outlook and conclusion we mention our ongoing work towards Rydberg excitation of atoms in the array and conclude.

List of publications

- A. Urech, I. H. A. Knottnerus, R. J. C. Spreeuw, and F. Schreck, *"Narrow-line imaging of single strontium atoms in shallow optical tweezers"*, Phys. Rev. Research 4, 023245, 2022. (Chapter 2 of this thesis)

  Contribution: Major work of this thesis. Modified ultracold strontium apparatus to a single atom optical tweezer experiment. Formulated plan for the experiment, optimized system, collected data, had the idea for site selective imaging and wrote the majority of the manuscript. I.H.A. Knottnerus also had a major contribution to this publication.

- J. R. Weggemans, A. Urech, A. Rausch, R. J. C. Spreeuw, R. Boucherie, F. Schreck, C. J. M. Schoutens, J. Minář, and F. Speelman, *"Solving correlation clustering with QAOA and a Rydberg qudit system: a full-stack approach"*, Quantum 6, 687, 2022. (Related to Section 3.4 of this thesis)

  Contribution: Major contribution to proposing and analyzing experimental implementation. Contributed to writing of the manuscript.

- O. Onishchenko, S. Pyatchenkov, A. Urech, C. C. Chen, S. Bennetts, G. A. Siviloglou, and F. Schreck, *"Frequency of the ultranarrow $^1S_0$-$^3P_2$ transition in ^{87}Sr"*, Phys. Rev. A 99, 052503, 2019.

  Contribution: Major contribution to assembling optical systems and characterizing new ultracold strontium apparatus used to perform the experiment. Constructed the spectroscopy laser and the optical cavity lock setup. Helped with initial frequency estimate, performed spectroscopy measurements, and helped

to make figures of the final manuscript.

- I. H. A. Knottnerus, S. Pyatchenkov, O. Onishchenko, A. Urech, F. Schreck and G. A. Siviloglou, *"Microscope objective for imaging atomic strontium with 0.63 micrometer resolution"*, Optics Express 28, 11106 (2020).

  Contribution: Minor contributions. Confirmed microscope characterization and commented on the manuscript.

Acknowledgements

The journey of completing a PhD is filled with many trials and tribulations in the struggle to achieve results. The work presented in this thesis would not have been possible without the help and support of many people to which I owe a lot. I know that this short section of acknowledgments will not come close to showing my appreciation to everyone who has been a part of my life during this journey, but I will still try.

First I have to thank my Supervisors Florian and Robert. Florian, thank you for the support and the opportunity to be apart of the lab. From inspiring me to explore a field that was totally new to me in my Master's degree, to the faith you had in my ability to figure out the problems of the experiment, to the shared enjoyment and excitement of nice results well earned, I appreciate all the time that we have spent together. You are a brilliant and contagiously motivated researcher. Robert, thank you as well for your support and endless answers to all my random questions. You are always ready with a great answer even if it means making a quick Mathematica notebook to calculate it! You have helped to increase my understanding of many different topics and been a large part of the work over the last five years. You also have impeccable timing for showing up in the lab in time for nice results! Thank you also to Klaasjan and Ben for the stimulating conversations over the years.

Thank you also to my committee members. Most of you I have known through most of my PhD and it has been a pleasure getting to discuss with you.

I want to thank the members of the SrMic team that have worked with me on the experiment throughout my time in the lab. Georgios, Sergey, and Oleksiy, thanks for your help learning about lasers and how to cool atoms during my Master project and for designing and constructing the main chamber and coils of our machine along with many of the initial injection locked lasers for cooling. It was fun working with you guys and getting our nice spectroscopy results and starting the tweezer project. Scott, thanks for your work with 767-nm laser and the fun couple days seeing the increase in red MOT atom number from your project. Thies, thank you for the time you spent in the lab as well.It was great to have your energy come into the lab and thank you for the great work you did constructing the Rydberg laser system that we are now putting to work. Jiri, thanks for all the great discussions over possible ideas for the experiment and your help with the qudit calculations and the large feat of assembling

all of this work into a beautiful paper. I look forward to finally getting to actually do some simulations soon. Ivo, I will never fit my thanks to you in a couple sentences. You are an amazing guy and great friend. I appreciate so much all the hard days of work, frustrating failures, great successes and results, and fun times we have spent together. I do not think many of the results of this thesis would have been possible with out your help. Having you in the lab and as a friend has been invaluable!

Next, I would like to thank the rest of the strontium BEC group at the UvA. I have enjoyed working with all of you, both past and present. More specifically, I want to thank some individuals starting with my colleagues whose experiment occupied the same room as ours, the SrPAL team. Benjamin, you taught me so much. I am grateful for all the times you helped me to debug problems. You approach problems with such a cool and collected manner that was always helpful to calm down a frustrated PhD student like myself at times, I am really grateful for that. Shayne, thanks for always having an ear to bounce random ideas off even in the late hours of the evening and your help in general. Chun-Chia thanks for the many great conversations and help with lasers and electronics. I learned a lot from you and enjoyed our time in the lab together. Rodrigo, thanks for all the time together in the lab, we started our PhD's basically at the same time and it was a pleasure to have you in the lab with me through out the years. Thanks for all the jokes, Disney music jam sessions, random singing, venting out of frustrations and friendship. Junyu, It has been nice having you around in more recent times as well!

Moving to the room next door, I would like to thank my colleagues from the RbSr experiment. Vincent, thanks for the help with laser maintenance of many of the critical lasers of the lab and for many nice conversations in the lab or over lunch. Lukas, thanks for the help with many problems and the encouragement to push on when the struggles got tough, I appreciate the time we got to spend together and the things that I learnt from you. Mateusz, thanks for the fun conversations, jokes, and great answers to random atomic/molecular physics questions that I would come up with. Severin, thanks for the nice conversations, friendship and fun times outside the lab! Prem, we have also had the opportunity to spend a lot of time together. Thanks for all the great quick conversations on random ideas, debugging tips, for always responding to my random yells of your name across the lab and for lots of great times in and out of the

lab, you are a brilliant and super friendly guy, it has been a pleasure to have you next door and as a friend.

Now to move across the hall to the clock teams. Francesca and Sheng, It has been to have you two across the hall over the past few years, thanks for the help with supplies, locked laser light, and tips on electronics. Camilla and Benedikt, It has been to get to know you two as well, and best of luck with your projects! Stefan, thanks for many nice discussions and useful tips as well. To all the newer group members, I look forward to working with you more as well. Also on the same side of the corridor, we have Rene's groups. Rene, thank you for many nice conversations over the years, it has also been to see your group grow! To the past and present members, thank you all for the help with borrowing supplies or wavemeter ports. It has always been nice to have kind colleagues doing Similar stuff to discuss with and share useful tips and supplies in a pinch. Norman, it was great to meet you and have such a close friend across the hall as well. Thanks for all the great times outside the lab and quick chats over a break.

I also have to thank all the members of the mechanical and Electrical workshops here at the UvA. Your help with designing, and debugging different pieces of equipment for the experiment is also crucial to the results presented in the thesis. Special thanks to the people who I frequently interacted with including Hans, Daan, Sven, Tristan,Jan, Johan, Tjeerd, Tijs, Gerrit, Gertjan and Alix.

I want to thank all my friends over the years in Amsterdam. You have all made these years so great and I can't thank you enough for that. Thanks for many nice days/evenings of random drinks, meals, parties, vacations and so many other great times. Thank you Anjelika, Giac, Eric, Grace, Kelly, Fen, Gijs, Henrique, Lara, Toni, Deniz, Yasmin, Koen, Donya, Kandi, Antigone, Jack, Clay, Jake, Tony and all the others I am forgetting for all the great times. Special thanks to Eric, you have been one of my closest friends over the years, it has been great to have you around. Also Oswald, thanks for all the crazy conversations (and sometimes arguments) over the years and fun trips and experiences together. You are a unique character, but so am I, which is maybe why we enjoy each others company. Thanks to my roommates, Al, Erdem, Tracian, Venuri, Gray, Stefan, and Andrea for making a great place to call home. Thanks also to all my friends from aboard and back home, Rich, Drew C., Drew F., Jason, Pete, Josh, Al, Mary Ann, Derrick, Brandon and many more that I am sure I am forgetting

for your support not only in my time in Amsterdam but also in the many years before. There are have been too many great times to count with all of you.

Thank you to my extended family in Suriname and Canada (and my few cousins else where) for all your support and encouragement over the years. The love I feel from all you is tremendous and your support has been very important to me, thank you so much. Also to my family here in the Netherlands, thank you so much for everything and your help over the years. You made moving across an ocean easy to call Amsterdam home so much easier. And to my immediate family. Thank you to my parents, Ron and Soraya, your support throughout my life has allowed for me to get to this point. Without you I could have never accomplished this or many other things in my life, thank you so much for everything. Thanks mom for the endless encouragement and blind belief that I will figure things out. Thanks Dad for all the invaluable experience working together in the shop for so many years, working at ICCTech is still some of my greatest memories. Diandra, thanks for always being an awesome sister, thanks for the many fun times we have had together. It has been an honour to be your big brother and see you grow and all the things you have accomplished. Daniel, I miss you everyday. I wish you were you here to pick up this book and make fun of me how much of a nerd I am. Some days I wish for nothing more than to be able to pick up the phone and here your voice. I know you would be proud of me if you were here today.

Last, but definitely not least, I have to thank Dani. We started hanging out on the first day of my PhD, so you have literally been around the whole time. You have brought me so much joy and amazing experiences over the years. Thank you for going on so many fun trips with me, for all the great adventures around Amsterdam, and for the many great days just spent hanging out together. I cherish every moment we get to spend together. Thanks for your understanding and compassion when I was stressed and for putting up with my craziness. I love you and look forward to our many adventures to come.

Completing a PhD is no easy task. I wouldn't have made it to this point without all the help. Thank you all for the help, support and friendship over the years and thank you to those I forgot to mention.